

Symmetry-Breaking Bifurcations and Reservoir Computing in Regular Oscillator Networks

vorgelegt von

M.Sc. André Röhm
geboren in Wolgast

Von der Fakultät II – Mathematik und Naturwissenschaften

der Technischen Universität Berlin

zur Erlangung des akademischen Grades

Doktor der Naturwissenschaften

– Dr. rer. nat. –

genehmigte Dissertation

Promotionsausschuss:

Vorsitzender: Prof. Dr. Michael Lehmann
Berichterin: Prof. Dr. Kathy Lüdge
Berichter: Prof. Dr. Ingo Fischer

Tag der wissenschaftlichen Aussprache: 16. November 2018

Berlin 2019

Abstract

The focus of this thesis is the investigation of regular oscillator networks with numerical and analytical tools. Such systems are ubiquitous in nature and can emerge in the shape of vastly different processes. Among others, they can be mathematically derived as discrete approximations of continuous wave equations or as a local approximation of coupled dynamical systems. In the most basic meaning of the word, an *oscillator* is a system that shows a periodic change in one of its state variables. This thesis will focus on two different mathematical models: The Stuart-Landau oscillator that is popular in bifurcation theory and the more applied Lang-Kobayashi model for laser dynamics. Lasers can be seen as optical oscillators and they are most accessible of all oscillatory systems for precise and fast experiments.

Many previous works have covered different aspects of coupled oscillators, with some effects such as synchronization having been studied in some form for more than three centuries. The overall literature on the topic of coupling-induced dynamics is vast, and many different subtopics can be identified, such as the influence of delay, the application of control schemes, the properties of biological and artificial neural networks, the causes of chaotic motion or the importance of stochastic processes. The focus in this thesis will be on highly symmetric networks of coupled oscillators, where the local dynamics follow very simple models. The focus is therefore on the coupling-induced effects in general and not on elaborate and extremely detailed descriptions of specific experiments. However, because the effects of coupling and especially those connected to symmetries are in some sense universal, generic models for oscillators and lasers more than suffice for the investigations done here. A particular focus will be on the emergence of symmetry-broken states in rings of oscillators. Several different novel aspects of these symmetry-breaking states are discussed and their connections to the established solutions from the literature are explored.

The second part of this thesis concerns itself with one of the possible uses of such oscillatory and laser networks: The neuro-inspired machine-learning concept called 'reservoir computing'. This neuromorphic computing approach allows the exploitation of the intrinsic complex behaviour of driven dynamical systems for analogue computing. The usability of regular networks of oscillators will be explored. Furthermore, as reservoir computing still suffers from a lack of quantitative theory, a few fundamental aspects of reservoir computing will also be explored with the help of the examples in this thesis. As will be shown, hybrid delay-network systems can be created that are very suitable as reservoir computers.

Deutsche Zusammenfassung

Diese Doktorarbeit beschäftigt sich mit den dynamischen Eigenschaften von regulären Netzwerken nichtlinearer Oszillatoren. Diese Systeme sind paradigmatisch für eine große Klasse von Effekten und erscheinen in verschiedensten Formen in der Natur. Unter anderem können Netzwerke von Oszillatoren als Näherung für Wellengleichungen in linearen und nichtlinearen Medien hergeleitet und viele gekoppelte komplexe System durch gekoppelte nichtlineare Oszillatoren angenähert werden. In der simpelsten und weitesten Definition ist ein *Oszillator* schlicht ein physikalisches oder mathematisches Modell, dessen wesentliche Eigenschaft die periodische Änderung mindestens einer ihrer Größen ist. In dieser Arbeit werden zwei Arten von oszillierenden Systemen untersucht werden: Zum einen das mathematische, abstrakte Modell des Stuart-Landau-Oszillators, zum anderen das physikalisch komplexere Lank-Kobayashi-Modell für Laser. Laser können als optische Oszillatoren gesehen werden und sind daher eines der besten Systeme zur experimentellen Erforschung der Dynamik nichtlinearer Oszillatoren.

Die wissenschaftliche Literatur zu gekoppelter Oszillatoren kann in Teilen auf eine lange Geschichte zurückgreifen. Synchronisierung wurde beispielsweise das erste mal bereits vor mehr als drei Jahrhunderten beschrieben. Daher ist die Zahl der wissenschaftlichen Arbeiten zu gekoppelten Oszillatoren und oszillierenden System sehr groß und beschäftigt sich mit vielen verschiedenen Themen, wie zum Beispiel dem Einfluss von Verzögerungen, Kontrollansätzen, biologischen und künstlichen neuronalen Netzwerken, den Ursachen deterministischen Chaos oder den Eigenschaften stochastischer Prozesse. Das Themefeld dieser Arbeit wird sich daher auf Netzwerke von hoher Symmetrie beschränken, wobei zusätzlich die lokale Dynamik möglichst simpel gehalten ist. Der Fokus liegt auf den durch die Kopplung verursachten Effekten, wodurch simple Modelle genügen. Da Symmetrie aber ein allgemeines Konzept der physikalischen Wissenschaften ist, können auch bereits in simplen Modellen viele relevante Effekte untersucht werden. Ein großer Fokus dieser Arbeit ist das Entstehen von symmetriebrochenen Lösungen in Ringen von Stuart-Landau Oszillatoren. Verschiedene neue Eigenschaften dieser symmetriebrochenen Zustände werden erörtert und in Bezug zu den bereits aus der bisherigen wissenschaftlichen Literatur bekannten Lösungen gesetzt.

Der zweite Teil dieser Arbeit untersucht eine der möglichen Anwendungen solcher Ringnetzwerke mit nichtlinearen Oszillatoren. Das neurologisch inspirierte ‘Machine Learning’-Konzept unter dem Namen ‘Reservoir Computing’ erlaubt die Ausnutzung der intrinsischen Rechenkraft dynamischer Systeme als analoge Computer. Die Nutzbarkeit von regulären Netzwerken bestehend aus Stuart-Landau-Oszillatoren wird untersucht. Das Gebiet des ‘Reservoir Computings’ besitzt noch keine ausgereifte quantitative Theorie, weswegen ein wesentlicher Teil dieser Arbeit die Erforschung einiger grundlegender Aspekte ist. Desweiteren wird ein neues System von Netzwerken mit verzögerter Kopplung untersucht und es wird gezeigt, dass diese sich sehr gut als analoge Computer eignen.

CONTENTS

1	Introduction	1
1.1	Mathematical description of physical phenomena	1
1.1.1	Nonlinear dynamics and lasers	3
1.2	Machine learning	5
1.2.1	History of computers	5
1.2.2	The drawbacks of explicit programming	6
1.2.3	Learning for Machines	7
1.3	Aim of this work	10
1.3.1	Interdisciplinary study	10
1.3.2	Structure of the thesis	10
2	Theory	13
2.1	A short overview of nonlinear dynamics and dynamical systems	13
2.1.1	Ordinary differential equations and mathematical formalism	13
2.1.2	Fixed points, limit cycles and stability analysis	14
2.1.3	Bifurcations	17
2.1.4	Numerical Integration	18
2.1.5	Delay-differential equations	18
2.2	Network theory	21
2.2.1	Introduction to networks: Nodes and links	21
2.2.2	Network topology and the adjacency matrix	23
2.2.3	Real networks and symmetries	25
2.2.4	Connection to spatially extended systems	26
2.2.5	Synchronization	28
2.3	Local model: Stuart-Landau oscillator	30
2.3.1	Derivation of the Stuart-Landau oscillator equations	30

CONTENTS

2.3.2	Andronov-Hopf bifurcation	32
2.3.3	Stable states	33
2.3.4	Literature overview: Stuart-Landau oscillator networks	36
2.4	Local model: Lang-Kobyashi-type equations	38
2.4.1	Laser history	38
2.4.2	Equations and dynamics	38
2.4.3	Reduction of the LK-equations to the Hopf-Normal form	40
2.4.4	Literature overview: Laser dynamics	41
2.5	The reservoir computing paradigm	44
2.5.1	Supervised machine learning and artificial neural networks	44
2.5.2	History of reservoir computing	47
2.5.3	Modern formulation	48
2.5.4	Mathematical details	52
2.5.5	Suitability of delay-systems for reservoir computing	53
2.5.6	Virtual networks	57
2.5.7	Benchmark tasks for reservoir computers	58
2.5.8	Analogue computing: non-von-Neumann architectures	64
2.5.9	Literature overview of reservoir computing	66
3	Symmetry-breaking in networks	69
3.1	Two coupled Stuart-Landau Oscillators	70
3.1.1	Symmetries of the system	71
3.1.2	Symmetric solutions	72
3.1.3	Symmetry-broken solutions	78
3.2	Two coupled Lang-Kobayashi-type lasers	86
3.2.1	Equations and symmetries	86
3.2.2	Solutions and their stability	88
3.3	Unidirectional ring networks	96
3.3.1	Unidirectional ring of Stuart-Landau oscillators	96
3.3.2	Special solutions: Rotating wave patterns or "Ponies on a merry-go-round"	97
3.3.3	Unidirectional ring of 4 oscillators	99
3.3.4	Symmetry-broken solutions for $N = 4$	106
3.3.5	Large unidirectional rings	110
3.3.6	Unidirectional rings with delay	114

3.4	Bidirectional Rings	117
3.4.1	Bidirectional ring of Stuart-Landau Oscillators	117
3.4.2	Symmetry-broken solutions in the bidirectional ring with $N =$ 4	125
3.4.3	Large bidirectional rings	128
3.4.4	Bidirectional rings with delay	137
3.5	Discussion	140
3.5.1	Outlook: Symmetry-breaking and small chimera states in laser networks	140
3.5.2	The role of symmetries for regular oscillator networks	143
4	Reservoir computing in networks	147
4.1	Single-node with delay	148
4.1.1	Stuart-Landau oscillator with delayed feedback	148
4.1.2	System parameter scan for NARMA10 task	151
4.1.3	Parameter scan of the memory capacity	156
4.1.4	Influence of the system timescales	162
4.1.5	Influence of hyper-parameter K_{training}	167
4.1.6	Possible extensions	170
4.2	Time-multiplexed Networks	172
4.2.1	Time-multiplexing in networks	172
4.2.2	Real and virtual nodes	173
4.2.3	Stuart-Landau time-multiplexed network equations	175
4.2.4	Importance of the system size	175
4.2.5	Constructing networks of constant size	177
4.3	Reservoir computing results for time-multiplexed networks	181
4.3.1	Unidirectional ring network	181
4.3.2	Unidirectional ring with jumps	185
4.3.3	Bidirectional ring	189
4.3.4	Bidirectional ring with self-feedback	191
4.3.5	General influence of the number of real nodes N_R	194
4.4	Discussion	199
4.4.1	Results	199
4.4.2	Towards a quantitative theory	200

CONTENTS

5	Conclusions and Outlook	205
A	Appendix	209
A.1	Symmetry-broken amplitude and phase-coupling	209
A.1.1	Analytical symmetry-broken solution	209
A.2	Unidirectional ring networks	212
	List of Figures	217
	List of symbols	221
	List of acronyms	222
	Bibliography	I
	Acknowledgements	XVII

1.1 Mathematical description of physical phenomena

Recent centuries have had an astounding explosion of knowledge, innovation and living standards. Many have credited this seemingly unstoppable progress of technology to the increasing trust in and application of 'the scientific method'. Scores of famous scientists have left their mark on history with ground-breaking ideas and revealing truths, allowing successive generations to build upon the knowledge of their predecessors. Often Galileo Galilei is credited with the invention of a form of scientific method in modern shape, with his focus on experimentation and observation. However, it is not only the measurement or the experiment that advances knowledge. The history of science in general and physics in particular is also strongly intertwined with the development of ever more sophisticated mathematical tools. One can roughly divide the evolution of these tools into three great categories.

Even the mathematicians of the classical antiquity knew how to solve and describe natural phenomena theoretically. They mostly relied on algebraic and geometric solution methods, allowing them to describe physical phenomena such as the motion of the stars, sun and moon in the sky or estimating the circumference of the earth. Many foundational findings of mathematics were first described in this first era of numbers and geometric shapes. These systems are *static* or *periodic* in nature, needing only the understanding of the current configuration to deduce their attributes. When the problems are geometric in nature, the methods of geometry suffice to solve them.

Arguably the biggest change for physics as a science was the arrival of modern calculus, as introduced by Sir Isaac Newton and Gottfried Wilhelm Leibniz. This sophisticated mathematical framework transformed and greatly enhanced the reach of physics. The powerful tool of differential equations and their analytical solutions allowed for a more quantitative description of natural phenomena, such as Maxwell's equations, the laws of thermodynamics, classical and quantum mechanics, and more. Because the prime object of calculus are functions, an inherent connection with a *dynamic, time-dependent* description of nature exists. The solutions of the differential equations represent the trajectories of the state variables

1 INTRODUCTION

of a system, but these trajectories may start at arbitrary configurations. Already within the framework of Newtonian mechanics and celestial motion the question of self-repeating or eternal solutions arose, which arguably represents the early beginnings of what would later develop into the field of nonlinear dynamics, i.e. the study of the stability of solutions of complex systems. Some solutions may be resilient against disturbances, e.g. Lagrange points in the three-body problem, while other solutions may easily diverge. Questions like these are investigated by stability analysis theory, which is a formalisation of the methods applied by the first adopters of calculus. This *era of differential equations* can be said to have been a second spring of physics.

Despite the ongoing great success and prevalence of differential equations, one could argue that we currently experience the transition to a third mathematical revolution of physics: the era of numerics. This directly ties into one of the great problems of nonlinear dynamics and the differential equation framework: Despite their great success in describing nature, many of the more complex and nonlinear problems are hard or impossible to solve analytically, i.e. purely by hand or deduction. One prime example are the Navier-Stokes equations, which despite being known for well over a century, still lack definitive proof for many of their mathematical properties [DOE09a]. Fields that profit immensely from this new trend are those, where limiting approximations are rare and the physics cannot be simplified without loss of descriptive power, such as soft matter, mesoscale systems or systems with many interacting elements. Where analytics fail, numerics allow us (given enough computing power) to investigate even the most complex equations. This in turn also often gives circumstantial evidence for new hypotheses - that in turn then can sometimes be proven analytically again.

The era of numerical simulations is a golden age for nonlinear dynamics: Not only can differential equation systems be numerically integrated to obtain 'numerical experiment data', but also the methods of path continuation allow a direct investigation of the stable objects that organize these systems. Tools such as `AUTO` or `ddeBiftool` allow the direct numerical investigation of the complex interaction between different stable and unstable solutions of a given system. This ansatz would have been entirely futile only a few decades ago, when such computations would have been too costly in terms of computation time. Despite the intrinsically numerical approach, one should not think of these methods as inferior to the analytical approaches: A large body of mathematical works is concerned with proving and refining the accuracy of numerical integration methods. Numerics are therefore not just a new way, but also, if used correctly, a reliable method to explore complex systems.

1.1.1 Nonlinear dynamics and lasers

Since its inception, nonlinear dynamics has had a very close connection with laser physics. The field of laser dynamics is at least as old as the first demonstration of a Ruby-based laser by Maiman in 1960 at Bell Labs [MAI60]. Early semiconductor laser devices were only able to operate under extreme cryogenic cooling and in a pulsed mode, as the optical and electric losses were too high to sustain a constant intensity operation. But the first semiconductor lasers capable of *continuous wave* (cw) output followed soon after. As early as 1969 Broom [BRO69] noticed however, that even these advanced devices could switch to a pulsed operation, if an external reflection of the laser light re-entered the laser cavity - i.e. if a delayed optical feedback disturbed the laser.

Not only did this susceptibility to optical feedback pose a problem to the usability of such devices, but it also proved to be pathway to dynamical richness. Both from the fundamental aspect of trying to understand this behaviour and the simple engineering goal of optimizing the devices, the field of nonlinear laser dynamics was eventually born.

At the same time, the seminal work of Edward Lorenz began to investigate the causes, effects and properties of chaos in meteorological systems [LOR63]. While calculating time traces of large scale weather patterns with the help of a 1960 supercomputer, he noticed a peculiar effect: Whenever he stopped the calculation and restarted them at a later stage, the new calculations would dramatically diverge from the old ones after a while. The reason turned out to be related to *how* Lorenz re-entered the data: When the program was re-started, the digital numbers were not reinstated to their entire length, but only the leading digits were marked down. Further experimenting revealed that *any* deviation of initial conditions would lead to an eventual divergence of time traces. Lorenz used the term 'deterministic non-periodic flow' to describe this astonishing phenomenon, which nowadays is called 'Chaos'. This is another example of a novel type of science that was only possible with the help of digital computers.

For the large-scale weather patterns of this world, the findings of Lorenz would mean that even one additional flap of a butterfly's wing could eventually decide whether a storm appears on the other side of the planet or not. This notion is now famously known as the 'butterfly effect' and describes the extreme susceptibility of chaotic systems to initial conditions.

Lasers are also able to exhibit chaotic dynamics. Lang and Kobayashi presented a simple yet powerful numerical model to describe lasers subject to external feedback [LAN80b], which now are called the Lang-Kobayashi equations. The works of Rosanov in the Soviet Union even partly predate the Western literature. Important aspects of the mathematical description of laser systems subject to optical feedback

1 INTRODUCTION

is the notion of time-delay and feedback-induced bifurcations. Nowadays people have come to understand that the complex dynamical behaviours of lasers, initially likely thought of as a purely detrimental effect, can also be exploited for several applications. One obvious application is the generation of random numbers with the help of optical devices. A more advanced application is the masking and encryption of data within the chaotic time-trace of a laser, called Chaos Communication.

One of the main aspects of laser dynamics is the interplay of the phase and amplitude of the electromagnetic field of the laser. Lasers therefore represent just one specific example from the more general field of 'oscillator dynamics'. In particular, this thesis will also deal with amplitude oscillators, which can always be seen as an abstract version of a laser. The laser is the most easily experimentally accessible example of an amplitude oscillator, and thus many important aspects of the theoretical side have also first been discussed in the context of lasers.

Currently, nonlinear dynamics seems to be on the verge of undergoing another massive transformation due to the influx of new ideas and concepts from machine learning.

1.2 Machine learning

Machine learning has shown rapid advancements in recent times and is one of the fastest growing scientific fields. It is related to a lot of high-impact publications and will play an important role in the last part of this thesis. This short introduction only covers the concepts necessary to understand the thesis at hand, machine learning as a whole, however, is too large of a field.

1.2.1 History of computers

‘Computer’ was originally the name of a profession, not that of a machine. A person performing computations, i.e. additions, multiplications or divisions of numbers professionally was a ‘computer’. Armed with tools like the abacus and logarithmic tables, a group of ‘computers’ was used to numerically solve a given problem. For example, famous physicist and noble prize winner Richard Feynman himself was part of the leadership of such a group of human computers in the Manhattan project in the 1940s. The scientists would decide on all the parameters, formulas and solution methods to be used and construct a set of instructions. The task of the computers then was to merely follow these instructions - as fast as possible and up to a certain level of precision, i.e. significant digits. The scientist would then look at the results and interpret them.

Of course, the human mind, ever eager to reduce work load and increase efficiency has devised machines to help with the monotonous task of adding, subtracting etc. The first generation computer machines were entirely mechanical, with later punch-card based systems and electro-mechanical computers (which were in use during the time of the Manhattan project). These still required a human operator though - someone to input the current input, someone to power the crank or to read and record the output. Despite their apparent primitiveness these machines are the spiritual ancestors of our modern day digital computer systems. What connects them, is the need for *instructions*. Be it the human hand pulling a mechanical crank, a punch-card or a modern program, every computer needs and merely executes instructions.

The central processing unit (CPU) of modern computers has a set of instructions that it can execute, as did the old mechanical computers. These instructions could be the addition of two binary numbers, or a logical evaluation of a Boolean system state. As Alan Turing proved, if these basic instructions are powerful enough (and contain memory with read/write operations), a machine can become a *general computer*. We call these systems ‘Turing-complete’ in the inventors honour, and they are capable of emulating all other computers. And while much less obvious, this instruction-imperative even holds true for modern smartphones: Modern electron-

1 INTRODUCTION

ics are not fundamentally different than their primitive counterparts. The CPU of a modern computer only understands the instructions it is capable of performing. But instructions can be combined to produce much more complex behaviour, especially when the CPU is as fast as a modern one.

The CPU can only execute instructions if it gets them in the only language it understands - machine code. Many of the programs for the first electronic computers were directly written in this language of machine-readable instructions. In contrast, modern programmers no longer directly write machine code and even may no longer understand in detail which instructions will eventually be executed by the CPU. Many modern programs and Apps are developed using higher-level programming languages such as `C/C++` or `Fortran`. These programming languages are not readable for the CPU. A compiler or an interpreter (for script-based languages such as `Python`) is needed to translate the ‘Human-readable’ instructions into ‘machine-readable’ code. For many users of computing systems, e.g. smartphones, the graphical user interfaces acts as another layer between them and the actual instruction-based computing. The fact that at the core of every digital computer an array of nanometre-scale NAND-gates merely stupidly follows a fixed set of instruction, not unlike how the human computers of old followed the instructions of their supervisors, can easily be forgotten.

In view of this, the hunt for the holy grail of computer science - artificial general intelligence - may appear like a folly. After all, the only (certain) example of high-level intelligence we know of are humans themselves. And a typical human does not have a clearly identifiable set of instructions that they are mechanically following. Much the opposite, the human mind seems messy, containing conflicting emotions and goals and is never static. Nevertheless, the dream of emulating and reaching human-level intelligence or aspects thereof has become more realistic in recent years with the arrival of several astonishing advancements in the field of machine learning.

1.2.2 The drawbacks of explicit programming

The imperative nature of modern computers has some advantages and disadvantages. The ability to always reconstruct (at least in principle) what the system is doing step-by-step to illuminate possible problems or understand the behaviour of a program is valuable in maintaining control and fixing errors. Furthermore, as these instructions are written for a general-purpose computing system there are often ways to transfer a program from one machine to another, even when they are not identical models. However, on the other hand every single instruction is ultimately derived from the explicit computer code of a developer or programmer. In a sense, this means that the written code cannot exceed the intelligence of its

creator. The programmer has to understand the scientific or practical problem they are trying to solve and has to come up with an explicit algorithm to arrive at the desired solution under all possible conditions. This is usually done by imagining how a human would solve the problem at hand and breaking that into easy steps.

Explicit programming is complicated by the fact that many of the more hidden workings of the human mind are not consciously accessible, e.g. we do not control every single individual muscle consciously when climbing stairs while holding a cup of tea. However, this directly leads to a problem: when the programmer does not understand how they themselves solve a problem, how can they make an explicit algorithm to do it? And in fact, the motion control of robots is a difficult problem - despite the ease with which even children learn to walk.

In 2016 Google Deepminds AlphaGo [SIL16] program defeated Lee Sedol, one of the best Go players of the world. It can be assumed that none of the programmers would have actually been able to defeat Lee Sedol themselves. Nevertheless, they managed to create a program that was *better than their creators* at playing Go. At first glance, this may seem to be similar to when *Deep Blue* defeated G. Kasparov in western chess for the first time in 1996. However, that defeat was enabled by a combination of clever programmer heuristics for chess coupled with the brute-force combinatorial power of a 1996 supercomputer. Disparagingly, it could be said that *Deep Blue* merely won by being able to virtually try out many orders of magnitude more moves than Kasparov. Go on the other hand is a game that has many many more positions [SIL16]: The average length of a chess game is 80 turns, with an average of 35 relevant legal moves per position. Go games last for 150 turns and have about 250 legal moves per position. Because the game is so much more complex ($35^{80} \ll 250^{150}$) it is harder to solve by pure-brute force tree search.

To successfully play Go, a player needs to decide *where* to concentrate their attention. Thinking or computational power should not be wasted on moves that will never yield victory. However, to observe a board position and find the critical moves to investigate is one of these abilities that human players only develop to do intuitively after many hours of gameplay. If the programmer trying to write a Go program would understand how to decide which moves are critical with an explicit algorithm, they would likely be a Go grand master themselves. Nevertheless Google Deepminds AlphaGo defeated Lee Sedol - with the power of *machine learning*.

1.2.3 Learning for Machines

Machine learning is the method of creating the instruction sets for computers not by explicit deduction, but by training. In the end, the code will still be run on a general purpose computer, but the set of instructions are not derived step-by-step by some programmer. The way that the program is created itself more looks like a

1 INTRODUCTION

numerical approximation. Important elements of Machine learning are *goal functions* that allow the quantitative evaluation of the learned behaviour and *learning rules* to improve the behaviour. Many different machine learning algorithms exist, suiting different needs and having different strengths and drawbacks. Many of these machine learning algorithms rely on a long and difficult *training stage*, where a lot of data is required. One could even argue, that machine learning substitutes large amounts of data instead of understanding the problem. The aforementioned AlphaGo program was trained on a large set of professional Go games [SIL16] to learn the important aspects of professional play.

An easy example to illustrate one form of machine learning are evolutionary algorithms. Evolutionary algorithms are a form of meta-programming, whereby a program or meta-algorithm is designed that in turn produces another program. Evolutionary algorithms are inspired by the process of natural selection and work as follows: For a given task, such as playing a game or predicting a quantity from data, a vast program with many free parameters is created. Imagine, that the instruction set of this vast program may consist of thousands of lines, and somewhere in the central part is a line that states to multiply some state variable with the free parameter a . The human instructor does not know what the optimal value of this parameter a should be to produce a well-functioning program, especially when combined with the other free parameters of the system b , c , d etc.

Instead of deciding on any specific set of the free program parameters, multiple instantiations of the program are randomly produced, each with different parameters. This set of semi-randomly produced programs is called the ‘first generation’. Some of these programs will perform better than others. However, as they are all randomly generated, in general all of them will perform horribly. The *goal function* can now be used to rank the program parameter sets in order of their performance from best to worst. From this first generation, only the best performing programs are kept, while the rest is discarded. This is similar to biological evolution, where only the fit specimen survive and generate offspring, while the others die out. A ‘second generation’ of programs is produced by inheritance, recombination and mutation/alteration of the free program parameters of the parent generation. Merely copying the parameter set of the original best cases of the first generation is not enough as this would never improve the performance. The technical details of the mutation, evolution and recombination steps can be complex and are an active field of research. All of them are inspired by the natural mutation active in the evolution of life forms. The second generation is also evaluated using the *goal function* and sorted similarly. From the best samples of the second generation a third generation is derived. This process repeats until a final generation is created or a performance threshold is reached. This approach represents a form of stochastic

exploration of the parameter space. The resulting program may contain elements or combinations of parameters that no human would have used.

It is important to stress, that the resulting program is of course still an imperative algorithm run on a CPU - but the steps of derivation are so far removed from normal programming, that this 'machine learning' must be classified as its own separate approach. Through the evolutionary process, the program can help solve problems, for which it is impossible to derive explicit algorithms. Evolutionary algorithms are just used as an illustrative example of machine learning; they are not used in this thesis. *Reservoir computing* is a different type of machine-learning and is especially connected to the idea of analogue computing. It will be discussed in the second half of this thesis.

1.3 Aim of this work

The aim of this work is to investigate the effect, causes and exploitability of the *intrinsic complexity* of *dynamical systems*, with a special focus on oscillator dynamics and networks. While the complexity will be explored with a focus on symmetry-breaking and non-trivial phase-locked states in regular oscillator, the exploitation of these dynamic systems is studied with the neuro-inspired machine learning concept of *reservoir computing*.

1.3.1 Interdisciplinary study

This thesis deals with questions at the interface of different fields of science. While the complexity of networks can be investigated with the tools of nonlinear dynamics, the actual models are deduced from real-world photonic systems like lasers or represent generic models of bifurcation theory from applied mathematics. When oscillator and laser systems are coupled in larger groups to form networks, the system can be treated within the general framework of pattern formation in complex networks. Despite being a specialized field of study, laser and oscillator network dynamics is still firmly within the realm of theoretical physics. Additionally, concepts from equivariance theory and group theory to describe the symmetries and symmetry-breaking patterns of the underlying system are borrowed from mathematics.

When the concept of reservoir computing is added, questions regarding computation, machine learning and analogue computing become important. This extends the involved disciplines to the information and computer sciences. The methods of applied mathematics and theoretical physics, however, are not misplaced in such an environment: Many of the current day rapid advances in machine learning are being conducted not by a meticulous study of basic principle, but are rather being advanced on concrete examples and applications. This leads to the whole field being advanced more as an engineering than a science problem by the programmers involved. The present thesis is an attempt to unify some of the concepts from these different disciplines. Some excellent reservoir computing reports have covered different aspects before and will be sufficiently highlighted.

1.3.2 Structure of the thesis

This thesis is divided into three main parts. The first main chapter, Chap. 2 starting after this brief introduction, discusses the general concepts and nomenclature of this thesis. Additionally, a literature overview is given for the different fields touched upon in this work. First, Sec. 2.1 gives a brief introduction to nonlinear

dynamics as a subfield of theoretical physics and applied mathematics. Practical questions of direct numerical integration are briefly discussed. Sec. 2.2 provides an overview of network science, with the concepts relevant to this thesis outlined, in particular synchronization. The notion and definition of networks, nodes and links are introduced. Then, two different local models, the Stuart-Landau oscillator and the Lang-Kobayashi-type laser equations, are introduced in Sec. 2.3 and 2.4. The theory chapter finishes with a brief introduction to supervised machine learning and reservoir computing in Sec. 2.5.

Chapter 3 is centred on the study of dynamics in networks of coupled oscillators and lasers. The focus is on the study of symmetry-broken states, especially those still exhibiting amplitude- and phase-locking. To this end, Sec. 3.1 first introduces the system of two instantaneously coupled Stuart-Landau oscillators. In this system, symmetry-breaking patterns can be found and the full bifurcation scenario can be analytically studied. This is then also extended and compared to results from the literature for the laser case in Sec. 3.2. These results are then generalized to ring networks, first to the unidirectional rings in Sec. 3.3 and then the bidirectional rings in Sec. 3.4.

The last main part shown in Chap. 4 is focused on the machine-learning inspired concept called *Reservoir Computing*, which aims to utilize the intrinsic computational power of dynamical systems. The dynamical systems in question in this work are the aforementioned oscillator ring networks. Sec. 4.1 reproduces the results for delay-based reservoir computing known from the literature with a Stuart-Landau oscillator model. The dependence on the system parameters, the training stage and on the system size is discussed. Sec. 4.2 introduces time-multiplexed networks, which incorporate elements from delay-based reservoirs and earlier echo state networks. Different topologies are investigated in Sec. 4.3. Finally, Sec. 4.3.5 discusses general size-dependent properties of time-multiplexed networks.

Chapter 5 summarizes the results of this thesis and discusses open questions for future investigations.

1 INTRODUCTION

2.1 A short overview of nonlinear dynamics and dynamical systems

This section gives a short overview of the general concepts of nonlinear dynamics, bifurcation theory and numerical integration. It does not go into all the details nor does it state the touched upon theories in full mathematical rigour. To get a full understanding, the reader is advised to consult one of the many introductory books to nonlinear dynamics, e.g. Ref. [OTT02] or Ref. [STR94a].

2.1.1 Ordinary differential equations and mathematical formalism

The theoretical description of natural phenomena hinges on the time evolution of physical variables. The important physical quantities to keep track of differ from problem to problem and can range from fundamental properties like position, mass or speed, to averaged or ensemble variables like temperature and pressure, and relative properties like phase differences or amplitude ratios. In general, any of these properties will be described by a time-dependent function $x(t)$ that measures the value of that physical quantity with some units. These system variables $x(t)$ are usually complex or real-valued numbers.

Many systems in nature can be described with ordinary differential equations (ODEs), which are a way to relate the derivatives of the physical quantities of a system with its current state. A general form for a D-dimensional time-domain ODE is:

$$\frac{d\mathbf{X}(t)}{dt} = F(\mathbf{X}(t), t, \rho), \quad (2.1)$$

where \mathbf{X} is the vector of state variables:

$$\mathbf{X}(t) = \begin{pmatrix} x_1(t) \\ \vdots \\ x_D(t) \end{pmatrix}, \quad (2.2)$$

2 THEORY

with D individual components $x_d(t)$, that each are time-dependent. The evolution function F describes how the system state changes with time t . In general, the right hand side of Eq. (2.1) will depend on a set of different parameters ρ that will also influence the evolution function $F(\mathbf{X}(t), t) = F(\mathbf{X}(t), t, \rho)$. To allow for explicit solutions, F needs to be known and its shape is usually deduced from fundamental laws and approximations thereof. For many systems where F is relatively simple, a full solution for $\mathbf{X}(t)$ for arbitrary starting values $\mathbf{X}(t_0)$, starting times t_0 and parameters ρ can be found. For example the solutions of the harmonic oscillator are derived in many university classes on ODEs. This level of description comprises the 'standard' analytical approach to describe physical systems and requires the scientist or engineer to be competent at analytically solving differential equations. For example, solving the time-independent Schrödinger equation for the hydrogen atom requires detailed knowledge of spatial functions.

However, in general such analytical solutions will only be possible for some of the observable behaviour in a system. If one solely relies on an analytical treatment of Eq. (2.1) one may falsely assume that periodic or asymptotically stationary behaviour are the only relevant solutions: However, dynamical systems can also exhibit *chaotic motion* for which standard analytical function approaches do not work [OTT02]. Furthermore, when the dependence on parameters ρ and system state \mathbf{X} becomes complex, Eq. (2.1) may become too hard to solve analytically.

2.1.2 Fixed points, limit cycles and stability analysis

Even when the direct treatment of Eq. (2.1) for a given problem is not possible, a weaker form of analysis may still apply. It is often useful to study the *steady states* or *fixed points* of a system $\mathbf{X}_{\mathbf{FP}}(t) = \text{const.}$ which do not change once attained. This directly implies that their derivative must be zero, i.e. $\dot{\mathbf{X}}_{\mathbf{FP}} = 0$, where the dot indicates the time-derivative. This corresponds to setting the left hand side of Eq. (2.1) to zero to obtain:

$$0 = F(\mathbf{X}_{\mathbf{FP}}, t, \rho). \quad (2.3)$$

This, for normal ODEs, leads to a set of coupled algebraic equations that need to be solved to obtain closed expressions for the fixed points $\mathbf{X}_{\mathbf{FP}}$ as a function of the parameters ρ . This approach can reveal multiple, or with symmetries even infinitely many, fixed points. There is no guarantee that Eq. (2.3) can be solved at all. The evolution function F can be arbitrarily complex and the resulting algebraic equations can become transcendental or non-polynomial or worse. Where no solution of even the algebraic equations is possible, the system has to be studied with other methods, either path continuation toolboxes like `ddeBiftool` or direct numerical integration (see Sec. 2.1.4).

2.1 A SHORT OVERVIEW OF NONLINEAR DYNAMICS AND DYNAMICAL SYSTEMS

A second type of solution that can be obtained relatively easily are *periodic solutions*, also called limit cycles $\mathbf{X}_{\text{LC}}(t)$. In general, a limit cycle is any solution to Eq. (2.1) that satisfies:

$$\exists T_{\text{LC}} : \forall t : \mathbf{X}_{\text{LC}}(t) = \mathbf{X}_{\text{LC}}(t + T_{\text{LC}}), \quad (2.4)$$

so that there is a period T_{LC} after which the limit cycles recovers its previous state. Finding limit cycles analytically in general is harder, as the object is a function instead of a simple set of unknown variables. Different strategies exist. In this thesis, only simple limit cycles will be studied where their shape can be deduced relatively easily without much effort. When drawn in a phase-space diagram, a limit cycle is a closed curve. Even higher-dimensional objects may also exist, such as quasiperiodic motion. When such a state is projected into phase space, it fills out a two-dimensional solution manifold, i.e. a Torus, from which the state $\mathbf{X}(\mathbf{t})$ never leaves once it is on that surface. Hence, quasiperiodic solutions are sometimes also called Torus solutions.

Stability of solutions

Some fixed points \mathbf{X}_{FP} and limit cycles $\mathbf{X}_{\text{LC}}(t)$ are stable, while others are not. The stability of a solution to Eq. (2.1) describes the evolution of a disturbance acting on that state. Without going into the formal mathematical definitions (see e.g. Ref. [OTT02]), a phenomenological description will suffice here: The stability of fixed points \mathbf{X}_{FP} and limit cycles $\mathbf{X}_{\text{LC}}(t)$ describes the reaction to infinitesimal deviations. If the system returns to the solution for sufficiently small perturbations, the fixed point or limit cycle is called *stable*. Accordingly, it is *unstable* if arbitrarily small perturbations lead the system to diverge. In general, the direction of the disturbance in phase space can determine if the system diverges or not. Hence, a system is only stable if it is stable for all possible deviations of sufficiently small amplitude. There can also be neutral modes, i.e. directions or states where perturbations neither decay nor grow. These definitions are formalized with Lyapunov stability analysis theory as presented in many introductory books such as Ref. [OTT02].

A simple example to illustrate fixed points and their stability is to consider a (perfectly cylindrically symmetrical) egg on a table. Fig. 2.1 shows an illustration of this. Trying to balance it such that it does not topple is difficult, but three different positions are possible: It can be balanced either on its top (Fig. 2.1 a)), on its bottom (Fig. 2.1 b)), or on its side (Fig. 2.1 c)) . Both the top and bottom positions are unstable, i.e. the egg will topple with the slightest disturbance (at least in the mathematical limits without friction). However, when laid on its side it is stable against small perturbations in most directions. It may oscillate for a

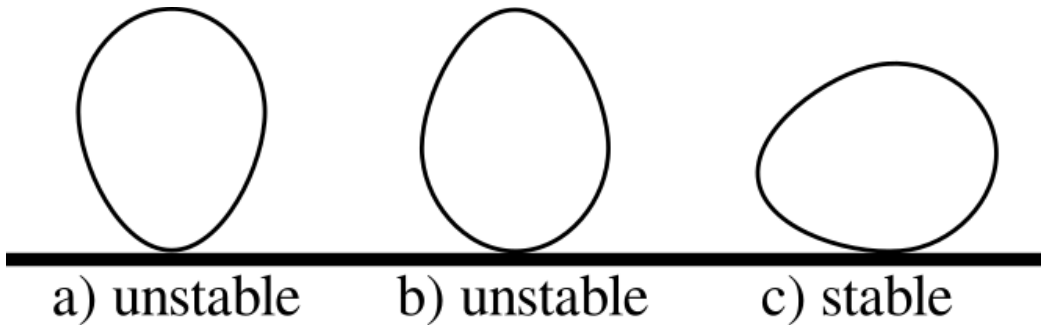


Figure 2.1: The three possible fixed points of balancing an egg: On its top, on its bottom and on its side. Only the last one is stable.

while, but it will eventually recover its rest position. The egg-example of Fig. 2.1 is also useful, as it illustrates the importance of symmetries as well: The egg is cylindrically symmetric, i.e. it can be rotated around its longest axis arbitrarily without any global change in its mass distribution or surface positions. This cylindrical symmetry is also apparent in the stable solution: the egg can be rotated around its symmetry-axis without problems, while being balanced on its side without inducing any transient motion. In fact, the symmetry of the system has led to a whole set of stable fixed points that are neutrally stable in the direction of the rotation around the axis of symmetry. The role of symmetries in shaping the solutions of a given system is not only important in this system, but is a general property of dynamical systems and will become important in later chapters.

The stability of a given fixed point \mathbf{X}_{FP} can be found with the tools of linear stability analysis. By linearising Eq. (2.1) around the fixed point \mathbf{X}_{FP} and deducing a differential equation for the evolution of a tiny disturbances $\Delta\mathbf{X}$, a system of linear algebraic equations is obtained, see the introductory literature for details, e.g. Ref. [OTT02]:

$$\frac{d\Delta\mathbf{X}}{dt} = \mathbf{J}(\mathbf{X}_{\text{FP}}, \rho)\Delta\mathbf{X}, \quad (2.5)$$

where \mathbf{J} is the Jacobian matrix of F evaluated at \mathbf{X}_{FP} . The eigenvalues of \mathbf{J} define the stability of the fixed point \mathbf{X}_{FP} . If all eigenvalues are negative, \mathbf{X}_{FP} is linearly stable. If some are positive, \mathbf{X}_{FP} is unstable in the direction given by the corresponding eigenvector. These eigenvalues are also called Lyapunov-exponents λ and the largest or ‘leading’ eigenvalue λ_{max} determines the long-time behaviour of a random perturbation $\Delta\mathbf{X}$:

$$\Delta\mathbf{X}(t) \approx \Delta\mathbf{X}(0)e^{\lambda_{\text{max}}t}. \quad (2.6)$$

2.1 A SHORT OVERVIEW OF NONLINEAR DYNAMICS AND DYNAMICAL SYSTEMS

Like fixed points, limit cycles can be stable or unstable. Advanced linear stability analysis tools have to be used to investigate the stability of periodic solutions, like the Poincaré projection.

Most systems in nature contain at least some small amount of noise due to coupling to their environment and parameter drift. Thus, any state that is linearly unstable will decay due to these fluctuations on long enough time scales. If the noise is small, it can be easily justified that the system state at any given time will be very likely close to a stable steady state, stable limit cycle or another stable solution. Studying the linear stability of all solutions of a system therefore allows for the abstract deduction of all possible long-term behaviours without the need of an explicit analytical solution. Because ODEs can describe vastly different problems, this method has been successfully applied to such different fields as the stability of predator-prey systems [LOT20, VOL26a], the long-term evolution of alien civilizations exploiting the planetary resources of their host planet [FRA18] and to determine the dynamics of a laser, as is done in this thesis, see for example Sec. 2.4.

2.1.3 Bifurcations

So far, the dependence of the solutions of ODEs such as Eq. (2.1) on the parameter set ρ has been addressed in detail. It is clear, that the shape of the solutions will in general depend on the parameters ρ and so will their stability. However, it is even more important to realize, that even the existence of some solutions may be dependent on the parameters. When the solutions are analytically derived in a system, one automatically gains this additional information. The analytical deduction will yield necessary conditions on the parameters for their existence.

In the simplest case, one is interested only in the influence of a single parameter ρ_i . Then, the solution may only exist for a large enough $\rho_i > \rho_{crit}$. Similarly, ρ_{crit} may signify a point where the stability of a solution changes. The points where solutions change their stability, are born or destroyed, i.e. $\rho_i = \rho_{crit}$ are the *bifurcations points*. A *bifurcation* is the qualitative change of the set of solutions or their relationship in phase space of a dynamical system. Bifurcations occur at critical parameters, and they appear in a variety of shapes. Bifurcations are the subject of bifurcation theory and play an important role in the analysis of nonlinear dynamical systems. Bifurcations may affect fixed points \mathbf{X}_{FP} , limit cycles \mathbf{X}_{LC} and any other solution. Bifurcations can be deduced analytically, with path continuation methods or be deduced from the qualitative behaviour of numerical simulations.

2.1.4 Numerical Integration

The numerical integration of differential equations allows for a third way of analysing the structure of solutions and time-series. Instead of trying to solve Eq. (2.1) directly, a discretisation is used: The time is divided into small parts h that represent a single step, and Eq. (2.1) is transformed into an algebraic map:

$$\tilde{\mathbf{X}}(t+h) = \tilde{\mathbf{X}}(t) + hF(\tilde{\mathbf{X}}(t), t). \quad (2.7)$$

This is called an explicit method and allows numerically obtaining time series of the ODE (2.7) and this simplest form is called Euler-integration [PRE92]. As can be instantly seen, $\tilde{\mathbf{X}}(t)$ will no longer be a continuous function when a numerical integration scheme is used. Instead, a finite number of $\tilde{\mathbf{X}}(t)$ is obtained for fixed successive time points $t_0 + nh$ with $n \in \mathbb{N}$. When the numerical integration is successful, the discrete points $\tilde{\mathbf{X}}(t)$ will be very close to the real solution $\mathbf{X}(t)$ of the ODE. The discrepancy is influenced by the discretisation step length h , which cannot be too large. The Euler-scheme is mathematically proven to converge towards the real solution - but only when the step length h converges to 0. In reality, choosing step size h in such a way, that it is smaller than the smallest dynamical time-scale in the system usually ensures a stable numerical scheme. On the other hand, smaller h also mean that more iterative steps of Eq. (2.7) have to be evaluated for the same absolute time window, which increases the computational cost. It is therefore often necessary to search for the largest h that still reasonably works.

More advanced schemes exist which alleviate some of the drawbacks of the simplistic Euler-scheme. These include Runge-Kutta and higher-order explicit methods, automated error estimates for on-the-fly step size controls and implicit methods [PRE07].

The numerical integration method used in this thesis for systems of ODEs was a 5th and 6th order explicit Runge-Kutta solver with the scheme of Cash and Karp [CAS90] and adaptive step size control. The solver was written in C++ using the C++11 standard and making use of lambda functions. The code was compiled with gcc 6.3.0 20170516 on a DebianStretch system with the GNU/Linux 4.9.0 kernel. The optimization option of the compiler was `-Ofast`.

2.1.5 Delay-differential equations

While ordinary differential equations (ODEs) are very powerful in solving problems of classical mechanics, many spatially extended systems require a more sophisticated treatment to represent their inherent complexity. For example, diffusive processes, such as a blot of ink that is dropped into a glass of water, occur both in space and over extended periods of time and cannot be described by a set of scalar

2.1 A SHORT OVERVIEW OF NONLINEAR DYNAMICS AND DYNAMICAL SYSTEMS

variables. Instead, the information of the current state of the system \mathbf{X} is better understood as a function $\mathbf{X}(r, t)$ of both position r and time t , e.g. a field or set of fields. Such systems often lead to differential equations containing differentiation with respect to both space and time. These types of equations are called partial differential equations and are in general much harder to solve than ODEs.

While less known, alternatives to the partial differential equation framework for the description of continuous variables do exist [GIA96]. A single-mode laser that is emitting light towards an external mirror, where it is reflected in turn, will form a complex standing wave pattern between its facet and the mirror. This, in principle, can be described by the travelling wave equations of electrodynamics. The electromagnetic wave will propagate along the path between laser and mirror, and therefore also is an object that evolves both in space and time. However, when the medium between the facet and external mirror is inert, i.e. if dispersion, nonlinear losses and gain can be neglected outside the laser cavity, the emitted electromagnetic wave will simply perform a linear motion on the way to and back from the external mirror. When modelling the dynamics of such a laser with external optical feedback, it is therefore not even necessary to keep track of the spatial intensity profile in the external cavity. Instead, the emitted electric field $E(t)$ can simply be assumed to return to the laser after some round trip time $\tau = d/c$, where d is the distance travelled and c the speed of light. When the equations of motion are then derived, a delay-differential equation (DDE) is obtained.

In general, a delay-differential equation with a single fixed delay-time τ takes the form :

$$\frac{d\mathbf{X}(t)}{dt} = F(\mathbf{X}(t), \mathbf{X}(t - \tau), t, \rho), \quad (2.8)$$

where the evolution function F not only depends on the instantaneous state variables $\mathbf{X}(t)$, but also the delayed variables $\mathbf{X}(t - \tau)$. This may seem like a small change from the ODE ansatz of Eq. (2.1), however, the mathematical implications are vast. The initial value problem changes from determining $\mathbf{X}(t = t_0) = \mathbf{X}_0$ for the ODE to the more complex

$$\mathbf{X}(t) = \Phi_i(t), \quad -\tau \leq t \leq 0, \quad (2.9)$$

for the DDE. Because the evolution of the system depends on delayed state-variable $\mathbf{X}(t - \tau)$, this has to be known for all t . Hence, to give complete initial conditions, $\Phi_i(t)$ is a function that needs to be defined over the entire interval $[-\tau, 0]$. This interval is also called the 'history' of the system, as it contains previous values of the system state \mathbf{X} .

2 THEORY

Recall that the phase space of a system is the space where the evolution is uniquely defined for every element. In an ODE this is the space spanned by all possible entries of the state vector \mathbf{X} and is therefore usually isomorph to \mathbb{R}^P with the number of dimensions $P \in \mathbb{N}$. However a DDE requires the entire history function to be completely defined, and thus a finite number of real-valued variables is not sufficient. The dimensionality of a DDE system becomes infinite, as functions are infinite dimensional in the mathematical description. This is of course not too surprising, because here the DDE ansatz was explicitly derived from a spatially continuous system. The history array therefore fulfils the same role that an initial spatial profile in a PDE would: The history function ‘encodes’ some spatial dimension in which patterns are conserved, e.g. electromagnetic waves travelling through a passive medium.

The study of DDEs was initially investigated with respect to a time-delayed control [CAL36, HAR37], but later a more general interest in the dynamics of such systems popularized DDEs [BEL54]. Despite more than half a century of work, novel fundamental properties of DDEs are still being discovered and proven, e.g. Ref. [YAN09].

The numerical treatment of DDEs is also made more difficult by the need to keep track of the history. The explicit Euler-integration can cope with DDEs by adopting a discretisation of the history interval $[-\tau, 0]$ with the time step h . It is computationally much more efficient, to chose h such that $\tau \bmod h = 0$. Higher order Runge-Kutta methods are more difficult to implement for DDEs, Ref. [THO90a] gives an overview of the problems and possible solutions.

The DDE solver for this thesis was written in C++ and compiled on the same system under the same conditions as the ODE solver. The fixed integration time step h and time delay τ are always chosen to fulfil $\tau \bmod h = 0$. The solver is a fourth-order explicit Runge-Kutta solver, where the delay-array is interpolated with a third-order Hermite polynomial, using the values and derivatives at the neighbouring history array entries.

2.2 Network theory

So far, a general overview of the concepts of nonlinear dynamics has been given. This section now introduces the network theory used to describe coupled units, which are the main system of interest in this thesis.

2.2.1 Introduction to networks: Nodes and links

Science is the discipline of understanding and categorizing the effects and observations of reality. For the human mind to understand the often complex phenomena, simplifications, abstractions and reductions have to be used. By a strict process of observation and mathematical description, many fundamental laws of physics have been uncovered this way. However, once these fundamental laws have been understood, scientists are tempted to try and apply them to more complex settings, despite all the difficulties that usually entails.

One source of complexity is the physical or functional size of the systems of study. Many objects in nature are multipartite, i.e. made up of many individual elements. Even when the individual element is well understood, the complex whole may exhibit properties not directly corresponding to those of its fundamental constituents. This is also sometimes referred to as ‘emergence’, the generation of complexity from simpler parts. The essence of this initially paradoxical appearance of properties and structures ‘out of thin air’ can be illustrated with the famous quote of Aristotle’s *Metaphysics*: "The whole is greater than the sum of its parts." The ‘whole’, the physical system, may consist of many well-understood elements, but in addition these elements also *interact*.

The world consists of many interacting components, which themselves are already multipartite: The ecosphere is influenced by weather, flora and fauna; the weather is influenced by air, water and aerosol flows; animals and plants are interlocked in complex predator-prey systems; each individual life form consists of organs and internal chemistry; and so forth. Every modelling description has to stop at some level and make some simplifications. Sometimes it is enough to study one individual example. In other cases the phenomena may be described by a model consisting of many individual, similar or even identical elements that are coupled. Such systems could be fish in a swarm, power stations in the electric grid or lasers that share an external optical cavity.

Arguably one of the most fascinating examples of such a coupled system is the human brain. The brain consists of billions of individual neurons, which are connected via axons and synapses to form a large *network*. This network processes vast amounts of information. However, each individual neuron is a (comparatively)

2 THEORY

simple unit, only exhibiting low-dimensional dynamics. The complexity lies not in the individual units, but in their collective behaviour on the large scale.

When trying to describe such a system it is natural to adapt a mathematical formalism that mirrors the physical reality. Instead of describing the brain *in toto* from first principles, a more structured approach can be taken: First the equations of motions for a single neuron are derived and investigated, ignoring the complexity of the brain landscape. Once the solitary neuron is well understood, its behaviour when coupled to other neurons is investigated, e.g. the input of the other neurons is treated as a perturbation. This example illustrates the basic principle of network dynamics: there are individual elements, the nodes, which are coupled via links.

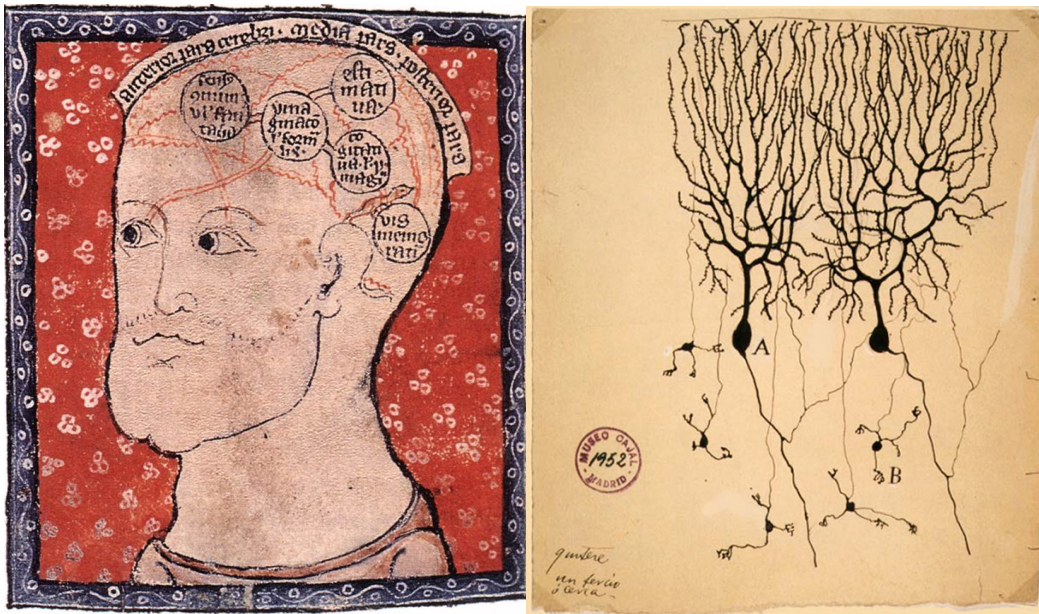


Figure 2.2: The human brain is a large organ made up of billions of neurons. Left: 14th century diagram of the human brain, unknown artist, circa 1300, Cambridge University Library; Right: Drawing of neurons of a pigeon, Santiago Ramón y Cajal, 1899. Instituto Santiago Ramón y Cajal, Madrid, Spain.

The ‘nodes’ or ‘units’ in a network describe the individual systems that are the elementary building blocks of the network. A ‘node’ can be a neuron, as in the case of the brain, but it could also be a laser, a person, a gene or any other system. The local equations of motions are known for the nodes, e.g. how often a neuron with a certain set of parameters emits a spike or how the laser output depends on its pump current. The local dynamics in this work will mostly focus on laser and oscillatory systems, but in general any system can be used. A network consists of multiple nodes. To be useful as a model, the nodes should be sufficiently isolated

and independent, so that the influence of their coupled neighbours can be seen as a perturbation. All the information of the system state is encoded in the state of the nodes.

The ‘links’ or ‘edges’ of a network are the connections between nodes. They are what turns a set of isolated, independent systems into a network. An edge from node i to node j indicates that the state of node i influences the state of node j . These links can be physical links, as in the case of the synapses in the brain or they can be functional, e.g. an abstract representation of which chemical species density influences which other. In the most common case a link always connects exactly two nodes. Multiple edges can originate at or connect to the same node, e.g. a typical neuron has connections to thousands of other neurons [SPO05]. The links are usually assumed to be fixed, which represents a reasonable simplification for short time-scale dynamics. Hence, the phase space of the network system is entirely described by the sum of the phase space of the individual oscillators (and possibly their history). The links do not carry any dynamic information.

2.2.2 Network topology and the adjacency matrix

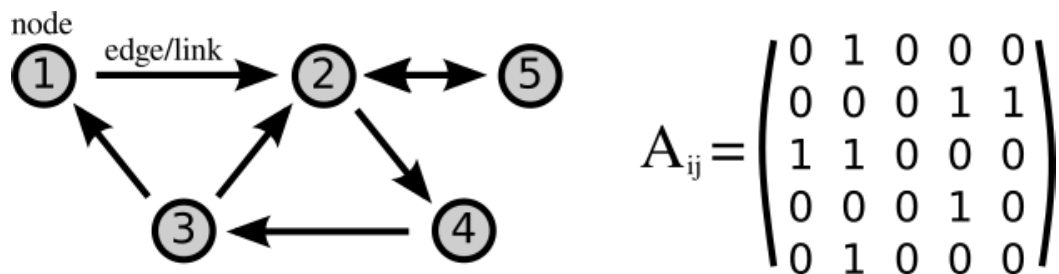


Figure 2.3: The graph of an example network with $N = 5$ nodes is shown on the left. Nodes are indicated by circles, while edges/links are shown with arrows. In this example, the network is directed. The corresponding adjacency matrix is shown on the right.

The defining feature of any network is its *topology*. Which of the nodes are connected with which other node plays an important role to determine the resulting collective dynamics. The topology of the network is a ‘graph’ and is the subject of study of the mathematical field of ‘graph theory’. In the most general case each edge has both a direction and a strength, e.g. synapses have weights and only pass information in one direction. This general case results in a ‘weighted and directed’ graph. An edge with a higher weight results in a higher influence on the target node. A weighted and directed graph could for example be used to describe the water flow between different lakes, where the weight indicates the throughput of the connecting rivers. In other setups all links can be thought of as having the same strength, resulting in an ‘unweighted graph’. Similarly, if interactions are always

2 THEORY

mutual, connections are bidirectional. This is the case of an ‘undirected graph’. Bidirectional graphs occur naturally where isolating the influence of one system to the other is difficult, for example in the power grid.

Figure 2.3 illustrates a small directed and unweighted network. The individual nodes are shown as circles and labelled. The connections or links are indicated via arrows or lines. The left side of Fig. 2.3 shows an example for $N = 5$ nodes. The placement of the nodes and the length of the arrows do not carry any information. Their arrangement is chosen for convenience and visual clarity.

A common approach to mathematically encode and define the topology of a network, i.e. the entirety of its links including directions and weights, is the *adjacency matrix* A . In a network of size N , i.e. a network consisting of N nodes, the adjacency matrix A has dimension $N \times N$:

$$A = \begin{pmatrix} a_{11} & \dots & a_{1N} \\ \vdots & & \vdots \\ a_{N1} & \dots & a_{NN} \end{pmatrix} \quad (2.10)$$

Each entry a_{ij} of the adjacency matrix represents the edge from node i to node j . The absence of a connection or edge from node i to node j corresponds to $a_{ij} = 0$. For an unweighted graph the entries a_{ij} of the adjacency matrix are 1 if there is a connection, while for a weighted graph the magnitude of a_{ij} indicates the strength of the connection. The adjacency matrix of the directed example network is shown on the right of Fig. 2.3. The adjacency matrix is also often referred to as ‘coupling matrix’, however sometimes the adjacency matrix is explicitly used only for the topology without the weights. In this thesis these two types will not be distinguished and both adjacency and coupling matrix will be used as interchangeable terms.

The adjacency matrix is also useful to describe a mathematical formalism of network dynamics in a short differential equation. This thesis will deal only with networks of time-continuous systems, i.e. not with maps. Hence all time-dependent dynamics will be derived from ODEs and DDEs. For the simplest case of a network of N nodes, the equations of motions are given by:

$$\dot{\mathbf{X}}_i = \mathbf{f}_i(\mathbf{X}_i) + \sum_{j=1}^N a_{ij} \mathbf{h}_{ij}(\mathbf{X}_i, \mathbf{X}_j), \quad (2.11)$$

where \mathbf{X}_i is the local state of node i , $\dot{\mathbf{X}}_i$ is the derivative with respect to time and $\mathbf{f}_i(\mathbf{X})$ are the local (uncoupled) dynamics of node i . The last term in Eq. 2.11 is

the coupling between nodes. $\mathbf{h}_{ij}(\mathbf{X}_i, \mathbf{X}_j)$ is the coupling function between node i and j and a_{ij} the corresponding entry of the coupling matrix.

Many problems can be described with networks of identical units, and hence once can assume every node to have the same dimension, set of state variables X_i and local dynamics $\mathbf{f}_i(\mathbf{X}_i) = \mathbf{f}(\mathbf{X}_i)$. Similarly, when all connections are of the same kind, the coupling function becomes independent of the node index $h_{ij}(\mathbf{X}_i, \mathbf{X}_j) = h(\mathbf{X}_i, \mathbf{X}_j)$. One common and simple example of coupling is diffusive coupling:

$$h(\mathbf{X}_i, \mathbf{X}_j) = \mathbf{X}_j - \mathbf{X}_i, \quad (2.12)$$

where a simple difference equation is taken. With such a diffusive coupling, the general equation Eq. (2.11) can be rewritten into a multidimensional equation to describe the system. Let \mathbf{X} be the vector that contains all node variables $(\mathbf{X}_1, \dots, \mathbf{X}_N)$, then Eq. (2.11) becomes

$$\dot{\mathbf{X}} = \mathbf{f}(\mathbf{X}) + A\mathbf{X} - \mathbf{X}, \quad (2.13)$$

where A is the adjacency matrix and \mathbf{f} is assumed to act on every element of \mathbf{X} .

When all links in the network are undirected, the resulting adjacency matrix A is symmetric. The diagonal elements a_{ii} denote the self-coupling of node i and are often absorbed into the local dynamics $\mathbf{f}(\mathbf{X})$.

2.2.3 Real networks and symmetries

The study of dynamical systems is interested in the time-evolution of a specific target set of equations that usually approximates a given physical experiment or environmental observation. When these systems are studied with respect to their solitary behaviour, i.e. their dynamics without external perturbation, the role of stable solutions is extremely important (see the Sec. 2.1.2). The same question posed for a network requires even more complex analysis: The stable states of a network system are, in general, dependent on the network topology. As every node in the network affects its neighbours through coupling, even two networks that differ just in the weight or existence of a single link can exhibit completely different stable solutions. For transport networks and the electric grid this is known as Braess's paradox: Even building just one additional power line to strengthen the connection of distant parts of the electric network can have the opposite effect and destabilize the wanted behaviour [WIT12].

Real world networks are often complex and without any obvious structure [BAR02a]. The topology of these systems reflects an underlying order of the real world. For example, the connections in the power grid are governed by geography and the distribution of large power plants and cities. When this underlying information

is removed, the abstracted adjacency matrix encodes this information and like geography does not have to conform to any mathematical symmetries. Studying the influence and importance of each individual node and link in such a network is time-consuming. Important network measures have been developed [ALB02a] to characterize the network as a whole instead, such as node degree, clustering factors and the average path lengths. However, this thesis will restrict itself to the study of simple and regular topologies, that can be described with simple measures. In the context of this thesis a ‘regular network’ will be a network with a highly symmetric adjacency matrix, which was constructed from a deterministic process, i.e. without randomness.

The most defining feature of a network are its inherent symmetries. These symmetries are apparent from the adjacency matrix A and are mathematically described with symmetry groups. As the set of all nodes in a graph is finite, these symmetries are the possible permutations of the nodes. A common symmetry for regular, i.e. non-random, networks are exchange symmetries \mathbb{Z} . For example, an all-to-all network is fully connected, i.e. all nodes have links to all other nodes. Any exchange of two nodes then leaves the resulting equations of motions unchanged. Ring networks follow discrete cyclic symmetries, while a bidirectional coupling, i.e. a graph with unweighted links, leads to a symmetric coupling matrix A so that $a_{ij} = a_{ji}$.

The symmetries of a system also influence the solutions. This is very apparent in regular network systems. For example, if the network has a discrete cyclic symmetry, the solutions must equally have said cyclic symmetry. However, there is one exception: Symmetry-breaking bifurcations can create new solutions, that no longer adhere to the underlying symmetry groups of the network. Because this can be very surprising, when it occurs, this has also been called ‘spontaneous symmetry-breaking’. However, according to the *equivariant branching lemma* [CRA91, HOY06] these symmetry-broken solutions do not exist in isolation: For every symmetry that is broken, a branch of solutions is created, so that together they still fulfil the underlying symmetry properties. This will become apparent later in the thesis, when it is applied to the concrete example of coupled Stuart-Landau oscillators and Lang-Kobayashi equations [LAN80b].

2.2.4 Connection to spatially extended systems

Spatially extended systems play an important role in the description of the natural world. Be it the evolution of waves, the diffusion of chemicals or the flow of a liquid, problems with an inherent spatial character require a special mathematical treatment. The description of choice is often a system of partial differential equations, i.e. a set of differential equations with derivatives with respect to multiple variables.

These systems are hard to analyse, as analytical solutions are rare and many of the numerical methods are computationally costly. A common case is that of spatial derivatives and time derivatives being combined to describe spatially extended systems. The most famous example of this likely are the Navier-Stokes-equations, for which many unanswered questions remain. Network systems can help overcome some of the inherent mathematical problems by simplifying the underlying required operations. For example, the one-dimensional heat equation is given by

$$\frac{\partial u}{\partial t} - \alpha \frac{\partial u^2}{\partial x^2} = 0, \quad (2.14)$$

and its solution is a spatio-temporal pattern $u(x, t)$ that has to be found. With a discretisation of the spatial dimension of x of the form $x_i = x_0 + ih$, where h is the discretisation length, Eq. (2.14) can be rewritten into a new set of equations for discrete spatial points $u_i(t) = u(x_i, t)$:

$$\frac{\partial u_i}{\partial t} - \alpha \frac{u_{i+1} - 2u_i + u_{i-1}}{h^2} = 0, \quad (2.15)$$

here, the second derivative of Eq. (2.14) has been replaced with the second difference $(u_{i+1} - 2u_i + u_{i-1})/h^2$. Because the derivative with respect to space has been replaced, the partial derivative with respect to time is the total derivative for u_i . The equation can now be seen as a network of coupled nodes, with the nodes indicating different spatial positions x_i . The state of each node thus is $u_i(t)$ and is influenced by the two neighbouring points u_{i+1} and u_{i-1} . Equation 2.15 can then be rewritten as:

$$\frac{du_i}{dt} = \frac{\alpha}{h^2} \sum_j a_{ij} u_j, \quad (2.16)$$

where a_{ij} are the entries of the corresponding coupling matrix A . The topology corresponding to the one-dimensional heat equation will be either an open chain for normal boundary conditions or a ring for periodic boundary conditions. In higher dimensions the topology of the resulting network description will reflect a (usually regular) discretisation, e.g. a two-dimensional problem results in nodes that are coupled in a 2D-grid.

These discretisations allow for simple treatment of complex partial differential equations. Because the underlying networks are often highly symmetric, it can be easier to understand the effects than in the continuous system. However, as any discretisation, the reduction produces an error that generally increases with larger h , i.e. a more coarse grid. The continuous system is only reached for infinitesimally small spatial discretisation step $h \rightarrow 0$ and infinite number of nodes $N \rightarrow \infty$. An example of a network approach for a continuous system can be found in Ref. [HAK92,

GAR12b], where the complex Ginzburg-Landau equation has been explored with a network of Stuart-Landau oscillators.

2.2.5 Synchronization

Synchronization is a phenomenon in networks of similar or identical dynamical systems with time-varying behaviour, i.e. periodic, quasiperiodic or chaotic motion. In the strictest sense, when two systems are fully synchronized their states become identical at all times, $\mathbf{X}_1(t) = \mathbf{X}_2(t)$. In particular, all dynamical events occur at the same time, which is the origin of the term 'synchronization' (from old Greek).

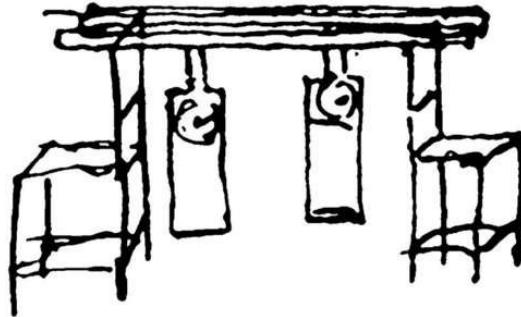


Figure 2.4: The famous 17th century study of synchronized mechanical clocks by Christiaan Huygens. Cited in [KAP12]

Figure 2.4 shows a sketch made by the famous 17th century natural scientist Christiaan Huygens, who in particular studied this system of ‘two clocks on a beam’. He observed that, despite the physical separation of the clocks, their pendulums would eventually synchronize. Both clocks even had different frequencies, as natural manufacturing discrepancies were sufficient to detune the period of oscillation of the driving pendulum. Nevertheless, vibrations would travel through the beam and exact a small force on both pendulums. The force acts in such a way, that timing-mismatches are discouraged and synchronized motion of the pendulums is enhanced, eventually leading to complete synchronization. Despite the fame of this experiment, modern versions have to rely on a more complex setup to find the mechanical synchronization of oscillators [KAP12]. Synchronization has now been observed in a wide array of systems where vibrations can couple different oscillatory systems, such as in the synchronization of organ pipes [ABE06] or in nano-mechanical oscillators [SHI07a].

Synchronization is not limited to mechanical systems. In fact, the most common examples are biological systems. Swarms of fireflies have been observed to synchronize their flashing lights, crickets synchronize their chirping and pacemaker cells in the heart tissue send excitation pulses simultaneously [MAT90]. Synchronization

of neural activity in the human brain is hypothesized to play an important role in epilepsy [JIR13]. Furthermore, coupled Josephson-junctions were also an early test bed for synchronization theory [HAD87]. In many of these cases, simple phase-oscillator models can be used to describe the synchronization [ACE05]

Biological systems naturally carry a frequency distribution, and therefore initially there was a large interest in understanding synchronization in networks of non-identical oscillators [MAT90], which generally leads to complex mathematical models and dynamics. But even in networks of identical oscillators with full exchange symmetries synchronization is not the only solution, as the example of chimera states demonstrates [KAN90, ABR04, KUR02a].

There are multiple definitions for synchronization, with a focus on different aspects. As this work is focused on oscillatory and laser networks, the distinctions between phase, frequency and lag synchronization are important. Let $Z_i(t) \in \mathbb{C}$ be the time-dependent complex amplitude of an oscillator, then the following definitions will be used in this thesis:

In-phase synchronization Two oscillators i and j are *in-phase-synchronized*, if their states are identical for all times, $Z_i(t) = Z_j(t)$. This is varyingly called ‘zero-lag synchronization’, ‘isochronous synchronization’ or ‘in-phase synchronization’ [LEH15b]. This thesis will declare ‘synchronization’ to be ‘in-phase synchronization’, if no further explanation is given.

Lag synchronization Two oscillators i and j are *lag synchronized*, if their time-traces are identical for all times, when one is shifted by some constant $T \neq 0$, $Z_i(t) = Z_j(t + T)$.

Frequency synchronization Two oscillators i and j are *frequency synchronized*, if their average phase velocity $\langle \omega \rangle$ is identical, $\langle \omega_i \rangle = \langle \omega_j \rangle$, with $\omega = \dot{\theta}$ and $\theta = \arg(Z)$. This is also called ‘general synchronization’ and is a weaker condition than the former two, as any lag or in-phase synchronized oscillator is also necessarily frequency synchronized.

2.3 Local model: Stuart-Landau oscillator

So far, the focus has been to introduce networks in general. However, to explicitly write down a closed system as in Eq. (2.11) the local dynamics $f(\mathbf{X})$ have to be defined. This thesis is concerned with laser networks for optical computing purposes and therefore the local dynamics will reflect the lasing system. However, lasers are just one example of the large class of ‘oscillatory systems’ and many of the effects found in laser networks can be understood as being examples of more general concepts. The most important model system for amplitude oscillators is the Stuart-Landau system, which will be introduced in this section.

2.3.1 Derivation of the Stuart-Landau oscillator equations

This section loosely follows the derivation found in Ref. [GAR12b]. The harmonic oscillator is perhaps the most important dynamical system used in physics to describe nature. Its applications range from the classic examples of the spring and the mathematical pendulum, to the LC-circuits of electrodynamics and the particle fields of quantum field theory. Vastly different systems can be approximated or described with this simple equation. The differential equation describing an undamped harmonic oscillator is given by

$$\frac{dZ}{dt} = i\omega Z, \quad (2.17)$$

where $Z \in \mathbb{C}$ is the complex state variable and ω is the frequency of oscillations. In its complex form Eq. (2.17) has the solution

$$Z(t) = Ae^{i\omega t + \phi}, \quad (2.18)$$

with arbitrary, but fixed, amplitude A and phase-shift ϕ ; e is Euler’s number. This is a perfectly harmonic, eternal oscillation. However nice this system may be from a mathematical perspective, its simplicity also limits its applications to real-world problems. Many systems in nature are not fixed, eternal oscillations, but subject to environmental noise, driving or other influences. Equation (2.17) is capable of producing harmonic limit cycles of arbitrary amplitudes, but none of these limit cycles are stable. In fact, the whole phase space volume of Eq. (2.17) is indifferent to perturbations, i.e. the real part of all eigenvalues of the system are always zero.

Of course, the system stops having infinitely many solutions once damping is introduced to the Eq. (2.17):

$$\frac{dZ}{dt} = \lambda Z + i\omega Z, \quad (2.19)$$

2.3 LOCAL MODEL: STUART-LANDAU OSCILLATOR

with $\lambda < 0$. However, the only stable solution for the damped harmonic oscillator of Eq. (2.19) is the trivial off-solution $Z = 0$. In contrast, many systems in nature exhibit a self-regulating amplitude. Oscillations neither die out towards zero, nor are they of arbitrary strength. A self-regulating system approaches a well-defined solution, i.e. a single stable limit cycle exists. Examples of self-regulating oscillatory systems include the population dynamics in predator-prey systems [LOT20, VOL26a], the periodic changes in the density of the chemical species in chemical oscillations [BEL59, ZHA64], or the electric field inside an active laser cavity [ERN10b].

A simple way to extend Eq. (2.17) to contain self-regulating amplitudes requires a change of coordinate system: The complex variable Z is transformed to its polar form $Z = r \exp(i\theta)$ with new variables $r, \theta \in \mathbb{R}$. The equations of motion for radius r and argument θ are:

$$\frac{dr}{dt} = 0, \tag{2.20}$$

$$\frac{d\theta}{dt} = \omega, \tag{2.21}$$

which also makes visible once again that the amplitude r of oscillations can be chosen arbitrarily. To obtain a self-regulating amplitude Eq. (2.20) must be extended to higher orders. Arguably the simplest approach is to assume a Taylor Series:

$$\frac{dr}{dt} = c_0 + c_1 r + c_2 r^2 + c_3 r^3 + \dots, \tag{2.22}$$

with real-valued constants c_0, c_1, c_2, c_3 , which have to be found. The aim now is to find equations of motions that are as simple as possible, while allowing for a self-regulating amplitudes r . However, it is natural to demand that the equations not only be of a simple form in the polar coordinates of Eq. (2.20)-(2.21) but also in the complex view of Eq. (2.17). The term c_0 in equation Eq. (2.22) would correspond to the term $c_0 Z/|Z|$ in non-polar description, which when expanded for $\text{Re}(Z)$ and $\text{Im}(Z)$ will be non-polynomial. To exclude these non-polynomial elements it is therefore necessary to set $c_0 = 0$. A similar argument can be made for c_2 , which corresponds to the term $c_2 |Z|Z$, with $|Z|$ as the absolute value of Z . Because $|Z| = \sqrt{\text{Re}(Z)^2 + \text{Im}(Z)^2}$ this is also clearly non-polynomial.

The preceding considerations mean that Eq. (2.22) becomes:

$$\frac{dr}{dt} = c_1 r + c_3 r^3 + \dots, \tag{2.23}$$

which means the smallest extension of the harmonic oscillator that preserves both the angular symmetry and is polynomial in polar and Cartesian description is a linear term $c_1 r$. However, this linear term allows for only two cases to exist: If

2 THEORY

$c_1 > 0$, the system is unstable and the radius grows indefinitely, while for $c_1 < 0$ we recover the damped harmonic oscillator. Neither of these cases contains stable limit cycles. Hence, to obtain a self-regulating amplitude the lowest order polynomial extension of the harmonic oscillator includes both c_1 and c_3 . After transforming Eq. (2.23) back to complex coordinates with those assumptions, the Stuart-Landau oscillator equation is then obtained:

$$\frac{dZ}{dt} = (\lambda + i\omega + \gamma|Z|^2) Z, \quad (2.24)$$

where the common variable designations have been used $c_1 = \lambda$ and $c_3 = \gamma$. In the sense as introduced above, Eq. (2.24) is the simplest extension of a harmonic oscillator to include self-regulating amplitudes. The equation is named after Russian mathematician Lev Landau [LAN44] and American applied mathematician Trevor Stuart [STU60], which proposed this equation in the context of the onset of turbulence in fluid dynamics.

The Stuart-Landau equation Eq. (2.24) is usually extended in a small way: The parameter γ is assumed to be complex. $\text{Re}(\gamma)$ is important for the direction and nature of the underlying Andronov-Hopf bifurcation (see next section), with a supercritical Andronov-Hopf bifurcation occurring for $\text{Re}(\gamma) < 0$. The addition of an imaginary part $\text{Im}(\gamma) \neq 0$ induces a coupling between amplitude and phase and is sometimes called ‘shear’ [HAK92]. This extension will not destroy the polynomial nature nor the rotational symmetry of the system and is therefore compatible with the derivation as shown in this section. A similar extension of $c_1 = \lambda$ will not yield any new terms, as $\text{Im}(\lambda)$ can be absorbed by the frequency ω .

2.3.2 Andronov-Hopf bifurcation

The field of nonlinear dynamics is devoted to understanding the universal behaviour of classes of systems. This is done by studying the topology of the state space for different parameters and connecting it with knowledge of the underlying bifurcations thereof.

The number of possible bifurcations in low-dimensional systems is finite. One of the most common and fundamental bifurcations is the so-called Andronov-Hopf bifurcation [HOP42, AND49], named after Russian mathematician A. Andronov and German-American mathematician E. Hopf. The Andronov-Hopf bifurcation describes the case when two complex-conjugate eigenvalues cross the imaginary axis simultaneously. The resulting behaviour of the system is the creation (or annihilation, depending on direction) of a limit cycle. No matter how high-dimensional the dynamical system viewed is, in the vicinity of an Andronov-Hopf bifurcation, the onset of oscillations can be approximated with a reduced equation, a so-called

normal form. This fact is also known as the centre manifold theorem. As a limit-cycle needs at least two dimensions to exist, the normal form of an Andronov-Hopf bifurcation is also two-dimensional. The obtained normal form is Eq. (2.24), the Stuart-Landau oscillator [KUR84, KUZ95].

Thus, any nonlinear system close enough to an Andronov-Hopf bifurcation can be approximated by a Stuart-Landau oscillator. However, in reality the projection required to obtain Eq. (2.24) may be very complex. Nonetheless, the above-mentioned facts mean, that the study of the Stuart-Landau system has wide-ranging implications for a large class of systems. Indeed, as will be shown in Sec. 2.4.3, the laser equations are one such example.

2.3.3 Stable states

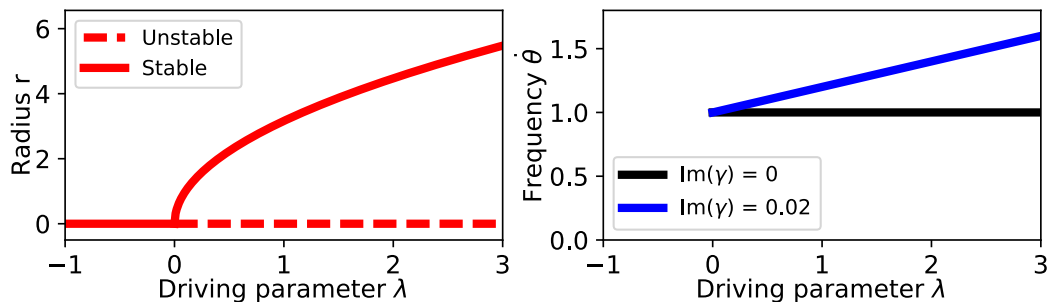


Figure 2.5: Sketch of the evolution of the radius (left) and frequency of the limit cycle (right) for a supercritical Hopf bifurcation modelled by its normal form, i.e the Stuart-Landau equation, cf. Eq. (2.24). In the supercritical case, the fixed point loses stability at $\lambda = 0$, where the limit cycle is born. For $\text{Im}(\gamma) = 0$ (black line, right), the frequency does not change with λ , whereas it changes linearly for $\text{Im}(\gamma) \neq 0$ (blue line, right), cf. Eq. (2.29). Parameters: $\text{Re}(\gamma) = -0.1$ (supercritical case), $\omega = 1$.

Because the Stuart-Landau oscillator is of such a simple mathematical form, the basic solutions can be derived analytically. The Stuart-Landau equation Eq. (2.24) with general $\gamma \in \mathbb{C}$, written in polar coordinates, is:

$$\frac{dr}{dt} = \lambda r + \text{Re}(\gamma)r^3, \quad (2.25)$$

$$\frac{d\theta}{dt} = \omega + \text{Im}(\gamma)r^2, \quad (2.26)$$

2 THEORY

where once again r is the radius and θ the phase. As Eq. (2.25) contains no θ , it can be solved separately. Looking for solutions with a fixed radius $r = \text{const.} \rightarrow \dot{r} = 0$ leads to:

$$0 = \left(\lambda + \text{Re}(\gamma)r^2 \right) r. \quad (2.27)$$

Equation (2.27) has two solutions with $r \geq 0$, which subsequently also allow Eq. 2.26 to be solved under the constraint $\dot{\theta} = \text{const.}$. First, the trivial off-state with no oscillations:

$$r = 0 \rightarrow Z = 0, \quad (2.28)$$

for which θ is not well-defined due to the polar coordinates. The second solution describes the limit cycle

$$r = \sqrt{-\frac{\lambda}{\text{Re}(\gamma)}} \quad \dot{\theta} = \omega - \lambda \frac{\text{Im}(\gamma)}{\text{Re}(\gamma)}, \quad (2.29)$$

which requires $\lambda/\text{Re}(\gamma) \leq 0$. A linear stability analysis reveals that the Andronov-Hopf bifurcation point is $\lambda = 0$. Additionally, $\text{Re}(\gamma)$ determines whether the Andronov-Hopf bifurcation is sub- or supercritical.

The supercritical case is sketched in Fig. 2.5. After the limit cycle is created in the Andronov-Hopf bifurcation at $\lambda = 0$, the radius grows with the square root of λ . The stability of the limit cycle and trivial fixed point can be calculated with standard linearisation approaches, see for example Ref. [KUZ95]. In the supercritical case, the limit cycle inherits the stability of the fixed point solution, which turns unstable at the bifurcation point. The right side of Fig. 2.5 shows the evolution of the frequency $\dot{\theta}$ of the limit cycle. As dictated by Eq. (2.29), the frequency is fixed if there is no shear $\text{Im}(\gamma) = 0$ (Fig. 2.5, black line), whereas it changes with λ for $\text{Im}(\gamma) \neq 0$ (Fig. 2.5, blue line).

In the polar coordinates of Eq. (2.25)-(2.26) the limit cycle is indicated by the non-zero fixed point of the radius. Simultaneously the phase grows linearly with time. Mathematically the system does not undergo an Andronov-Hopf bifurcation in polar coordinates, as no limit cycle is created. This does not invalidate the calculations using polar coordinates, but it means that this representation is unsuited to see the oscillatory nature of the created limit cycle. For better illustration Fig. 2.6a shows a numerically obtained time-series slice of Eq. 2.24. The real part of the complex variable Z (solid red line, Fig. 2.6a) oscillates sinusoidally with a quarter period phase shift with respect to the imaginary part $\text{Im}(Z)$ (red dashed line in Fig. 2.6a). Viewed in the complex plane (Fig. 2.6b), this behaviour describes a circular motion around the origin with constant angular velocity. The

2.3 LOCAL MODEL: STUART-LANDAU OSCILLATOR

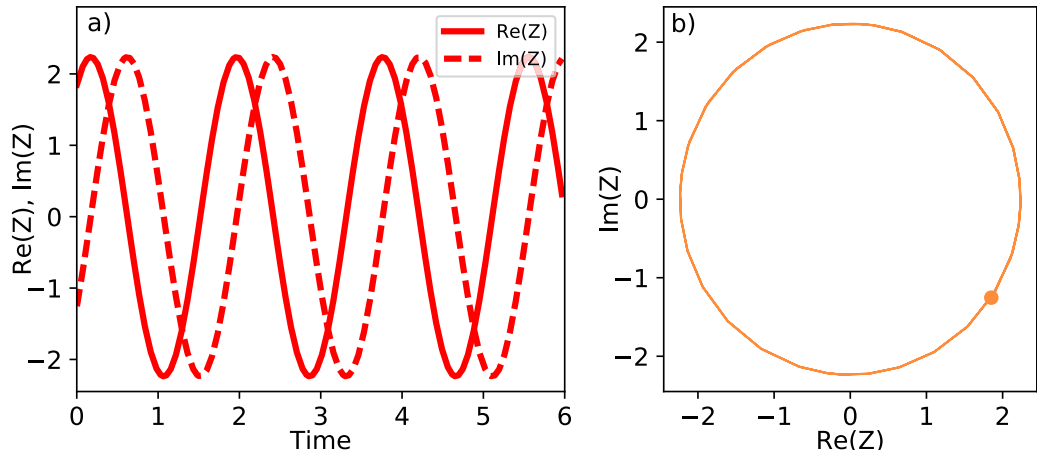


Figure 2.6: a: Time series of the real part $\text{Re}(Z)$ (solid lines) and imaginary part $\text{Im}(Z)$ of a single Stuart-Landau oscillator as described by equation Eq. (2.24) after a transient time of 50000 time units. b: Projection into the complex plane with a single time-snapshot shown with the circle. Parameters: $\lambda = 0.5$, $\text{Re}(\gamma) = -0.1$, $\text{Im}(\gamma) = 0.5$, $\omega = 1$.

projection into the complex plane of Fig. 2.6b is perhaps the best visualization for the solutions of the system (and later the network systems) and will be used often throughout this thesis.

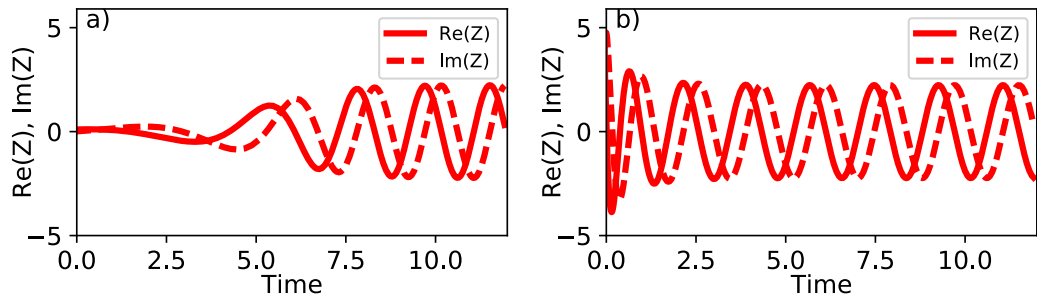


Figure 2.7: Visualization of the self-regulating amplitude property of the Stuart-Landau oscillator (Eq. (2.24)). a: Time evolution of the real part $\text{Re}(Z)$ (solid lines) and imaginary part $\text{Im}(Z)$ (dashed lines) when starting from amplitudes close to zero $Z = 0.1$. b: Time evolution starting from $Z = 6$. Parameters: $\lambda = 0.5$, $\text{Re}(\gamma) = -0.1$, $\text{Im}(\gamma) = 0.5$, $\omega = 1$.

The important self-regulating amplitude property is shown in Fig. 2.7, where two transient time series are shown. These simulations were obtained by direct numerical integration of Eq. 2.24 for two different starting conditions. In Fig. 2.7a the system was initialised close to the trivial off state $Z(t = 0) = 0.1$. The system then undergoes a rapid growth in amplitude. This growth is initially exponential,

because as long as λ is large compared to $\gamma|Z|^2$ Eq. (2.24) can be approximated by an exponential with a growth rate of λ . The system approaches the limit cycle visualized in Fig. 2.6 as the same parameters were used. When the amplitude of oscillations in Fig. 2.7 a gets close to the limit cycle, growth slows down, and when the system is close enough that the linear stability will be the dominating term, the difference to the limit cycle will decay exponentially with a growth rate of the leading Lyapunov-exponent. Fig. 2.7 b shows the timeseries for a starting amplitude larger than the limit cycle ($t = 0$) $Z = 6$. The oscillations approach the limit cycle from large amplitudes, but eventually also get exponentially close.

2.3.4 Literature overview: Stuart-Landau oscillator networks

In the following, a short overview of important literature concerned with coupled Stuart-Landau oscillators and related systems is given. Examples of networks of oscillators cover a wide range of applications, numerical models and experiments from coupled lasers [SOR13, GAR99a, JAV03, YAN04c, CLE14, KOZ00, ERZ05, ERZ09, HOH99b] to nanomechanical systems [SHI07a], chemical oscillators [TOT15, WEI92] and coupled tunnel diodes [HEI10]. Many fascinating phenomena of coupled oscillators can also be studied in pure phase-oscillators [KUR02a, ABR04, DHU08] or in chaotic maps [KAN90]. Nonetheless, the Stuart-Landau oscillatory system of Eq. (2.24) is a popular choice for the local dynamics f in a network system like Eq. (2.11).

The early works sometimes referred to the Stuart-Landau system of Eq. (2.24) as one example of ‘limit cycle oscillators’. The study of large collective effects like synchronization has become easier by the increased availability of scientific computing power in the later half of the 20th century and accordingly the amount of published results increased. The study of systems of Stuart-Landau oscillators developed together with the similar simple systems like networks of van-der-Pol oscillators [AIZ76, YAM84a, SHI89] or chaotic maps [KAN90].

Of the many papers on coupled Stuart-Landau oscillators, Ref. [ARO90] stands out. It goes into great detail exploring the underlying bifurcations of a system of two directly coupled Stuart-Landau oscillators, investigating the case of symmetric coupling of identical oscillators with and without shear, as well as exploring the effects of non-identical oscillators with frequency detuning. This was inspired by the observation of the phenomenon described by Bar-Eli in Ref. [BAR85] for the Brusselator system: The stabilization of inhomogeneous steady states by means of the coupling, nowadays called ‘oscillation death’ [KOS13]. Among bifurcation theorists in the mathematical community, the bifurcation structure of coupled Stuart-Landau oscillators has been thoroughly studied by Golubitsky and co-workers [GOL88a].

Apart from ‘oscillation death’ a second effect exists in coupled Stuart-Landau networks. ‘Amplitude death’ is the coupling-induced stabilization of the *trivial*

2.3 LOCAL MODEL: STUART-LANDAU OSCILLATOR

off-state in oscillatory networks [RAM98a]. Both amplitude and oscillation death are a field of active study [KOS13] with respect to Stuart-Landau oscillatory networks. These types of solutions are typically seen in systems with delay [STR98a, RAM98a, RAM99, RAM00, ATA03] or systems with a symmetry-breaking coupling [ZAK13, KAR07].

A natural solution for large systems of oscillators are cluster states, wherein the system splits into several groups which are in-phase synchronized within the group, but not with other groups. The Stuart-Landau system is a test bed for understanding cluster states [CHO09, LEE13, LEH14, KU15]. These cluster states can also lead to chaotic motion [HAK92, NAK93, NAK94a, KU15].

Another phenomenon in large networks is the so-called ‘chimera state’ [KUR02a, ABR04] and this has also been observed for the case of Stuart-Landau oscillators [ZAK14], where once again a symmetry-breaking coupling was employed. The combination of oscillation death and chimera states has been reported in Ref. [ZAK15b, BAN15] and been termed ‘chimera death’. Stuart-Landau systems have also been used to study the control of synchronization [POP05]. When noise is added to Eq. (2.24), coherence resonance [USH05, GEF14] can be observed.

In the limit of strong, global coupling the set of oscillators in a network can be thought of as a homogeneous field. One then obtains a system of partial differential equations, i.e., the Ginzburg-Landau-equations [GAR08, GAR12b]. This can be approximated by a network of coupled Stuart-Landau oscillators, and has been done in Ref. [SCH15e]. Additionally, a similar Stuart-Landau system with a conservative coupling is studied in Ref. [SCH14a, SCH14g, SCH15a], where different cluster and chimera states were found.

2.4 Local model: Lang-Kobayashi-type equations

In this section, the second type of model for the local dynamics \mathbf{f} in Eq. (2.11) is introduced. After a brief overview of laser history, the Lang-Kobayashi laser equations are shown and the literature on coupled lasers is reviewed.

2.4.1 Laser history

The beginnings of laser theory start in the late 19th and early 20th century, when the physics of the atom and light were being uncovered. Inspired by Max Planck's foundational works on the origin of the thermal spectrum of a black body radiator, the notion of 'quantized light' was introduced by Albert Einstein in his explanation of the photoelectric effect [EIN05a]. Many important works followed in the years after, which lead to the creation of Quantum Theory and Bohr's model of the atom. In 1916 Albert Einstein once again returned to the topic of quantized light and black-body radiation, presenting a new derivation of Planck's law [EIN17]. In his derivation, he postulated the existence of a way for an incoming radiation field to trigger emission of photons, a process that we nowadays call 'stimulated emission'.

The modern formulation envisions light-matter interaction of photons and particles to have three distinct processes: First, a photon can be absorbed, transferring its energy $h\nu$ to and exciting the particle. Second, an excited particle can spontaneously decay into a lower energy state, emitting a photon of energy $h\nu$ with random phase and direction. Third, the process of 'stimulated emission' occurs only when a photon of matching energy interacts with an already excited particle; instead of being absorbed, the material emits a new photon of energy $h\nu$, which shares phase and direction of the original. Einstein was able to show that the process of absorption and stimulated emission are inversely related and have the same Einstein coefficient.

2.4.2 Equations and dynamics

The general model of the semiconductor laser equations can be derived with different approximations and levels of detail. The typical derivation starts from a Hamiltonian describing the light-matter interaction and successively derives the equations of motion for the photons and carriers. For the laser, the exchange of energy from the *gain medium*, i.e. the material with resonant optical transitions that feed the laser light, is governed by stimulated emission. Meanwhile, the wave character of the electric field and its propagation and longitudinal modes are described with the classical set of Maxwell's equations. When these two aspects are combined - the classical propagation and standing wave patterns with the quantized

2.4 LOCAL MODEL: LANG-KOBYASHI-TYPE EQUATIONS

energy transfer between photons and electrons - one arrives at the semi-classical Maxwell-Bloch equations. The derivation and their implications is shown in many introductory laser theory textbooks, such as Ref. [CHO94] and will not be repeated here.

The focus in any network system of the form of Eq. (2.11) is on the *collective dynamics*. Thus the individual model for the local dynamics \mathbf{f} should be a strongly simplified laser rate equation. The form used in this thesis was deduced by Lang and Kobayashi in Ref. [LAN80b] for a laser with optical feedback, but can just as easily be adapted to optical coupling of multiple lasers. The specific parametrization and the derivation of the Lang-Kobayashi equations used here can be found in Ref. [ALS96].

As discussed in Sec. 2.4.1, the most important aspect of lasers are the light-matter interactions. As the time-scales of the electrons in semiconductor lasers are usually not negligible, a single evolution equation for the electric field amplitude is not sufficient to capture all dynamical features. Therefore, in contrast to the Stuart-Landau oscillator of Eq. (2.24), a laser has both amplitude, phase and carrier density. The system has three dimensions and is therefore more complex than the Stuart-Landau oscillator. The equations of motion of the Lang-Kobayashi laser with optical feedback [LAN80b] for the complex electric field amplitude $E \in \mathbb{C}$ and the excess carriers $N_e \in \mathbb{R}$ are given by:

$$\frac{dE}{dt} = (1 + i\alpha)EN_e + \kappa e^{i\phi}E(t - \tau) \quad (2.30)$$

$$\frac{dN_e}{dt} = \frac{1}{T}(p - N_e - (1 + 2N_e)|E|^2). \quad (2.31)$$

To remove unnecessary parameters, the time has been renormalized with respect to the photon lifetime [ALS96]. T is the ratio of electron to photon lifetime, as typically electron lifetimes are much longer. Amplitude-phase coupling α determines the imaginary part of the nonlinearity and is therefore similar to $\text{Im}(\gamma)$ in Eq. (2.24). p is the pump current, which drives the population of the excess carriers.

Equation (2.30) contains the feedback term with coupling phase ϕ and delay time τ . The feedback strength κ is determined both from the reflectivity of the external mirror, as well as the transmissivity of the laser cavity mirrors. The original Lang-Kobayashi equations represent a case of a laser with delayed feedback. The feedback term can also be seen as a self-coupling when the whole system is viewed as a small network. Thus, the corresponding 'local laser model' underlying

2 THEORY

the Lang-Kobayashi system can be obtained by setting $\kappa = 0$ in Eq. (2.30), which will be the model in this thesis:

$$\frac{dE}{dt} = (1 + i\alpha)EN_e \quad (2.32)$$

Similar to the fixed point analysis of Eq. (2.24) of Sec. 2.3.3, the possible steady-state solutions of Eqs. (2.32) and (2.31) can be found by setting all derivatives to 0 and solving for E and N_e . The first solution that can be found yields

$$|E|^2 = 0 \quad N_e = p, \quad (2.33)$$

which is the trivial fixed point or ‘off state’. No electric field is emitted and the carriers population freely follows the pump current p . The second steady state solution is given by

$$|E|^2 = p \quad N_e = 0, \quad (2.34)$$

which is the lasing solution. Here, the intensity $|E|^2$ is determined by the pumping of the laser, while the carriers are fixed at $N_e = 0$. The lasing solution has a freedom of the phase θ of the electric field $E = Ae^{i\theta}$ that is purely determined by the initial conditions. In the free-running setup it will be oscillating with a frequency Ω so that $E(t) = |E| \exp(i(\Omega + \theta))$.

The stability of the lasing and off-state solutions can be investigated with linear stability analysis. It can be easily deduced, that the trivial off-state is stable for $p < 0$, while the lasing solution is stable for $p > 0$. At the threshold pump current $p_{th} = 0$, both branches of solutions exchange stability in a transcritical bifurcation when viewed in $|E|^2$ - N_e -coordinates. When the complex amplitude E is observed, the bifurcation instead is an Andronov-Hopf-bifurcation. This allows Eq. (2.32) and (2.31) to reduce to the Hopf-normal form, which will be done in the following section.

2.4.3 Reduction of the LK-equations to the Hopf-Normal form

The Lang-Kobayashi laser as modelled by Eq. (2.32)-(2.31) is a simple model for a laser, yet due to the incorporation of the carrier dynamics it is a more complex model than the basic Stuart-Landau oscillator of Eq. (2.24). The laser threshold was identified as an Andronov-Hopf bifurcation in the previous section. Thus, the Lang-Kobayashi equations can be reduced to the Stuart-Landau oscillators under certain assumptions, as the Stuart-Landau oscillator is the normal form of an Andronov-Hopf bifurcation. To facilitate this reduction, the number of dimensions has to be reduced. As both the Stuart-Landau oscillator and the Lang-Kobayashi

2.4 LOCAL MODEL: LANG-KOBYASHI-TYPE EQUATIONS

equations possess a complex amplitude, it is obvious that their main difference lies in the additional degree of freedom of the carrier population N_e . Hence, one way to reduce Eq. (2.32)-(2.31) to the Stuart-Landau case is to adiabatically eliminate the excess carrier Eq. (2.31). This is justified, when carrier dynamics are very fast. Setting $\dot{N} = 0$ yields

$$0 = p - N_e - (1 + 2N_e)|E|^2. \quad (2.35)$$

It can now be assumed that carriers are close to the threshold which lies at $N_e = 0$ and thus $N_e \ll 1$. The term $(1 + 2N_e)$ can be approximated as 1, leading to the equilibrium distribution:

$$N_e \approx p - |E|^2. \quad (2.36)$$

Note, that this still correctly contains both solutions Eqs. (2.33) and (2.34). Substituting Eq. 2.36 into Eq. (2.32) then yields:

$$\frac{dE}{dt} = (p + i\alpha p - (1 + i\alpha)|E|^2)E, \quad (2.37)$$

which structurally is identical to a Stuart-Landau oscillator shown in Eq. (2.24). The following parameter equivalences between the Lang-Kobayashi laser and the Stuart-Landau oscillator can be found: The bifurcation parameter λ of the Stuart-Landau system acts like the pump current p of the laser. The nonlinearity prefactor γ of the Stuart-Landau system is related to the complex gain $1 + i\alpha$ of the laser. The real part of the gain corresponds to $\text{Re}(\gamma) = -1$, i.e. the supercritical case, and is no longer a free parameter due to the normalization of the time to the photon life time [ALS96]. The normalized imaginary part $\text{Im}(\gamma)/\text{Re}(\gamma)$ of the Stuart-Landau oscillator describing the 'shear' corresponds to the amplitude-phase coupling factor α of the laser. Equation (2.37) contains the imaginary part $i\alpha p$ which will introduce a frequency like ω in the Stuart-Landau oscillator. The fact that it depends on the pump parameter p in Eq. (2.37) is not important as long as p is static, because any rotating frame can be removed.

2.4.4 Literature overview: Laser dynamics

Laser dynamics is a large and active field that covers a wide array of different topics. Lasers are a very popular experimental platform due to several key factors: First, their theory is very well established, such that quantitative agreement between theory and measurement can be reached even in complex setups. Second, the original lasers were one of the first experimentally accessible non-equilibrium systems, allowing for the investigation of many different aspects of non-equilibrium

2 THEORY

dynamics. Third, lasers are very fast and bright, which allows for a high rate of data collection on the dynamic phenomenon of interest. This also ties into their valuable use as tools for different kinds of experiments, such as pump lasers in solid state physics. Lasers are also widely used in commercial applications, such as data communication on long and intermediate distances through optical fibres, making it very important for them to not exhibit unwanted behaviour. Luckily for the nonlinear dynamics community and somewhat to the frustration of the engineers involved, lasers are sometimes very easily perturbed and can then exhibit rich nonlinear dynamics. They have traditionally been one of the most important test beds of chaos and synchronization theory.

In this thesis, the main focus lies on coupled laser systems. Typically, such coupling comes with a delay in experiments, so that most of the literature is focused on the delay-coupling case. Ref. [SOR13] gives a broad and extensive overview of delay-coupling in semiconductor lasers. The interest in the coupling of lasers goes back to the early days of laser physics, with first experiments on the injection of a laser by another [BOG73] or arrays of coupled lasers as in Ref. [BOT86, WAN88]. The most important case is a laser with self-coupling, i.e. coupling to an external cavity leading to delayed self-feedback [LEN85, HEN86, MOR92, VAN95, ALS96, HUY99, WOL02]. These modifications of the simple laser system can have a profound effect on the dynamics and lasers subject to feedback and coupling are liable to exhibit higher order and chaotic dynamics [HEN86, HEI99b, HEI00c, HEI03a]. However, chaotic intensity and phase fluctuations are not seen entirely negatively in the semiconductor photonics community. Applications of laser chaos include random number generation [UCH08, VER17], solving the two-armed bandit problem [NAR17] and chaos communication [MIR96, KAN08a, KAN10a].

The simplest example of laser coupling is the case of just two lasers, which has been extensively covered both theoretically and experimentally [WIN88, HOH97, HEI01b, KIM05, ROG06, HIC11, CLE14, SEI17]. An analytical investigation of the leading bifurcations for two-coupled Lang-Kobayashi type equations (cf Eq. (2.32)-(2.31)) with negligible coupling delay time τ can be found in Ref. [YAN04c]. Both synchronized and anti-synchronized solutions were found, which can be easily described by simple mathematical models. A more complex laser model was investigated in Ref. [JAV03], but ultimately yields quite similar results. Further theoretical and path-continuation investigations for the case with delay are given in Ref. [ERZ05, ERZ05a, ERZ06a].

An experiment with three non-identical lasers coupled via non-identical delay-lines exhibiting synchronization is shown in Ref. [GON07b]. Larger networks become more complicated to experimentally construct, the largest example likely being Ref. [ARG16] with 16 different lasers. Large networks can however be still studied theoretically [NIX12], where the case of ring networks [BUL07] and global coupling

2.4 LOCAL MODEL: LANG-KOBYASHI-TYPE EQUATIONS

[KOZ00, GAR99a] have been studied. Additionally, on-chip fabrication of laser networks are being proposed as future analogue computing platforms [BRU15].

2.5 The reservoir computing paradigm

This section introduces reservoir computing, a form of supervised machine learning that is distinct from both feed-forward and fully-trained recurrent networks due to its construction and history. It was developed both from a biological inspiration, as well as machine learning considerations. The mathematical details of the training and testing procedures used in this thesis are also given.

2.5.1 Supervised machine learning and artificial neural networks

Supervised machine learning is a subset of machine learning that comprises most of the advanced systems used today to solve narrow tasks. A task is called narrow, if the trained AI is only able to solve a very specific problem. For example, the previously mentioned Google Deepmind AlphaGo program cannot play chess, despite its great aptitude at Go. Many of the promising applications of artificial intelligence, such as self-driving cars or Apple's Siri voice assistant, are entirely created using supervised training methods. For now it seems that far fewer unsupervised programs exist.

Supervised machine learning heavily relies on the presence of training data. The goal is to create a program that converts an input to the correct output. The input and output data can in principle be of any kind or shape, as ultimately any format can be transformed into binary data. The training data not only needs to contain a set of representative inputs, but also their corresponding correct outputs. This knowledge of the 'correct answer' is similar to how a teacher knows the correct answers for a test in school and is the origin of the term 'supervised' machine learning. Such data sets could be images with corresponding annotations to train a computer at recognizing these images. For example, these sort of algorithms are used in the automatic detection of material that violates the terms of service of popular user-created content platforms such as Facebook, YouTube or Instagram

A popular implementation of supervised machine learning are the so called 'artificial neural networks'. These bio-inspired but highly abstracted networks consist of simple 'artificial neurons'. The connections between the neurons are trained, in a way that is inspired by the change of synaptic weights in the brain. As borrowed from the biological context, the state of each artificial neuron is called its 'activation'. The local model for the neurons is usually extremely simple, as the main part of the complex information processing is achieved through the network structure. To save on computational cost and to avoid convergence issues, the neurons are usually modelled with maps, i.e. they are defined with respect to a discrete time. The activation of a neuron then influences the activation of all neurons that it is connected to. The connections are, in general, assumed to be weighted and di-

rected, so that artificial neural networks are an example for a weighted and directed graph. Due to a fundamental difference in complexity and behaviour, the artificial neural networks are commonly divided into two distinct classes: ‘feed-forward neural networks’ and ‘recurrent neural networks’.

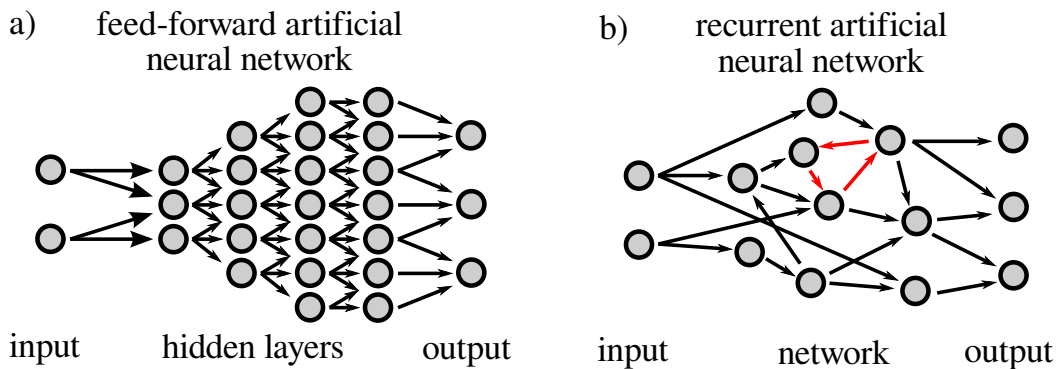


Figure 2.8: a): Sketch of a feed-forward artificial neural network. The information always passes from left to right with no recursion. b): Sketch of a recurrent neural network. A recurrent neural network is allowed to have loops, such as the loop marked in red.

Fig. 2.8 a) shows the sketch of a feed-forward network. The system is divided into different ‘layers’, with three distinct groups: The first layer is the input layer, where the information enters the system. This layer should have appropriate dimensions. For example, if the goal is to analyse pictures of resolution 480×640 pixels, then the input layer could consist of one node per pixel, with the activation representing the brightness. If the input image was a colour image, then the input layer should be tripled to account for the three colours of RGB image encoding. The second group of layers comprises the main part of the feed-forward architecture and consists of all layers except the first and the last. These layers perform most of the information processing and because they are not directly coupled to the outside, they are sometimes called ‘hidden layers’. The final layer is the output, where the activation of the nodes indicates the desired result, e.g. certain classifications or measures of the input. As the name implies, information solely flows from left to right in a feed-forward network as in the sketch of Fig. 2.8 a), i.e. ‘forward’. No intra-layer connections or backwards connections exist. This also guarantees the absence of any ‘loops’ or recurrence.

2 THEORY

The simple nature of feed-forward networks is also apparent in the mathematical form. Let $x_i^n(t)$ be the activation of an arbitrary node i in layer n at time t , then evolution will be written as:

$$x_i^n(t) = f \left(\sum_j a_{ij}^n x_j^{n-1}(t-1) + b_i^n \right), \quad (2.38)$$

where b_i^n is a bias and $f()$ the activation function. The synaptic weights a_{ij}^n encode the connection strength from node j of layer $n-1$ to node i of layer n . The time t is discrete and increased in steps, i.e. the system consists of coupled maps. As mentioned, this is advantageous as it decreases the computational cost for the forward time evolution. Furthermore, note that Eq. (2.38) contains no self-state dependence, i.e. there is no x_i^n on the right hand side. The activation of nodes in layer n at time t only depends on the activation of the previous layer in the previous time-step $x_i^{n-1}(t-1)$. The system has no memory and in the absence of any input in the first layer, the system will reach its resting state within one time step for every layer. This also justifies the layer structure.

The task of supervised machine learning is now to find the optimal value of all weights a_{ij}^n and biases b_i^n in Eq. (2.38) to obtain the best possible transformation into the desired output. This is similar to fitting functions to data points, only with many, many more degrees of freedom. The choice of f is usually very simple, e.g. sigmoidal functions $f(x) = \tanh(x)$ or linear rectifiers $f(x) = x\Theta(x)$, where Θ is the Heavyside step function. This allows for the direct fit of input to output, given enough training data.

In general, a feed-forward artificial neural network becomes more powerful, the more data it is fed and the more hidden layers it contains. Additionally, multiple feed-forward networks can also be stacked to obtain a ‘deep neural network’. If the training is successful, the system will not only be able to produce the desired output for the training data, but also be able to correctly classify previously unseen data. This corresponds to the system ‘generalizing’ from the examples it has seen and could be thought of as some ‘interpolation’ or ‘extrapolation’ from the finite data points of the training to the whole continuous set of possible input data. For this generalization to occur, the training data needs to be sufficiently diverse and capture all essential feature for the whole input data space. Needless to say, it is hard to be ever sure that one has captured all of the essential data, and therefore some companies view data as the ‘oil of the 21st century’. You can hardly have too much.

Data sets can also be generated by the learning system itself. In a later iteration of their Go program called AlphaGo Zero, the team at Google Deepmind created the data for the training entirely by self-play [SIL17]. The only thing that the program

was given *a priori* were the rules of Go - but nothing more. For the first set of self-play games, every legal move was deemed equally good. So a lot of random play happened at first. However, from this generated training data, the system was able to learn. As the system learns, so the quality of the self-play games increased, and thus a better system could be trained with its help. This allowed AlphaGo Zero to exceed Human performance and it is considered to be the best Go program of the world at the moment.

The second type of artificial neural networks are the recurrent neural networks. As sketched in Fig. 2.8 b), in a recurrent network the connections are no longer restricted to follow any particular structure. Any node can in principle be linked to any other, which in turn means that the system can contain many more free parameters than an equally sized feed-forward network. Additionally, this also allows for the appearance of loops as shown in red in Fig. 2.8 b). These loops prevent the system from settling into the resting state instantaneously, but instead induce an autonomous dynamic of the system itself. This not only brings problems in the shape of possible oscillations or chaotic motion in the absence of any input, but also vastly complicates the deduction of optimal parameters a_{ij} and b_i [PEA95]. An overview of the state-of-the-art deep learning algorithms for 2014 can be found in Ref. [SCH14h]. It is however assumed, that a fully trained recurrent neural network is much more powerful than a simple feed-forward variant. Especially considering that the human brain definitely includes loops, this seems also an important aspect for machine learning.

2.5.2 History of reservoir computing

In 2002 Maass *et al.* published their paper "Real-time computing without stable states: A new framework for neural computation based on perturbations" [MAA02], proposing a new way of performing computation using neuron models. They reported, that a network of neurons could act as a simple computer in what they called 'liquid state machine'. At its core, this novel system did not operate by encoding information in steady states or fixed systems, but by being permanently transient. On a first glance, the system is very similar to a recurrent neural network, however the training procedure is fundamentally different (and easier to implement).

In their paper [MAA02], they demonstrate that a sufficiently complex network of neurons that is driven by an external input will retain some *memory* of this input for a finite time. This is caused both by the recurrent loops in the system and the more complex local model for the nodes. When the neural network is constructed non-symmetrically, the time-traces of each individual neuron will differ. A class of 'read-out' neurons can now be added, which merely linearly combines

the traces of the neurons inside the network. When the weights to these read-out neurons are chosen correctly, a ‘liquid state machine’ allows for surprisingly powerful computations on time-dependent input data streams.

Independently of this neuro-inspired work, Jäger had already published his report on "The ‘echo state’ approach to analysing and training recurrent neural networks" in 2001 [JAE01]. Therein the author describes a method to circumvent the difficult training of recurrent neural networks. He proposes to divide the weights of the system into two classes: internal links inside the network, and all links directly leading to the output nodes. Still working from the background of machine learning, he envisioned these ‘echo state networks’ to be constructed from simple local functions and the coupling matrix to be random but fixed. The training would only be performed on the output-weights, which he could show can be rewritten as a simple linear regression or matrix (pseudo-)inversion. This is conditional on the ‘fading memory’ property, wherein the system retains some, but not infinite memory of past inputs.

In practical terms, both the construction rules introduced by Mass *et al.* and those by Jäger yield similar structures, which are nowadays called ‘reservoir computers’ [LUK09]. It has also been observed that the tripartite nature of ‘reservoir computers’ can naturally emerge in a general training scheme for recurrent networks, as is shown in Ref. [SCH04g]. Reservoir computing therefore represents a small subset of a supervised training algorithm for recurrent artificial neural networks. However, modern versions have long superseded some of the restrictions of the original approach and do not even require a neural network at all.

2.5.3 Modern formulation

The modern formulation of the reservoir computing paradigm used in this section will rely on a simple yet powerful realization: Any dynamical system possesses computational power. This fact has not been sufficiently considered or exploited in the nonlinear dynamics community so far, despite some major efforts. The focus is slowly changing and in large part this is due to an increased interest in non-conventional computing concepts, see Ref. [CRU10a].

To avoid the difficult question of a general definition of computation, a signal-processing view of computation will be adopted here: A time-dependent input function $u(t)$ should be transformed into a desired output function $o(t)$. Both $u(t)$ and $o(t)$ can be continuous functions, a discretized version thereof, or data that is inherently sequential. We are however only interested in input/output relationships with an inherent temporal nature, or those that can be effectively transformed into one. For many *static* problems, such as image recognition or Go games past inputs

can and should be neglected, as only the current input state is important. For those problems, a deep neural network is the state-of-the-art solution.

When processing a signal, both instantaneous information of the current input $u(t)$ and the input one or multiple time steps in the past $u(t - \tau_i)$ can be important, which is where the fading memory property is essential. The following simple example clarifies, how dynamical systems in general can perform this type of computation: An arbitrary dynamical system with state variables $\mathbf{X}(t)$ is driven by the input $u(t)$. In the simplest case of an ODE equation for the solitary behaviour of the dynamical system, the equivalent equation with input to Eq. (2.1) would be

$$\frac{d\mathbf{X}(t)}{dt} = F(\mathbf{X}(t), t) + W_{in}u(t), \quad (2.39)$$

where W_{in} is a fixed vector of input weights, with at least one non-zero entry. The input weights W_{in} are usually taken randomly. As previously discussed, the dynamics in the absence of any input of the ODE in Eq. (2.39) will be dictated by the evolution function F . However, with the inclusion of the input, the system is now perturbed and differs in its behaviour. If the system was in a fixed point \mathbf{X}_{FP} at the beginning of the input, it will be perturbed away from the steady state values. This is especially apparent, when the solitary dynamics are weak and the input is strong. The system will perform some trajectory in its phase space, with the exact shape dependent on the input $u(t)$. If a different input $\tilde{u}(t)$ is fed into the system, the resulting dynamics of Eq. (2.39) will also differ. The individual entries of the state vector $\mathbf{X}(t)$ can then be viewed as a complex transformation of the input and according to the signal processing view this automatically means that the system has performed a computation. The importance of this simple realisation should not be understated, as it allows to view the complex field of analogue computing, computation theory and nonlinear dynamics in a new light. Furthermore, if the system is large, each entry of the state vector $\mathbf{X}(t)$ will likely correspond to a different transformation. For example, the motion of a driven pendulum can be analysed both with respect to its velocity and its position, and their values and shape over time will not be identical.

One can be tempted to protest at this stage, that the nonlinear system has in fact done nothing other than reacting to input. Furthermore, the system merely follows the dynamics prescribed by its ODE of Eq. (2.39), so there is no new information being produced. However, in the signal processing view any deterministic transformation of the input $u(t)$ is a computation. So as long as Eq. (2.39) is noiseless and well-behaved, the system is essentially an analogue computer (or a discretised approximation thereof if Eq. (2.39) is numerically solved).

However, the transformation performed by an arbitrary dynamical system will rarely be desired. The motion of each of the individual degrees of freedom of the

2 THEORY

state vector $\mathbf{X}(t)$ will be some complex transformation of the input. But the space of all possible transformations of input data $u(t)$ is very large (it is a space of mappings from functions to functions), and thus a randomly chosen transformation will not be producing the desired output $o(t)$. The reservoir computing paradigm uses an additional step to obtain the desired output $o(t)$. One could attempt to tune the dynamical system in such a way, that the performed computation becomes optimal, i.e. adapt the local function F in Eq. (2.39) so that at least one of the degrees of freedom becomes $o(t)$. However, this in general is a very hard problem as this is essentially equivalent to designing a custom analogue computer for arbitrary tasks. The recurrent neural network community has developed some ways to facilitate such a training, but these methods are computationally costly and require full control over the target system. The alternative approach leads to reservoir computing: If the desired output $o(t)$ is not reflected in any individual entry of the state vector $\mathbf{X}(t)$, it still may be obtainable by a suitable linear combination thereof:

$$\hat{o}(t) = \mathbf{X}(t) \cdot W_{out}, \quad (2.40)$$

where W_{out} represents the vector of optimally chosen output-weights, \cdot the scalar product and \hat{o} the approximately reconstructed desired output. The quality of the approximation increases, if more degrees of freedom are combined, i.e. if the phase space of $\mathbf{X}(t)$ is large. Thus, complex dynamical systems are more suitable for computation than small and simple ones. Because they contain many degrees of freedom to hold information, these systems are called ‘reservoirs’. To be useful, a reservoir should fulfil several criteria to enable effective computing [MAA02]:

Consistency The same or a very similar input $u(t)$ should result in similar phase space trajectories $\mathbf{X}(t)$, so that computation is reproducible. This property is strongly linked to the solitary dynamics of the system, the number of attracting states and noise levels.

Separability The system should react differently to sufficiently different inputs to allow classification.

Fading memory The system should continuously absorb new information and forget old, irrelevant information, i.e. should permanently be in a transient state.

One of the great advantages of reservoir computing compared to other machine learning approaches, is that the reservoir itself is never trained. Hence, even the imperfect systems of the real world that are subject to noise and small parameter shifts can be used as reservoirs. This opens the possibility to use substrates for the dynamics that are fast, i.e. not simulating an artificial neural network on a

computer, but using an intrinsically fast system as a dynamic core. The digital computers based on silicon microchips have had more than 50 years of development, making them very advanced systems. With today's price levels, computational power on a digital computer is relatively cheap and thus much of the machine learning is done *in silico*. Even for concepts that are intrinsically suited for analogue computing such as reservoir computing, it is often more effective to emulate an analogue system on a digital computer. However, this may be mainly caused due to the comparatively immature technology used for hardware-based analogue computers and may change in the coming years. Especially photonic systems have the potential to vastly out-class conventional transistor-based microchips in terms of both speed and price.

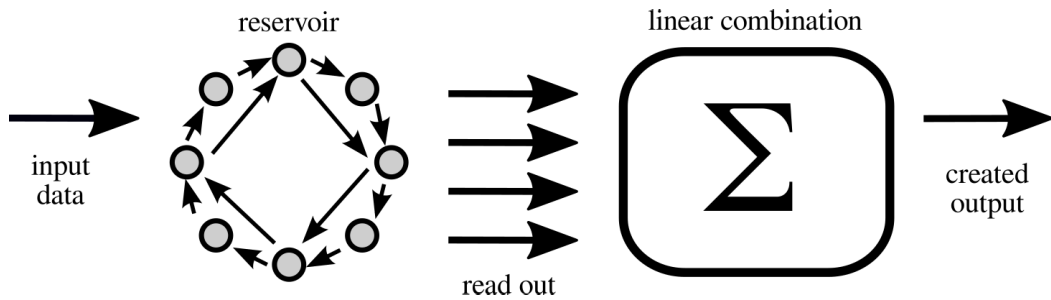


Figure 2.9: Sketch of the reservoir computing paradigm: An input is fed into a complex dynamical system, which is called the 'reservoir'. The high-dimensional phase space trajectory is read-out and then linearly combined in an optimal fashion to obtain the output.

Figure 2.9 shows a sketch that sums up the reservoir computing principle. An input $u(t)$ is fed into a dynamical system. As mentioned the dynamical system can be anything, but should have a large phase space. Traditionally, as a neuro-inspired computing scheme these systems have often been depicted as 'artificial neural networks' and thus a small network is sketched in Fig. 2.9. This drives the system and results in some non-trivial response. The reservoir will perform a high-dimensional trajectory in its phase space. To capture as much as possible of this complex behaviour, as many state variables as possible are read out from the system. The individual time-traces of the read-out are then linearly combined according to Eq. (2.40) to obtain an output signal $o(t)$. The next section will cover the mathematical formalism in more detail and describe how to obtain the output weight vector W_{out} in Eq. (2.40).

2.5.4 Mathematical details

Reservoir computing is usually applied to discretised functions, as a fully continuous system cannot be modelled on modern digital computers. Hence, both the input $u(t)$ and output $o(t)$ can be represented as sequences, which can be seen as a discretisation of an originally continuous function:

$$u_k = u(kT)o_k = o(kT), \quad (2.41)$$

with a clock cycle of T . Similarly, let \mathbf{X}_k denote the discretised system state of $\mathbf{X}(t)$. Recall, that the system state itself is a vector as the reservoir is a high-dimensional system and let the dimension be denoted with D :

$$\mathbf{X}_k = \begin{pmatrix} x_k^1 \\ \vdots \\ x_k^D \end{pmatrix} \quad (2.42)$$

For now it will be assumed that all signals are discretised with respect to the same clock T , but will usually not coincide with the numerical integration step. Furthermore $u(t)$ is not necessarily fed into the same system as the original time series it was produced with. This is for example the case, if the reservoir computer operates at a much higher or lower speed than the computational task demands. The predicted output \hat{o}_k of the reservoir depends on the discretised system state \mathbf{X}_k and the output weight matrix W_{out} :

$$\hat{o}_k = \mathbf{X}_k \cdot W_{out}. \quad (2.43)$$

Let \hat{o} now denote the entire sequence of predicted outputs \hat{o}_k . Let the total number of input samples u_k and output targets o_k be K . Then let the matrix S denote the state matrix of the system for all discretised time steps, where $S_{ij} = x_i^j$, i.e. the rows of the state matrix S are the discretised system states \mathbf{X}_k . Additionally, the last entry in every row of S shall be 1. This is called a bias and is a typical addition in supervised machine learning algebra [JAE01]. Thus, the whole state matrix S is a $(D + 1) \times K$ matrix and given by:

$$S = \begin{pmatrix} x_1^1 & \dots & x_1^D & 1 \\ \vdots & & \vdots & \vdots \\ x_K^1 & \dots & x_K^D & 1 \end{pmatrix} \quad (2.44)$$

and Eq. (2.43) can be rewritten as a matrix equation:

$$\hat{o} = SW_{out}. \quad (2.45)$$

2.5 THE RESERVOIR COMPUTING PARADIGM

The question of what the *optimal* weights W_{out} are hinges on the desired definition of the *goal function*. For reservoir computing, it is assumed that the squared distance between target output o and predicted output \hat{o} should be minimized, i.e. find weights to express:

$$\min_{W_{out}} |o - \hat{o}|^2 = \min_{W_{out}} |o - SW_{out}|^2. \quad (2.46)$$

The solution of this minimization problem can be found [JAE01] and it is in fact a very common problem for linear algebra. Different formulations use the pseudo-inverse of the matrix S . However, finding a linear regression such that

$$o \approx SW_{out}, \quad (2.47)$$

in the sense of Eq. (2.46) is a common feature of different linear algebra packages. Due to the choice of the goal function as the squared distance, Eq. (2.46) corresponds to the regression of a hyperplane to a sample of data points. This thesis will not rely on creating a separate pseudo-inverse of S , but rather solve Eq. (2.47) directly using the *solve*-functionality of the Armadillo linear algebra package for C++, which in itself is a wrapper for OpenBlas. The library contains all the functions necessary to find the optimal solution for W_{out} to Eq. (2.46).

Note, that the number of test samples K can be changed independently of the system size D . With the inclusion of the bias term, the output weight vector W_{out} has $D + 1$ elements. Hence, if $K < D + 1$, the system of Eq. (2.47) is under-determined and the euclidean distance between prediction \hat{o} and target output o becomes 0. On the other hand, if $K > D + 1$, the system is overdetermined, and the error can only be minimized but not completely removed. This is the desirable case, as one wants the system to find the best compromise of all possible output weights over a large amount of training data. Thus, $K \gg D + 1$ is the normal case for reservoir computing.

2.5.5 Suitability of delay-systems for reservoir computing

The original concept of reservoir computing was inspired by machine learning based on artificial neural networks [JAE01] and neuromorphic computing concepts, which naturally led to the constructions of ‘reservoirs’ as networks. However, any dynamical system possesses computational power (see Sec. 2.5.3), which enables the use of more than just network systems. This is in contrast to more complex machine learning algorithms, which constantly adapt many parameters to try to optimize a recurrent neural network. No ‘trainable’ substrate is necessary for reservoir computing. The fixed nature of the reservoir also allows the use of ‘flawed systems’ in experiments, i.e. real hardware implementations. The parameters only need to

2 THEORY

be kept fixed. If, on the other, one wanted to implement a full training algorithm for a recurrent artificial neural network in hardware, one would have to be able to adapt the strength every link and parameters of every node very precisely.

When it comes to large dynamical systems, a natural class of physical platforms are spatially extended systems. Indeed, a simple reservoir computing problem has been successfully solved with the use of the surface of water in a bucket [FER03]. One disadvantage of such a 2d-surface (or even more complex 3d volume systems) is that complex versions require a spatially resolving read-out mechanisms, which increases the complexity of the involved components.

Delay systems described by DDEs (see Sec. 2.1.5) can be viewed as an alternative way of describing certain classes of spatially extended systems, cf. Sec. 2.2.4. Delay-systems have an infinite phase-space dimension, as the state of the system is not only dependent on the instantaneous variables, but also the recent history thereof. The phase space is only truly infinite in a mathematical sense, as in reality finite resolution, discrete read-out times and noise limit the exploitable dimensionality of the system. Nevertheless, DDE systems can serve as powerful reservoirs [APP11] and especially when photonic systems are used such systems can be very fast [BRU13a]. This form of reservoir computing with delay will also be referred to as the ‘delay-line approach’ from here on.

The delay-line approach for photonic or electro-optic reservoir computing has been very successful [SAN17a] and profits from the availability of already mature telecommunication technologies. In the simplest setup, a single laser subject to optical feedback is used and can be described by the Lang-Kobayashi rate equation approach [ALS96], see Sec. 2.4.

Delay-based reservoirs always contain at least one additional time-scale in the shape of the delay-time τ as compared to systems without delay, cf. Eq. (2.8). The delay term leads to a reinjection of information and rejuvenates the dynamical complexity of phase space trajectories. When the delay is short or comparable to the intrinsic dynamical time-scales of the system, the effect of delay can largely be absorbed into an effective model that hides the feedback mechanisms. Therefore a typical delay-based reservoir employs a delay time τ that is much larger than the intrinsic time scales of the system and thereby extends the lifetime of transient behaviour.

Masking

In the simplest case, a delay-line based reservoir computer consists of only a single active unit and a delay-line. This delay-line can be seen like a hidden network or a hidden spatial dimension, where the information is stored to be reinjected later. To make use of this dimension, it is important to realize that the information

must be encoded *in time*. Hence, for a delay-based reservoir computer information must be sequentially injected, and the system state has to be recorded at periodic intervals. However, a simplistic application of the injection and read-out procedure proves to be inadequate, i.e. simply reading out at a clock cycle T is not enough: the system only contains a single active node, which means that in the simplest case only a single input and readout channel exist. For the purpose of reservoir computing, a single read-out channel would limit the effective dimension used for the computation of the system to $D = 1$, the level of a network with just $N = 1$ oscillator. This would be a very poor reservoir. Hence, one has to make better use of the temporal dynamics in the system to obtain a richer response to an input signal.

The read-out bottle neck can be overcome by sampling the system response, i.e. recording the state of the oscillator multiple times during one input timing window T . In principle, any arbitrary collection of timings in the interval $[0, T]$ could be used, as long as these timings do not drift with respect to the input timeseries, i.e. both input and output must adhere to the same clock cycles T . However, in reality every signal has characteristic time scales, e.g. autocorrelation times. The sampling of two parts of the system response that are very close to each other temporally will not provide much independent information. Furthermore, for purely photonic systems this readout sampling is one of the limiting factors, as a very fast out-coupling mechanism is necessary. Therefore the system usually is constantly sampled at a rate of $1/\theta$, with θ being the time between read-outs (and as fast as oscilloscopes or other limiting equipment allows). For example, a 40 GHz oscilloscope will sample the system state every $25ps$. If the clock cycle is $T = 10ns$, the system state would be read out 400 times per input, bringing the effective dimension to $D = 400$.

The second drawback that can limit the efficiency of reservoirs with a single unit with delay is that the delay-line often consists of a ‘closed loop’ that merely returns a previously emitted signal of the system. The content of the delay line, and correspondingly the history function of the governing DDE is therefore not directly accessible. This is roughly similar to the case when information is only injected at one place into a network, or when only a single point in a spatially extended system is perturbed by $u(t)$. The resulting dynamics will be relatively low-dimensional, and therefore computational power may be low.

To increase the complexity of the transients and to elucidate a dynamically rich response to the input, delay-based reservoir computers employ a *masking procedure*. This technique, as introduced by Appeltant *et al.* in Ref. [APP11], greatly enhances the performance of such reservoir computers. Let $u(t)$ be the piece-wise constant input function with piece-lengths as long as the clock cycle T based on the time-discrete input series u_k . The masked signal will be produced by the following

2 THEORY

procedure: a function $M(t)$ called the *Mask* is multiplied with $u(t)$, resulting in the masked signal $J(t) = u(t)M(t \bmod T)$. The mask $M(t)$ is defined on the interval $[0, T]$. Using the definition of both the mask and the discretised input sequence u_k this leads to

$$J(t) = u_k M(t \bmod T), \quad \text{where} \quad (k-1)T < t \leq kT. \quad (2.48)$$

Often the mask M is defined as a piece-wise constant function with step-length θ and values M_j :

$$M(t) = M_j, \quad \text{where} \quad (j-1)\theta < t \leq j\theta, \quad (2.49)$$

and if $T \bmod \theta = 0$, the masked input signal becomes

$$J(t) = u_k M_j, \quad \text{where} \quad (k-1)T < t \leq kT, \quad (j-1)\theta < t \bmod \theta \leq j\theta. \quad (2.50)$$

Figure 2.10 shows a sketch of the masking procedure. The piece-wise constant input function $u(t)$ (left) is relatively uniform. With a complex multi-valued masking, the masked input $J(t)$ (right side of Fig. 2.10) is much better for reservoir computing.

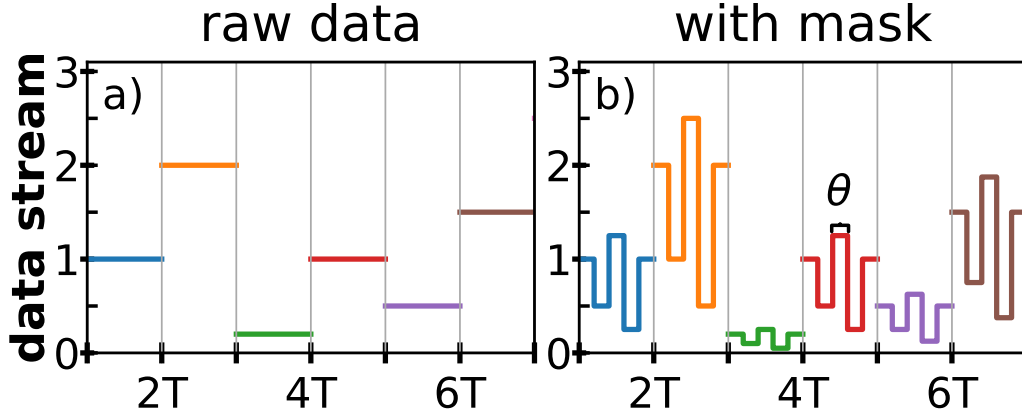


Figure 2.10: Comparison of the input data stream for the raw (unmasked) data (left) and the masked data (right). The data and mask are piece-wise constant functions with piece-lengths T and θ , respectively. A binary mask was used.

The shape of the masking signal can, in principle, be arbitrary and is not limited to the piece-wise constant nature introduced here. In fact, Ref. [NAK16] shows the advantage of using continuously varying signals, such as coloured noise or chaotic time-traces. This masking approach can also be extended to more complex systems: When the input is multi-dimensional and $u(t)$ is a vector, then a fixed but different mask will be generated for every entry of $u(t)$. Similarly, when more than a single input-channel into the system exists, e.g. there are two oscillators with delay-lines

instead of one, $u(t)$ will be masked with a different mask for every channel. Hence in a system with N_R input channels and M -dimensional input signal, $N_R M$ masks are needed.

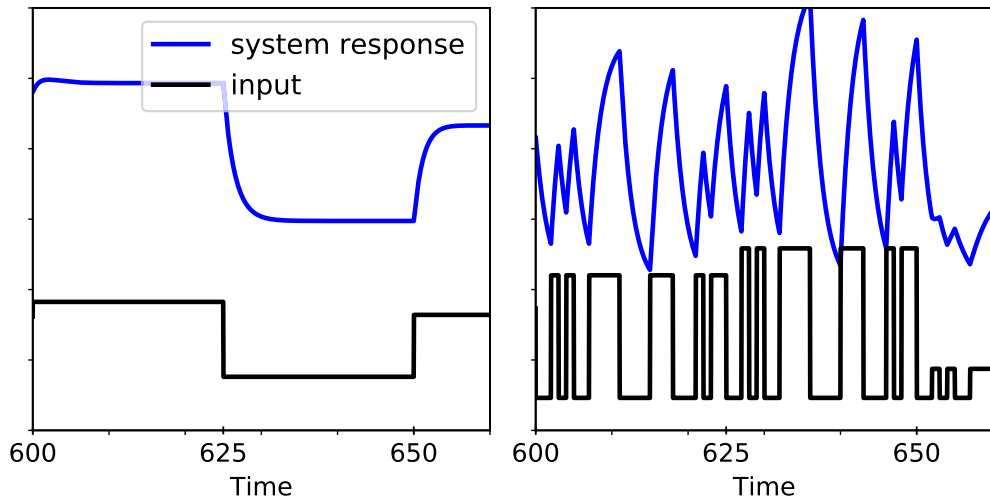


Figure 2.11: Illustration of the advantages of the masking procedure. When a system is driven with a piece-wise constant input (black, left), the response (blue) will only be 'dynamically rich' at the beginning of the interval (left). With the masked input (black, right), the system is constantly kept in a transient state, allowing for a higher dimensional system response (right). $\tau = T = 25$, $\theta = 1$.

To illustrate the great increase in dynamical richness, Fig. 2.11 shows the response (blue lines) of a single Stuart-Landau oscillator with delay when driven by the raw input $u(t)$ (left) and the masked signal $J(t)$ (right). When the system is driven by the unmasked signal, it quickly approaches a steady state value and the transient response dies out (blue line on the left of Fig. 2.11). Conversely, with the reservoir driven by a masked signal, the system is kept constantly in a transient state (blue line, right of Fig. 2.11). The masks used in this thesis will be binary masks, as shown in Fig. 2.11. The input timing window T and the delay time τ were both chosen to be 25 in Fig. 2.11 in the unitless units of the Stuart-Landau equation of Eq. (2.24). The input looks more complex on the right of Fig. 2.11 only because of the masking, as none of the other factors were changed.

2.5.6 Virtual networks

In some way, the reservoir computer based on the delay-approach is not so different from the network approach. While the network has N discrete units, that produce different transformations of the input, at first glance it may seem that the delay-line is infinite dimensional as it contains a continuous history of the system state.

However, the readout of the delay-line reservoir is only produced at fixed temporal positions in the delay-loop. In a good reservoir computer, each of these temporal positions produces a different transformation of the input signal. These T/θ fixed temporal positions are then similar to a reservoir computer based on a network.

When the reservoir computer contains simple equations, it is even possible to find a ‘virtual network’ representation that corresponds to the different temporal positions in the delay-line. This has been done in Ref. [APP12] and Ref. [SCH13].

2.5.7 Benchmark tasks for reservoir computers

Different benchmark tests exist to evaluate the performance of reservoir computing systems. Any of these tests can be applied to any reservoir computer. All the benchmarks are time-discrete in nature, i.e. they are represented by sequences, not functions. Each task is posed as a problem, where from a certain input sequence u_k a correct output sequence o_k is to be computed. The tests used in this thesis are outlined in the following. The errors of the test can be quantified with different measures. The mean squared error (MSE) is a measure of the average deviation between prediction \hat{o}_k and target o_k [DAM12], and is natural to evaluate, as it is the property that the reservoir computing training minimizes:

$$MSE(\hat{o}_k) = \frac{1}{K} \sum_{k=0}^K (o_k - \hat{o}_k)^2. \quad (2.51)$$

The lowest possible MSE is 0, when there is a perfect agreement between prediction \hat{o}_k and target o_k . However, there is no upper bound to the error and therefore a comparison between different tasks is difficult. This can be corrected by a normalization:

$$NMSE(\hat{o}_k) = \frac{1}{K} \frac{\sum_{k=0}^K (o_k - \hat{o}_k)^2}{\sigma^2(o)}, \quad (2.52)$$

and the resulting quantity is called the normalized mean squared error (NMSE). Here, $\sigma^2(o)$ is the variance of the target series o_k :

$$\sigma^2(o) = \frac{1}{K} \sum_{k=0}^K (\langle o \rangle - o_k)^2, \quad (2.53)$$

where $\langle o \rangle$ is the average of the target series o_k . The worst behaviour that any machine learning system should offer is to not learn any dynamic prediction for o_k . Instead, the minimal learning is to predict a static $\hat{o}_k = \langle o \rangle$, i.e., always predict the average of the target. With such a static prediction Eq. (2.52) becomes solvable and the NMSE is 1. The normalized mean squared error therefore ranges from 0

(perfect learning) to 1 (minimal learning, worst case), allowing also for a cross-comparison between different tasks.

Many reservoir computing systems are quite successful at their benchmark tasks, and therefore NMSE very close to 0 are often found. To better distinguish between different regimes of performance, the normalized root mean squared error (NRMSE) is given by:

$$NRMSE(\hat{\theta}_k) = \sqrt{NMSE(\hat{\theta}_k)}. \quad (2.54)$$

The NRMSE has the same upper and lower bounds as the NMSE as $\sqrt{1} = 1$ and $\sqrt{0} = 0$.

Santa Fe chaotic time-series prediction

The Santa Fe time series challenge was a collection of machine learning tasks that were considered difficult and proposed by the Santa Fe Institute [WEI93]. As the name implies, these sets of data were generally posed as the continuation problem of a timeseries, i.e. a recorded but complex time series was to be continued based on an analytical or numerical scheme. These kinds of problems are not merely academic in nature, but were intended to be solved to help with stock market trading or parameter inference of complex systems.

The data sets were made publicly available and scientists were encouraged to submit their works. First, they should continue the data sets. The correct continuation as measured or calculated for that specific task was not made publicly available but was known to the organizers. Furthermore, the authors should also submit their used algorithm, and they should give an estimate of the noise characteristics, dimensionality of the time series and attempt to recreate the governing equations.

The data sets were collected from different fields and contained recorded astrophysical, physiological, economical data and data numerically generated by an analytical systems. Furthermore, the authors even included the beginnings of Johan S. Bach's last unfinished musical piece from Die Kunst der Fuge [WEI93]. All of the data sets were non-periodic and therefore hard to predict. Finally, one data set was that of a NH_3 -laser with chaotic behaviour.

Fig. 2.12 shows the first 1000 data points of the laser time series. This is an experimentally recorded intensity time trace. The laser exhibits an almost-periodic oscillatory behaviour with undamped relaxation oscillations interspersed with drop-outs. As with the other tasks in the Santa Fe challenge set, the goal is to predict a future intensity value $I(t + n)$, given the intensities up to time t . This n-step

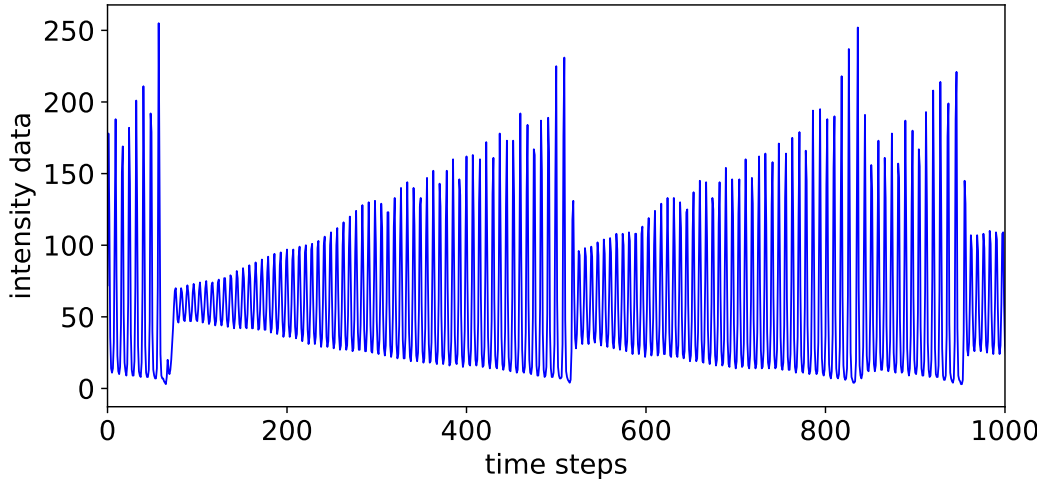


Figure 2.12: The first 1000 data points of the Santa Fe time series prediction task for the NH_3 -laser chaos. The whole time series is 9000 data points long.

prediction becomes harder for larger n . In the reservoir computing formalism, this can be expressed as

$$u_k = I_k \qquad o_k^n = I(k+n), \qquad (2.55)$$

where o_k^n is the n -step prediction, with $n > 0 \in \mathbb{N}$ and I_k is the sequence of intensities. The results of the original competition, as outlined in Ref. [WEI93], showed that most systems could not predict more than the first 15 data points. One drawback of the Santa Fe chaotic laser time series prediction task is its experimental origin: the resolution is limited by the noise and instruments used in the original experiment. Hence, the prediction is not perfectly possible, even for a very powerful machine learning scheme. It is only useful for roughly estimating the computational power of a system as the task performance saturates for finite levels of computational power. In the reservoir computing setup this means, that no reservoir of too large dimensions should be used, as otherwise the performance will already be saturated and no parameter dependences can be reliably investigated. Nevertheless, the Santa Fe task is a classic benchmark and often used throughout the literature.

Nonlinear autoregressive moving average (NARMA)

Another type of test for the computational capabilities of a system for temporal signal processing and the main benchmark for this thesis is the nonlinear autore-

gressive moving average (NARMA) task. This task was introduced by Atiya and Parlos in Ref. [ATI00]. The NARMA task can be posed for different *lengths*, where the length represents the required memory. A typical choice for the reservoir computing community is the NARMA task of length 10, the NARMA10.

The input for the NARMA10 is a series of uniformly distributed u_k in the interval $[0, 0.5]$. The NARMA10(u_k) is defined by an iterative formula o_k as given by:

$$o_{k+1} = 0.3o_k + 0.05o_k \left(\sum_{i=0}^9 o_{k-i} \right) + 1.5u_{k-9}u_k + 0.1, \quad (2.56)$$

where it is assumed for the initialization, that all $u_{k<0}, o_{k<0} = 0$. This task requires the system to retain a long memory of past inputs, as the Eq. (2.56) explicitly depends on u_{k-9} and o_{k-9} . Unfortunately, the NARMA10 task of Eq. (2.56) is not well defined, and in rare cases if the random numbers u_k happen to all be rather large, the sequence will diverge. For the numerical part of this thesis, the NARMA10 target o_k is therefore capped at $o_k \leq 1$, which prevents it from diverging.

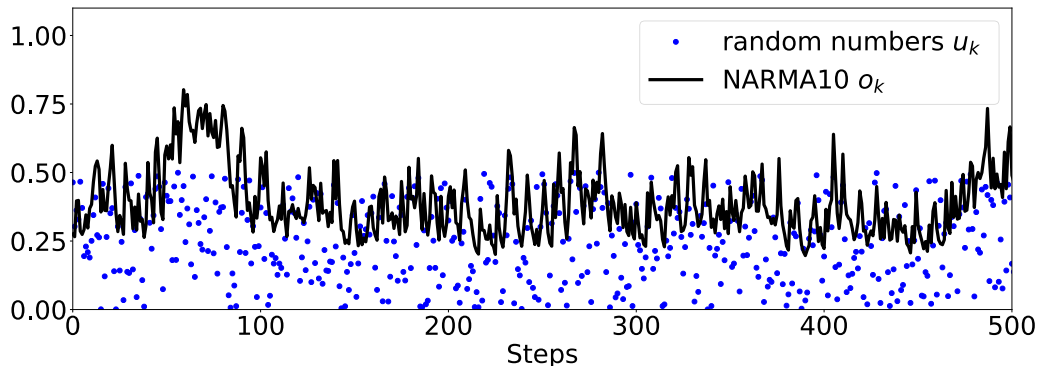


Figure 2.13: Example of a NARMA10 series. The blue dots represent the random numbers u_k , from which the NARMA10 o_k is calculated.

Figure. 2.13 shows an example of a NARMA10 series, with the initial random numbers u_k in blue, and the resulting NARMA10 according to Eq. (2.56) in black. Note, that while the original random number sequence u_k is uncorrelated, the resulting NARMA 10 sequence is not. Unlike the Santa Fe task, the NARMA10 task can be calculated for arbitrary precision and thus does not suffer from noise or fundamental resolution limits.

Memory capacity

An important property for a reservoir computer is the ability to hold *memory*. This was first quantified for echo state networks in Ref. [JAE02]. Let u_k be an arbitrary input for the reservoir computer, then the memory capacity can be derived by training the system to calculate

$$o_k^m = u_{k-m}, \quad (2.57)$$

where o_k^m is the m -step *linear recall*. This conceptually is the opposite of the timeseries prediction of the Santa Fe tasks; the system has to be able to reconstruct previously seen entries, which requires the information to still be present in the reservoir. The corresponding m -step memory capacity C_L^m is then given by [JAE02]:

$$C_L^m = 1 - NMSE(\hat{\delta}_k^m), \quad (2.58)$$

with the the normalized mean squared error (NMSE) as given by Eq. (2.52). The m -step memory capacity C_L^m is 0 if the system is unable to recall any information m steps in the past, and correspondingly $C^m = 1$ for a perfect linear recall. In general, any input sequence u_k that is varying can be used, but to numerically obtain a general measure for the linear recall, the input sequence should not have correlations, i.e. it should be a white noise sequence. In this thesis, the memory is always tested for an input sequence drawn from a uniform distribution between 0 and 0.5, as this allows the simultaneous evaluation of the memory and NARMA10 task and no difference between this and a Gaussian white noise sequence was found.

Typically, the linear memory capacity decreases with larger m , i.e., $C_L^m > C_L^{m+1}$. The total linear memory capacity of a system $C_{L,tot}$ is given by the sum of all C_L^m :

$$C_{L,tot} = \sum_{m=0}^{\infty} C^m. \quad (2.59)$$

However, when numerically evaluating the memory capacity C_L^m for large m , the numerical noise and finite precision will result in a residual non-zero C_L^m , even when in reality the system has lost almost all the information. A numerically evaluated $C_{L,tot}$ must therefore be truncated at an appropriate C_L^m , typically when C_L^m has approached zero within the level of training precision.

Nonlinear extensions

Nonlinear extensions for the memory capacity exist and are shown by Dambre *et al.* in the excellent paper Ref. [DAM12]. The simple linear memory target of Eq. (2.57) can be extended to

$$o_k = f[u_k], \quad (2.60)$$

where f is an arbitrary, possibly nonlinear transformation of u_k . For $f[u_k] = u_k$ Eq. (2.60) turns back into Eq. (2.57) with $m = 0$, while choosing $f[u_k] = u_{k-1}$ recovers the 1-step linear recall and so forth. Furthermore, transformations such as $f[u_k] = u_k u_{k-1}$ that use multiple different entries of the sequence u_k are explicitly allowed. In order to be able to capture a reservoir's ability to store information in any nonlinearly transformed format, a set of base vectors spanning the entire space of nonlinear functions f needs to be found. Dambre *et al.* propose to restrict oneself to the weighted L^2 Hilbert space of functions, see Ref. [DAM12] for mathematical details. In principle, any family of nonlinear functions $f_{\{\epsilon\}}$ with index family $\{\epsilon\}$ is applicable if it spans the entirety of the L^2 space of functions. However, it is best to use a set of orthogonal functions $f_{\{\epsilon\}}$, such as Legendre or Hermite polynomials.

Similar to the linear memory, the nonlinear memory can be tested by inserting an arbitrary input u_k , for which white noise is once again suited best. The corresponding *nonlinear memory capacity* for index $\{\epsilon\}$ is obtained by training the system to approximate $o_k = f_{\{\epsilon\}}[u_k]$:

$$C_{\{\epsilon\}} = 1 - NMSE(\hat{o}_k^{\{\epsilon\}}). \quad (2.61)$$

In this notation, the linear memory capacity is just one of many memory capacities $C_{\{\epsilon\}}$ and a certain subfamily of indices in $\{\epsilon\}$. Like its linear counterpart, the nonlinear capacity is bounded $0 < C_{\{\epsilon\}} < 1$. The total linear and nonlinear memory capacity is then given by:

$$C_{tot} = \sum_{\{\epsilon\}} C_{\{\epsilon\}}. \quad (2.62)$$

It can be shown that the maximum total linear and nonlinear memory capacity cannot exceed the dimensionality of the system [DAM12], i.e. $C_{tot} \leq D$.

While the considerations by Dambre *et al.* in Ref. [DAM12] only apply to time-discrete functions, it seems likely that similar concepts could be deduced for time-continuous functions (at least if one is not too worried about full mathematical proofs). It would be interesting to see what the corresponding measure of memory is, as C_{tot} will have to become some integral. However, this will have to be left for future investigations.

2.5.8 Analogue computing: non-von-Neumann architectures

Having introduced the framework of reservoir computing, the typical mathematical details and the common tasks or benchmarks, it is important to reflect on the somewhat exceptional position that hardware-based reservoir computing is at, compared to conventional computers. The standard desktop of today is a Turing-complete digital binary computer based on the von-Neumann architecture and reservoir computers are not.

Modern computers store their internal state not in some analogue signal, but in a fixed set of internal physical quantities, e.g. voltages on a microchip. The different levels of the microscopic quantities represent the fundamental unit of the computer. When the system only distinguishes quantized levels, it becomes inherently more robust against noise and it is easier to obtain reproducible computations. The internal state can then be expressed abstractly with integers, i.e. digits. A *digital* computer therefore is first and foremost a computer that is constructed in a way that it performs actions on discrete levels of voltages. Most modern computers can only distinguish between two states: on/off also called 1/0 or True/False corresponding internally to high voltage/low voltage and they are therefore *binary*.

The von-Neumann architecture is a way of constructing a general-purpose electrical computer. A programmable computer is called general-purpose, when it is Turing-complete in the sense of Ref. [TUR36]. The von-Neumann architecture is sometimes also called Princeton-architecture (after the Princeton University) and was proposed by American-Hungarian Polymath John von Neumann, albeit earlier works for electro-mechanical computers such as Konrad Zuse's Z1 machine are said to predate it. The principle components of a computer are the memory, the instruction set, i.e. the algorithm, to be executed and the central processing unit (CPU). The von-Neumann architecture is a way of constructing such a general-purpose computer and allowing both the program itself and the data that the program uses to be stored in the same memory. The EDVAC and EDSAC computers were the first to fully incorporate these principles and are seen by many as the first modern computers.

The von-Neumann architecture is sequential by its nature, as the CPU or control unit of the computer reads out the memory as directed by its current active instruction. Because data and instructions are stored in a shared environment, any manipulation of data must first finish, before a new instruction can be obtained. This is contrasted with the Harvard-architecture, where the instruction set and the data are always separate. In the Harvard-approach, a computer must be constructed in a way that allows the simultaneous manipulation of the data in the memory by multiple instructions. When implemented correctly, this makes it inherently safe for multi-threading and an efficient approach for programs that can

2.5 THE RESERVOIR COMPUTING PARADIGM

be largely parallelized. Most of the modern computing architecture follows the von-Neumann approach. However, with the increased use of multi-core CPUs the strict von-Neumann architecture has been left behind in recent years and aspects of the Harvard-architecture are finding more use. Both the Harvard and von-Neumann architecture are designed for digital computers, albeit not necessarily for binary systems, as not all early computers used Bits initially. Furthermore, the instruction set is a logically separate entity in both the Harvard and von-Neumann architecture, as this separation of code and data allows for a much easier programming.

In a modern context, the brain and other biological control systems are sometimes considered non-von-Neumann. The information processing and storage in such a neural network is inherently distributed, which generates a more complex and parallel computing. However, one could argue that the brain is not just non-sequential in nature - but that there is, in fact, not even a separation between processing and memory. In that sense, even other binary computer architectures like the Harvard-architecture seem to not apply to the brain. It would therefore seem to be more useful to speak of 'non-digital computing' or 'analogue computing'. Whether these analogue computers are inherently as computationally powerful as Turing-machines is not initially clear, but it seems hard to argue for the opposite case.

The field of reservoir computing with dynamical systems is deeply linked to the idea of an analogue computing. As mentioned, most modern computers are binary, i.e. their states are defined by binary signals and the operations are defined on binary inputs. Nanometer-sized transistors are used that can manipulate the voltage in the circuit, but only two states of voltages are effectively distinguished: A 'high level' and a 'low level', representing logical '1' and '0' states to form the binary basis. The computations occur at regular intervals as dictated by the clock cycle, which effectively regulates it such that the states are well-defined. However, a voltage signal can in principle have an almost arbitrary shape. To distinguish only two distinct levels that are only evaluated at regular intervals means reducing the dimensionality of the signal a lot.

When a signal is treated and used without discrete levels, this is called 'analogue computing' or 'analogue data transmission'. The first telephone cables, television and radio applications were analogue in nature. While analogue signals theoretically allow a much larger information storage, this is limited by the noisiness of the real world. Furthermore, powerful error-correction mechanism exist for digital data, but not for analogue data. How much computational power is lost by restricting oneself to the binary and digital systems, and whether this effects all possible computational tasks equally is very much an open question. It seems only natural to assume that many of the tasks that the human brain - an analogue computer - is so good at, such as object recognition, body movement or spatial awareness,

may be intrinsically easier in an analogue substrate. On the other hand, many of the mathematically rigid problems - such as simple arithmetic or combinatorics - suffer greatly even from tiny errors, and therefore a binary approach is much better suited for them.

In the future it may become common, that different computing substrates will be used for different tasks. With the high speed and multitude of accessible nonlinear elements, photonic reservoir computing could form the first generation of a new set of analogue computers, that are used in specific, targeted tasks. These will likely never make the classic binary von-Neumann computers obsolete, as the latter are still very useful for highly abstract and formal tasks. But there is a place for photonic analogue computers in the future. Additionally, the computational power for certain operations could be further boosted with the advent of quantum computers, such as the factorization of large numbers.

2.5.9 Literature overview of reservoir computing

The original reservoir computing concept was introduced by Jaeger in Ref. [JAE01] and Maass *et al.* in Ref. [MAA02], where the proposed schemes were called ‘echo state networks’ and ‘liquid state machines’, respectively (see also the history of reservoir computing in Sec. 2.5.2). A review article presenting the the state of research for 2009 can be found in Ref. [LUK09]. A 2017 review for photonic reservoir computing is presented in Ref. [SAN17a].

While many of the earlier publications focused on computer-simulated network-based reservoirs, the field of photonic reservoir computing has especially flourished since the introduction of delay-based reservoir computing. These were first experimentally demonstrated by Appeltant *et al.* in 2011 [APP11]. The thesis of Hermans [HER12] gives a good overview for delay-based reservoir computing. Different platforms can be distinguished by their information injection and manipulation type: Opto-electronic implementations use a combination of light and voltages [LAR12, PAQ12, SOR13a, LAR17], while purely electronic implementations [SOR15] use only electronic components. The consistency properties of photonic systems have been analysed in Ref. [OLI16]. A very fast system using lasers was shown by Brunner *et al* in 2013 [BRU13a]. Since then, more experiments [NGU17] and simulations have also explored lasers with delay [HIC13]. Possible modifications for delay-based reservoirs include the use of additional degrees of freedom such as polarization [NGU14], counter-propagating waves in ring lasers [NGU15], reduction of the phase sensitivity [NGU16], double feedback [HOU18], interleaving of multiple tasks [DUP16a] or truly all-optical [DUP12, DEJ14] and fully analogue systems [DUP16]. The importance of choosing the right input masks has also been shown and both chaotic or

2.5 THE RESERVOIR COMPUTING PARADIGM

noisy analogue masks [ROD11] and maximum length sequences binary masks [APP14] have been investigated.

Implementations of optical and electro-optical networks are also being researched. A system of semiconductor optical amplifiers was investigated in Ref. [VAN08a], with the influence of noise and spontaneous emission further investigated in Ref. [VAN11c]. To overcome the limitations of this noise, Ref. [VAN14] later showed the benefits of using a passive reservoir, with follow-up work extending the task and dimensions of the system [VIN15]. A network of lasers coupled via optical elements is proposed in Ref. [BRU15].

Boolean systems, i.e. transistor-based logic gates on a semiconductor chip, represent another interesting substrate for reservoir computing. Both the delay-architecture [HAY15] and networks of coupled elements [SCH08k, SNY13] have been used. Here, experiments made use of 'field-programmable gate arrays' (FPGAs), which are becoming more powerful and cheaper every year. Similarly, atomic switch networks have also been shown to function as reservoirs [SIL13d].

As a neuro-inspired computing scheme, more realistic biological and neural models for reservoir computing have also been investigated [HAE03], with some extensions trying to copy the inherent plasticity of synaptic connections [STE07c, SCH08n, LAZ09a]. Especially the part of the brain known as the cerebellum is assumed to have similar properties to a reservoir computer [YAM13]. Furthermore, an implementation of reservoir computing using real biological neurons contacted by electrodes was also demonstrated [DOC09].

Attempts to reunify reservoir computing with the general training of recurrent networks have also been made. Training the mask by back-propagation through time [HER15, HER15a] or online-training algorithms [ANT16] are promising avenues. An evolutionary algorithm for a complex setting was investigated in Ref. [ROE10a], showing that the network parameters can greatly influence the performance of the system, see also Ref. [CHA13e].

The question of how to find the optimal operating parameters has been often discussed, with many authors favoring the 'edge of stability' or the 'edge of chaos' [BER04]. Transitions from stability to chaos are influenced by the node dynamics and change performance [BUE10b]. This has also led to attempts to analytically construct powerful reservoirs by manipulating the eigenvalue spectrum of the coupling matrix [OZT07]. Alternatively, calculating optimal architectures [GRI15] or better input masks [ROD11] from first principles has been tried, although the success of such approaches has arguable not been very convincing.

An important milestone in the theory of reservoir computing was the introduction of the linear memory capacity, see Ref. [JAE02]. This has also been investigated for different topologies [HER10]. A quantification using Fisher information for a lin-

2 THEORY

ear reservoir driven by white noise was outlined in Ref [GAN08]. Fisher information was later shown to be equivalent to the linear memory capacity under certain conditions [TIN13]. The nonlinear extensions supplied by Dambre *et al.* in Ref. [DAM12] presents a concise and beautiful unification of memory and nonlinear transformation capabilities of dynamical systems. The trade-off between nonlinearity and memory was further investigated in Refs. [BUT13b, INU17].

Finding even better connections between quantifiable properties of the reservoir and reservoir computing performance has proven difficult [PRO05]. Ref. [VER07] represents a very detailed investigation, where different tasks are investigated with their connection to the Lyapunov exponents of the solitary system. A similar attempt is made in Ref. [ROD12]. For the case of lasers, experimental studies of consistency [OLI16] and memory can be linked to full or partial injection locking [BUE17].

Applications of reservoir computing are still rare, despite the fact that the aptitude of reservoir computing systems for real-world tasks such as market trading [GRI14], hydrological predictions [COU10] or emulating a guitar amplifier [KEU17] has been shown. Like many machine-learning concepts, reservoir computing has also been tried in robotic motion [ANT08a] or image recognition [MES15a]. For the nonlinear dynamics community, reservoir computers are interesting, as they can successfully emulate the behaviour of complex dynamical attractors. This makes reservoir computing systems interesting for model reduction and timeseries analysis [CHA11a, GRI14, PAT18]. Especially interesting are recent results that prove the ability to calculate Lyapunov exponents from the resulting trained reservoir computer [PAT17].

This thesis will extend the knowledge of reservoir computing by looking at the more general case of Stuart-Landau oscillators. This simple setting allows relatively fast numerical integration and thus larger parameter scans. Different features can be efficiently evaluated. Furthermore, the feasibility of hybrid network-delay systems is systematically studied. This in turn can serve as inspiration for future photonic neuromorphic computing platforms.

3

SYMMETRY-BREAKING IN NETWORKS

This chapter studies the synchronization patterns that can be found in networks of lasers and Stuart-Landau oscillators. It highlights the differences and similarities between networks of different size, local model and topology. This is a large field with a plethora of previously published literature. The focus in this theses will be on systems with symmetry-breaking bifurcations leading to non-trivial amplitude- and phase-coupling. The networks studied will be non-random and have highly symmetric topologies, and are unidirectional and bidirectional ring networks. The local models will mostly be the Stuart-Landau oscillator as introduced in Sec. 2.3.1. Additionally, a comparison is made with the Lang-Kobayashi class of laser equations as shown in Sec. 2.4.

A common theme throughout this chapter will be the emergence of phase-synchronized patterns from the local off-state, i.e. the non-oscillatory resting state of the system. Depending on the coupling phase, different constant phase shifts between the oscillators appear, but initially all of them adhere to the underlying symmetries of the system. These basic oscillatory patterns then typically undergo either a secondary Andronov-Hopf bifurcation, at which point quasiperiodic behaviour may be found, or a pitchfork of limit cycles. It is these regions where a pitchfork of limit cycles occurs, where complex symmetry-broken patterns are found. Furthermore, the important role of shear or amplitude-phase coupling is prevalent throughout this chapter.

The structure of the analysis follows different networks in order of increasing complexity and size. First the fundamental case of two instantaneously coupled Stuart-Landau oscillators is presented in Sec. 3.1, which also includes contents that have been published in Ref. [ROE18] about symmetry-broken amplitude and phase-locking states (SBL). These results are compared with bifurcation structure of two coupled Lang-Kobayashi systems from the literature. The results of the fundamental case of two coupled Stuart-Landau oscillators can then be generalized to unidirectional rings of Stuart-Landau oscillators, which is done in Sec. 3.3. Finally, one can also extend the system to bidirectional ring networks, which is presented in Sec. 3.4.

3.1 Two coupled Stuart-Landau Oscillators

To start investigating the synchronization of lasers and oscillators, it is best to begin with the simplest and most fundamental case. Once the local dynamics of a single oscillator are understood, cf. Sec. 2.3.3, the system of two instantaneously coupled identical Stuart-Landau oscillators represents a minimal network. This extension of Eq. (2.24) is described by the complex variables $Z_{1,2} \in \mathbb{C}$ in the following system of ODEs:

$$\dot{Z}_1 = (\lambda + i\omega + \gamma |Z_1|^2)Z_1 + \kappa e^{i\phi} Z_2, \quad (3.1)$$

$$\dot{Z}_2 = (\lambda + i\omega + \gamma |Z_2|^2)Z_2 + \kappa e^{i\phi} Z_1, \quad (3.2)$$

where the driving parameter $\lambda \in \mathbb{R}$, solitary frequency $\omega \in \mathbb{R}$ and nonlinearity $\gamma \in \mathbb{C}$ act as for the solitary case of Sec. 2.3.3. The coupling between the oscillators is defined by the coupling strength $\kappa \in \mathbb{R}$ and coupling phase $\phi \in [0, 2\pi]$. This complex coupling allows for a more general treatment of coupled oscillators than a purely real-valued coupling. Complex coupling terms can easily arise in the context of delays and are especially common in lasers. Some parameters will not be varied throughout this thesis, so that it always holds that $\omega = 1$, $\kappa = 0.1$ and $\text{Re}(\gamma) = -0.1$. The focus here is on the simple, minimal case necessary and hence no delay-coupling is used. Many possible extensions of Eqs. (3.1) and (3.2) exist, but these have the disadvantage of possessing a large number of parameters on which the dynamics critically depends. Furthermore, the more degrees of freedom that are introduced into a system, the more one can expect to find a large number of solutions and the less certain one can be about which precise mechanism causes the observed patterns.

The case of two coupled Stuart-Landau oscillators has been extensively investigated by Aronsen *et al.* in Ref. [ARO90], alas with a different parametrization and a focus on the case of two non-identical oscillators. The model presented in Eqs. (3.1) and (3.2) can also be seen as the simplest case of a mean-field or globally coupled network of Stuart-Landau oscillators. This system has been studied with respect to chaos and clusters in the large oscillator limit [HAK92, NAK93, NAK94a, KU15]. This section will derive the standard solutions for the two instantaneously coupled Stuart-Landau oscillators. Additionally, new analytical results for a special kind of symmetry-broken solution are presented. The results of this section also will be heavily used when larger networks are investigated later in this thesis. The contents of this section were published in Ref. [ROE18], albeit with a slightly different parametrization: the coupling included a self-coupling, which can be removed via parameter transformations.

3.1.1 Symmetries of the system

The choice of coupling of Eqs. (3.1) and (3.2) induces a symmetry in the coupled system: First, the solitary Hopf normal form possesses a S^1 rotational symmetry, which represents the global phase freedom: $e^{i\theta}f(Z) = f(e^{i\theta}Z)$ for all angles $\theta \in [0, 2\pi]$ for $f(Z) = (\lambda + i\omega + \gamma|Z|^2)Z$. The S^1 rotational symmetry is also preserved in the coupled case of Eqs. (3.1) and (3.2), because $Z_{1,2}$ only enter linearly in the coupling term. The symmetry is best expressed, when the system variables and relevant parameters are listed before and after the transformation [ERZ06a]. For the S^1 -symmetry, this means that a transformation of:

$$(Z_1, Z_2, \phi) \rightarrow (e^{i\theta}Z_1, e^{i\theta}Z_2, \phi), \quad (3.3)$$

leaves the system globally unchanged. This symmetry will be referred to as the ‘(global) phase freedom’, and equally applies to the case of two Lang-Kobayashi-type lasers as well as for the case with delay.

A second symmetry is induced by the coupling: the coupling terms are identical in type and parametrization in both oscillators, only the indices are switched. The coupled system therefore also possesses a Z_2 exchange symmetry: Relabelling $Z_1 \leftrightarrow Z_2$ and vice versa, and swapping Eq. (3.1) and (3.2) leaves the system unchanged.

$$(Z_1, Z_2, \phi) \rightarrow (Z_2, Z_1, \phi), \quad (3.4)$$

This is also the most trivial case of cyclic symmetry, that will later be shown in the Ring networks. This symmetry will simply be referred to as exchange symmetry.

Furthermore, the coupling phase is naturally invariant to multiples of 2π , such that a 2π -translational symmetry exists:

$$(Z_1, Z_2, \phi) \rightarrow (Z_1, Z_2, \phi + 2\pi). \quad (3.5)$$

Lastly, there also exists a symmetry that will link in-phase and anti-phase solutions (introduced in the next section), and will be referred to as the π -translational symmetry as in Ref. [ERZ06a]:

$$(Z_1, Z_2, \phi) \rightarrow (Z_1, -Z_2, \phi + \pi), \quad (3.6)$$

which consists of flipping the sign of the complex amplitude of one of the two oscillators, while also shifting the coupling phase ϕ by π . Each of the symmetries can be easily checked by inserting into Eqs. (3.1) and (3.2) and verifying that the equations of motion do not change afterwards.

3.1.2 Symmetric solutions

These symmetries are also reflected in the fundamental solutions for Eqs. (3.1) and (3.2) and will be discussed in this section. First recall that a single oscillator (cf. Sec. 2.3.3) will exhibit an ‘off-state’ for low λ , where no oscillations are stable. This directly extends to two coupled oscillators, where the trivial off-state is given by $Z_1 = Z_2 = 0$, which shall also be called the ‘off-state’ for the system of Eq. (3.1) and (3.2). There are no solutions, with exactly one of the two oscillators turned off $Z_1 = 0, Z_2 \neq 0$, as the coupling would always leak at least an amplitude of order $\kappa|Z_2|$ from the oscillating unit to the other, i.e. there are no partial off-states.

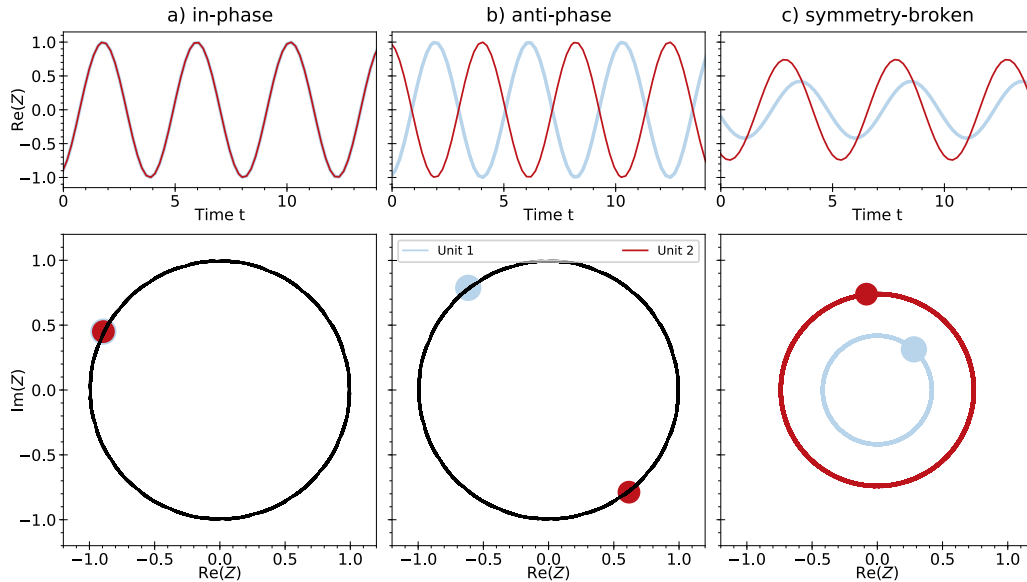


Figure 3.1: Example timeseries for the fundamental patterns of two instantaneously coupled Stuart-Landau oscillators as defined by Eqs. (3.1) and (3.2) obtained by direct numerical integration. The top panel shows a time series slice of the real part of the time series of the complex amplitude $\text{Re}(Z)$ with different colours for the two oscillators. Bottom panels show the time-trace (black line if identical for both, coloured lines if different) and simultaneous positions (coloured circles) for the same timeseries in the complex plane. Column a) shows the in-phase (IP) synchronized solution, column b) the anti-phase synchronized solution and c) is an example of symmetry-broken amplitude- and phase-locking (see Sec. 3.1.3) Parameters: $\lambda = 0.00$, $\omega = 1$, $\text{Re}(\gamma) = -0.1$, $\text{Im}(\gamma) = 0.5$, $\phi = 0, 1\pi, \pi, 0.2\pi$

The single oscillator exhibits stable oscillatory solutions of fixed amplitude for $\lambda > 0$ (cf. Sec. 2.3.3). This generalizes into two different basic oscillatory solutions for the two instantaneously coupled Stuart-Landau oscillators of Eqs. (3.1) and (3.2): The in-phase (IP) and the anti-phase (AP) synchronized solutions. Fig-

3.1 TWO COUPLED STUART-LANDAU OSCILLATORS

Figure 3.1 shows timeseries samples of the real part $\text{Re}(Z)$ (top panels) and projections in the complex plane (bottom panels) for solutions of Eqs. (3.1) and (3.2) obtained by direct numerical integration. The in-phase synchronized solution can be seen in Fig. 3.1 a) and is characterized by two identical time traces for both oscillators, i.e. their amplitudes are identical for all times $Z_1(t) = Z_2(t)$. The real part of the in-phase synchronized solution $\text{Re}(Z_n)$, as shown in Fig. 3.1 a) on the top, is very similar to the time-series of an individual oscillator, cf. Fig. 2.6 a).

The anti-phase (AP) synchronized solutions are shown in Fig. 3.1 b). Here, the amplitudes of the oscillators are exact opposites $Z_1 = -Z_2$, as can also be seen in the complex plane on the bottom panel of Fig. 3.1 b), where the blue and red circle indicate position at one point in time of Z_1 and Z_2 . The black line in the bottom panel of Fig. 3.1 a) and b) is the time-trace of the system projected into the complex plane. Because both oscillators perform harmonic oscillations $\exp(i\omega t)$, this is a circle centred around the origin for both in-phase and anti-phase synchronization. Anti-phase synchronized solutions can also be seen as an example of *lag-synchronization*, where the second oscillator is half a period delayed $Z_2(t) = Z_1(t + P/2)$, with period P . Finally, Fig. 3.1 c) shows a symmetry-broken solution that will be explained in Sec. 3.1.3.

The generalized oscillatory solutions shown in Fig. 3.1 a) and b) can be systematically deduced by considering the symmetries of the system. A single Stuart-Landau oscillator has a global phase θ that can be freely chosen. Similarly the coupled system, Eqs. (3.1) and (3.2), have a global phase freedom. However, the complex amplitudes Z_1, Z_2 are directly coupled in Eqs. (3.1) and (3.2) and therefore also the phases of both oscillators θ_1, θ_2 become linked. This means that as opposed to the global phase, the phase difference $\theta_1 - \theta_2$ is not free. As mentioned in Sec. 3.1.1, the system also possesses a \mathbb{Z}_2 exchange symmetry. To preserve this in a generalized oscillatory case, solutions have to also be exchange-symmetric with respect to the phase difference $\theta_1 - \theta_2$. Due to the circular nature of complex phases, i.e. adding 2π to a phase does not change it, this exchange property can be stated as:

$$\theta_1 - \theta_2 = \theta_2 - \theta_1 + k2\pi, \quad k \in \mathbb{N} \quad (3.7)$$

This allows for two solutions: Either the phase difference is zero $\theta_1 - \theta_2 = 0$ (in-phase (IP) solution) or half a rotation apart $\theta_1 - \theta_2 = \pi$ (anti-phase (AP) solution), which are the solutions shown in Fig. 3.1 a) and b). A second link with respect to the IP and AP synchronization is also apparent: The anti-phase patterns are the image of in-phase solutions under the π -translational symmetry. This will become more clear in the next section, where the parameter dependence is shown.

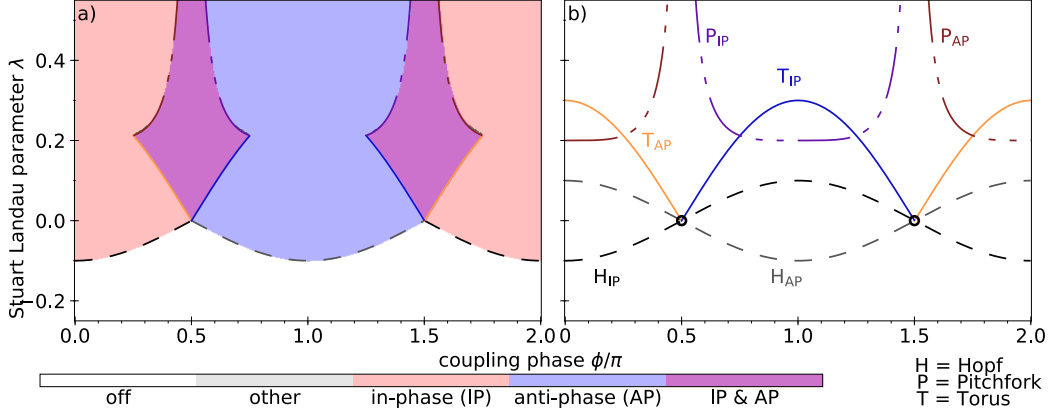
Parameter scans for $\text{Im}(\gamma) = 0$ 

Figure 3.2: Regions of numerical stability for two instantaneously coupled Stuart-Landau oscillators as described in Eqs. (3.1) and (3.2) as a function of λ and coupling phase ϕ . a): White areas indicate the trivial off-state, light peach areas the in-phase and bright blue areas the anti-phase state. Purple regions are multistable between in-phase and anti-phase orbits. b): Analytically derived bifurcation lines given by Eqs. (3.11) and (3.12) for the Hopf of the in-phase (H_{IP}) and anti-phase solution (H_{AP}), Eqs. (3.13) and (3.14) for the torus (T_{IP} and T_{AP}), and Eqs. (3.15) and (3.16) for the pitchfork bifurcation (P_{IP} and P_{AP}). Black circles mark a co-dimension 2 bifurcation point. Parameters: $\text{Re}(\gamma) = -0.1$, $\text{Im}(\gamma) = 0.0$, $\omega = 1$, $\kappa = 0.1$.

The logical next step is to analyse the stability of the fundamental solutions of the system with respect to varying parameters. This can in general be done with different methods, e.g. direct numerical integration, path continuation, experiments or analytical derivations. This thesis employs direct numerical integration for complex systems, as well as analytical derivations for the simple systems where this is possible.

Figure 3.2 a) shows numerically obtained regions of stability for the three principal solutions of two coupled Stuart-Landau oscillators as given by Eqs. (3.1) and (3.2): The trivial off-state (white), in-phase synchronization (light peach) and the anti-phase synchronization (bright blue) for $\text{Re}(\gamma) = -0.1$ (supercritical case), $\text{Im}(\gamma) = 0.0$ (without shear), $\omega = 1$, $\kappa = 0.1$. The axis are the coupling phase ϕ and the Stuart-Landau parameter λ , which corresponds to the threshold parameter of oscillations in a single oscillator and is similar to the pump current of a laser. Note, that the coupling phase ϕ is periodic and therefore Fig. 3.2 could be periodically extended for $\phi < 0$, $\phi > 2\pi$. The stability regions in Fig. 3.2 were obtained by starting a simulation close to each of the three generalized solutions (off-state, IP, AP) and then numerically integrating until all transients disappeared (typically several thousand time units). Different random initial conditions were also tried,

3.1 TWO COUPLED STUART-LANDAU OSCILLATORS

but no additional stable states were found. As can be seen from the coloured regions in Fig. 3.2 a), the different solutions have different regions of stability. There is also a substantial overlap between stable in-phase and anti-phase solutions, indicated by the purple region of multistability in Fig. 3.2 a). The stable in-phase (IP) synchronization is centred around the symmetric coupling phase $\phi = 0$, while the anti-phase (AP) synchronization is found around $\phi = \pi$. This is a general property of phase-locked oscillations: The coupling phases that they are found at are similar to the relative phase difference of the oscillators $\theta_1 - \theta_2 \approx \phi$. A generalized version of this will be seen later for ring networks. Note, that the in-phase (red in Fig. 3.2 a)) and anti-phase (Fig. 3.2 a)) synchronized regions are each others image under the π -translational symmetry, i.e. the π -translational symmetry does not only apply to individual solutions but by extension also to the shape of the entire region of stability.

The boundaries of the regions of stability of Fig. 3.2 a) can be calculated analytically, which is done in the following paragraphs and the appendix of Ref. [ROE18]. When the oscillators are assumed to be in-phase synchronized $Z_1(t) = Z_2(t) = r \exp(i\hat{\omega}t + \theta)$, Eqs. (3.1) and (3.2) decouple and can be transformed into a single Stuart-Landau equation:

$$\dot{Z} = (\tilde{\lambda} + i\tilde{\omega} + \gamma |Z|^2)Z, \quad (3.8)$$

with $\tilde{\lambda} = \lambda + \kappa \cos \phi$ and $\tilde{\omega} = \omega + \kappa \sin \phi$. An Andronov-Hopf bifurcation occurs at $\tilde{\lambda} = 0$, as it is the normal form of such a bifurcation. Using the formulas from Sec. 2.3.3, the phase velocity of this orbit is given by

$$\Omega = \tilde{\omega} + \text{Im}(\gamma) r^2 = \omega + \kappa \sin \phi - \lambda \text{Im}(\gamma) / \text{Re}(\gamma), \quad (3.9)$$

and the radius r grows with

$$r = \sqrt{-\tilde{\lambda} / \text{Re}(\gamma)}. \quad (3.10)$$

Corresponding to the Andronov-Hopf-bifurcation of a single oscillator, the in-phase (IP) synchronized solution are then created in an Andronov-Hopf bifurcation at:

$$\lambda_{H(IP)} = -\kappa \cos \phi. \quad (3.11)$$

Similar calculations can be executed for the anti-phase (AP) solution $Z_1(t) = -Z_2(t) = r \exp(i\hat{\omega}t + \theta)$ (see Ref. [ROE18]), which is created at

$$\lambda_{H(AP)} = \kappa \cos \phi. \quad (3.12)$$

3 SYMMETRY-BREAKING IN NETWORKS

For $\text{Re}(\gamma) < 0$, the case shown in Fig. 3.2, both of these Hopf bifurcations are supercritical. The in-phase Hopf H_{IP} is shown with black dashed lines in Fig. 3.2, the anti-phase Hopf H_{AP} with grey dashed lines. Further analytical calculations reveal two more kinds of bifurcations for the synchronized solutions (see the appendix of Ref. [ROE18]). Two Hopf-Hopf-points (black circles in Fig. 3.2) situated at $\phi = \pi/2, 3\pi/2$ give birth to two additional secondary Andronov-Hopf or torus-Bifurcations occurring for the in-phase (T_{IP} , dark blue) and anti-phase (T_{AP} , orange) limit cycle, respectively:

$$\lambda_{T(IP)} = -3\kappa \cos \phi, \quad (3.13)$$

$$\lambda_{T(AP)} = 3\kappa \cos \phi. \quad (3.14)$$

Additionally, a pitchfork of limit cycles, limiting the region of stability (P_{IP} , violet, and P_{AP} , brown in Fig. 3.2 b)), appears for:

$$\lambda_{P(IP)} = -\frac{\kappa \text{Re}(\gamma)}{\text{Im}(\gamma) \sin \phi + \text{Re}(\gamma) \cos \phi} - \kappa \cos \phi, \quad (3.15)$$

$$\lambda_{P(AP)} = \frac{\kappa \text{Re}(\gamma)}{\text{Im}(\gamma) \sin \phi + \text{Re}(\gamma) \cos \phi} + \kappa \cos \phi. \quad (3.16)$$

When looking at the analytic forms of the bifurcations shown in Eqs. (3.11) to (3.16) it is apparent that all the bifurcations related to the in-phase (IP) synchronized behaviour are identical to those of the anti-phase (AP) synchronized regions, if the coupling phase is shifted by π (which is the π -translational symmetry as introduced in Eq. (3.6)). This is not a coincidence, but a result of the symmetric coupling scheme in Eqs. (3.1) and (3.2) and the π -translational symmetry. This can also be proven more intuitively by introducing new coordinates $\tilde{Z}_2 = -Z_2$ and using $-\exp(i\phi) = \exp(i(\phi + \pi))$, such that the original equations for two coupled Stuart-Landau oscillators become:

$$\dot{Z}_1 = (\lambda + i\omega + \gamma |Z_1|^2)Z_1 + \kappa e^{i(\phi+\pi)} \tilde{Z}_2, \quad (3.17)$$

$$\dot{\tilde{Z}}_2 = (\lambda + i\omega + \gamma |\tilde{Z}_2|^2)\tilde{Z}_2 + \kappa e^{i(\phi+\pi)} Z_1, \quad (3.18)$$

where all parameters are as before. Because the new coordinate \tilde{Z}_2 is a π phase shift of the original $\tilde{Z}_2 = -Z_2$, the in-phase solutions of Eqs. (3.17) and (3.18) correspond to the anti-phase solutions of the original Eqs. (3.1) and (3.2). Comparing Eqs. (3.17)-(3.18) to Eqs. (3.1)-(3.2) reveals that they are identical except for a phase-shift in the coupling term of π . Therefore, in-phase and anti-phase solutions behave identically for coupling phases ϕ that differ by π , which is the π -translational symmetry of Eq. (3.6). In fact, *all solutions* have a corresponding "phase-flipped" mirror image: If $(Z_1(t), Z_2(t))$ is a solution of Eqs. (3.1) and (3.2),

3.1 TWO COUPLED STUART-LANDAU OSCILLATORS

then $(Z_1(t), -Z_2(t))$ will be a solution for the coupling phase $\phi + \pi$. This is once again a result of the underlying symmetries of the system. This behaviour will later be generalized to larger Ring networks in Secs. 3.3 and 3.4.

All of the analytical derived solutions are shown and labelled in Fig. 3.2 b), with the relevant parts also plotted on top of the numerically obtained regions of stability in Fig. 3.2 a). The agreement between numerics and analytics is perfect and proves the validity of the numerical integration scheme. It also illustrates how analytical deductions can help understand numerically obtained data.

Parameter scans for $\text{Im}(\gamma) \neq 0$

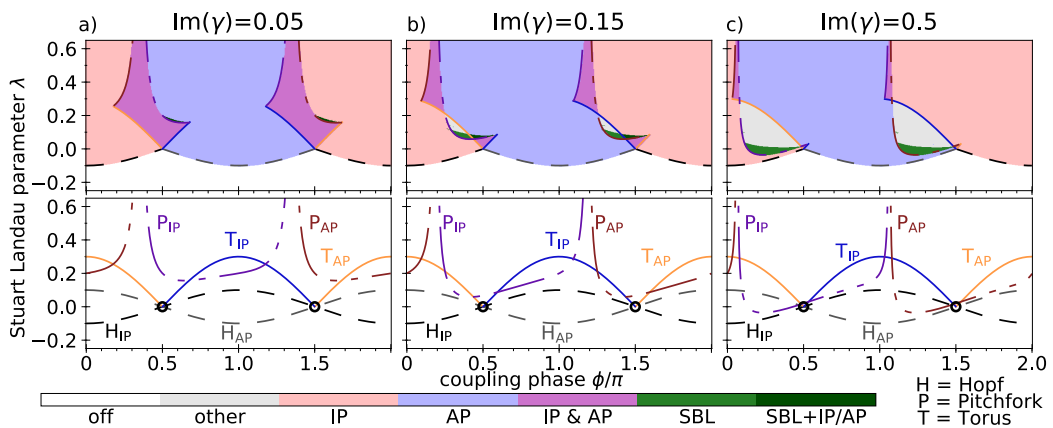


Figure 3.3: Regions of numerical stability for two instantaneously coupled Stuart-Landau oscillators as described in Eqs. (3.1) and (3.2) as a function of λ and coupling phase ϕ for different non-zero shear $\text{Im}(\gamma)$. White areas indicate the trivial off-state, light peach areas the in-phase and bright blue areas the anti-phase state. Purple regions are multi-stable between in-phase and anti-phase orbits. Green corresponds to symmetry-broken amplitude- and phase-locking (SBL), while dark green marks this state with multistability either with the in-phase or anti-phase orbits (SBL+IP/AP). Light grey indicates higher order dynamics, e.g. quasiperiodic behavior. Lower row shows analytically derived bifurcation lines given by Eqs. (3.11) and (3.12) for the Hopf of the in-phase (H_{IP}) and anti-phase solution (H_{AP}), Eqs. (3.13) and (3.14) for the torus (T_{IP} and T_{AP}), and Eqs. (3.15) and (3.16) for the pitchfork bifurcation (P_{IP} and P_{AP}). Black circles mark a co-dimension 2 bifurcation point. Parameters: $\text{Re}(\gamma) = -0.1$, $\text{Im}(\gamma)$ as indicated atop the columns, $\omega = 1$, $\kappa = 0.1$.

So far, the amplitude-phase coupling or shear parameter $\text{Im}(\gamma)$ had been set to zero. Fig. 3.3 shows the results of numerical simulations for varying λ and the coupling phase ϕ for increasing values of the shear parameter from a) $\text{Im}(\gamma) = 0.05$ to c) $\text{Im}(\gamma) = 0.5$. The lower half of Fig. 3.3 shows the corresponding bifurcation lines of which the relevant parts are reproduced in the top-panel.

The most obvious influence of non-zero shear $\text{Im}(\gamma) \neq 0$ in Fig. 3.3 is the deformation of the pitchfork bifurcations: Compare the violet line (P_{IP}) and brown line (P_{AP}) in Fig. 3.2 and Fig. 3.3. On the other hand, the Hopf bifurcations generating the in-phase (H_{IP}) and anti-phase (H_{AP}) solutions and the torus bifurcations (T_{IP} and T_{AP} , orange and blue lines in Fig. 3.3) do not change with shear. This is also apparent from the analytic formulas as given in Eqs. (3.11) to (3.16), where only the pitchfork bifurcations depend on $\text{Im}(\gamma)$. Furthermore, Fig. 3.3 reveals that the bifurcations and therefore the regions of stability for IP and AP solutions are no longer mirrored along $\phi = \pi$ and $\phi = 0$. This was an additional feature that is specific to the $\text{Im}(\gamma) = 0$ -case of Fig. 3.2. However, the π -translational symmetry is still preserved, so that IP and AP solutions are the image of each other with respect to coupling phases that are π apart.

At some value of $\text{Im}(\gamma)$ the torus (T) and pitchfork (P) bifurcation cross each other (compare Fig. 3.3 a) and b)) opening the regions marked in grey and dark green. Within these parameter regions, none of the previously described solutions of the system are stable. The grey regions of Fig. 3.3 contain higher-order limit cycles and quasiperiodic dynamics. In contrast, the regions marked in green contain a new solution with harmonic oscillations but non-trivial amplitude and phase relationship between the two oscillators, which will be called ‘symmetry-broken amplitude- and phase-locking’ (SBL) [ROE18].

3.1.3 Symmetry-broken solutions

The symmetry-broken amplitude and phase-locking states appear for parts of the two-dimensional parameter scan close to the pitchfork-bifurcations (the violet lines (P_{IP}) and brown lines (P_{AP}) in Fig. 3.3). These states are characterized by a non-trivial phase- and amplitude-relationship between the two oscillators, while simultaneously maintaining harmonic, regular oscillations with the same frequency for both oscillators. An example of such a symmetry-broken state is shown in Fig. 3.1 c). Especially note, that despite the non-trivial amplitude and phase relationship, the motion of both oscillations still inscribes a perfectly round circle when projected into the complex plane in the bottom panel of Fig. 3.1 c). They are therefore not just any kind of symmetry-broken solution, but rather an exceptionally well-behaved and clearly defined case. These symmetry-broken states are the third type of phase-synchronized oscillatory behaviour that can arise in the system of two coupled Stuart-Landau oscillators of Eqs. (3.17) and (3.18) after the IP and AP solutions. However, the solutions are no longer symmetric with respect to the \mathbb{Z}_2 exchange symmetry of the system. When a solution no longer adheres to the symmetries of the governing equations, this is called (spontaneous) ‘symmetry-breaking’ and thus these states are symmetry-broken.

3.1 TWO COUPLED STUART-LANDAU OSCILLATORS

Symmetry-breaking is a general property of dynamical systems and can occur in a variety of ways. Naturally, a symmetry-breaking can only occur for dynamical system that has symmetries to begin with, like the exchange symmetry of Eqs. (3.17) and (3.18). Furthermore, it is worth noting that even in a regime of symmetry-broken dynamics, a system will not exhibit those if a *symmetric* initial condition is chosen, but the symmetric solution usually is unstable in the direction of symmetry-breaking. In the symmetry-broken solutions shown in Fig. 3.1 c), one of the two oscillators has a larger amplitude. Which of the two oscillators this is, is solely decided by the initial conditions. If the initial conditions for Z_1 and Z_2 are exchanged, so will the final amplitudes be. Hence, every instance of SBL states shown in the green regions of Fig. 3.3 will consist of two separate branches of solutions, which are their mirror image under the exchange symmetry. This is a result of the *equivariant branching lemma*, which demands that symmetries must be obeyed by the sum of all solutions, even if individual examples do not. Symmetries, sub-symmetries and their relationship to the solution space of dynamical systems are the subject of the mathematical theory of *equivariance*. Most prominent here are the works of Golubitsky and Stuart [GOL88a].

The symmetry-broken amplitude and phase-locking states for two coupled Stuart-Landau oscillators had been found and mentioned by Aronson *et al.* [ARO90] in passing, but never seen to be stable. As can be seen in Fig. 3.3 these states only become sufficiently prevalent for high shear $\text{Im}(\gamma)$, which explains their relative absence from the literature. Their stability is a novel results and opens up the possibility to observe them experimentally or in other systems. There also exists recent analysis for large global networks of Stuart-Landau oscillators in in Ref. [KU15]. The authors study cluster states in detail and some of their implicit equations may also potentially coincide with the SBL states of this thesis if the two clusters have the same size. However, the relevant parameter regions are never shown in Ref. [KU15]. The connection of the SBL states with cluster states thus is an open question, that will be left for future investigations.

Analytic description

The symmetry-broken amplitude- and phase-locking states can also be described analytically. For this, a more general non-symmetric ansatz is made:

$$Z_2 = sZ_1 =: ae^{i\psi} Z, \quad (3.19)$$

3 SYMMETRY-BREAKING IN NETWORKS

Inserting this into Eqs. (3.1) and (3.2) and assuming harmonic oscillations $\dot{Z} = i\tilde{\Omega}Z$ leads to:

$$0 = (\lambda + i\Omega + \gamma |Z|^2) + \sigma s \quad (3.20)$$

$$0 = (\lambda + i\Omega + \gamma |s|^2 |Z|^2) s + \sigma, \quad (3.21)$$

with $\Omega = \omega - \tilde{\Omega}$ and $\sigma = \kappa \exp i\phi$. Equations (3.20) and (3.21) are two complex equations and are sufficient to determine the 4 unknowns Ω , $|Z|$, a and ψ . Solving for three of the four unknowns with these equations, a simple formula can be obtained for the amplitude ratio a as a function of the phase relationship ψ :

$$a = \sqrt{\frac{\text{Im}(\gamma) \cos(\phi - \psi) - \text{Re}(\gamma) \sin(\phi - \psi)}{\text{Im}(\gamma) \cos(\phi + \psi) - \text{Re}(\gamma) \sin(\phi + \psi)}}. \quad (3.22)$$

The general ansatz of Eq.(3.19) also implicitly contains the in-phase and anti-phase synchronized solutions. Thus solving Eq. (3.22) yields $a = 1$ for $\psi = 0, \pi$. Ultimately, Eqs. (3.20) and (3.21) can also be solved for all four unknown variables analytically, such that the measures of asymmetry a and ψ can be expressed as functions of the parameters λ , γ , and coupling parameters κ and ϕ . This has been done and is also shown in Ref. [ROE18]. However, these calculations lead to very lengthy expressions, and are therefore only shown in App. A.1.1.

The analytical description also allows the identification of one additional bifurcation line: The symmetry-broken amplitude- and phase-locking states are not only created in the pitchfork bifurcations of the in-phase and anti-phase synchronized solutions, but can also emerge independently from a saddle-node located at:

$$\lambda_{SN} = \frac{1}{\tilde{\alpha}^2 + 1} \sqrt{8\kappa^2(\tilde{\alpha} \cot \phi - 1)(\tilde{\alpha}^2 + 2\tilde{\alpha} \cot \phi)}, \quad (3.23)$$

with $\tilde{\alpha} = \text{Im}(\gamma)/\text{Re}(\gamma)$. This additional bifurcation is a novel result that has not been reported before, and it links the regions of existence for the different symmetry-broken amplitude- and phase-locking states.

Figure 3.4 shows the analytically derived regions of existence for symmetry-broken amplitude- and phase-locking states of the two two instantaneously coupled Stuart-Landau oscillators as described in Eqs. (3.1) and (3.2) in the parameter plane of λ and ϕ for different $\text{Im}(\gamma)$. The colours in Fig. 3.4 indicate the number of coexisting symmetry-broken amplitude- and phase-locked branches, where symmetrized pairs are not counted independently. pitchfork bifurcation lines as given by Eq. (3.15) and (3.16) are shown with dashed purple and brown lines, the torus bifurcations lines of Eq. (3.13) and (3.14) are shown as solid blue and orange lines. These lines correspond to the limits of the in-phase and anti-phase

3.1 TWO COUPLED STUART-LANDAU OSCILLATORS

synchronized regions of Figs. 3.3 and 3.2. Additionally, the saddle-node bifurcation of Eq. (3.23) is shown with a red line in Fig. 3.4. Important co-dimension two points are where matching pitchfork and torus lines meet (blue with purple for IP, orange with brown for AP) in a pitchfork-torus point (black squares in Fig. 3.4) and where the saddle-node intersects the pitchfork lines (red circles in Fig. 3.4). On these saddle-node-pitchfork points, the pitchfork turns from sub- to supercritical.

As Fig. 3.4 reveals, the symmetry-broken amplitude- and phase-locking states exist for a wide range of parameter combinations. In particular, they can even be found for $\text{Im}(\gamma) = 0$, albeit they were never observed to be stable in the numerics. Nevertheless, this analytical map of existence together with the exactly known shape of the amplitude and phase ratio allows for interesting applications. In particular, one could apply a Pyragas-type feedback control to stabilize the symmetry-broken patterns. However, this is outside the scope of this thesis and will be left for future investigations.

The symmetry-breaking pitchfork bifurcation can also be seen, when the system is investigated as a line scan over λ . Fig. 3.5 shows a linescan for increasing λ at coupling phase $\phi = 0.2\pi$. The shear is $\text{Im}(\gamma) = 0.5$, for which the two-dimensional parameter scan is shown in Fig. 3.3 c). Fig. 3.5 a) shows the extrema of $|Z_{1,2}|^2$ in blue and orange. Fig. 3.5 b) shows the corresponding amplitude ratio a and phase difference ψ for $Z_1 = a \exp(i\psi)Z_2$ over the same λ . The system is in the trivial off-state for $\lambda \leq -0.08$ and accordingly $|Z_{1,2}|^2 = 0$ in Fig. 3.5 a). The in-phase synchronized oscillations start for $\lambda \geq -0.08$. Both absolute squares are identical $|Z_1|^2 = |Z_2|^2$ and grow linearly, as is typical for an Andronov-Hopf bifurcation, while the phase difference is zero $\psi = 0$. For $\lambda \approx -0.035$ the symmetry-breaking in-phase pitchfork bifurcation occurs (P_{IP} in Fig. 3.3 c) as given by Eq. (3.15)), which is visible as a splitting of amplitude squares $|Z_1|^2 \neq |Z_2|^2$ in Fig. 3.5 a) and a change of the asymmetry parameters $a \neq 1$ $\psi \neq 0$ in Fig. 3.5 b). The dashed lines in Fig. 3.5 b) show the analytically predicted asymmetries for the symmetry-broken amplitude- and phase-locking states as derived in the Appendix. Then, for $\lambda \geq 0.02$ a secondary Andronov-Hopf bifurcation occurs, creating amplitude modulations. Due to the amplitude-phase coupling in Eqs. (3.1) and (3.2) this also means that there is no longer a fixed phase relationship ψ between the two oscillators. Finally, a symmetry-restoring bifurcation creating higher-order dynamics occurs at $\lambda \approx 0.05$.

Special coupling phases

In general, the symmetry-broken amplitude- and phase-locking states combines differences in both the amplitude and phase. However, for certain coupling phases ϕ , the system can be found to diverge only in amplitudes, but not in phase, i.e. $Z_2 = a \exp(i\psi)Z_1$ with either $\psi = 0$ or $\psi = \pi$ [ROE18]. The case of $\psi = 0$ represents

a generalized in-phase synchronization, and from the general analytical solutions of App. A.1.1 it can be calculated that this case occurs for:

$$\frac{\text{Im}(\gamma)}{\text{Re}(\gamma)} = \tan \phi, \quad (3.24)$$

Because of the trigonometric identity $\tan \phi = \tan(\phi + \pi)$, it follows that the generalized anti-phase synchronized solutions also fulfil Eq. (3.24) when the π -translational symmetry is used. Naturally, the branches can only occur if an underlying pitchfork bifurcation exists. Because the in-phase and anti-phase synchronized solutions never undergo a pitchfork bifurcation at the same parameters, their symmetry-broken generalized counterparts also never coincide. The special phases are indicated by the vertical black dotted line in Fig. 3.4.

Due to the equivariant branching lemma, each symmetry-broken state always has a mirror image under the exchange symmetry. For the two branches created at the special coupling phases indicated in Eq. (3.24) their phase differences are fixed at $\psi = 0$ or $\psi = \pi$. Along one of these branches the amplitude ratio a either goes to infinity or approaches 0 for $\lambda \rightarrow \infty$.

A second case of special phase relationships can be treated analogously for $\psi = \pi/2, 3\pi/2$. This state can not be linked to any general pattern, as the phase-relationship is not revertible. The case of $\psi = \pi/2$ always coexists with $\psi = 3\pi/2$ due to the exchange symmetry, thus there are two different branches of SBL states. The condition for this is:

$$\frac{\text{Im}(\gamma)}{\text{Re}(\gamma)} = -\cot \phi. \quad (3.25)$$

Hence a phase shift of $\psi = \pi/2, 3\pi/2$ occurs exactly for coupling phases ϕ where there is no pitchfork bifurcation and the symmetry-broken amplitude- and phase-locked states only emerge from saddle-node bifurcations, see the grey dotted vertical lines in Fig. 3.4.

The conditions shown in Eq. (3.24) and (3.25) describe the only coupling-phases ϕ for which ψ does not change while increasing λ , only the amplitude ratio a changes. Therefore, the four vertical dotted lines in Fig. 3.4 form a sort of 'organizing skeleton' at which the symmetry-broken amplitude- and phase-locking states are pinned. This is an interesting observation that needs further development. In particular, one could try to find similar structures in rings and other networks.

Significance of the symmetry-broken amplitude- and phase-locking states

The symmetry-broken amplitude- and phase-locking states shown in this section are a very accessible example of symmetry-breaking, that occurs for the paradigmatic

3.1 TWO COUPLED STUART-LANDAU OSCILLATORS

model of two coupled Stuart-Landau oscillators. As the individual oscillators are the normal form of the ubiquitous Andronov-Hopf bifurcations, a coupling scenario as described by Eqs. (3.1) and (3.2) is not rare. The symmetry-broken nature of these states nevertheless does not prevent them from exhibiting regular, harmonic oscillations (see the timeseries in Fig. 3.1 c)). Thus, they are a very neat example of symmetry-breaking, that allows further study. The fact that it can be completely analytically solved also differentiates it from similar states already known in the laser system (see next section).

The symmetry-broken nature also automatically lends itself to be used as a switch, as due to the broken exchange-symmetry exactly two branches of the solutions *must* exist. This has also been tested for the laser case in Ref. [CLE14]. The Stuart-Landau case is such a fundamental example, that studying all of the phase-locked patterns in itself reveals general insights. Additionally, with the properties of the symmetry-broken amplitude and phase-locked states in the Stuart-Landau case now known analytically and described in detail, one can also look through the literature of coupled oscillatory systems in general and find corresponding patterns in more complex circumstances. In particular, the case for lasers is interesting, which is investigated in the next section.

3 SYMMETRY-BREAKING IN NETWORKS

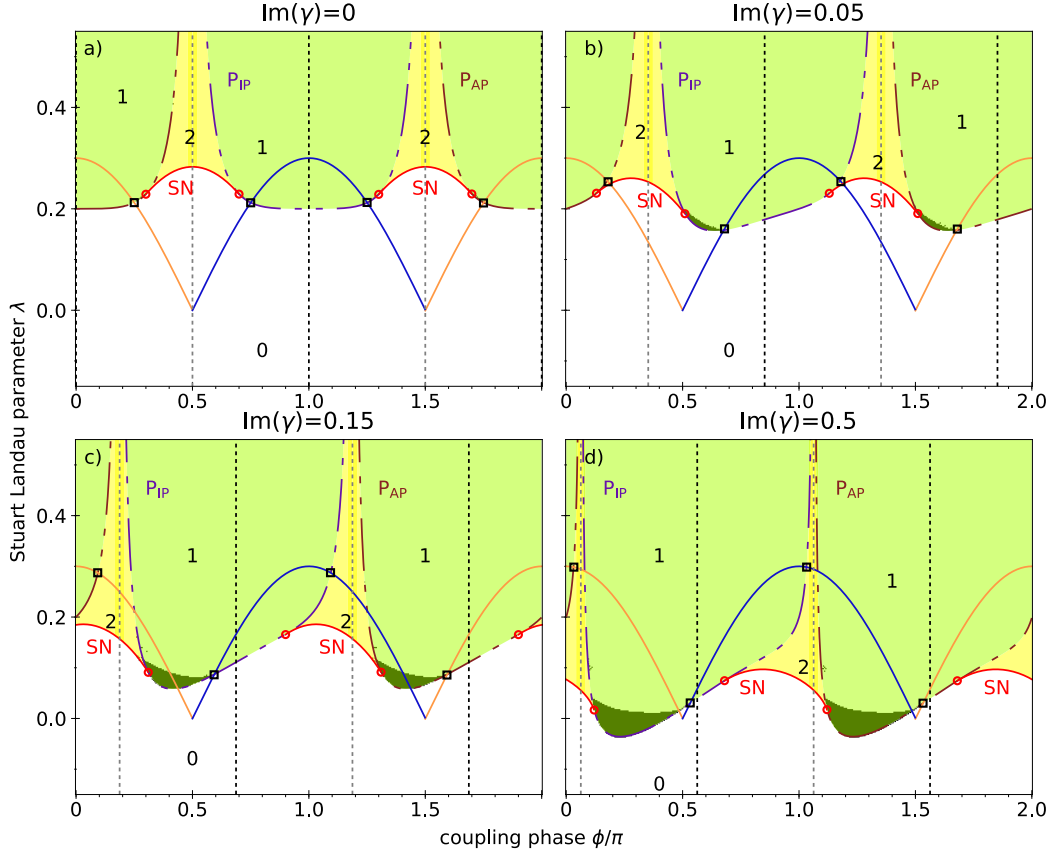


Figure 3.4: Regions of existence of symmetry-broken amplitude and phase-locking (SBL) states for two instantaneously coupled Stuart-Landau oscillators as described in Eqs. (3.1) and (3.2) as a function of λ and coupling phase ϕ for different non-zero shear $\text{Im}(\gamma)$. The numbers within the different regions indicate the number of coexisting branches of SBL states. White areas indicate none, green areas contain one branch and yellow areas two. Symmetrized versions were not counted independently. pitchfork bifurcation lines are given according to Eq. (3.15) and (3.16) (dashed lines), torus bifurcations lines according to Eq. (3.13) and (3.14) (solid blue and orange lines), and saddle-node lines as given by Eq. (3.23) (solid red lines). Saddle-node-pitchfork points are indicated by red circles, pitchfork-torus points by black squares. Vertical black dotted lines show where symmetry-broken amplitude- and phase-locking solutions with special phase differences $\psi = 0$ and $\psi = \pi$ exist according to Eq. (3.24), grey dotted lines show $\psi = \pi/2$ and $\psi = 3\pi/2$ as Eq. (3.25). Dark green areas show the numerically found regions of stable amplitude- and phase-locking, light green and yellow only analytically derived regions of existence. Parameters: $\text{Re}(\gamma) = -0.1$, $\text{Im}(\gamma)$ as indicated atop the columns, $\omega = 1$, $\kappa = 0.1$.

3.1 TWO COUPLED STUART-LANDAU OSCILLATORS

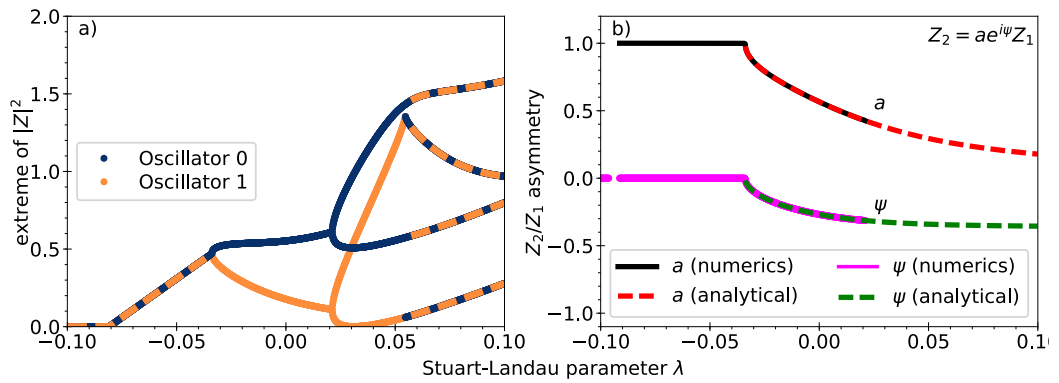


Figure 3.5: Linescan of the extrema of $|Z|^2$ (a) and asymmetry measures a and ψ (b) for two instantaneously coupled Stuart-Landau oscillators as in Eqs. (3.1) and (3.2) as a function of λ for coupling phase $\phi = 0.2\pi$. a): The system is in the in-phase symmetric solution for $\lambda < 0.05$, and in the symmetry-broken amplitude- and phase-locking state afterwards. Period-doubling bifurcations occur at $\lambda \simeq 0.02$ and symmetry-restoring at $\lambda \simeq 0.05$. b): amplitude ratio a and phase-difference ψ are plotted from the numerics (red, black) and with the analytic formulas (purple, green) from App. A.1.1. Parameters: $\text{Re}(\gamma) = -0.1$, $\text{Im}(\gamma) = 0.5$, $\omega = 1$, $\kappa = 0.1$, $\phi = 0.2\pi$.

3.2 Two coupled Lang-Kobayashi-type lasers

This section investigates the case of two coupled Lang-Kobayashi-type lasers with negligible transmission delay. The focus in particular lies on the amount of differences one can expect due to the inclusion of the carrier equations when compared with the more simple Stuart-Landau oscillator case of the previous section. After a short general introduction, the main aspect of interest here will be symmetry-breaking bifurcations.

3.2.1 Equations and symmetries

The solutions for two coupled lasers closely mirrors those of two coupled Stuart-Landau oscillators, as the system of Lang-Kobayashi type equations used to describe coupled lasers can be approximated by Stuart-Landau oscillators near the Hopf-bifurcation, see Sec. 2.4.3. The case of two coupled lasers in the Lang-Kobayashi framework has first been analytically studied in Ref. [YAN04c] by Yanchuk *et al*, including the case with delay and shear or amplitude-phase coupling $\alpha \neq 0$. However, some important differences arise due to the inclusion of the additional carrier equation.

To best illustrate the similarities with the case of the two coupled Stuart-Landau oscillators of Eqs. (3.1) and (3.2) the following parametrization and coupling will be investigated:

$$\dot{E}_1 = (1 + i\alpha) E_1 N_{e,1} + \kappa e^{i\phi} E_2, \quad (3.26)$$

$$\dot{N}_{e,1} = \frac{1}{T} \left(p - N_{e,1} - (1 + 2N_{e,1}) |E_1|^2 \right) \quad (3.27)$$

$$\dot{E}_2 = (1 + i\alpha) E_2 N_{e,2} + \kappa e^{i\phi} E_1, \quad (3.28)$$

$$\dot{N}_{e,2} = \frac{1}{T} \left(p - N_{e,2} - (1 + 2N_{e,2}) |E_2|^2 \right) \quad (3.29)$$

This is in contrast to Ref. [YAN04c], where the electric field was scaled by $\sqrt{2}$, resulting in a different N_e -equation.

The shear $\text{Im}(\gamma)$ was important in creating the SBL states for the case of two coupled Stuart-Landau oscillators. For a laser, the corresponding amplitude-phase coupling is determined by the well-known α -factor. To be precise, the α factor is a measure of the imaginary part of the gain normalized by the real part. Thus it directly correlates with $\text{Im}(\gamma)/\text{Re}(\gamma)$. However, as $\text{Re}(\gamma)$ is never changed for the Stuart-Landau systems throughout this thesis, changing α for the system of instantaneously coupled Lang-Kobayashi equations has the same effect as changing the shear $\text{Im}(\gamma)$ for the Stuart-Landau oscillator case, cf. Fig. 3.3.

3.2 TWO COUPLED LANG-KOBAYASHI-TYPE LASERS

The Lang-Kobayashi equations were originally derived for the setup of a single laser with delayed feedback, see Refs. [LAN80b, ALS96]. In particular, they have proven to be very accurate at describing experimental behaviour for large delay times τ and small coupling strengths κ . Hence, Ref. [YAN04c] by Yanchuk *et al* is particularly interested in the behaviour of two *delay-coupled* lasers. In this thesis the importance is not on the most realistic, complex system, but on the minimal set of equations that are required to describe a certain effect. Symmetry-broken amplitude- and phase-locking states were not a result of delay-coupling in the Stuart-Landau case. As will be shown, similar states can also be observed for the Lang-Kobayashi system of of Eqs. (3.26) to (3.29) which does not include delay. This is also justified, as systems with small delay inherit a lot of their bifurcation landscape from the case without delay. Furthermore, by looking at the bifurcations and stable states found for the case with and without delay, the delay-induced behaviour can be separated from the effects of the local dynamics and the effects of coupling lasers.

Symmetries of the coupled Lang-Kobayashi equations

The system of Eqs. (3.26) to (3.29) describing two instantaneously coupled Stuart-Landau oscillators possesses the same symmetries as the system of two coupled Stuart-Landau oscillators discussed in Sec. 3.1.1. Due to the local dynamics of the Lang-Kobayashi equations, the system possesses a global phase freedom, i.e. a global factor of $\exp(i\theta)$ for arbitrary but fixed θ can be multiplied to both electric fields E_n without changing the dynamics. Additionally, as the coupling is identical in shape and parametrization to the system of two coupled Stuart-Landau oscillators as defined in Eqs. (3.1) and (3.1), the two coupled Lang-Kobayashi also have \mathbb{Z}_2 -exchange, i.e. discrete cyclic, symmetry. Hence, switching all indices of Eqs. (3.26) to (3.29) leaves the system unchanged.

$$(E_1, E_2, N_{e,1}, N_{e,2}, \phi) \rightarrow (e^{i\theta} E_1, e^{i\theta} E_2, N_{e,1}, N_{e,2}, \phi), \quad (3.30)$$

$$(E_1, E_2, N_{e,1}, N_{e,2}, \phi) \rightarrow (E_2, E_1, N_{e,2}, N_{e,1}, \phi), \quad (3.31)$$

$$(3.32)$$

The symmetries of of Eqs. (3.26) to (3.29) als contain the 2π -translational symmetry and the π -translational symmetry, as discussed in Ref. [ERZ06a]:

$$(E_1, E_2, N_{e,1}, N_{e,2}, \phi) \rightarrow (E_1, E_2, N_{e,1}, N_{e,2}, \phi + 2\pi), \quad (3.33)$$

$$(E_1, E_2, N_{e,1}, N_{e,2}, \phi) \rightarrow (E_1, -E_2, N_{e,1}, N_{e,2}, \phi + \pi), \quad (3.34)$$

3.2.2 Solutions and their stability

The natural solutions for two symmetrically, instantaneously coupled lasers are the in-phase (IP) and anti-phase (AP) synchronized solutions $E_1 = \pm E_2$. The stability of these states is directly connected, as laid out in Ref. [YAN04c]: The system contains an intrinsic symmetry between in-phase and anti-phase solutions, if the coupling phase is shifted by π (π -translational symmetry). This can be easily checked by defining new coordinates $\tilde{E}_1 = E_1$ and $\tilde{E}_2 = -E_2$ and deriving the ODEs for this new coordinates system. The resulting transformation is analogue to the arguments made for two coupled Stuart-Landau oscillators (see Eqs. (3.17) and ((3.18)). It is therefore sufficient to study the secondary bifurcations of either the in-phase or anti-phase state, which can be done with standard bifurcation analysis tools.

The oscillatory phase-locked solutions are created in an Andronov-Hopf bifurcation that corresponds to the laser threshold. In a solitary laser, this threshold is $p_{th} = 0$ due to the normalization of Eqs. (3.26)-(3.29) (see Ref. [ALS96]). However, the coupling modifies the laser threshold, as constructive (destructive) interference between the lasers can decrease (increase) the photon losses. When the calculations are carried out under the assumption that $E_1 = \pm E_2$ and $N_{e,1} = N_{e,2} = N_E e$, the Andronov-Hopf bifurcations describing the thresholds are given by:

$$p_{H(IP)} = -\kappa \cos \phi. \quad (3.35)$$

$$p_{H(AP)} = \kappa \cos \phi. \quad (3.36)$$

which is identical to the Andronov-Hopf bifurcations in λ for two coupled Stuart-Landau oscillators as shown in Eqs. (3.11) and (3.12). Note, that Eqs. (3.35) and (3.36) recover the solitary threshold $p = 0$ for $\kappa = 0$, i.e. the uncoupled case.

The secondary bifurcations of the system are studied in great detail throughout the literature: Ref. [YAN04c] contains a detailed analysis of the case $N = 2$ with partially analytical results. The much more detailed and path-continuation based results of Erzgräber *et al.* in Ref. [ERZ06a] practically cover the entirety of solutions that can be found in the system of two delay-coupled lasers, including symmetry-breaking solutions. The symmetry-broken solutions were also discussed in more detailed in Ref. [CLE14] and [SEI17]. Finally, Ref. [KOM17] also highlights similar states, albeit using a different terminology and is least relevant here. Over all, the state of the literature for two (delay-)coupled Lang-Kobayashi-type lasers is so well researched, that this thesis will not present detailed derivations of the bifurcations, but rather refer to the just mentioned publications and directly cite the results, where applicable. However, the literature usually does not include a scan of the pump current p . To better highlight the correspondence between the Stuart-Landau and Lang-Kobayashi case, this thesis will shortly introduce this slightly different

3.2 TWO COUPLED LANG-KOBAYASHI-TYPE LASERS

parameter system and discuss the similarities and differences of symmetry-breaking bifurcations between the two systems.

Parameter scan for $\alpha = 0$

Typically, for two-dimensional parameter scans of the system of coupled lasers, the parameters to be varied are chosen to be those of the coupling, i.e. the coupling strength κ and coupling phase ϕ . However, in this thesis the coupling strength κ will be kept constant, and instead the driving pump current p will be scanned. This has three reasons: First, this allows a more direct comparison with the Stuart-Landau oscillator case, where the investigated parameters were coupling phase ϕ and λ . As Sec. 2.4.3 shows, λ for the Stuart-Landau system corresponds to pump current p in the laser case. Second, the generating Hopf-bifurcations, i.e. the laser threshold for coupled laser systems, is modified by the coupling. This is very visible in parameter scans that use the pump current p , but may entirely be absent when only the coupling strength κ is varied. The last reason to use pump current p as a bifurcation parameter instead of the coupling strength κ , is the fact that the coupling strength κ may not exceed a certain critical value, as otherwise the system diverges: Moreover, this critical coupling strength κ is dependent on the coupling phase ϕ as well. In contrast, the system is well defined for any p .

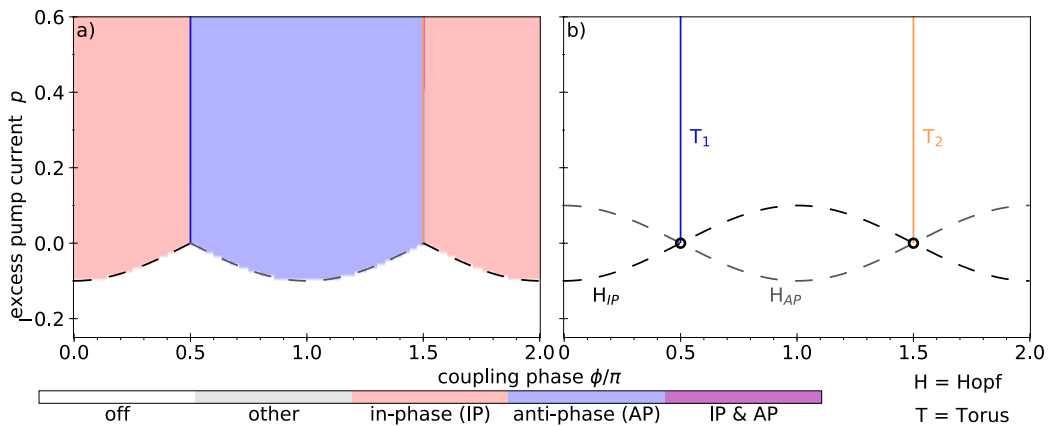


Figure 3.6: Regions of numerical stability for two instantaneously coupled Lang-Kobayashi-type lasers as described in Eqs. (3.26)-(3.29) as a function of pump current p and coupling phase ϕ . a): White areas indicate the trivial off-state, light peach areas the in-phase and bright blue areas the anti-phase state. Purple regions indicate multistability between in-phase and anti-phase orbits (none found for these parameters). b): Bifurcation lines given by Eqs. (3.11) and (3.12) for the Hopf of the in-phase (H_{IP}) and anti-phase solution (H_{AP}) and the torus lines T_1 and T_2 . Black circles mark a co-dimension 2 bifurcation point. Parameters: $T = 200$, $\alpha = 0.0$, $\kappa = 0.1$.

Figure 3.6 shows the regions of stability for two instantaneously coupled Lang-Kobayashi-type lasers (a) and the bifurcations (b). The light peach (blue) regions in Fig. 3.6 a) show the numerically found regions of stability of in-phase (anti-phase) synchronized solutions. These regions were obtained by initializing the system close to the target phase relationship (10^{-4}). The system was then numerically integrated, until a state of constant amplitude or the maximum integration time was reached. Afterwards, the reached system state was automatically classified. Fig. 3.6 a) combines the data from several two-dimensional parameter scans with different initial conditions, and therefore the blue and red regions in Figure 3.6 a) closely approximate the full mathematical region of stability of the in-phase and anti-phase solutions. Figure 3.6 showing the results for two coupled lasers uses the same colour code as Fig. 3.2 for two coupled Stuart-Landau oscillators.

Figure 3.6 a) can be divided into three main regions: First, the trivial off-state $E_1 = E_2 = 0$ is found for values below the laser threshold (white regions). The boundaries are given by the in-phase Andronov-Hopf H_{IP} (black dashed line) and anti-phase Andronov-Hopf (grey dashed line) as defined in Eq. (3.35) and (3.36). These in turn give rise to the in-phase synchronized orbit (light peach regions in Fig. 3.6 a)) and the anti-phase synchronized orbit (blue regions in Fig. 3.6 a)). The regions of stable in-phase and anti-phase oscillations are separated by the torus bifurcation lines marked T_1 and T_2 (blue and orange line in Fig. 3.6). These lines are in reality two tightly separated supercritical torus bifurcations, as can be seen in Ref. [CLE14] Fig. 7 ($\kappa > PH1$). The two Hopf-Hopf points (black circles in Fig. 3.6 b)) create two torus-bifurcation lines as in the case of two coupled Stuart-Landau oscillators (Fig. 3.2). However, here the torus bifurcations lines created in the same co-dimension 2 Hopf-Hopf point do not diverge and stay very close to each other.

The most striking difference between the parameter scans for the two coupled Lang-Kobayashi-type lasers shown in Fig. 3.6 and the case of two coupled Stuart-Landau oscillators, as shown in Fig. 3.2, is the complete absence of any multistability for the laser system (no purple regions in Fig. 3.6 a)). This can be related to the different bifurcation scenario that occurs with respect to the secondary bifurcations on top of the simple oscillatory IP and AP states: While the Stuart-Landau oscillator shows a complex border consisting of both pitchfork and torus bifurcations (Fig. 3.2 b)), the laser IP and AP solutions are purely limited by the torus bifurcations (T_1 and T_2 in Fig. 3.6 b)). This is also caused by the fact, that the torus lines connect both Hopf-Hopf points for the Stuart-Landau case (black circles in Fig. 3.2 b)), while they do not for the laser system ($T_{1,2}$ are straight lines in Fig. 3.6 b)). Following the deductions of Ref. [CLE14], it is also clear that the laser system contains some tiny regions of higher order dynamics along the torus lines (not visible in the scale of Fig. 3.6): As mentioned, every torus line is in reality

3.2 TWO COUPLED LANG-KOBAYASHI-TYPE LASERS

made up of two tightly separated torus bifurcations, in between which higher order dynamics can be found. The difference between the Stuart-Landau and Lang-Kobayashi case are in general smallest close to the Hopf-bifurcations, as this is where the Lang-Kobayashi system is well approximated by the Stuart-Landau system. Despite these differences, the laser case still obeys the same symmetry-rules, and hence the IP regions (light peach in Fig. 3.6 a)) are the image of the AP regions (blue in Fig. 3.6 a)) under the π -translational symmetry.

Parameter scan for $\alpha \neq 0$

The importance of the amplitude-phase coupling parameter α in determining the dynamics of laser systems is a well established fact. In particular, some laser systems may even require a description that goes beyond the linear α -factor approach used to describe amplitude-phase coupling in the Lang-Kobayashi model, e.g. see Ref. [LIN12b]. As mentioned, α is related to the shear $\text{Im}(\gamma)$ of the Stuart-Landau system. It was only in the presence of this shear $\text{Im}(\gamma) \neq 0$ that symmetry-broken amplitude- and phase-coupling states were found, see Fig. 3.3. Studying the influence of α is therefore of great importance.

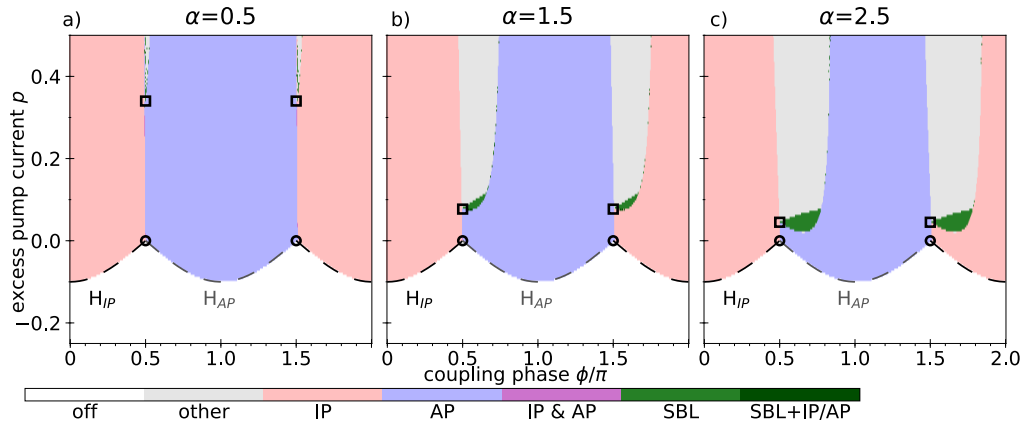


Figure 3.7: Regions of numerical stability for two instantaneously coupled Lang-Kobayashi-type lasers as described in Eqs. (3.26) to (3.29) as a function of excess pump current p and coupling phase ϕ . White areas indicate the trivial off-state, light peach areas the in-phase and bright blue areas the anti-phase state. Purple regions indicate multistability between in-phase and anti-phase orbits (none found for these parameters). Black circles mark a co-dimension two Hopf-Hopf point and squares mark a pitchfork-Hopf point. Parameters: $T = 200$, α as indicated on top of the panels, $\kappa = 0.1$.

Figure 3.7 shows the 2D-parameter scan for different excess pump currents p and coupling phases ϕ for $\alpha \neq 0$ (as indicated atop the panels). When comparing to the parameter scan without amplitude phase coupling in Fig. 3.6, it becomes ap-

parent that α does not influence the off-state (white regions in Fig. 3.7 and 3.6) or border to the in-phase (light peach regions) and anti-phase (blue regions) synchronized solutions. This is also apparent from the analytic formula of the generating Andronov-Hopf-bifurcations of Eqs. (3.35) and (3.36), which do not depend on α . On a more fundamental level of the physical processes involved, the border between off-state (white regions in Fig. 3.7) and continuous wave solutions (IP and AP, light peach and blue regions in Fig. 3.7) corresponds to the laser threshold of the involved lasers. As macroscopic lasers have a negligible emission below threshold, the α -factor mediated influence of the amplitude on the phase will also be negligible. For the Lang-Kobayashi-type of coupled laser equations, as given in Eqs. (3.26)-(3.29), the spontaneous emission is in fact entirely neglected and not included. Hence, the α -factor only grows in influence for higher intensities and thus pump-currents, and has no influence directly at the laser threshold.

The inclusion of non-zero amplitude-phase coupling α leads to the appearance of additional stable states in Fig. 3.7. First, on the border between the stable regions of in-phase (IP, light peach regions) and anti-phase (AP, blue regions) synchronized solutions a small region of higher order dynamics appears (grey regions for large p in Fig. 3.7). This is analogous to the appearance of stable higher order dynamics in the system of two coupled Stuart-Landau oscillators, which appeared for $\text{Im}(\gamma) \neq 0$ (grey regions in Fig. 3.3), highlighting the great similarity between the laser and pure amplitude oscillator system. Additionally, the regions marked in green in Fig. 3.7 b) and c) mark the appearance of symmetry-broken amplitude and phase-locking state (SBL) in the laser system.

The bifurcations and critical points in Fig. 3.7 are known from the literature, especially cf. Fig. 6 in Ref. [CLE14] obtained by path-continuation. Note, the different sign of the coupling phase ϕ in their definition. The black squares in Fig. 3.7 mark the pitchfork-Hopf point called 'PH1' in Ref. [CLE14]. One of the torus lines (coloured in blue and orange in Fig. 3.6, border between light peach and blue regions in Fig. 3.7) originating in the Hopf-Hopf point (black circles in Fig. 3.7) connects to the pitchfork-Hopf point (black squares in Fig. 3.7), while the other torus line passes close by. The vicinity of the pitchfork-Hopf point is explored in Fig. 8 of Ref. [CLE14]. The most important aspect of the bifurcation scenario underlying Fig. 3.7 for now is that with the parameters as chosen there exists both a pitchfork and a torus bifurcation bounding the stability of the in-phase and anti-phase synchronized solutions. The region where SBL states are found (indicated by the green coloured regions in Fig. 3.7) lie along the pitchfork bifurcation, analogue to how the SBL states emerge from a pitchfork bifurcation in the Stuart-Landau case (see Fig. 3.3). On the other hand, no SBL states are found along the other border that corresponds to the torus bifurcations. This is the same behaviour as in the Stuart-Landau case, where no symmetry-broken states were

3.2 TWO COUPLED LANG-KOBAYASHI-TYPE LASERS

found along the torus bifurcation lines (orange and blue lines in Fig. 3.3). Finally, it is worth noting that Ref. [CLE14] also predicts regions of multistability between SBL and in-phase and anti-phase solutions. However, these are not found here, which may be caused due to a slightly different parameter set but has not been further tested.

Symmetry-broken states in coupled Lang-Kobayashi-type lasers

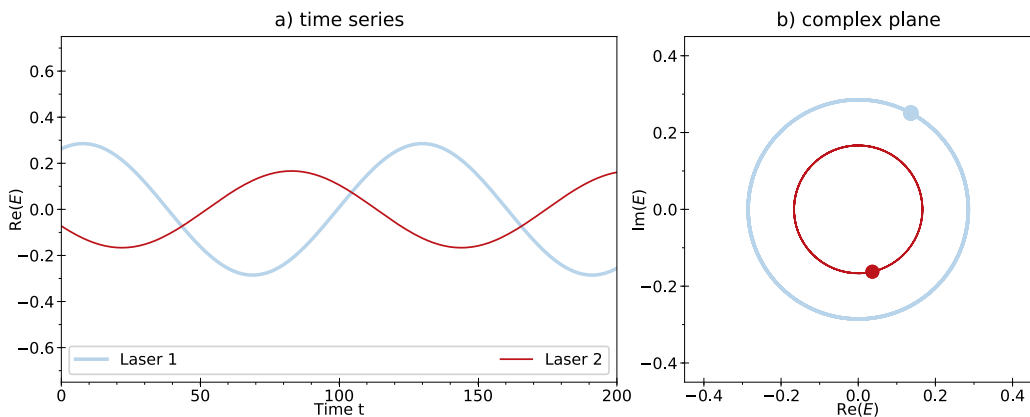


Figure 3.8: Example timeseries for the symmetry-broken amplitude- and phase-locking states of two coupled Lang-Kobayashi-type lasers as defined by Eqs. (3.26) to (3.29). a): time series slice of the real part of the complex electric field amplitude $\text{Re}(E)$ with different colours for the different oscillators. b): time-trace (coloured lines) and simultaneous positions (coloured filled circles) for the same timeseries in the complex plane. Parameters: $p = 0.05$, $T = 200$, $\alpha = 1.5$, $\phi = 0.65\pi$.

Figure 3.8 shows an example of a symmetry-broken amplitude- and phase-locking state from the parameter region marked in green in Fig. 3.7 b) with $\alpha = 1.5$. The state is characterized by a non-trivial phase and amplitude relationship between the two lasers (see coloured circles indicating the positions for one time in the complex plane in Fig. 3.8). However, as the name ‘symmetry-broken amplitude- and phase-locking’ (SBL) implies, this non-trivial amplitude and phase relationship is *fixed* in time, as it was for the corresponding SBL states in the Stuart-Landau case. This can also be seen by the time trace of the real parts of the electric field $\text{Re}(E)$ shown in Fig. 3.8 a). Moreover, if the phase relationship were time-dependent, this would automatically lead to a time-dependent coupling term in the electric field equations of the coupled Lang-Kobayashi-type laser system (cf. Eqs. (3.26) and (3.28)). Due to the amplitude-phase coupling induced by $\alpha \neq 0$, this would directly translate into amplitude oscillations as well. In contrast, the SBL states exhibit harmonic

oscillations of the form $E_n = A_n \exp(i(\omega t + \theta_n))$, $n = 1, 2$ with some $\omega, \theta_n, A_n \in \mathbb{R}$. They are therefore also an example of non-trivial phase-locking.

Figure 3.8 also visualizes the symmetry-breaking nature of the SBL states (green regions in Fig. 3.7): Despite having identical parameters and symmetric coupling, the lasers end up in different states: One laser exhibits a much larger amplitude than the other. Naturally, as the system still contains its basic symmetries, the result of which laser ends up with the large amplitude is only decided by the initial conditions, and swapping the initial conditions between the lasers would also lead to a flip of the amplitudes in the eventually reached SBL state. As in the Stuart-Landau oscillator case, this is a result of the *equivariant branching lemma* that deals with the symmetries and sub-symmetries of solutions of dynamical systems: While each *individual* solution does not need to abide all the symmetries of the underlying system of equations, the solutions can be grouped together to recover the fundamental symmetry group. In particular, this means that the SBL state shown in Fig. 3.8 is breaking the exchange symmetry of the coupled Lang-Kobayashi-type laser system of Eqs. (3.26)-(3.29). Hence, exchanging the amplitudes of the lasers as observed in the stable limit cycle of Fig. 3.8 must also be a stable orbit. This is all analogue to the symmetry-broken states in the Stuart-Landau case discussed in Sec. 3.1.3. The time traces of the complex electric field in Fig. 3.8 therefore also looks very similar to the complex amplitude of the Stuart-Landau oscillators in Fig. 3.1.

Symmetry-broken states, as shown in Figure 3.8, have already been investigated in great detail in the literature. This is in contrast to the coupled Stuart-Landau oscillator case, where seemingly only passing reference to symmetry-broken states had been made previously to Ref. [ROE18]. In the Lang-Kobayashi case, the state has been studied both with and without delay, albeit is often referred to by different names: Yanchuk *et al.* [YAN04c] call them ‘asynchronous continuous wave states’, which highlights both their symmetry-breaking (‘asynchronous’) and regular (‘continuous wave’) aspects. Similarly, Erzgräber *et al.* in Ref. [ERZ06a] refer to them as ‘intermediate phase compound laser mode’, as their bifurcation analysis reveals the connecting bifurcations between the SBL states and the in-phase and anti-phase synchronized states. Ref. [CLE14] and the follow-up paper of Ref. [SEI17] refer to these states as ‘symmetry-broken 1-colour states’, where ‘1-colour’ refers to the fact that both lasers share the same frequency and are thus phase-locked. The terminology of Ref. [KOM17], ‘asymmetric phase-locked states’, is similar to the previous ones.

3.2 TWO COUPLED LANG-KOBAYASHI-TYPE LASERS

The ansatz that can be made to describe the symmetry-broken amplitude and phase-locking states analytically is similar to that of the Stuart-landau case (compare Eq. (3.19)):

$$E_1(t) = sE_2(t) = s\hat{E}e^{i\Omega t}, \quad (3.37)$$

$$N_1(t) = N_1 = \text{const.}, \quad (3.38)$$

$$N_2(t) = N_2 = \text{const.}, \quad (3.39)$$

where Ω is the common frequency, $\hat{E} \in \mathbb{R}$ the amplitude of laser 1 and $s \in \mathbb{C}$ is complex amplitude- and phase-factor. This ansatz is already discussed by Yanchuk *et al.* in Ref. [YAN04c], who find an implicit transcendental equation to determine $s = A_1/A_2 \exp(i\psi)$ in Eq. (B20) of the Appendix in Ref. [YAN04c]. However, as opposed to the numerical simulations shown in Fig. 3.7 and Ref. [CLE14], Yanchuk *et al.* hypothesized that these states are always unstable, which we now know to be false.

Overall the SBL states found here for the case of two coupled Stuart-Landau oscillators and the variously named symmetry-broken states of two-coupled Lang-Kobayashi-type lasers throughout the literature are extremely similar: Both exhibit similar properties, appear in identical bifurcation scenarios (symmetry-breaking pitchfork of limit-cycle bifurcations), are connected to amplitude-phase coupling factors ($\text{Im}(\gamma)$ for Stuart-Landau and α for Lang-Kobayashi) and can be described with similar analytical approaches. However, while a full analytical description of the SBLs states is possible for the Stuart-Landau case (as deduced in Appendix A.1.1), no such complete description exists for the Lang-Kobayashi case. In particular, it is still an open question whether the appearance of ‘non-trivial in-phase’ and ‘non-trivial anti-phase’ ($E_1 = AE_2$ with $A \in \mathbb{R}$) states is possible for the Lang-Kobayashi case. These states are possible for the Stuart-Landau case (cf. Eqs. (3.24) and (3.25)).

3.3 Unidirectional ring networks

One of the ways to extend the results of two coupled lasers or oscillators is to look at ring networks. Both bidirectional ring networks and unidirectional ring networks contain solutions that are very similar to those of two coupled oscillators. These simple ring topologies employ a nearest-neighbour coupling, i.e. edges only connect directly adjacent nodes when sketched as a ring, see Fig. 3.9. Unidirectional rings are directed graphs with one incoming and one outgoing connection per node and are covered in this section. Bidirectional rings are undirected networks with every node connected to its two neighbours and will be covered in Sec. 3.4. This restriction in the coupling range is in contrast to more complex ring networks that employ next-nearest neighbour coupling or a coupling Kernel, as is often used in the Chimera state literature, e.g. see Ref. [KUR02a] or Ref. [ZAK15b].

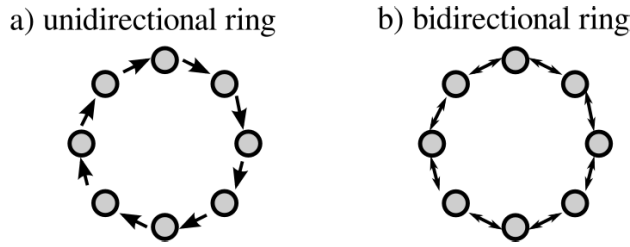


Figure 3.9: Sketch of the topology of ring networks. A unidirectional ring (a) has one incoming and one out-going edge and is a directed network. A bidirectional ring (b) is an undirected network with two edges connected to each node.

3.3.1 Unidirectional ring of Stuart-Landau oscillators

A unidirectional ring is defined by the adjacency matrix A with elements a_{ij} :

$$a_{ij} = \begin{cases} 1, & j = i + 1 \text{ || } (i, j) = (1, N) \\ 0, & \text{otherwise} \end{cases} \quad (3.40)$$

where N is the number of nodes. The unidirectional ring of N Stuart-Landau oscillators is then given by the following set of equations:

$$\begin{aligned}
 \dot{Z}_0 &= (\lambda + i\omega + \gamma |Z_0|^2)Z_0 + \kappa e^{i\phi} Z_{N-1}, \\
 &\vdots \\
 \dot{Z}_n &= (\lambda + i\omega + \gamma |Z_n|^2)Z_n + \kappa e^{i\phi} Z_{n-1}, \\
 &\vdots \\
 \dot{Z}_{N-1} &= (\lambda + i\omega + \gamma |Z_{N-1}|^2)Z_{N-1} + \kappa e^{i\phi} Z_{N-2},
 \end{aligned} \tag{3.41}$$

Note, that to simplify some equations appearing later, the index starts at $n = 0$.

Symmetries

The unidirectional ring of size N possesses an N -fold discrete cyclical symmetry \mathbf{Z}_N . This is an extension of the \mathbf{Z}_2 -symmetry of the case of two coupled Stuart-Landau oscillators. Additionally, the unidirectional ring and its Eqs. (3.41) retain the global phase-freedom of the Hopf-normal form, i.e. if a global factor $\exp(i\theta)$ is multiplied to all complex amplitudes Z_n , the system remains unchanged. The parametrization of the coupling in Eqs. (3.41) also ensures that the $2 - \pi$ -translational symmetry still exists. The π -translational symmetry of the $N = 2$ -case, however, does not exist in general (it only exists for even N), but a more general symmetry can be found, which is linked to the special solutions of the unidirectional ring: rotating wave patterns. These are introduced in the next section.

3.3.2 Special solutions: Rotating wave patterns or "Ponies on a merry-go-round"

The natural solutions of two coupled Stuart-Landau oscillators were the in-phase (IP) synchronization $Z_1 = Z_2$ and anti-phase (AP) synchronization $Z_1 = -Z_2$, see Sec. 3.1.2. In the unidirectional ring (Eqs. 3.41), these generalize to rotating wave patterns labelled with index $j \in [0, \dots, N - 1]$:

$$Z_n(t) = e^{i(n\xi_j + \theta)} Z(t), \tag{3.42}$$

where $Z(t) = A_j \exp(i\omega_j t + \theta)$ is a harmonic oscillation with fixed amplitude $A_j \in \mathbb{R}$, frequency ω_j and arbitrary θ (global phase freedom). The rotating wave solutions are characterized by a fixed and identical phase difference ξ_j between every pair of neighbouring oscillators, i.e. $Z_n/Z_{n-1} = \exp(i\xi_j)$, while they share the

3 SYMMETRY-BREAKING IN NETWORKS

same amplitude and frequency. Hence, all the oscillators are frequency and phase-synchronized. The off-set phase for index j is given by:

$$\xi_j = \frac{2\pi j}{N}. \quad (3.43)$$

This special choice of the phase difference ξ_j is a natural consequence of the fact that going once around the ring, one has to return to the same oscillator - and therefore the same phase. Hence it must hold that $N\xi_j = k2\pi$ for some $k \in \mathbb{N}$, which Eq. (3.43) fulfils. The rotating wave index j will be taken to be in the interval of integers $[0, \dots, N - 1]$. Any j outside of this interval will not yield different solutions, as ξ_j and $\xi_j + 2\pi$ yield identical dynamics. Thus, the rotating waves can also be seen as a standing wave pattern in the relative phases of the unidirectional ring. Due to the discrete nature, only N different patterns exist.

The validity and existence of these states can be checked by inserting the ansatz of Eqs. (3.42) into the unidirectional ring Eq. (3.41). Solving for the amplitude of such rotating wave patterns yields:

$$|A_j|^2 = - \frac{\lambda + \kappa \cos(\phi - \xi_j)}{\operatorname{Re}(\gamma)}, \quad (3.44)$$

which implicitly contains the condition for existence, i.e the generating bifurcation of the rotating wave of index j , as the right hand side of the equation has to be positive. One can safely assume this to be a Hopf-bifurcation from the $N = 2$ case and due to the square-root dependence of the amplitude. The Hopf bifurcation for the rotating wave of index j therefore occurs for:

$$\lambda_{H(j)} = -\kappa \cos(\phi - 2\pi j/N), \quad (3.45)$$

which is a generalization of the deductions of Sec. 3.1. The rotating wave of index $j = 0$ always corresponds to the in-phase solution. Hence, $\lambda_{H(j)}$ in Eq. (3.45) for $j = 0$ becomes identical to the in-phase Andronov-Hopf bifurcation of two coupled oscillators as deduced in Eq. (3.11) in Sec. 3.1. The rotating wave of index $j = N/2$ (if N is even) corresponds to a general anti-phase pattern, i.e. every oscillator is anti-phase to both of its neighbours. Hence Eq. (3.45) is identical to the H_{AP} -bifurcation of Eq. (3.12) for the $N = 2$ case if $j = N/2$. Additionally, if the anti-phase pattern exists, it will always initially be centred around $\phi = \pi$ just as in the $N = 2$ case. Other rotating wave patterns are centred around $\phi = 2\pi j/N$. If index j is a factor of the number of oscillators N the system forms clusters. Specific examples will be shown for $N = 4$ in the next section, which illustrate the properties of the rotating waves.

3.3.3 Unidirectional ring of 4 oscillators

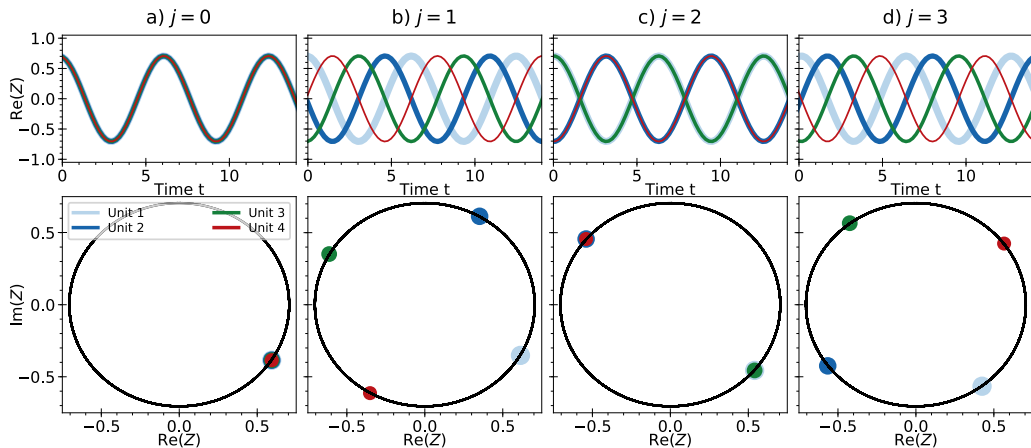


Figure 3.10: Example timeseries for the fundamental patterns of the unidirectional ring of $N = 4$ Stuart-Landau oscillators as defined by Eqs. (3.41). The rotating wave patterns are described by an index j according to Eq. (3.42). The top panel shows a time series slice of the real part of the complex amplitude $\text{Re}(Z)$ with different colours for the different oscillators. Bottom panels show a phase space projection of the time-trace (black line) and simultaneous positions (coloured circles) for the same timeseries in the complex Z plane. Parameters: $\lambda = 0.05$, $\omega = 1$, $\text{Re}(\gamma) = -0.1$, $\text{Im}(\gamma) = 0$, $\phi = 0, 0.5\pi, \pi, 1.5\pi$

Figure 3.10 shows the example for the unidirectional Stuart-Landau ring as given by Eqs. (3.41) for $N = 4$ oscillators. Accordingly the system possesses 4 different rotating wave states that can be obtained (excluding the trivial global phase freedom), which are shown from right to left in Fig. 3.10. The top panel shows a timeseries slice of the real part $\text{Re}(Z(t))$, with the different oscillators in colour. Note, that slightly different line widths have been used to see overlapping oscillations. The row of bottom panels of Fig. 3.10 shows corresponding projections of the time-traces (black) and simultaneous positions (coloured circles) for all the oscillators into the complex Z plane.

The in-phase synchronized case with $Z_0 = Z_1 = Z_2 = Z_3$ is shown in Fig. 3.10 a) and occurs for index $j = 0$ with a phase difference $\xi_0 = 0$. All 4 oscillators are identical for all times. Fig. 3.10 b) shows the first of the non-trivial extensions when compared to the two coupled Stuart-Landau oscillators. With index $j = 1$ the rotating wave results in a phase difference of $\xi_1 = \pi/2$. Every oscillator has a unique phase and therefore is visible as distinct trace in the top panel of Fig. 3.10 b) and the simultaneous positions (coloured dots in the bottom panel of Fig. 3.10 b)) are each a quarter of the circumference of the circle apart.

The anti-phase synchronized case is given by index $j = 2$ for the $N = 4$ oscillator case shown in Fig. 3.10 c). The oscillators are anti-phase with both of their neighbours $Z_1 = -Z_2 = Z_3 = -Z_4$. This necessarily leads to the system creating two in-phase synchronized clusters, as is visible in the time traces (top) and complex plane representation (bottom) in Fig. 3.10 c). Finally, the index $j = 3$ shown in Fig. 3.10 d) is another non-trivial rotating wave pattern. Note, that the order is reversed compared to index $j = 1$ of Fig. 3.10 b). It is a general rule that indices j and $N - j$ will be mirror images. Note, that an index $j = 4$ would simply recover the in-phase synchronized state of $j = 0$.

The bottom panels of Fig. 3.10 also illustrate the informal name of these rotating wave patterns: ‘ponies on a merry-go-round’. In the complex plane, the oscillators will perform a circular motion around the origin with constant angular velocity, while keeping their distance. This is reminiscent of the ‘ponies’ (and elephants, fire trucks etc.) on a merry-go-round, which also simply rotate around a common axis. These solutions also represent primitive ‘cluster states’ for index $j \neq 0$, as different oscillators exhibit different phases [LEH15b]. Thus, the anti-phase case of $j = 2$ for $N = 4$, as shown in Fig. 3.10 c), is a cluster state. If the rotating wave index j is not a factor of the number of oscillators N , then each unit will have its own unique complex amplitude $Z_n \neq Z_m$ for $m \neq n$. These states of constant, identical phase shift between oscillators are also called ‘splay states’. For example, $j = 1$ and $j = 3$ are not a factor of $N = 4$ and therefore Fig. 3.10 b) and d) are also splay states.

Symmetry-abiding coordinate transformations

The existence of all these different rotating wave patterns can also be deduced by a calculation using coordinate transforms and using the symmetries of the system. Similar to the deductions for two coupled Stuart-Landau oscillators in Sec. 3.1.2 used to obtain Eqs. (3.17) and (3.18). First, new variables are defined:

$$\tilde{Z}_n = e^{in\xi_j} Z_n. \quad (3.46)$$

Eq. (3.46) actually describes N different coordinate transforms, as one for each different rotating wave index j can be used. In particular, the transformation of Eq. (3.46) for $j = 0$ leaves the system unchanged, while $j = N/2$ is similar to the

3.3 UNIDIRECTIONAL RING NETWORKS

transformation introduced in Sec. 3.1.2. Inserting these transformations into the equations of motion of the unidirectional Stuart-Landau ring, Eqs. (3.41), yields:

$$\begin{aligned}
 \dot{\tilde{Z}}_0 &= (\lambda + i\omega + \gamma |\tilde{Z}_0|^2) \tilde{Z}_0 + \kappa e^{i(\phi + \xi_j)} \tilde{Z}_{N-1}, \\
 &\vdots \\
 \dot{\tilde{Z}}_n &= (\lambda + i\omega + \gamma |\tilde{Z}_n|^2) \tilde{Z}_n + \kappa e^{i(\phi + \xi_j)} \tilde{Z}_{n-1}, \\
 &\vdots \\
 \dot{\tilde{Z}}_{N-1} &= (\lambda + i\omega + \gamma |\tilde{Z}_{N-1}|^2) \tilde{Z}_{N-1} + \kappa e^{i(\phi + \xi_j)} \tilde{Z}_{N-2},
 \end{aligned} \tag{3.47}$$

Thus, these transformed equations are identical to the original Eqs. (3.41), with the exception of a new coupling phase $\tilde{\phi} = \phi + \xi_j$. Due the nature of the transformation introduced in Eq. (3.46), the in-phase synchronized solutions of the transformed system Eqs. (3.47) correspond to a rotating wave of index j in the original system. Thus, if an in-phase synchronized solution is found for ϕ in the original Eqs. (3.41), then there must also exist a corresponding rotating wave of index j for a shifted coupling phase of $\phi + \xi_j$. In fact, *any solution* found in the original equations, has a corresponding phase-shifted solutions with index j in the transformed system. This is the generalization of the π -translational symmetry for a phase shift of π of two coupled Stuart-Landau oscillators in Sec. 3.1.2. It will therefore be called the ξ_j -translational symmetry. This simple algebraic trick again uses the symmetries of the underlying system. It not only connects the solutions for different coupling phases ϕ and rotating wave index j , but it can also be used to deduce the existence of the non trivial rotating wave patterns $j \neq 0$, as this transformation leaves the overall system of ODEs unchanged.

To study the secondary bifurcations of the oscillatory solutions of Eqs. (3.41), i.e. the rotating wave patterns with index j , it is therefore sufficient to investigate the bifurcations of the in-phase synchronized oscillations $j = 0$. The behaviour for $j \neq 0$ then simply follows with the ξ_j -translational symmetry introduced in the previous paragraph. The in-phase synchronized solution is given by $Z_n = Z$, which leads to Eqs. (3.47) decoupling completely, and seems easiest to solve. Using the ξ_j -translational symmetry therefore reduces the number of explicit equations to be deduced by a factor of N .

Parameter scan for $N = 4$ and $\text{Im}(\gamma) = 0$

So far, the symmetries and basic solutions for the unidirectional Stuart-Landau ring of $N = 4$ were discussed, which are the rotating wave patterns of index j . Fig. 3.11 a) shows numerical simulations of a unidirectional network of $N = 4$

3 SYMMETRY-BREAKING IN NETWORKS

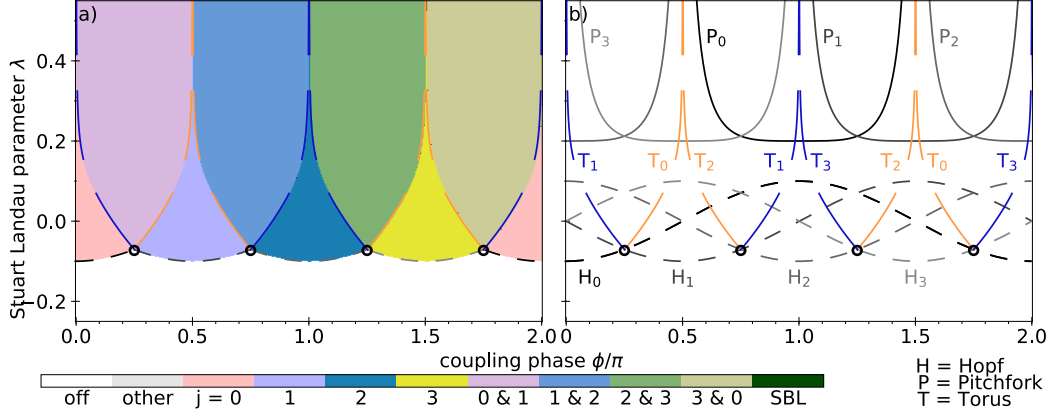


Figure 3.11: a:) Regions of numerical stability for $N = 4$ instantaneously coupled Stuart-Landau oscillators in a unidirectional ring as described in Eqs. (3.41) as a function of λ and coupling phase ϕ for shear $\text{Im}(\gamma) = 0$. White areas indicate the trivial off-state. The colours indicated in the legend with ‘ $j = 0$ ’, ‘1’ etc. are rotating wave patterns as described by Eq. (3.42) as shown in Fig. 3.10. Labels such as ‘0 + 1’ indicate multistability between rotating waves of different index j . The right panel (b) shows analytically and semi-analytically derived bifurcation lines given by Eq. (3.45) for the Hopf of the the different indices j (H_j), and Eqs. (3.48) for the pitchfork bifurcation (P_j). The torus lines were calculated by numerically finding the roots of the real part of the last (analytically expressible) eigenvalue branches. Black circles mark a co-dimension 2 bifurcation point. Parameters: $\text{Re}(\gamma) = -0.1$, $\text{Im}(\gamma) = 0$, $\omega = 1$, $\kappa = 0.1$.

oscillators for different coupling phases ϕ and driving parameters λ as given by Eqs. (3.41) for the case without amplitude-phase coupling $\text{Im}(\gamma) = 0$. The colour code indicates the observed regions of stability for the 4 fundamental rotating wave patterns $j = 0, 1, 2, 3$. Time series samples for these states in this system are shown in Fig. 3.10. Fig. 3.11 a) contains the information of 4 different batches of simulation: 4 different initial conditions were numerically integrated for each parameter combination of coupling phase ϕ and λ . One each was initialised very close (10^{-3}) to each of the four fundamental rotating waves. An automatic transient detection routine determined the time the system needed to evolve: at least 1000 time units and at most 20000 time units. After that time, the final state was observed and categorized. Due to the finite numerical integration time and computer precision, any state that was close to a mathematically precise rotating wave was counted as such. Thus, Fig. 3.11 a) should realistically represent the regions of stability for all the different rotating wave types.

Fig. 3.11 a) also shows the regions of multistability between different rotating waves. The regions of stability of the rotating wave with index j should be identical to those of the in-phase synchronized solution $j = 0$, once the coupling phase is

3.3 UNIDIRECTIONAL RING NETWORKS

shifted by $\xi_j = j\pi/2$ due to the ξ_j -translational symmetry. This is confirmed by the numerics here, and it in turn validates the numerical approach taken. Because the region of stability never stretches for more than π in the coupling phase ϕ , this also means that there never are more than two simultaneously stable states (because for $N = 4$ it follows that $4/2 = 2$). Numerical simulations indicate, that this should generalize to a maximal multistability of $N/2$ simultaneously stable rotating wave patterns for rings of arbitrary size N . The regions of stability for each j as seen by the coloured regions in Fig. 3.11 a) generally grow with λ , and unlike the case of two-coupled oscillators shown in Fig. 3.2 it never contracts. Therefore the multistability strictly increases with λ .

For the case of $N = 4$ it is possible to solve the characteristic equation along the rotating wave states explicitly. This is done in Appendix A.2. The secondary bifurcations are also derived. The Andronov-Hopf bifurcation H_j that generates the oscillations of Eq. (3.45) is recovered (dashed dark and grey lines in Fig. 3.11). Two additional bifurcations are also derived in Appendix A.2. First, a pitchfork can be explicitly expressed:

$$\lambda_P = -\frac{3\kappa + \kappa \cos(2\phi) + \tilde{\alpha}\kappa \sin(2\phi)}{2 \cos \phi + 2\tilde{\alpha} \sin \phi}, \quad (3.48)$$

with $\tilde{\alpha} = \text{Im}(\gamma)/\text{Re}(\gamma)$. Additionally, a last branch of 4 related eigenvalues is obtained, as shown in the lengthy expression Eq. (A.34). This last branch corresponds to a secondary Andronov-Hopf or torus bifurcation.

Figure 3.11 b) shows the bifurcation structure of the ring of $N = 4$ unidirectionally coupled Stuart-Landau oscillators of Eqs. (3.41). The generating Hopf bifurcations for the rotating waves of index j are given by the dark and grey dashed lines on the bottom of Fig. 3.11 b). The labels indicate the phase relationship of the created phase-locked solution H_j , where $j = 0$ corresponds to the in-phase synchronized solution. As in the case of the two coupled Stuart-Landau oscillators shown in Fig. 3.2, only the first Andronov-Hopf bifurcation that occurs for lowest λ produces stable oscillations. Thus, despite every Andronov-Hopf line H_j spanning the entire coupling phase range ϕ , the corresponding rotating wave patterns only emerge for one quarter of the length along it. This generalized to a length of $2\pi/N$ for larger unidirectional rings, i.e. for every coupling phase there is always only a single stable rotating wave created through a Hopf-bifurcation from the off-state. All other rotating wave patterns are only created unstable and multistability only arises through secondary bifurcations.

On rotating waves created in H_j secondary bifurcations occur. Where two fundamental Andronov-Hopf-bifurcations H_j meet a co-dimension 2 Hopf-Hopf point is located (black circles in Fig. 3.11 b)). In these Hopf-Hopf points two secondary

Andronov-Hopf or torus bifurcations T_j are created (orange and blue lines in Fig. 3.11 b)). Note, that there are two lines called T_j for every j in Fig. 3.11 b)). These branches are both obtained from Eq. (A.34) in the appendix, but represent two different roots of that eigenvalue, i.e. they are independent lines. They will also react differently, once the symmetry is broken for $\text{Im}(\gamma) \neq 0$. Nonetheless, in the symmetric case $\text{Im}(\gamma) = 0$ shown in Fig. 3.11, the region of stability of the different states as shown by the numerics are always limited by the torus bifurcations T_j . The pitchfork bifurcations (black and grey solid lines in Fig. 3.11 b)) only occur in regions where the original rotating wave of index j is already unstable. This is in contrast to the $N = 2$ case, where these pitchfork bifurcations also limited the regions of stability. The parts of the bifurcation lines that limit regions of stability are also reproduced in Fig. 3.11 a), where they perfectly frame the numerically obtained data (H_j and T_j , but not P_j due to the solution already being unstable).

In general, the $N = 4$ unidirectional ring of Stuart-Landau oscillator has a more complex bifurcation landscape than the case of two oscillators. Nevertheless, this increase in the number of possible solutions does not drastically increase the difficulty of studying the system analytically and numerically. This is mostly due to the ξ_j -translational symmetry, which reduces the number of required calculations by a factor of N . However, due to the closer spacing of the different rotating wave patterns, it is also apparent that the influence of the coupling phase ϕ has increased when compared to the $N = 2$ case. This is a trend that continues towards even larger networks, which will be discussed later. Additionally, the regions of multistability have increased for the unidirectional ring. Both the higher phase sensitivity and larger multistability could potentially be difficult to control in experimental setups, and thus a unidirectional network may be a difficult topology to investigate.

Parameter scan for $N = 4$ and $\text{Im}(\gamma) \neq 0$

As before, the importance of the amplitude-phase coupling for $\text{Im}(\gamma) \neq 0$ should not be neglected, and will now be investigated. Figure. 3.12 shows the evolution of the regions of stability for different amplitude-phase coupling $\text{Im}(\gamma)$ as indicated atop the columns. This is the generalization of the system that is shown for $\text{Im}(\gamma) = 0$ in Fig. 3.11. The colour code and legend are identical in both figures, with the regions of stability for different rotating wave patterns shown. When comparing Fig. 3.11 and 3.12 the influence of the shear can be studied: First, as can also be seen from Eq. (3.45), the position of the generation Hopf bifurcations H_j does not change with shear. However, while the regions of stability for the rotating wave states are always centred and symmetric in coupling phase around $\phi = \xi_j$ if $\text{Im}(\gamma) = 0$, in the presence of amplitude-phase coupling $\text{Im}(\gamma)$ this is only true for small λ ;

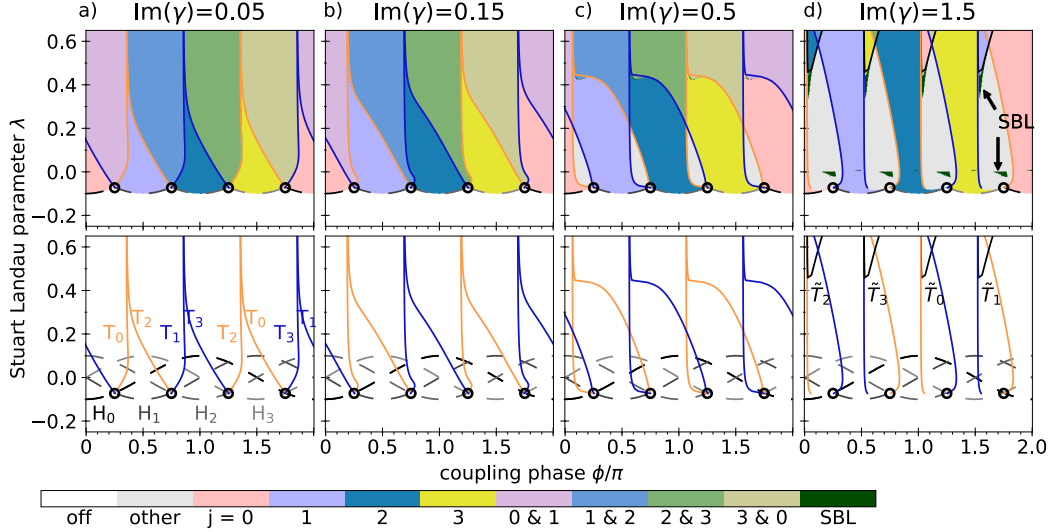


Figure 3.12: Top: Regions of numerically obtained stability for $N = 4$ instantaneously coupled Stuart-Landau oscillators in a unidirectional ring as described in Eqs. (3.41) as a function of λ and coupling phase ϕ for different shears $\text{Im}(\gamma)$. White areas indicate the trivial off-state. The colours indicated in the legend with ‘ $j = 0$ ’, ‘1’ etc. are rotating wave patterns as described by Eq. (3.42) as shown in Fig. 3.10. Labels such as ‘ $0 + 1$ ’ indicate multistability between rotating waves of different index j . Grey areas contain higher-order dynamics. Dark green areas contain symmetry-broken amplitude and phase-locking states. The bottom panels show analytically and semi-analytically derived bifurcation lines given by Eq. (3.45) for the Hopf-lines with different indices j (H_j), and the roots of Eqs. (A.34) for the torus (orange and blue lines T_j and black lines \tilde{T}_j). Black circles mark co-dimension 2 Hopf-Hopf points. Parameters: $\text{Re}(\gamma) = -0.1$, $\text{Im}(\gamma)$ as indicated atop the column, $\omega = 1$, $\kappa = 0.1$.

e.g. compare the symmetric regions of stability for $j = 0$ in Fig. 3.11 a) with the increasingly asymmetric regions of $j = 0$ for high λ in Fig. 3.12. This naturally also extends to the regions of multistability. For high λ , the amplitude-phase coupling induced by $\text{Im}(\gamma) \neq 0$ bends the region of stability towards lower coupling phases ϕ in Fig. 3.12. This breaks the mirror symmetry in the coupling phase ϕ , that existed for each of the tongues in Fig. 3.11 a) with $\text{Im}(\gamma) = 0$. Nevertheless, the general ξ_j -translational symmetry that links the bifurcation scenario for different j still persists: The two torus lines T_j for each index j (blue and orange lines in Fig. 3.12) are no longer mirror images, but the same bifurcation lines for the different j are still exactly ξ_j apart in the coupling phase ϕ . This is also visible for the lower panels of Fig. 3.12, where the pure bifurcation lines are shown again. This also confirms the symmetry argument deduced from the transformation of Eq. (3.46).

While for lower shear (Fig. 3.12 a) and b)), the regions of stability are merely distorted, the situation fundamentally changes in Fig. 3.12 c) for $\text{Im}(\gamma) = 0.5$. There, new regions open up, where none of the rotating wave patterns of any index are stable (grey regions). This is similar to what happened for $\text{Im}(\gamma) = 0.15$ in Fig. 3.3 b) for $N = 2$. However, a distinctive difference is apparent for the unidirectional ring with $N = 4$ units: No symmetry-broken states appear in these newly opened-up regions. This is a result of the different bifurcation scenario. The basic, symmetry-abiding rotating waves of the unidirectional ring are entirely limited by the torus-bifurcations T_j (orange and blue lines in Fig. 3.12). In contrast, the regions with symmetry-broken amplitude- and phase-locking were limited by a pitchfork bifurcation in the $N = 2$ case. While a pitchfork bifurcation is a symmetry-breaking bifurcation, a torus bifurcation does not have to be. Furthermore, a torus bifurcation also always creates amplitude oscillations, but the interest here is in *phase-locked* symmetry-broken states. Hence, no SBL states are directly created in Fig. 3.12 c). This is a natural pattern of these highly symmetric coupled oscillator systems: Symmetry-breaking states are mostly found close to the pitchfork bifurcations, and where pitchfork bifurcations are missing, these states are not directly created.

3.3.4 Symmetry-broken solutions for $N = 4$

Figure 3.12 d) shows the two-dimensional landscape for even higher shear $\text{Im}(\gamma) = 1.5$. The grey-coloured regions of higher order dynamics have significantly expanded. Additionally, symmetry-broken amplitude- and phase-locking states are now apparent in eight regions (dark green spots in Fig. 3.12 d), two of which are indicated by the arrows labelled ‘SBL’. These originate from 2 groups of fundamentally different parameter combinations and their images under the ξ_j -translational symmetry (each solution can be linked to three related states for $N = 4$). These two different groups of symmetry-broken states will be investigated separately to study their dynamics.

The first group of symmetry-broken solutions

First, for $\lambda \approx 0$ and $\phi \approx 0.25\pi, 0.75\pi, 1.25\pi, 1.75\pi$ isolated patches of symmetry-broken amplitude- and phase-locking states can be found deep inside the regions of higher order dynamics (grey regions) in Fig. 3.12 d). These states are found to be stable suddenly without connections to the surrounding tongues of rotating waves. The bifurcation scenario leading to their stability is therefore likely to be complex and may include subcritical bifurcations.

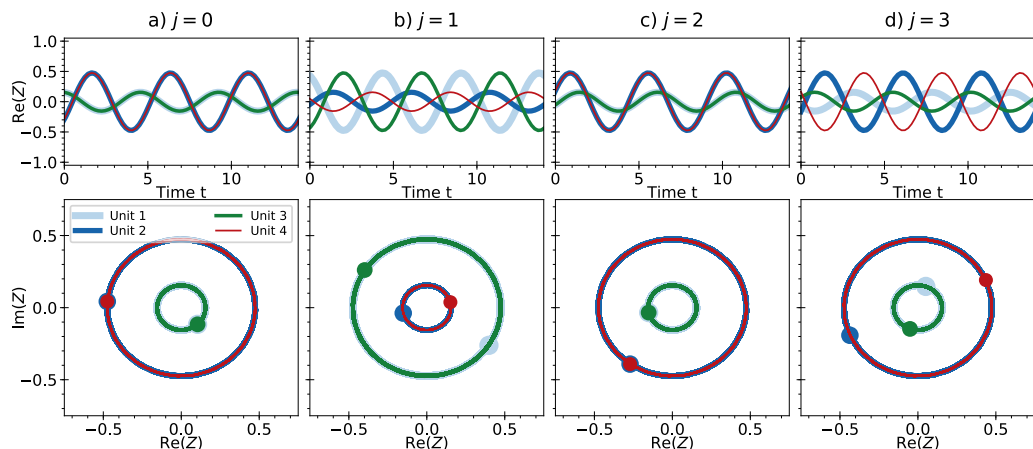


Figure 3.13: Example timeseries for the first type of symmetry-broken amplitude- and phase-locking (SBL) states of the unidirectional ring of $N = 4$ Stuart-Landau oscillators as defined by Eqs. (3.41). The top panel shows a time series slice of the real part of the complex amplitude $\text{Re}(Z)$ with different colours for the different oscillators. Bottom panels show the time-trace (color line) and simultaneous positions (coloured filled circles) for the same timeseries in the complex plane. Parameters: $\lambda = -0.01$, $\omega = 1$, $\text{Re}(\gamma) = -0.1$, $\text{Im}(\gamma) = 1.5$, $\phi = 1.25, 1.75\pi, 0.25\pi, 0.75\pi$

Figure 3.13 shows time series of the real part $\text{Re}(Z_n)$ (top) and projections in the complex plane (bottom panels) for the SBL states in the isolated patches $\lambda \approx 0$ of Figure 3.12 d). The coupling phases for the four related parameter regions are $\phi = 1.25, 1.75\pi, 0.25\pi, 0.75\pi$ and each is labelled with a rotating waves of index $j = 0, 1, 2, 3$, respectively (also see the labels on the top of the columns in Fig. 3.13). Here, the rotating wave indices indicate the nearest stable rotating wave solution in the 2D-parameter plot of Fig. 3.12 d). As these SBL states exist in isolated regions, this is not necessarily the rotating wave state from which the particular SBL solution split off originally. This can only be rigorously proven with a comprehensive bifurcation analysis.

The SBL states shown in Fig. 3.13 represent a single solution and its symmetrized versions. Each SBL solution is defined by two amplitude clusters of two oscillators each, that have the same amplitudes within the clusters $|Z_0|^2 = |Z_2|^2$ and $|Z_1|^2 = |Z_3|^2$, but different amplitudes between the clusters $|Z_0|^2 \neq |Z_1|^2$. Between the two amplitude clusters, the phase relationship is non-trivial, i.e. not a multiple of any ξ_j . The amplitude ratio of the clusters is similarly complex. The amplitude and phase relationship between the clusters also changes within the parameter region marked with 'SBL' in Fig. 3.12 d). As opposed to the inter-cluster relationship, the phase relationship within the clusters is ordinary: For the even rotating wave indices $j = 0, 2$ (Fig. 3.13 a) and c)) phases within the clusters are

identical $Z_0 = Z_2$ and $Z_1 = Z_3$, while for the uneven rotating wave indices $j = 1, 3$ (Fig. 3.13 b) and d)) oscillators are anti-phase within the clusters $Z_0 = -Z_2$ and $Z_1 = -Z_3$. Furthermore, when comparing $j = 0$ and $j = 2$ the phase between the clusters is flipped by π (compare the position of the coloured dots in the bottom panel of Fig. 3.13 a) and d)). Once again, the seemingly strange zoo of solutions can be made sense of, with knowledge of the symmetries of the system: The transformation of Eq. (3.46) shows that all states of Fig. 3.13 will behave identically, when the coupling phase is changed to $\phi + \xi_j$. Despite the first impression one can have, especially when looking at the real part time series in the top panels of Fig. 3.13 a) and b), all solutions in Fig. 3.13 are each others image under the ξ_j -translational symmetry.

One can analytically explore the SBL state for $j = 0$ shown in Fig. 3.13 a) with a simple ansatz, reflecting the observed pattern: Two oscillators are sharing the same amplitude each. As in Sec. 3.1.3, the amplitude and phase relationship can then be described with a complex number s :

$$Z_1 = sZ_2 = Z_3 = sZ_4 \quad (3.49)$$

Additionally, only harmonically oscillating solutions are considered $\dot{Z}_n = i\tilde{\Omega}Z_n$. Inserting this into the unidirectional Stuart-Landau ring equation (3.41) yields 4 equations, of which two each are identical. The two remaining equations are identical to Eqs. (3.20) and (3.21) of Sec. 3.1.3, which described the symmetry-broken amplitude- and phase-locking solutions for $N = 2$. Hence, the first kind of SBL states for the unidirectional ring shown in Fig. 3.13 directly corresponds to the original SBL states that were described in Ref. [ROE18]. Where in the original $N = 2$ case the symmetry-breaking expressed itself in two different amplitudes for the two Stuart-Landau oscillators, this turns into a symmetry-broken state with two oscillators sharing their amplitude each. The symmetry-broken states for two coupled Stuart-Landau oscillators of Sec. 3.1.3 emerged through a single pitchfork bifurcation. A similar emergence seems plausible here, but no pitchfork bifurcation can be seen in the numerics, indicating that they may be created as unstable limit cycles at first. Because all the examples in Fig. 3.13 are so closely related, the states in Fig. 3.13 share their origin, with only the original rotating wave patterns that their limit cycles split off from differing.

The states for $N = 4$ shown in Fig. 3.13 are also cluster states. This is most apparent for Fig. 3.13 a) and c). The assumptions of Eq. (3.49) implicitly assumes that these clusters already exists, i.e. only the stability on the synchronization manifold can be calculated that way. For the SBL states for $N = 4$ to be actually stable, the clusters also have to be internally stable. Internal stability here means, that a small deviation of the amplitudes of oscillators within the same cluster, e.g.

Z_1 and Z_3 , does not grow but decays. The symmetry-broken states for $N = 4$ Stuart-Landau oscillators in a unidirectional ring are likely also linked to the works of Ref. [KU15], who looked exactly at this type of problem of cluster stability of Stuart-Landau oscillators. Sadly, the authors never looked at small unidirectional ring networks, so that no results for this particular case exist. Considering that the numerical simulations of this thesis did find symmetry-broken states that also are cluster states, it would be an interesting avenue of future research to study their relationship to clustering and symmetry-breaking in larger networks.

The second group of symmetry-broken solutions

The two-dimensional scan in Fig. 3.12 d) revealed two different groups of symmetry-broken amplitude- and phase-locking states, of which the first was studied in the previous paragraphs. The second group of SBL states can be found close to $\lambda \approx 0.5$ for $\phi \approx 1.03, 1.53\pi, 0.03\pi, 0.53\pi$. These are connected to one side of the rotating wave states - along a special part of the torus line marked as \tilde{T}_j in Fig. 3.12 d). This torus line is derived from the roots of the last eigenvalue cluster of Eq. (A.34) in the appendix. No full analytic form for this bifurcation line exists, but the eigenvalues themselves can still be expressed analytically. In the case of the upper SBL in Fig. 3.12 d), the roots are still complex conjugates, but the real and imaginary parts are crossing zero almost at the same time.

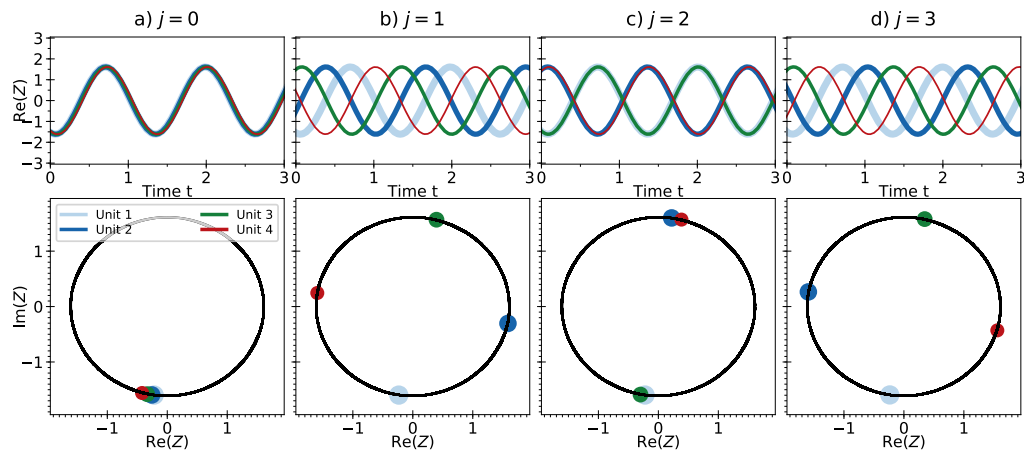


Figure 3.14: Example timeseries for the second type of symmetry-broken amplitude- and phase-locking states of the unidirectional ring of $N = 4$ Stuart-Landau oscillators as defined by Eqs. (3.41). The top panel shows a time series slice of the real part of the complex amplitude $\text{Re}(Z)$ with different colours for the different oscillators. Bottom panels show the time-trace (black line) and simultaneous positions (coloured filled circles) for the same timeseries in the complex plane. Parameters: $\lambda = 0.36$, $\omega = 1$, $\text{Re}(\gamma) = -0.1$, $\text{Im}(\gamma) = 1.5$, $\phi = 1.03, 1.53\pi, 0.03\pi, 0.53\pi$

Figure 3.14 shows time series slice (top) and complex plane representations (bottom) of the SBL states found for $\lambda \approx 0.5$ in Fig. 3.12 d) (dark green regions next to the upper ‘SBL’ arrow). The different columns of Fig. 3.14 show the different symmetrized versions, sorted by rotating wave index j . In contrast to the first group of SBL states shown in Fig. 3.13, the states of the second group smoothly bifurcate directly from the underlying phase-synchronized rotating wave state, i.e. they are only separated from the normal rotating wave states by the torus-line \tilde{T}_j in Fig. 3.12 d). Thus, all of the time series and complex plane projections shown in Fig. 3.14 are close to the original rotating waves. In particular, $j = 0$ (Fig. 3.14 a)) is still very close to the in-phase synchronized state, and thus the small phase differences between the amplitudes Z_n of the different oscillators are easy to overlook (coloured circles in the bottom panel of Fig. 3.14 a) are not perfectly aligned, this is not a plotting artefact). For $j = 1, 3$ it would be easy to overlook the small deviations from the rotating wave state (Fig. 3.14 b) and d)).

This second group of symmetry-broken amplitude- and phase-locked states seems to only differ in phase between the oscillators, the amplitudes are very similar $|Z_0| \approx |Z_1| \approx |Z_2| \approx |Z_3|$. There potentially is a very long-term slow oscillation of the phases, but this was hard to numerically distinguish from transients and must be left for future investigations. To understand the nature of the second type of SBL states for the unidirectional ring, it is useful to look at larger networks.

3.3.5 Large unidirectional rings

Figure 3.15 shows parameter scans for larger unidirectional rings in coupling phase ϕ and λ . However, the number of rotating wave patterns grows with N , and therefore the numerical simulations required to produce an accurate map of all states also increases. Additionally, the number of multi-stable solutions coexisting also increases as $N/2$ as discussed in Sec. 3.3.3, and it becomes difficult to portray the structure of the system easily (not enough distinguishable colours). Hence, Fig. 3.15 is based entirely on one batch of numerical simulations that were started close the in-phase synchronized state $j = 0$. Accordingly, only the extent of the pink region in Fig. 3.15 outlines the true region of stability of a solution. The other states are only randomly sampled in those regions, where the numerical integration did not converge to the in-phase solutions $j = 0$. However, the regions of stability for $j \neq 0$ can in principle be obtained by applying the ξ_j -translational symmetry.

Several facts become apparent when studying Fig. 3.15: First, the region of stability for the in-phase state never exceeds a length of π in the phase dimensions, which it reaches for high λ (width of the red region in Fig. 3.15). This can likely be proven, with an external cavity mode (ECM) ansatz for the case of instantaneously coupled Stuart-Landau oscillators, but is left for future investigations here. Second,

3.3 UNIDIRECTIONAL RING NETWORKS

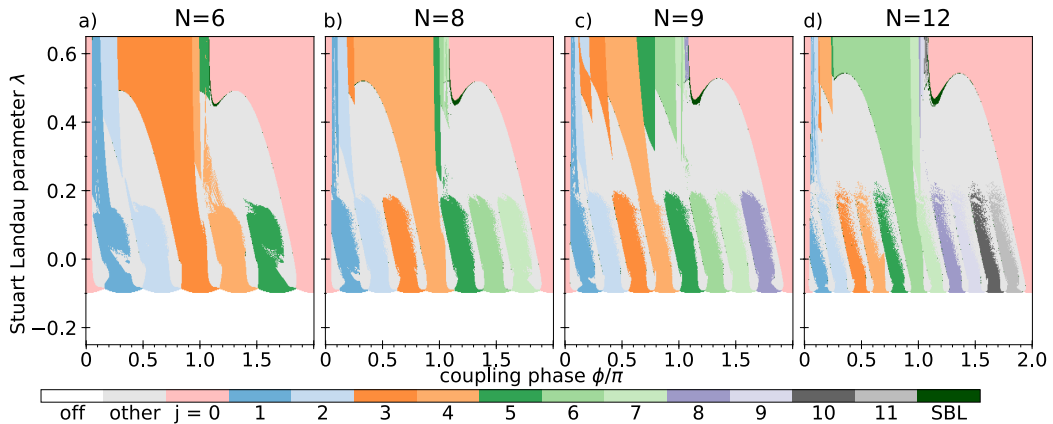


Figure 3.15: Regions of numerical obtained stability for the in-phase oscillatory solution ($j = 0$, red regions) of instantaneously coupled Stuart-Landau oscillators in large unidirectional ring as described in Eqs. (3.41) as a function of λ and coupling phase ϕ for different oscillator numbers N . White areas indicate the trivial off-state. The colours indicated in the legend with ‘ $j = 0$ ’, ‘1’ etc. are rotating wave patterns as described by Eq. (3.42) as shown for $N = 4$ in Fig. 3.10. Grey areas contain higher-order dynamics. Dark green areas contain symmetry-broken amplitude and phase-locking (SBL) states. Parameters: $\text{Re}(\gamma) = -0.1$, $\text{Im}(\gamma) = 0.5$, $\omega = 1$, $\kappa = 0.1$.

as follows from the equation of the fundamental Hopf bifurcations H_j Eq. (3.45), the line dividing rotating waves from the off states (border of white to coloured regions in Fig. 3.15) gets closer to $-\kappa$ for higher N . Third, from calculating the intersections of different generating Andronov-Hopf bifurcations H_j Eq. (3.45), it can be deduced that the regions of stability for a given rotating wave state will cover $2\pi/N$ in the coupling phase dimension for small λ (compare the width of the coloured regions for $\lambda \approx -0.1$ across the different panels of Fig. 3.15, which become thinner for higher N). This also implies that the torus bifurcations T_j cannot have an analytic form independent of the oscillator number N , as their position and shape changes with N . However, the regions of stability of individual rotating wave states seemingly asymptotically approach the same phases ϕ for large λ independent of N , compare the extent of the pink region ‘ $j=0$ ’ across the different panels of Fig. 3.15. This once again is something that could be investigated with a compound cavity mode ansatz known from laser dynamics.

When the regions of stability of the in-phase state $j = 0$ (pink regions) are compared between the unidirectional ring of size $N = 4$ of Fig. 3.12 c) and larger rings in Fig. 3.15, it is apparent that the qualitative shape is similar: A small and narrow tongue for low λ widens towards high λ . This also extends to the location of the symmetry-broken amplitude and phase-locking states. These appear along the borders of the in-phase solution for $\phi \approx 1.13\pi$ and $\lambda \approx 0.44$ (dark green regions).

This location corresponds to the second group of symmetry-broken solutions of the smaller unidirectional ring with $N = 4$ discussed in the previous section. In contrast, the first group of symmetry-broken states around $\lambda \approx 0$ for $N = 4$ discussed previously is not visible for larger N . This may in part be caused by the lower amplitude-phase coupling $\text{Im}(\gamma)$ in the study of the large rings in Fig. 3.15 compared to the highest investigated amplitude-phase coupling for the $N = 4$ case of Fig. 3.12 d).

Symmetry-broken states in large unidirectional rings

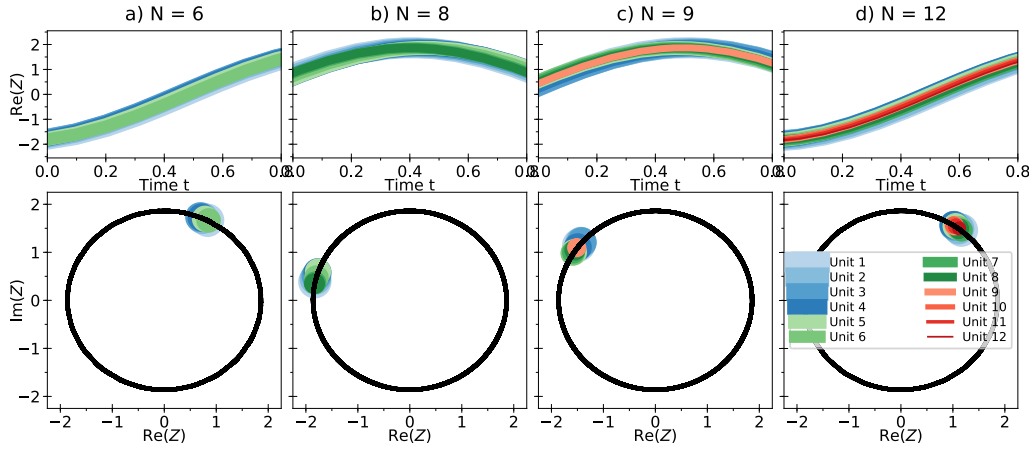


Figure 3.16: Example timeseries for the second type of symmetry-broken amplitude- and phase-locking states of the unidirectional ring for different numbers N of Stuart-Landau oscillators. The system equation is shown in Eqs. (3.41). The top panel shows a time series slice of the real part of the complex amplitude $\text{Re}(Z)$ with different colours for the different oscillators. Bottom panels show the time series (black line) and simultaneous positions (coloured filled circles) in the complex plane. Parameters: $\lambda = 0.44$, $\omega = 1$, $\text{Re}(\gamma) = -0.1$, $\text{Im}(\gamma) = 0.5$, $\phi = 1.13\pi$

Figure 3.16 shows the time-series (top) and complex plane projections of the SBL states found in Fig. 3.15 for different sized unidirectional ring networks. These types of states were found in numerical simulations for unidirectional ring networks, independent of the size of those rings. They appear to be a universally appearing pattern. The SBL states shown in Fig. 3.16 are characterized by a sudden divergence of *all phases*, which destroys the previously stable in-phase solution. If amplitude oscillations exist, they must be either very small or very slow. This is the extension of the states shown in Fig. 3.14 for $N = 4$, i.e. the second group of SBL states. In the $N = 4$ case, it was possible to study the eigenvalues analytically and the limiting bifurcation was identified as a torus bifurcation with very small imaginary part (\tilde{T} -line in Fig. 3.12 d)). A similar creation mechanism

3.3 UNIDIRECTIONAL RING NETWORKS

likely underlies the SBL states found in Fig. 3.16. As a result, the phase differences between the oscillators shown in Fig. 3.16 are relatively small, as the system is still close to the bifurcation. These symmetry-broken states quickly lose stability and it is therefore difficult to analyse them far away from the bifurcation. Fig. 3.14 for $N = 4$ showed all 4 symmetrized patterns ($j = 0, 1, 2, 3$ in panels a)-d)). Naturally, symmetrized versions for the SBL states shown in Fig. 3.16 also exist, but are omitted for brevity. For the ring of size N , $N - 1$ symmetrized SBL states exist in addition to the $j = 0$ case shown in Fig. 3.16. The additional symmetrized versions can be obtained by use of the ξ_j -translational symmetry.

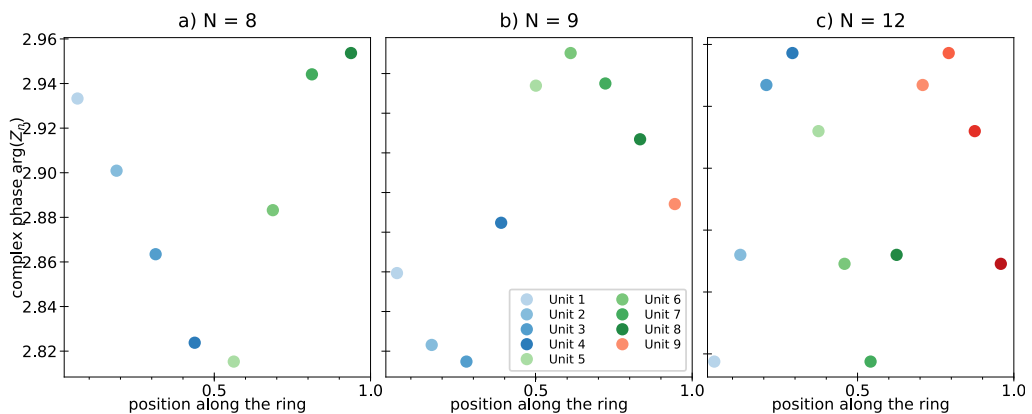


Figure 3.17: Phase representation for the second type of symmetry-broken amplitude- and phase-locking states of the unidirectional ring for different numbers N of Stuart-Landau oscillators given by Eqs. (3.41). The panels shows the phase of the complex amplitude $\arg(Z)$ for the same symmetry-broken states as Fig. 3.16. Parameters: $\lambda = 0.44$, $\omega = 1$, $\text{Re}(\gamma) = -0.1$, $\text{Im}(\gamma) = 0.5$, $\phi = 1.13\pi$

Figure 3.17 shows the SBL states for $N = 8, 9, 12$ of Fig. 3.16 in a different way: The phases of the oscillators (y-axis) are shown over the oscillator index normalized over the length of the unidirectional ring n/N (x-axis). Thus, the complicated phase-relationship between oscillators can be observed. Fig. 3.17 offers some intriguing evidence that these SBL states are created in a modulational instability. However, this cannot conclusively be proven with the numerical approach taken here. A detailed investigation, possibly including path-continuation to better understand the bifurcation scenario, is left for future investigations. A tempting hypothesis is to assume, that the SBL states shown in Fig. 3.17 will converge to a Turing-type modulational instability solution in the continuous system $N \rightarrow \infty$.

3.3.6 Unidirectional rings with delay

The final aspect of unidirectional ring networks of Stuart-Landau oscillators to be investigated will be the influence of delay. Delay can arise in many systems and has profound implications for the mathematical properties of the system, as ordinary differential equations are turned into delay-differential equations, also see Sec. 2.1.5.

The equations of motion for the unidirectional ring of Stuart-Landau oscillators with delay are given by:

$$\begin{aligned}
 \dot{Z}_0 &= (\lambda + i\omega + \gamma |Z_0|^2)Z_0 + \kappa e^{i\phi} Z_{N-1}(t - \tau), \\
 &\vdots \\
 \dot{Z}_n &= (\lambda + i\omega + \gamma |Z_n|^2)Z_n + \kappa e^{i\phi} Z_{n-1}(t - \tau), \\
 &\vdots \\
 \dot{Z}_{N-1} &= (\lambda + i\omega + \gamma |Z_{N-1}|^2)Z_{N-1} + \kappa e^{i\phi} Z_{N-2}(t - \tau),
 \end{aligned} \tag{3.50}$$

where all parameters are as in the case without delay, see Eq. 3.41. The delay time τ only appears in the coupling terms and all other oscillator amplitudes Z are instantaneous.

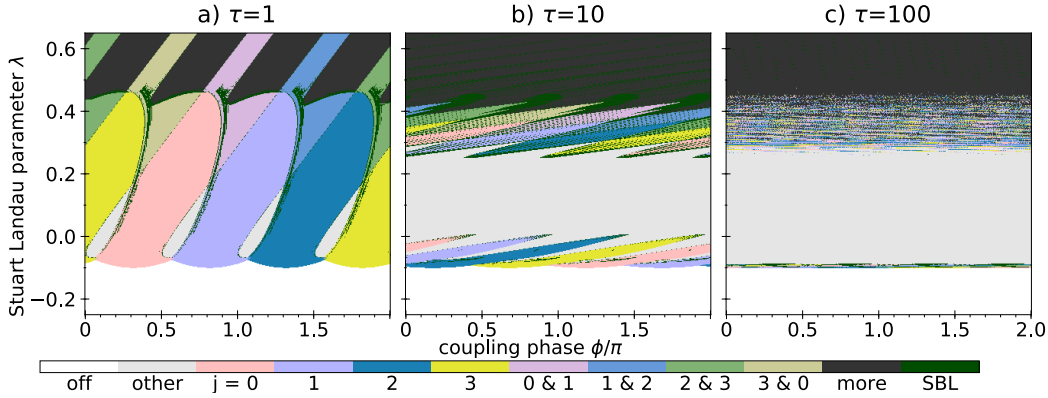


Figure 3.18: Regions of numerically obtained stability for $N = 4$ delay-coupled Stuart-Landau oscillators in a unidirectional ring as described in Eqs. (3.50) as a function of λ and coupling phase ϕ for different delay times τ . White areas indicate the trivial off-state. The colours indicated in the legend with ‘ $j = 0$ ’, ‘1’ etc. are rotating wave patterns as described by Eq. (3.42) as shown in Fig. 3.10. Labels such as ‘ $0 + 1$ ’ indicate multistability between rotating waves of different index j , with dark grey areas containing at least three simultaneously stable solutions. Light grey areas contain higher-order dynamics. Dark green areas contain symmetry-broken amplitude and phase-locking states. Parameters: $\text{Re}(\gamma) = -0.1$, $\text{Im}(\gamma) = 0.5$, $\omega = 1$, $\kappa = 0.1$, τ as atop the columns.

3.3 UNIDIRECTIONAL RING NETWORKS

Figure 3.18 shows the results for the numerical parameter scan of a unidirectional ring with delay of size $N = 4$ as given by Eqs. (3.50). The delay-time has to be compared with internal system time scales to study its effect, as delays that are much shorter than the system time scales typically have only minor effects. The characteristic time scale of the Stuart-Landau oscillator as used in this thesis, with parameter as chosen, is determined by the frequency $\omega = 1$ and nonlinearity prefactor $\text{Re}(\gamma) = -0.1$, leading to the Stuart-Landau oscillator dynamics to usually occur in 1 to 10 units of the system time. To explore different regimes of the delay time, three different delay-lengths were applied in Fig. 3.18: A short delay of $\tau = 1$ in Fig. 3.18 a), an intermediate delay of $\tau = 10$ in Fig. 3.18 b) and a large delay $\tau = 100$ in Fig. 3.18 c). The other parameters correspond to the $\text{Im}(\gamma) = 0.5$ -case of the unidirectional ring without delay in Fig. 3.12 c).

The inclusion of a delay in the coupling term has a strong influence on the system behaviour, especially with respect to the coupling phase ϕ . This influence increases with larger delay times and thus the shortest delay of $\tau = 1$ in Fig. 3.18 a) is still relatively similar to the case without delay of Fig. 3.12 c). As for the system without delay, all different rotating wave patterns (coloured regions) exist and appear for low λ in a narrow parameter tongue which widens towards higher λ . However, the position of these tongues has already changed. For example, the in-phase synchronized region ‘ $j = 0$ ’ (pink regions in Fig. 3.18) so far had always been centred around coupling phases $\phi = 0$, but are now somewhere near $\phi \approx 0.3\pi$ for $\tau = 1$. This is due to the interplay of the free frequency ω and the delay, which causes an additional phase-offset of $\omega\tau$ to accrue for the coupling term in Eqs. (3.50).

The delay also causes a higher degree of multistability to occur. This can already be seen for the case of short delay $\tau = 1$ in Fig. 3.18 a), where regions with 3 multistable rotating wave patterns exist (dark grey regions). This is in contrast to the unidirectional ring networks without delay, where never more than $N/2$ rotating waves were simultaneously stable. This was caused by the fact that the regions of stability for each rotating wave never covered more than π in the coupling phase ϕ dimension. In Fig. 3.18, the delay has extended the region of stability for rotating wave patterns for sufficiently large λ , reducing the influence of the coupling phase ϕ .

For intermediate delays of $\tau = 10$ shown in Fig. 3.18 b) the delay causes a large expansion of regions of higher-order dynamics (light grey regions). These regions occur for large ranges in λ . The different rotating wave patterns (coloured regions in Fig. 3.18 b)) are only visible for low and high λ . The phase-sensitivity of the oscillation threshold (upper border of the white regions in Fig. 3.18) also reduces with larger delay times. The individual tongues of stable rotating wave patterns

3 SYMMETRY-BREAKING IN NETWORKS

are tilted strongly for Fig. 3.18 b). Already for the intermediate delays of $\tau = 10$ there are large regions where all rotating waves are simultaneously stable.

The influence of delay grows even more extreme for the case of $\tau = 100$ in Fig. 3.18 c), where individual rotating wave states are almost entirely absent. Their regions of existence are confined to a very small parameter region extremely close to the threshold ($\lambda \approx -0.1$) and a large region where all rotating wave patterns are simultaneously stable (dark grey areas in Fig. 3.18 c) for large λ .

Over all the coupling phase becomes less important of a parameter for the study of systems with long delays. Symmetry-broken states can be found for small and intermediate delays, where their time series is similar to the previously discussed symmetry-broken amplitude- and phase-coupling states of unidirectional rings. However, in the case of large delays, SBL states are only found very close to the threshold $\lambda \approx -0.1$. Thus, in experiments with delays (and therefore also in many laser systems) it may be difficult to observe symmetry-broken amplitude- and phase-locking. Small delays, on the other hand, can be included without completely destroying the coupling phase dependence and SBL states.

3.4 Bidirectional Rings

After having studied the unidirectional ring networks in the previous section, the second type of ring network to be investigated are bidirectional rings. Here, the oscillators are coupled in both directions to their neighbours, see the sketch Fig. 3.9 b). These system, though only varying slightly in the adjacency matrix, exhibit a quite different behaviour when compared to the unidirectional rings shown in Sec. 3.3. The content of this section will follow the same structure as the previous one. The starting point will be the investigation of the symmetries of the system and the resulting 'natural solutions' of the system. Then the numerical investigations will start with the $N = 4$ case. As previously, the case of four oscillators is intimately linked with the case of two coupled Stuart-Landau oscillators, that were investigated in Sec. 3.1. The case of non-zero shear $\text{Im}(\gamma) \neq 0$ again causes the appearance of symmetry-broken amplitude- and phase-locking (SBL) states, which resemble the $N = 2$ case. However, due to the higher symmetries in the system, a richer zoo of such states is found. The case of large bidirectional rings is also investigated, revealing a different scaling behaviour from the unidirectional ring, especially for uneven numbers of oscillators. Finally, the influence of delay is shortly studied.

3.4.1 Bidirectional ring of Stuart-Landau Oscillators

The bidirectional ring of N Stuart-Landau oscillators described by their complex amplitudes Z_n with $n \in (0, N - 1)$ is given by:

$$\begin{aligned}
 \dot{Z}_0 &= (\lambda + i\omega + \gamma |Z_0|^2)Z_0 + \frac{\kappa}{2}e^{i\phi} (Z_{N-1} + Z_1), \\
 &\vdots \\
 \dot{Z}_n &= (\lambda + i\omega + \gamma |Z_n|^2)Z_n + \frac{\kappa}{2}e^{i\phi} (Z_{n-1} + Z_{n+1}), \\
 &\vdots \\
 \dot{Z}_{N-1} &= (\lambda + i\omega + \gamma |Z_{N-1}|^2)Z_{N-1} + \frac{\kappa}{2}e^{i\phi} (Z_{N-2} + Z_0),
 \end{aligned} \tag{3.51}$$

with the parameters as described in Sec. 2.3 and Sec. 3.1. The scaling of the coupling strength to $\kappa/2$ is a convenient definitions, that allows a clearer connection to be drawn to the $N = 2$ case. Additionally, now every oscillator is coupled to both of its neighbours. As for the unidirectional ring, the index starts at $n = 0$ to simplify some equations appearing later and from now all indices should be taken modulus N .

The coupling matrix that corresponds to Eqs. (3.51) contains 0 on the main diagonal (no self-feedback), 0.5 for all the terms on the sub- and superdiagonal and the top right and bottom left entry, and 0 every where else. The coupling matrix of the bidirectional ring of size N can be created from the unidirectional ring of size N by symmetrization: the coupling matrix of the unidirectional ring and its transposed version are added together and then divided by 2. For example, the coupling matrix for $N = 4$ of the bidirectional ring is given by:

$$\begin{pmatrix} 0 & 0.5 & 0 & 0.5 \\ 0.5 & 0 & 0.5 & 0 \\ 0 & 0.5 & 0 & 0.5 \\ 0.5 & 0 & 0.5 & 0 \end{pmatrix} \quad (3.52)$$

Symmetries and natural solutions of the bidirectional ring

The bidirectional ring of Eqs. (3.51) still contains the global phase freedom S_1 , which allows any global phase factor $\exp(i\theta)$ for fixed arbitrary θ to be multiplied to the Z_n , but leaves the dynamics unchanged. This is the symmetry, that is contained within all the networks of Stuart-Landau oscillators where the coupling is linear in every Z_n . Additionally, the coupling topology adds an additional symmetry: While the unidirectional ring has an overall *direction* caused by the locally directed coupling, the bidirectional ring does not. The coupling in the bidirectional ring is undirected and therefore the coupling graph and matrix are identical to their mirror images. This is not the case for the unidirectional ring. The symmetry group of the bidirectional ring of size N is the dihedral group D_n , which contains both rotations $\tilde{Z}_n \rightarrow Z_{n\pm k}$ and reflections, e.g. $\tilde{Z}_n \rightarrow Z_{-n}$. The bidirectional ring hence has a higher symmetry than the unidirectional ring: the symmetry group of the former contains all and more elements than that of the latter. This of course is no new result, but has a profound influence on the natural solutions of the system.

The 'natural' solutions of the unidirectional ring were given by the 'ponies-on-a-merry-go-round' or rotating wave patterns of index j (Eq. (3.42)):

$$Z_n(t) = e^{i(n\xi_j + \theta)} Z(t),$$

where $Z(t) = A_j \exp(i\omega_j t + \theta)$ with fixed amplitude $A_j \in \mathbb{R}$, frequency ω_j , arbitrary θ (global phase freedom) and $\xi_j = \frac{2\pi j}{N}$. These in principle also act as the natural solutions to the bidirectional ring as shown in Eqs. (3.51). However, the coupling of the bidirectional ring is more complicated. The coupling term contains both Z_{n-1} and Z_{n+1} . The phase relationship between Z_n and both coupling terms should be independent of n in any of the natural solutions (as otherwise different oscillators

along the ring would behave differently, breaking the symmetry). For the rotating wave pattern the constant phase condition can be expressed as the fraction

$$\frac{Z_{n-1} + Z_{n+1}}{Z_n} = e^{-i\xi_j} + e^{+i\xi_j}, \quad (3.53)$$

which should be constant. This is fulfilled for the bidirectional ring in the rotating wave states, so that these are solutions for Eqs. (3.51). However, the rotating wave states do not all behave the same in the bidirectional ring. Their parameter dependence differs, which can be deduced by a symmetry-abiding transformation.

In the unidirectional ring case it was possible to find the transformation given in Eq. (3.46). The transformed equations were identical in shape and parametrization to the original system of equations, which means that every rotating wave of index j could be seen as a transformed version of the in-phase synchronized solution ($j = 0$). This convenient fact no longer holds for the bidirectional ring, as the coupling cannot be transformed in the same way. In particular, the problem is that the coupling terms in Eqs. (3.51) depend on *two different* oscillators, namely Z_{n-1} and Z_{n+1} . This prevents that a transformation as general as Eq. (3.46) for the unidirectional ring can be found for the bidirectional ring.

However, a different type of symmetry-transformation can be obtained for the system of Eqs. (3.51). Assuming an even number of oscillators N , a new set of coordinates can be defined as:

$$\tilde{Z}_n = (-1)^n Z_n, \quad (3.54)$$

that is, the sign of every second oscillator is flipped. This is a subset of the transformations of the unidirectional ring shown in Eq. (3.46) with $j = N/2$. Inserting this into Eqs. (3.51) yields a new system of ODEs for the transformed coordinates:

$$\dot{\tilde{Z}}_n = (\lambda + i\omega + \gamma |\tilde{Z}_n|^2) \tilde{Z}_n + \frac{\kappa}{2} e^{i\phi} (-\tilde{Z}_{n-1} - \tilde{Z}_{n+1}), \quad (3.55)$$

which can be easily rewritten as:

$$\dot{\tilde{Z}}_n = (\lambda + i\omega + \gamma |\tilde{Z}_n|^2) \tilde{Z}_n + \frac{\kappa}{2} e^{i(\phi+\pi)} (\tilde{Z}_{n-1} + \tilde{Z}_{n+1}), \quad (3.56)$$

which is identical to the original Eqs. (3.51) except for a phase shift of π in the coupling phase ϕ . Hence, the same argument as for the unidirectional ring can be made: Any solution found in the original system of Eqs. (3.51) will have a symmetrized version, when the phase is shifted by π and the sign of every second oscillator is flipped. In particular, this means that the in-phase ($j = 0$) and anti-phase ($j = N/2$) solutions are linked as in the case of two coupled Stuart-Landau oscillators. This will be called the π -translational symmetry, as it directly

corresponds to the symmetry of the same name that was studied in the $N = 2$ case.

Fundamental Andronov-Hopf bifurcations

The rotating waves are the fundamental solutions of the bidirectional ring, and their bifurcations shall now be investigated. Inserting the rotating wave ansatz Eq. (3.42) into the bidirectional ring equation Eqs. (3.51) yields the amplitude A_j :

$$\operatorname{Re}(\gamma)|A_j|^2 = \lambda + \frac{\kappa}{2} (\cos(\phi - \xi_j) + \cos(\phi + \xi_j)). \quad (3.57)$$

As the amplitude squared $|A_j|^2$ has to be positive, Eq. (3.57) implicitly contains the generating Hopf bifurcations H_j of the rotating wave of index j for the bidirectional ring. Rearranging the right hand side of Eq. (3.57) yields:

$$\lambda_{H_j} = -\frac{\kappa}{2} (\cos(\phi - \xi_j) + \cos(\phi + \xi_j)) = -\kappa \cos(\phi) \cos(\xi_j). \quad (3.58)$$

Note, that this is a more complex equation as compared to the unidirectional ring case: It is either the sum of two cosine functions or the product. However, for the in-phase case $j = 0$, $\xi_j = 0$ and the anti-phase case $j = N/2$, $\xi_j = \pi$ Eq. (3.58) is identical to the $N = 2$ case studied in Sec. 3.1.

$$\lambda_{H_0} = -\kappa \cos(\phi), \quad (3.59)$$

$$\lambda_{H_{N/2}} = \kappa \cos(\phi). \quad (3.60)$$

Parameter scans for $N = 4$ and $\operatorname{Im}(\gamma) = 0$

To better understand the implications of the bidirectional coupling, the system of $N = 4$ oscillators will now be investigated. This system is then also compared to the unidirectional ring of $N = 4$ oscillators.

Figure 3.19 shows the two-dimensional parameter scan of the bidirectional ring as described in Eqs. (3.51) as a function of λ and coupling phase ϕ for shear $\operatorname{Im}(\gamma) = 0$. Fig. 3.19 a) combines results from four different sets of numerical simulations: Each simulation was started close (10^{-4}) to one of the 4 basic rotating wave patterns $j = 0, 1, 2, 3$. Hence, the regions indicated by the different colours in Fig. 3.19 and labelled $j = 0, 1, 2, 3$ should represent the complete region of stability of these solutions. Additionally, the trivial off-state $Z_n = 0$ is marked by the white regions. Multistability of the $j = 0$ with the $j = 2$ rotating wave is indicated by the purple regions.

Overall, the shape of the numerically obtained regions of stability shown in Fig. 3.19 a) are strikingly similar to those of two coupled Stuart-Landau oscillators

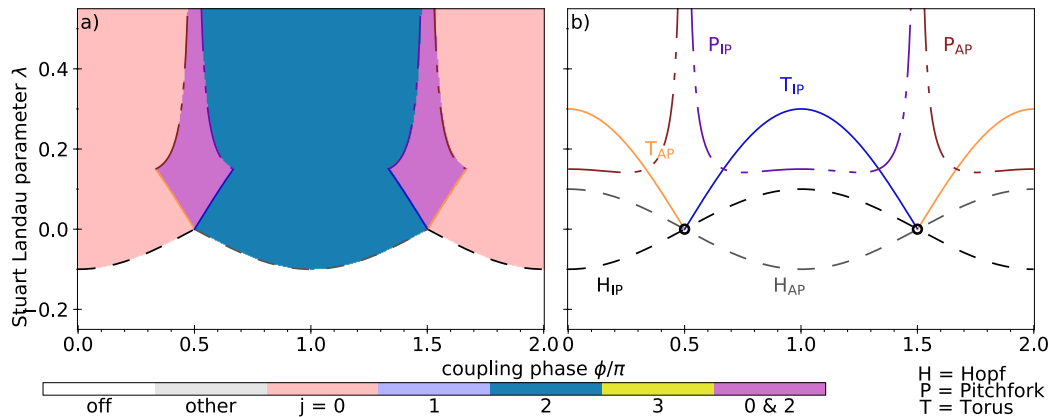


Figure 3.19: a:) Regions of numerical stability for $N = 4$ instantaneously coupled Stuart-Landau oscillators in a bidirectional ring as described in Eqs. (3.51) as a function of λ and coupling phase ϕ for shear $\text{Im}(\gamma) = 0$. White areas indicate the trivial off-state. The colours indicated in the legend with ‘ $j = 0$ ’, ‘1’ etc. are rotating wave patterns as described by Eq. (3.42). The purple regions labelled ‘ $0 + 2$ ’ indicate multistability between rotating waves of index $j = 0$ (in-phase) and $j = 2$ (anti-phase). The right panel (b) shows bifurcation lines given by Eq. (3.58) for the generating Andronov-Hopf-bifurcations of the the in-phase $j = 0$ (H_{IP} , black dashed line) and the anti-phase $j = 2$ (H_{AP} , grey dashed line) orbit. The pitchfork bifurcation (P_{IP} and P_{AP} , purple and brown lines) are given in Eq. (3.62), while the torus bifurcations torus (T_{IP} and T_{AP} , blue and orange lines) are as in Eq. (3.61). The relevant parts of the bifurcations are also reproduced and overlaid in a) with the same formatting and colour. Parameters: $\text{Re}(\gamma) = -0.1$, $\text{Im}(\gamma) = 0$, $\omega = 1$, $\kappa = 0.1$.

shown in Fig. 3.2: Only the in-phase ($j = 0$, light red regions) and anti-phase ($j = 2$, dark blue regions) synchronized solutions were found to be stable. The rotating waves of uneven index $j = 1, 3$ were never found to persist in the numerical simulations. This is in contrast to Fig. 3.11 a) for the unidirectional ring, where all the rotating waves had regions of stability with identical size and shape. The bidirectional coupling that is locally symmetrical between neighbours forces the system to collapse to either the in-phase (IP) or anti-phase (AP) state. As for the case of two coupled Stuart-Landau oscillators, the in-phase ($j = 0$, light red regions) and anti-phase ($j = 2$, dark blue regions) solutions can coexist in some regions (purple in Fig. 3.19 a)). As was the case for two coupled Stuart-Landau oscillators and for the unidirectional ring, the basic symmetry-abiding solutions cover the entire parameter plane for the case without shear ($\text{Im}(\gamma) = 0$).

The fact that only the $j = 0$ and $j = 2$ case are visible in Fig. 3.19 a) can also be explained from the perspective of their Hopf-bifurcations: When coming from low λ , only the rotating wave pattern with the lowest oscillation threshold will

become stable. Due to the more complex dependence on ξ_j and ϕ in the H_j Hopf bifurcations as shown in Eq. (3.58), only the in-phase and anti-phase rotating wave patterns can emerge from a supercritical Hopf bifurcation for even N .

Figure 3.19 b) shows analytically described bifurcation lines for the in-phase ($j = 0$, IP) and anti-phase ($j = 2$, AP) solutions. The border between the off-state (white regions in Fig. 3.19 a)) and the simple rotating wave patterns (coloured regions in Fig. 3.19 a)) is denominated by the generating Andronov-Hopf bifurcation of Eq. (3.58), labelled H_{IP} for $j = 0$ and H_{AP} for $j = 2$. These are identical to the $N = 2$ case (due to the convenient definition of the coupling term with $\kappa/2$ in Eqs. (3.51)). As was the case in Fig. 3.2 for two coupled Stuart-Landau oscillators, the Hopf bifurcations H_{AP} and H_{IP} meet at $\lambda = 0$, $\phi = \pi/2, 3\pi/2$. From these Hopf-Hopf points (black circles in Fig. 3.19 b)), two torus bifurcations are created. The in-phase torus T_{IP} and the anti-phase torus bifurcation T_{AP} are identical to the $N = 2$ case:

$$\lambda_{T(IP,AP)} = \mp 3\kappa \cos \phi, \quad (3.61)$$

which correspond to the orange and blue lines in Fig. 3.19 b). Additionally, the pitchfork bifurcations are shown as P_{IP} (purple line) for the in-phase and P_{AP} (brown line) for the anti-phase orbits in Fig. 3.19 b). These pitchfork bifurcations are not identical to the $N = 2$ case and given by:

$$\lambda_{P(IP/AP)} = \pm \frac{\kappa \operatorname{Re}(\gamma)}{2(\operatorname{Im}(\gamma) \sin \phi + \operatorname{Re}(\gamma) \cos \phi)} \pm \kappa \cos \phi, \quad (3.62)$$

which differs by a factor of 2 in the denominator. This could likely be adjusted by a different scaling of the coupling term in the bidirectional ring equation (Eqs. (3.51)), but it seems more convenient to keep the fundamental generating Andronov-Hopf bifurcations $H_{IP,AP}$ of Eq. (3.58) unchanged. The relevant parts of the bifurcation lines are reproduced also on top of the numerical results in Fig. 3.19 a). The agreement of numerics and the bifurcation lines given is perfect. As was the case for the $N = 2$ case, the in-phase and anti-phase solutions are limited by the torus and pitchfork bifurcations in different parts of the parameter plane. This is in contrast to the unidirectional ring, where only a limiting torus bifurcation was found, while a pitchfork still existed, but never limited a region of stability (the solution was already unstable when it reached the pitchfork). Conversely, the region of stability for any index j was never found to exceed π in the coupling phase ϕ -dimension for unidirectional ring (Fig. 3.12 and 3.15). In contrast, the regions of stability for the in-phase ($j = 0$) and anti-phase ($j = 2$) solutions clearly extend for more than π in the coupling phase dimension in Fig. 3.19 a) at $\lambda = 0.15$. Nevertheless, both the unidirectional ring and the bidirectional ring of size $N = 4$

show the simultaneous stability of more than one rotating wave pattern. In the case of the bidirectional ring shown in Fig. 3.19 a) this is due to the total absence of stable regions for the rotating wave solutions of index $j = 1, 3$. Note, that due to the slightly different shape that the pitchfork bifurcation given in Eq. (3.62) takes, the regions of multistability are slightly smaller for $N = 4$ shown in purple in Fig. 3.19 a), when compare to the case of $N = 2$ shown in Fig. 3.2.

In the numerical simulations, long living transients were detected for coupling phases close to $\phi = \pi/2, 3\pi/2$ and starting conditions close to $j = 1, 3$. This likely indicates that these rotating wave patterns are only barely unstable, and could therefore potentially be stabilized with a feedback control scheme [PYR92]. Furthermore, the lifetime behaviour of these transients indicate that they could potentially obtain a neutral largest eigenvalue, i.e neither be attracting (stable) nor repelling (unstable), for values exactly at $\phi = \pi/2, 3\pi/2$. However, a detailed investigation of this will have to be left for future investigations.

Parameter scans for $\text{Im}(\gamma) \neq 0$

Both for the unidirectional ring and the case of just two coupled Stuart-Landau oscillators, the amplitude-phase coupling or shear $\text{Im}(\gamma)$ played a crucial role in generating higher order dynamics, especially the symmetry-broken patterns. Figure 3.20 shows the numerically obtained regions of stability (top, colours) for all rotating waves $j = 0, 1, 2, 3$ and analytically described bifurcations (bottom, lines), and can be directly compared to the corresponding figures for the unidirectional ring (Fig. 3.12) and two coupled Stuart-Landau oscillators (Fig. 3.3). As was already the case for $\text{Im}(\gamma) = 0$, the bidirectional ring behaves more like the system of two coupled oscillators than the unidirectional ring. In particular, the rotating waves of index $j = 1$ (light blue in Fig. 3.20) and $j = 3$ (yellow regions in Fig. 3.20) are never found to be stable. Long-living transients were once again found for these states at particular coupling phases $\phi = \pi/2, 3\pi/2$.

The bifurcations defining the regions of stability behave differently to increasing shear $\text{Im}(\gamma)$ (compare the bottom row across columns in Fig. 3.20). While the generating Andronov-Hopf bifurcations (H_{IP} , black dashed line, and H_{AP} , grey dashed line) and the torus bifurcations (T_{IP} and T_{AP} , blue and orange lines) are independent of the shear $\text{Im}(\gamma)$, the pitchfork bifurcations (P_{IP} and P_{AP} , purple and brown lines in Fig. 3.20) distort and shift for $\text{Im}(\gamma) \neq 0$. This can also be seen in the analytical formulas given in Eqs. (3.58)-(3.62). With increasing shear $\text{Im}(\gamma)$, i.e. going through the columns from left to right in Fig. 3.20, this distortion of the pitchfork bifurcation once again opens up regions, where previously at least one of the rotating wave solutions was stable. These regions are mostly marked in grey in the top row of Fig. 3.20 and contain higher-order limit cycles

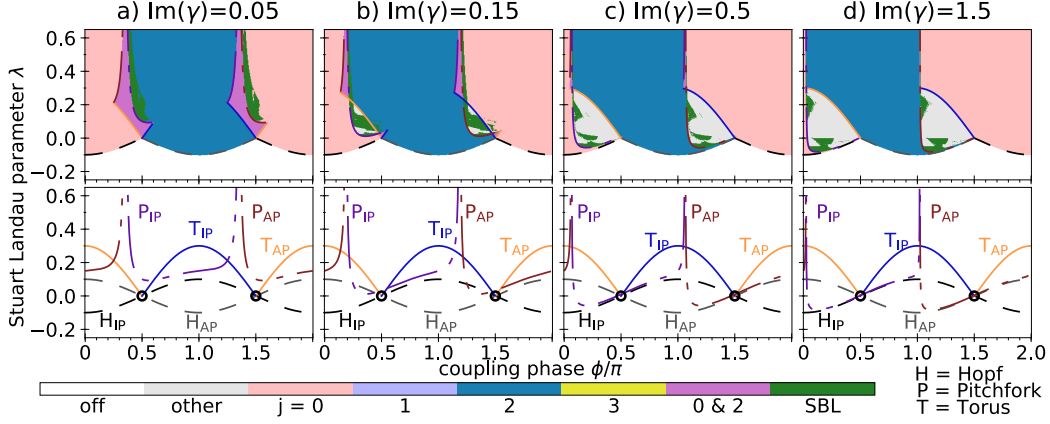


Figure 3.20: Top row: Regions of numerical stability for $N = 4$ instantaneously coupled Stuart-Landau oscillators in a bidirectional ring as described in Eqs. (3.51) as a function of λ and coupling phase ϕ with shear $\text{Im}(\gamma)$ as indicated atop the column. White areas indicate the trivial off-state. The colours indicated in the legend with ‘ $j = 0$ ’, ‘1’ etc. are rotating wave patterns as described by Eq. (3.42). The purple regions labelled ‘ $0 + 2$ ’ indicates multistability between rotating waves of index $j = 0$ (in-phase) and $j = 2$ (anti-phase). Green areas contain symmetry-broken amplitude- and phase-coupling states (SBL), potentially multistable with other solutions. Grey areas only contain higher-order solutions. The bottom row shows bifurcation lines given by Eq. (3.58) for the generating Andronov-Hopf-bifurcations of the the in-phase $j = 0$ (H_{IP} , black dashed line) and the anti-phase $j = 2$ (H_{AP} , grey dashed line) orbit. The pitchfork bifurcation (P_{IP} and P_{AP} , purple and brown lines) are given in Eq. (3.62), while the torus bifurcations torus (T_{IP} and T_{AP} , blue and orange lines) are as in Eq. (3.61). The relevant parts of the bifurcations are also reproduced and overlaid on the top with the same formatting and colour. Parameters: $\text{Re}(\gamma) = -0.1$, $\text{Im}(\gamma)$ as indicated atop the column, $\omega = 1$, $\kappa = 0.1$.

and quasi-periodic dynamics. These regions of complex dynamics grow in size with $\text{Im}(\gamma)$ but the maximum extent is limited by the asymptotic behaviour of the pitchfork bifurcations (P_{IP} and P_{AP} , purple and brown lines in Fig. 3.20) and the unchanging generating Andronov-Hopf (H_{IP} , black dashed line, and H_{AP} , grey dashed line) and torus (T_{IP} and T_{AP} , blue and orange lines) lines. Hence the grey regions, containing no stable rotating waves, shown in Fig. 3.20 d) represent almost the maximum extent they can fill. Overall, the agreement between numerics and analytics also holds for non-zero shear.

The green areas contain symmetry-broken amplitude and phase-locking (SBL) solutions. The green colour also indicates regions, where these states coexist with the in-phase or anti-phase synchronized solutions. These will be investigated in more detail in the next section.

3.4.2 Symmetry-broken solutions in the bidirectional ring with $N = 4$

Symmetry-broken amplitude and phase-locking states (SBL) were found in the case of $N = 2$ oscillators as described in Sec. 3.1.3. As a system of complex coupled oscillatory units, the bidirectional ring also contains many symmetry-broken solutions. Many of the complex, high-dimensional objects, such as high-order limit cycles and quasiperiodic torus attractors that populate the grey regions in Fig. 3.20 are in fact not adhering to all of the underlying symmetries of the bidirectional ring as discussed in Sec. 3.4.1. However, these complicated system behaviours are hard or impossible to analytically describe, and they do not offer much potential for applications. In a sense, the symmetry-breaking is just part of a more general ‘loss of simplicity’ for these states. Without a particular application or setup in mind, it is hard to justify to look at all the possible states in great detail.

The SBL states, however, are not just characterized by symmetry-breaking leading to non-trivial solutions - they are also simultaneously mathematically simple objects: Every oscillator merely performs a fixed, harmonic oscillation, i.e. $Z_n(t) = A_n \exp(i(\Omega t + \theta_n))$ with some fixed A_n and θ_n . They are therefore the most simple symmetry-broken patterns and the mathematically easiest to describe. Expressing their phase and amplitude relationship with complex numbers s_0, \dots, s_{N-1} yields:

$$s_0 Z_0 = s_1 Z_1 = \dots = s_n Z_n = \dots s_{N-1} Z_{N-1}, \quad (3.63)$$

where exactly one of the complex prefactors can be set to $s_n = 1$ without loss of generality. These types of states were already described for the unidirectional ring in Sec. 3.3.4. As outlined in Sec. 3.4.1, the unidirectional ring has a *lower* symmetry than the bidirectional ring, as the latter also contains reflections. Hence, more symmetries are available to be broken in in the bidirectional ring. On the other hand, fewer stable symmetry-abiding patterns exist: While the unidirectional ring of size $N = 4$ contained all the rotating wave patterns $j = 0, 1, 2, 3$ (see Fig. 3.11), only the in-phase $j = 0$ and anti-phase $j = 2$ was found to be stable in the bidirectional ring (see Fig. 3.19). It is therefore not clear *a priori*, which of the topologies will be more prone to showing SBL states. The comparison of numerical 2D-parameter scans shown in Fig. 3.12 for the unidirectional and in Fig. 3.20 for the bidirectional ring reveals, that (at least for the parameters chosen), SBL states are a lot more prevalent in the bidirectional rings. This will especially be true, for larger bidirectional ring networks investigated later.

The green regions found in Fig. 3.20 that indicate symmetry-broken amplitude- and phase-locking contain two fundamentally different sets of SBL solutions. Time series slices for the SBL states found for $\text{Im}(\gamma) = 0.15$ are shown in Fig. 3.21. Those

3 SYMMETRY-BREAKING IN NETWORKS

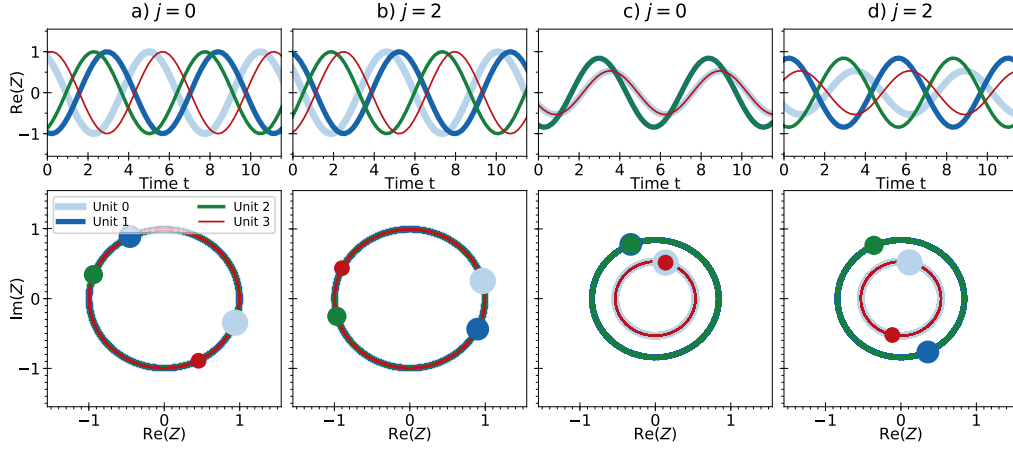


Figure 3.21: Example timeseries for the symmetry-broken amplitude- and phase-locking states of the bidirectional ring of $N = 4$ Stuart-Landau oscillators as defined by Eqs. (3.51). The top panels show a time series slice of the real part of the complex amplitude $\text{Re}(Z)$ with different colours for the different oscillators. Bottom panels show the time series (coloured lines) and simultaneous positions (coloured filled circles) projected into the complex plane. Parameters: $\lambda = 0.10, 0.10, 0.02, 0.02$, $\omega = 1$, $\text{Re}(\gamma) = -0.1$, $\text{Im}(\gamma) = 0.15$, $\phi = 0.35\pi, 1.35\pi, 0.35\pi, 1.35\pi$

for the other non-zero shear cases shown in Fig. 3.20 all fall into one of these two categories.

Figure 3.21 shows both a time-series slice of the real part (top) and a projection in the complex plane (bottom) coloured differently for the different oscillators, and can therefore directly be compared to the SBL states found in the unidirectional rings shown in Fig. 3.13 and Fig. 3.14. Figure 3.21 shows one type of SBL state for the bidirectional ring in panels a) and b), and a different type of SBL states in panels c) and d). The first major difference between the unidirectional and bidirectional ring is once again based on its symmetry: While every set of SBL solutions in the unidirectional ring can be translated via the ξ_j -translational symmetry to every index of rotating waves j , symmetry-broken states only have one other related SBL state under the π -translational symmetry. In the bidirectional ring, one SBL state of each group is related to the in-phase $j = 0$ rotating wave pattern (Fig. 3.21 a) and c)) and one to the anti-phase $j = 2$ rotating wave pattern (Fig. 3.21 b) and d)). Thus overall, the unidirectional ring for $N = 4$ has 4 variants of each SBL, see Fig. 3.14 and Fig. 3.13, while the bidirectional ring only has two. This scales to N variants of every SBL for large unidirectional rings, while the SBL states always only come in pairs even in larger bidirectional rings.

Figure 3.21 a) shows a symmetry-broken amplitude and phase-locking states where the oscillators in the bidirectional ring exhibit 4 different phases, while they

3.4 BIDIRECTIONAL RINGS

all share the same amplitude. This is similar to the SBL states shown in Fig. 3.14, however, here in the case of the bidirectional ring phases are much further apart. Additionally, Fig. 3.21 a) also shows that two oscillators are in anti-phase with each other, e.g. $Z_1 = -Z_3$ (green and light blue in Fig. 3.21 a)). In contrast, the states found for the unidirectional ring contained no such reflection symmetries. The SBL state shown in Fig. 3.21 a) exists in the parameter space inside the regions of higher order dynamics (grey regions in Fig. 3.20 b)) and along the upper parts of the in-phase pitchfork (purple line P_{IP} in Fig. 3.20 b)).

As mentioned, for every symmetry-broken amplitude- and phase-locking state in the bidirectional ring a single symmetrized version exists (not counting rotationally relabelling oscillators). The symmetrized version can be obtained by applying the π -translational symmetry and the image under this symmetry of the SBL state shown in Fig. 3.21 a) is shown Fig. 3.21 b). Note the different order of the oscillators in the complex plane projection (bottom panels) compared to panel a): While in Fig. 3.21 a) the oscillators go in anti-clockwise order around in the complex plane, in Fig. 3.21 b) oscillators are sorted clock-wise in ascending index n . The SBL state in Fig. 3.21 a) is found for $\phi = 0.35\pi$, while panel b) is for a coupling phase of $\phi = 1.35\pi$. Both Fig. 3.21 a) and b) share all other parameters. They may look very similar, but if evaluated carefully, the original SBL state and its symmetrized version are discernible by their unique properties. It is important to stress, that there exists no set of initial conditions at the parameters of Fig. 3.21 a) that could lead to an oscillator order as shown in Fig. 3.21 b): The ‘chirality’ of ascending node number when counting anti-clockwise in the complex plane around the origin in the bottom of Fig. 3.21 a) is never reversed, no matter the initial conditions used. This is fascinating, because the *equivariant branching lemma* does not even imply the existence of the SBL state shown in Fig. 3.21 b). This is a more subtle result of the π -translational symmetry between AP and IP states. The preceding considerations once again exemplify how subtle many aspects of symmetry-breaking in highly symmetric systems can be, and therefore also how valuable the SBL states found in Stuart-Landau oscillator networks are, as they offer a very clean and neat example.

Figure 3.21 c) and d) show the second kind of symmetry-broken amplitude- and phase-locking states (SBL) for the bidirectional ring of size $N = 4$, which is found in the green regions of Fig. 3.20 b) for $\phi = 0.35\pi, 1.35\pi$ and $\lambda = 0.02$. This SBL state therefore lies in the exact parameter position that corresponds to the SBL states found for two coupled Stuart-Landau oscillators $N = 2$ as discussed in Sec. 3.1 and shown in Fig. 3.1 c). In particular, it is found along the regions in Fig. 3.20 b) close to the in-phase and anti-phase pitchfork bifurcations (P_{IP} and P_{AP} in Fig. 3.20 b)). These were already identified with creating symmetry-broken amplitude- and phase-locking states in the case of two oscillators (see also

Ref. [ROE18]). Accordingly, the states shown in Fig. 3.21 c) and d) are exact analogues of the original SBL states found for two oscillators in Fig. 3.1 c): Two clusters are formed in Fig. 3.21 c) with a non-trivial amplitude and phase-relationship between the clusters. Presupposing the formation of these clusters and inserting the ansatz $Z_0 = Z_2$ and $Z_1 = Z_3$ into Eqs. (3.51) directly recovers the equations for two coupled Stuart-Landau oscillators. The stability of these states given the clusters therefore is identical to the analytical calculations used for the $N = 2$ case. In addition, for larger bidirectional ring the clusters also have to be stable internally, which requires an analysis of the transverse stability. This is left for future investigations, as the details will certainly be more subtle still, considering that the pitchfork bifurcations are not identical. Notably, every large bidirectional ring with even number of oscillators can be reduced to the equations for just two coupled Stuart-Landau oscillator, if it is assumed that all oscillators with even index form one cluster, and oscillators with uneven index the other.

The SBL state shown in Figure 3.21 d) may seem less symmetrical at first, in particular when looking at the time series of the real part (top panel). Nevertheless, it is merely a symmetrized version of Fig. 3.21 c) and obtained by shifting the coupling phase ϕ by π , which yields a state where the sign of every second oscillator amplitude Z_n is flipped (cf. the transformation Eq. (3.54)).

3.4.3 Large bidirectional rings

Next, the focus will be on larger bidirectional ring networks, where the scaling behaviour of the different states discussed in the previous section will become apparent. This parallels the investigations for unidirectional rings of large N shown in Sec. 3.3.5.

Figure 3.22 shows 2D-parameter scans in the plane of coupling phase ϕ and λ for large bidirectional rings as given by Eqs. (3.51) for a shear of $\text{Im}(\gamma) = 0.5$ and number of oscillators as written atop the columns. As was done for the unidirectional ring, here Fig. 3.22 only represents the results of one numerical simulation that was started close to the in-phase synchronized state. Hence, only the red regions in Fig. 3.22 adequately represent the full extent of stability for $j = 0$, while all other solutions are sampled less reliably. This is done, because the high number of oscillators and potentially symmetrized solutions would make the numerical effort too high.

As can be seen in Fig. 3.22, the regions of stability of the in-phase synchronized solution $j = 0$ (pink regions in Fig. 3.22) are almost identical to those of the two oscillator case (Fig. 3.3) and the case of a bidirectional ring of size $N = 4$ in Fig. 3.20. The bottom row of Fig. 3.22 shows the limiting bifurcations for the in-phase (IP, $j = 0$) and anti-phase (AP, $j = N/2$) oscillations. The generating Andronov-Hopf

bifurcations of the in-phase $j = 0$ (H_{IP} , black dashed line) and the anti-phase $j = N/2$ (H_{AP} , grey dashed line) follow Eq. (3.58). Hence, the Hopf-Hopf points have not moved (black circles in Fig. 3.22). The torus bifurcations (orange and blue lines in Fig. 3.22) are also independent of N as given in Eq. (3.61). However, the pitchfork bifurcations (P_{IP} and P_{AP} , purple and brown lines in Fig. 3.22) apparently depend on N . An explicit analytic formula has not yet been derived, but an approximation was estimated from the numerical simulations:

$$\lambda_{P(IP/AP,N)} \approx \pm \frac{\kappa \operatorname{Re}(\gamma)}{N (\operatorname{Im}(\gamma) \sin \phi + \operatorname{Re}(\gamma) \cos \phi)} \pm \kappa \cos \phi, \quad (3.64)$$

The results of the numerical simulations shown in Fig. 3.22 can be divided into two classes: while the even numbers $N = 6$ (a), $N = 8$ (b) and $N = 12$ (d) behave qualitatively similarly, the odd numbered $N = 9$ of Fig. 3.22 c) exhibits a different stability landscape. For the even-numbered bidirectional ring networks shown in Fig. 3.22 a), b) and d), the numerical simulations essentially converge to 4 major solutions: First, the trivial off-state marked in white in Fig. 3.22 is once again apparent for small λ as given by the generating Andronov-Hopf bifurcations of the in-phase and anti-phase solutions (H_{IP} , black dashed line) and the anti-phase $j = 2$ (H_{AP} , grey dashed line) as given by Eq. (3.58). Second, the pink regions indicate the in-phase synchronized solutions, that are found for parameters that are close to those of smaller bidirectional rings and the case of two Stuart-Landau oscillators, with the exception of the limiting pitchfork bifurcations (P_{IP} and P_{AP} , purple and brown lines in Fig. 3.22) that shift with N . For the bidirectional rings with even number of oscillators, a second type of rotating wave pattern is also strongly present, namely the one that corresponds to the anti-phase pattern $j = N/2$, e.g. $j = 3$ (orange regions) in $N = 6$ in Fig. 3.22 a). The shape of their stability region also closely matches the one that can be inferred by looking at the limiting bifurcations. Additionally, due to the symmetry that is outlined by the transformation of the bidirectional ring equation system in Eq. (3.54), the anti-phase and in-phase regions have to match in size and shape and only differ in the coupling phase ϕ by a phase-shift of π . This is almost completely confirmed by the numerical simulations, despite not being explicitly tuned to find the full extent of the anti-phase regions. Finally, the grey regions in Fig. 3.22 once again contain higher order dynamics, as was already previously the case for the unidirectional ring and the system of two coupled Stuart-Landau oscillators. The even-numbered large bidirectional rings thus are very closely linked to the case of two coupled Stuart-Landau oscillators.

However, the case of an uneven number of oscillators in the bidirectional ring as shown in Fig. 3.22 c) for $N = 9$ is worthy of a more detailed study: Here, no anti-phase pattern can exist as $j = N/2$ is not an integer and therefore not a solution

of the bidirectional Stuart-Landau ring equations Eqs. (3.51). Interestingly, it appears from viewing Fig. 3.22 c) near coupling phases $\phi = 0.6\pi$, that the system compensates this by a multistability between the closest 'approximation' of such an anti-phase pattern, i.e. $j = N/2 \pm 0.5$, which turns into $j = 4, 5$ for $N = 9$. The speckled features (orange and green dots in Fig. 3.22 c)) here are a result of the non-aligned initial condition, that will lead to the system randomly converging to one of the two stable states and hence is very likely an indicator of multistability between both states. Also noteworthy for $N = 9$ is the fact, that because there no longer is a true anti-phase pattern $j = N/2$ for odd numbers of oscillators, the anti-phase Andronov-Hopf bifurcations (H_{AP} , grey dashed line in Fig. 3.22 c)) is no longer the boundary to the off-solution. The more accurate formula given in Eq. (3.58) has to be used. Odd-numbered bidirectional rings therefore behave fundamentally different. This is different from the case of unidirectional rings, where the number of oscillators could be even or odd without major changes.

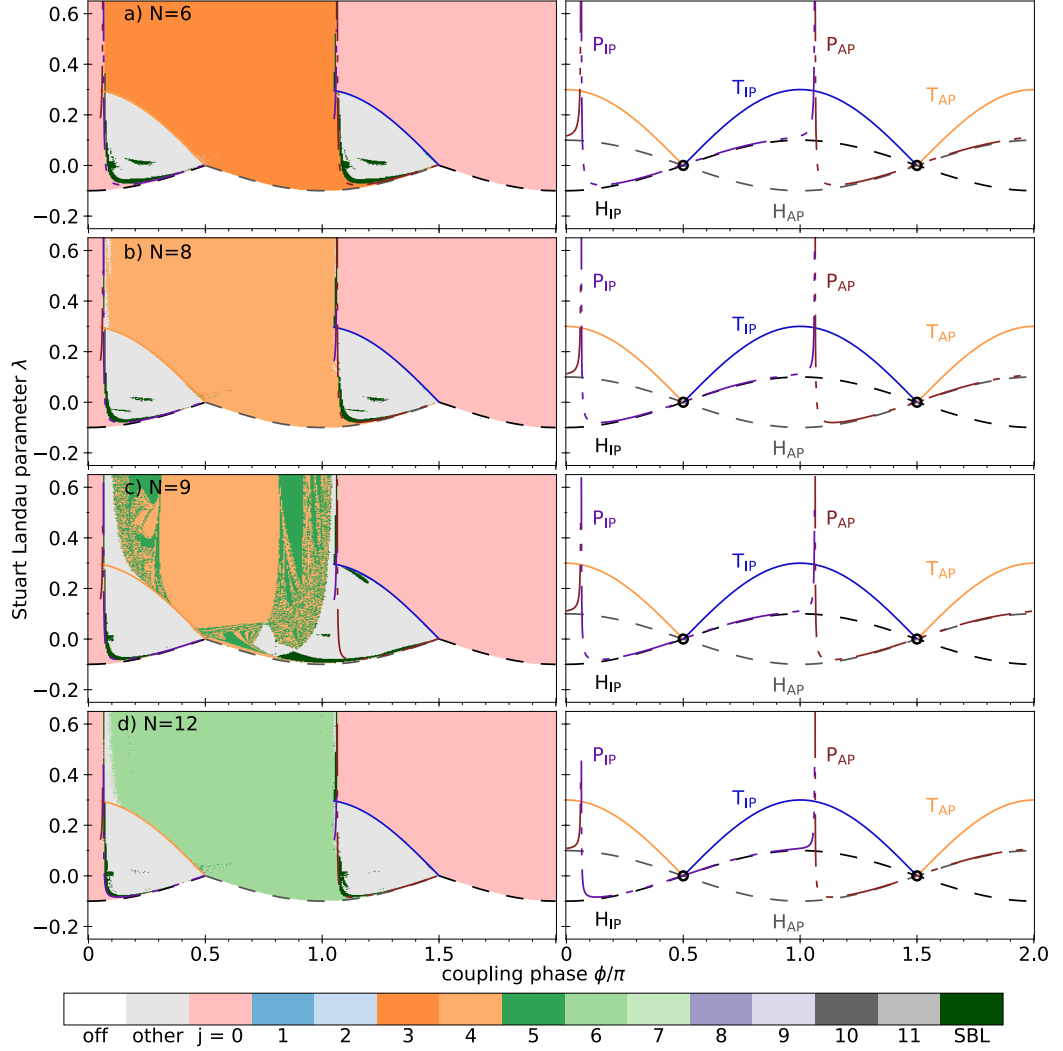


Figure 3.22: Top row: Regions of numerical obtained stability for the in-phase oscillatory solution ($j = 0$, red regions) of instantaneously coupled Stuart-Landau oscillators in large bidirectional ring as described in Eqs. (3.51) as a function of λ and coupling phase ϕ for different oscillator numbers N . White areas indicate the trivial off-state. The colours indicated in the legend with ‘ $j = 0$ ’, ‘1’ etc. are rotating wave patterns as described by Eq. (3.42). Grey areas contain higher-order dynamics. Dark green areas contain symmetry-broken amplitude and phase-locking (SBL) states. The bottom row shows bifurcation lines given by Eq. (3.58) for the generating Andronov-Hopf-bifurcations of the the in-phase $j = 0$ (H_{IP} , black dashed line) and the anti-phase $j = N/2$ (H_{AP} , grey dashed line) orbit. The pitchfork bifurcation (P_{IP} and P_{AP} , purple and brown lines) are given in Eq. (3.64), while the torus bifurcations torus (T_{IP} and T_{AP} , blue and orange lines) are as in Eq. (3.61). The relevant parts of the bifurcations are also reproduced and overlaid on the top with the same formatting and colour. Parameters: $\text{Re}(\gamma) = -0.1$, $\text{Im}(\gamma) = 0.5$, $\omega = 1$, $\kappa = 0.1$.

Symmetry-broken solutions in large bidirectional rings

The regions marked in dark green in Fig. 3.22 contain symmetry-broken amplitude and phase-locking (SBL) solutions. For the bidirectional ring of size N , these states appear in different regions, sometimes close to one of the limiting pitchfork bifurcations, and other times deep inside the regions of higher order dynamics (grey regions in Fig. 3.22). Because the variety of SBL states increases drastically for large bidirectional rings, this section will restrict itself to a few paradigmatic examples of such states. To adequately predict and define all *possible* SBL states for an arbitrarily large bidirectional ring is very much an open problem. The use of equivariance theory of mathematics will likely yield some insights into the zoo of SBL states that is found here, but must be left for future investigations.

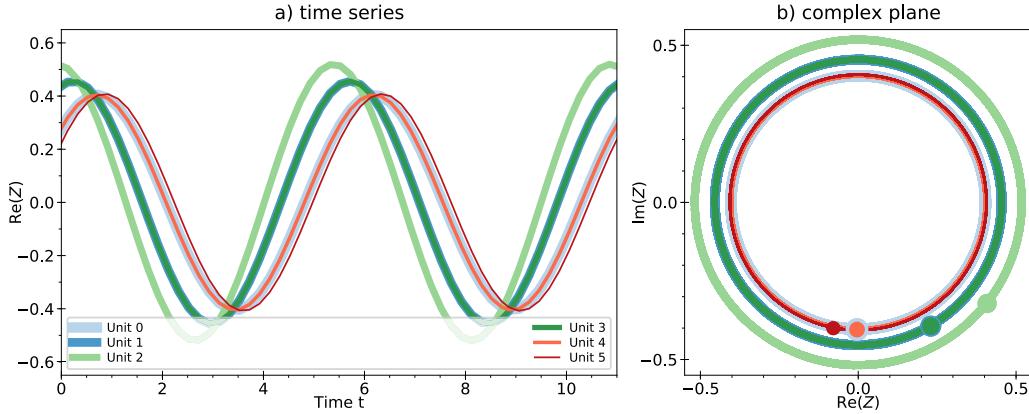


Figure 3.23: Example timeseries for the symmetry-broken amplitude- and phase-locking states of the bidirectional ring of $N = 6$ Stuart-Landau oscillators as defined by Eqs. (3.51). a): time series slice of the real part of the complex amplitude $\text{Re}(Z)$ with different colours for the different oscillators. b): time-trace (coloured lines) and simultaneous positions (coloured filled circles) for the same timeseries in the complex plane. The symmetrized version according to Eq. (3.54) is shown in Figure 3.24. Parameters: $\lambda = -0.06$, $\omega = 1$, $\text{Re}(\gamma) = -0.1$, $\text{Im}(\gamma) = 0.5$, $\phi = 0.16\pi$

Figure 3.23 shows an example timeseries of an SBL state for $N = 6$. The clustering, symmetry-breaking and phase relationship becomes more complex with larger number of oscillators N , which is most apparent when looking at the limit cycle representation in Fig. 3.23 b). The oscillators have formed 4 different amplitude clusters, of which two are of trivial size. In particular, $Z_3 = Z_1$ and $Z_0 = Z_4$, while Z_2 and Z_5 are solitary. This is a type of SBL state that has not been described in this thesis before, as so far clusters were always of the same size. The creation mechanism for this state and the underlying bifurcation scenario is likely to be complex, and is potentially linked to $j = 2$ or $j = 4$ rotational wave states, which

would naturally lead to 3 clusters of size 2 for $N = 6$. However, this is only a hypothesis and would need to be investigated with dedicated bifurcation analysis software such as AUTO. It is useful to describe the state portrayed in Fig. 3.23 with a string that encodes the amplitudes of the clusters: Let a be the smallest amplitude and d the largest, then going along the ring starting from oscillator $n = 0$ to $n = N_1$ the amplitudes read as ‘acdcab’. Hence, this pattern is characterized by each solitary oscillator being surrounded by both oscillators from the same cluster, while oscillators in the non-trivial clusters are surrounded by neighbours that exhibit different amplitudes. In Fig. 3.23 this means that the solitary oscillator $n = 5$ is neighbouring $n = 0$ and $n = 4$, which exhibit the same amplitude $Z_4 = Z_0$. Similarly, $n = 2$ is surrounded by $Z_3 = Z_1$. Due to this fact, the solution in Fig. 3.23 still is mirror-symmetric for reflections centered on $n = 5$ or $n = 2$, but is no longer rotationally symmetric with respect to the symmetry group \mathbb{Z}_n . This is another case, where in coupled Stuart-Landau oscillator systems, states can be found that break some symmetries, but not others.

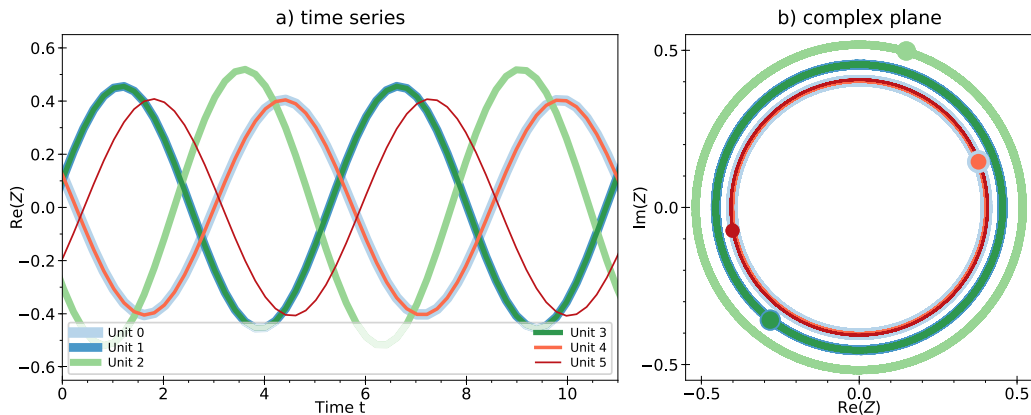


Figure 3.24: Example timeseries for the symmetry-broken amplitude- and phase-locking states of the bidirectional ring of $N = 6$ Stuart-Landau oscillators as defined by Eqs. (3.51). a): time series slice of the real part of the complex amplitude $\text{Re}(Z)$ with different colours for the different oscillators. b): time-trace (coloured lines) and simultaneous positions (coloured filled circles) for the same timeseries in the complex plane. This is the symmetrized version of Figure 3.23 according to Eq. (3.54). Parameters: $\lambda = -0.06$, $\omega = 1$, $\text{Re}(\gamma) = -0.1$, $\text{Im}(\gamma) = 0.5$, $\phi = 1.16\pi$

Figure 3.23 no longer exhibits any recognizable features of either the in-phase ($j = 0$) or anti-phase ($j = 3$ because $N = 6$) synchronized solutions. Nevertheless, the transformation according to Eq. (3.54) that describes the π -translational symmetry also works for such SBL states. A corresponding symmetrized version where the sign of every second oscillator is flipped, if the coupling phase is shifted by π can therefore be found. This is shown in Fig. 3.24. The usefulness of the

3 SYMMETRY-BREAKING IN NETWORKS

mathematical understanding of the system symmetries is visualized with this example, because when the system grows larger the relationship between different SBL states becomes more complex and harder to understand intuitively.

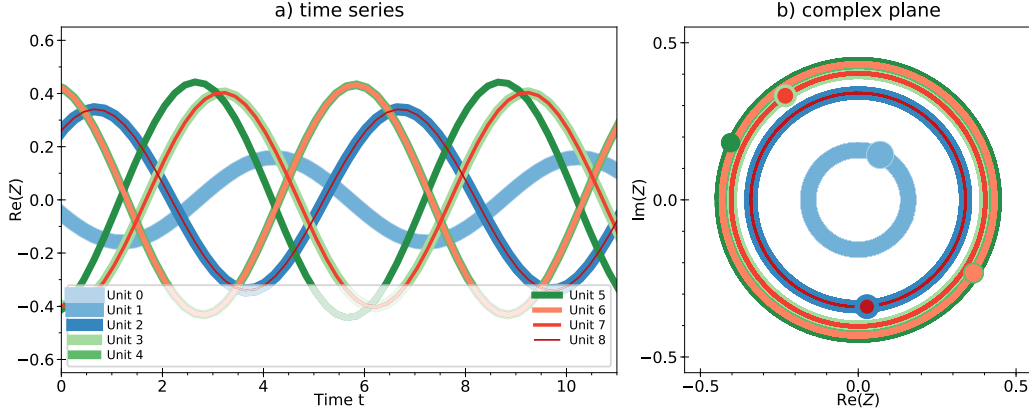


Figure 3.25: Example timeseries for the symmetry-broken amplitude- and phase-locking states of the bidirectional ring of $N = 9$ Stuart-Landau oscillators as defined by Eqs. (3.51). a): time series slice of the real part of the complex amplitude $\text{Re}(Z)$ with different colours for the different oscillators. b): time-trace (coloured lines) and simultaneous positions (coloured filled circles) for the same timeseries in the complex plane. Parameters: $\lambda = -0.06$, $\omega = 1$, $\text{Re}(\gamma) = -0.1$, $\text{Im}(\gamma) = 0.5$, $\phi = 0.85\pi$

Next, an SBL state for a bidirectional ring with odd number N of oscillators shall be studied. Figure 3.25 shows a SBL state for $N = 9$. This is relevant, because the bifurcation landscape for odd numbers of oscillators N is different than for even numbers in bidirectional ring networks, as can be seen in the two-dimensional parameter scan of Fig. 3.22. As for the SBL example for $N = 6$ shown in Fig. 3.23, the system mostly consists of clusters of size 2. However, in contrast to the $N = 6$ case, here in Fig. 3.25 for $N = 9$, only a single oscillator is unpaired (dark green, $n = 5$). Using the same system of encoding the amplitude with letters, the SBL state in Fig. 3.25 can be described (starting from $n = 1$) as 'abcdedcba'. Hence, the system is symmetric around the unpaired oscillator $n = 5$, with oscillators that have the same distance from $n = 5$ along the ring sharing the same amplitude and phase. Note, that because $N = 9$, i.e. there is an odd numbers of oscillators, the symmetry-transformation of the bidirectional ring according to Eq. (3.54) cannot be applied: Flipping the sign of every second oscillator is not well-defined. Thus, the SBL state shown in Fig. 3.25 does not have a symmetrized version under the π -translational symmetry, as do none of the states found for $N = 9$.

Figure 3.26 shows another peculiar type of symmetry-broken amplitude- and phase-locking state for $N = 9$. There, the system exhibits 3 clusters that each share the amplitude, but within the cluster are exactly $2\pi/3$ apart in phase (see

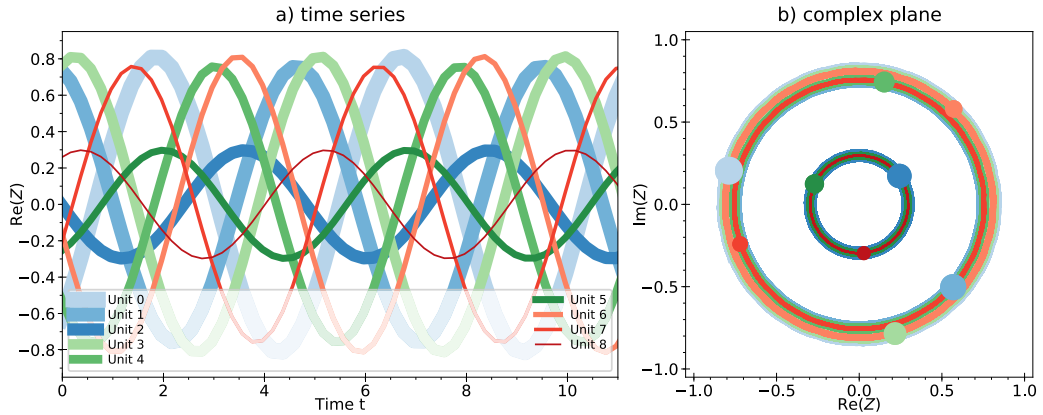


Figure 3.26: Example timeseries for the symmetry-broken amplitude- and phase-locking states of the bidirectional ring of $N = 9$ Stuart-Landau oscillators as defined by Eqs. (3.51). a): time series slice of the real part of the complex amplitude $\text{Re}(Z)$ with different colours for the different oscillators. b): time-trace (coloured lines) and simultaneous positions (coloured filled circles) for the same timeseries in the complex plane. Parameters: $\lambda = 0.015$, $\omega = 1$, $\text{Re}(\gamma) = -0.1$, $\text{Im}(\gamma) = 0.5$, $\phi = 1.03\pi$

Fig. 3.26 b) for the complex plane projection). The amplitude can be encoded as ‘cbacbacba’. This state therefore is in essence a combination of three rotating wave patterns or ‘ponies’. Each oscillator is adjacent to the other two clusters and does not directly connect to its own cluster. It breaks some of the system symmetries but not all. As was the case for Fig. 3.25, the SBL state shown in Fig. 3.26 does not have a symmetrized version.

Symmetry-broken solutions based on anti-symmetry

Figure 3.27 shows a final type of qualitatively different SBL states for the ring of bidirectionally coupled Stuart-Landau oscillators as given by Eqs. (3.51) of size $N = 9$. Like in Fig. 3.25 this state contains 4 amplitude clusters of size 2. However, the most significant difference to Fig. 3.25 is that the solitary oscillator $n = 0$ (light blue in Fig. 3.27) exhibits no amplitude $Z_0 = 0$. Additionally, the phases of the oscillators within a cluster are anti-phase, e.g. $Z_1 = -Z_8$ (blue and dark red in Fig. 3.27), where they were in-phase before. In the complex plane picture shown in Fig. 3.27 this SBL state therefore almost looks like a planetary system. However, if this projection was turned into video, it would become apparent that all oscillators share the same phase velocity (as their phases are locked), unlike the different angular velocity of planets as demanded by Kepler’s second law and conservation of angular momentum.

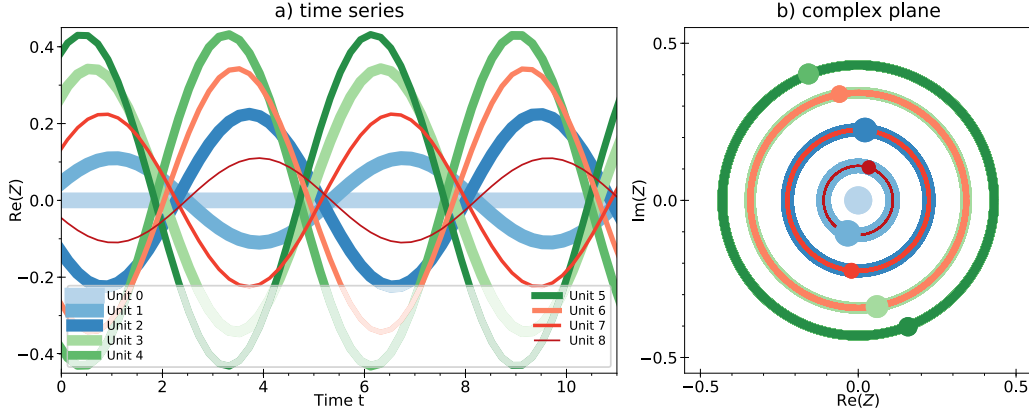


Figure 3.27: Example timeseries for the symmetry-broken amplitude- and phase-locking states of the bidirectional ring of $N = 9$ Stuart-Landau oscillators as defined by Eqs. (3.51). a): time series slice of the real part of the complex amplitude $\text{Re}(Z)$ with different colours for the different oscillators. b): time-trace (coloured lines) and simultaneous positions (coloured filled circles) for the same timeseries in the complex plane. Parameters: $\lambda = -0.04$, $\omega = 1$, $\text{Re}(\gamma) = -0.1$, $\text{Im}(\gamma) = 0.5$, $\phi = 1.3\pi$

The type of SBL states are shown in Fig. 3.27 can also be found for larger or smaller states, in particular a similar state also exists for $N = 3$ (not shown). The fact that oscillators are anti-phase within the clusters of same amplitude can easily be deduced from Eqs. (3.51): Suppose, that $Z_n = 0$ is the oscillator with no amplitude, then the corresponding ODE reads (from Eqs. (3.51)):

$$\dot{Z}_n = \frac{\kappa}{2} e^{i\phi} (Z_{n-1} + Z_{n+1}), \quad (3.65)$$

which directly translates to $Z_{n-1} = -Z_{n+1}$ if $\dot{Z}_n = 0$ is demanded. Thus, *given that* one of the oscillators has no amplitude, its two neighbours will exhibit the same amplitude and be anti-phase. Inserting this into the equations for the oscillators $n + 1$ and $n - 1$ yields:

$$\dot{Z}_{n-1} = (\lambda + i\omega + \gamma |Z_{n-1}|^2) Z_{n-1} + \frac{\kappa}{2} e^{i\phi} (Z_{n-2}), \quad (3.66)$$

$$\dot{Z}_{n+1} = (\lambda + i\omega + \gamma |Z_{n+1}|^2) Z_{n+1} + \frac{\kappa}{2} e^{i\phi} (Z_{n+2}). \quad (3.67)$$

Because $Z_{n-1} = -Z_{n+1}$ for all times, this also implies that $\dot{Z}_{n-1} = -\dot{Z}_{n+1}$ and thus $\dot{Z}_{n-1} + \dot{Z}_{n+1} = 0$ which when calculated yields the condition $Z_{n+2} = Z_{n-2}$. The same argument can then also be used for $Z_{n\pm 3}$ and so forth. Thus, all oscillator phases are mirrored or anti-phase, when one oscillator has zero amplitude $Z_n = 0$. This is what happens for $N = 9$ in Fig. 3.27, where it is most easily seen in the complex plane in panel b). This ‘anti-phase mirror rule’ also implies that a

bidirectional ring network with even number of oscillators would have to contain at least two zeros, as otherwise the condition that $Z_{n+k} = -Z_{n-k}$ is not fulfilled for all k . However, such a state was never found to be stable in the numerical simulations so far.

Overall, the bidirectional ring networks show a much larger variety of symmetry-broken amplitude and phase-locking states. This is especially interesting under the consideration, that a bidirectional ring seems much more natural than a unidirectional ring: Most interactions in nature are reciprocal and thus an undirected adjacency matrix seems more easily realised in reality. The bidirectional ring can also be seen as an approximation of diffusive coupling [HAK92]. What kind of state corresponds to a symmetry-broken amplitude- and phase-coupling in the continuous limit $N \rightarrow \infty$ is an open questions. In particular, this is also interesting from the perspective of different types of SBL states and their scaling behaviour. Of course, it is entirely possible that SBL states will not exist at all in the continuous limit, as the coupling strength κ is typically scaled inversely with the system size. A detailed investigation of these scaling patterns is left for the future.

3.4.4 Bidirectional rings with delay

The final aspect of bidirectional ring networks of Stuart-Landau oscillators to be investigated here will be the influence of delay, as was done for the unidirectional case in Sec. 3.3.6.

The equations of motion for the bidirectional ring of Stuart-Landau oscillators with delay are given by:

$$\begin{aligned}
 \dot{Z}_0 &= (\lambda + i\omega + \gamma |Z_0|^2)Z_0 + \frac{\kappa}{2}e^{i\phi} (Z_{N-1}(t - \tau) + Z_1(t - \tau)), \\
 &\vdots \\
 \dot{Z}_n &= (\lambda + i\omega + \gamma |Z_n|^2)Z_n + \frac{\kappa}{2}e^{i\phi} (Z_{n-1}(t - \tau) + Z_{n+1}(t - \tau)), \\
 &\vdots \\
 \dot{Z}_{N-1} &= (\lambda + i\omega + \gamma |Z_{N-1}|^2)Z_{N-1} + \frac{\kappa}{2}e^{i\phi} (Z_{N-2}(t - \tau) + Z_0(t - \tau)),
 \end{aligned} \tag{3.68}$$

where all parameters are as in the case without delay, see Eq. 3.51. The delay time τ only appears in the coupling terms and all other oscillator amplitudes Z are instantaneous. The case of $N = 4$ will now be studied.

Figure 3.28 shows the influence of the delay time τ on the two-dimensional parameter scans for the bidirectional ring of delay-coupled Stuart-Landau oscillators as given by Eqs. (3.68). The pink coloured regions show stable in-phase solutions $Z_0 = Z_1 = Z_2 = Z_3$, blue regions stable anti-phase rotating waves $j = 2$ with

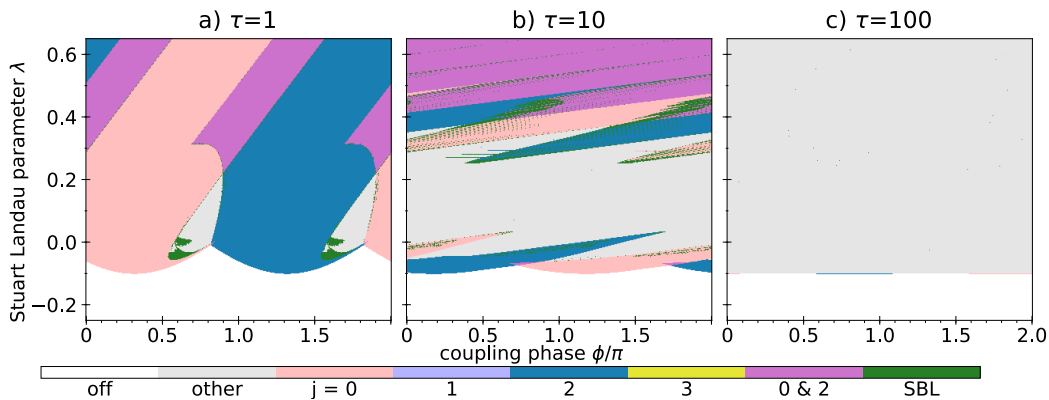


Figure 3.28: Regions of numerically obtained stability for $N = 4$ delay-coupled Stuart-Landau oscillators in a bidirectional ring as described in Eqs. (3.68) as a function of λ and coupling phase ϕ for different delay times τ . White areas indicate the trivial off-state. The colours indicated in the legend with ‘ $j = 0$ ’, ‘1’ etc. are rotating wave patterns as described by Eq. (3.42). ‘0 + 2’ indicate multistability between rotating waves of the in-phase ($j = 0$ IP) and anti-phase ($j = 2$ AP) states. Light grey areas contain higher-order dynamics. Dark green areas contain symmetry-broken amplitude and phase-locking states. Parameters: $\text{Re}(\gamma) = -0.1$, $\text{Im}(\gamma) = 0.5$, $\omega = 1$, $\kappa = 0.1$, τ as atop the columns.

$Z_0 = -Z_1 = Z_2 = -Z_3$, and multistability between the two occurs for the parameter combinations marked in purple. White regions correspond to the off-state, grey regions to higher-order dynamics. The parameter scan with delay of Fig. 3.28 can be directly compared to the study of $N = 4$ without delay shown in Fig. 3.20 c) with $\text{Im}(\gamma) = 0.5$, as they share all parameters except delay time τ . The different panels of Fig. 3.28 show different delay times τ , as was done for the unidirectional ring in Fig. 3.18 (the same parameters are used).

The bidirectional ring with small feedback $\tau = 1$ shown in Fig. 3.28 a) exhibits most of the properties of the bidirectional ring of size $N = 4$ without delay. The regions of in-phase (pink) and anti-phase (blue) stable rotating wave patterns are located close to their original position and have a similar shape to the case without delay. However, for large λ , it is once again observable that the region of multistability has increased. This is the same effect that was also discussed for unidirectional rings with delay. The case of small delay still contains symmetry-broken amplitude and phase-locking states (dark green in Fig. 3.28 a)), showing that small delay times τ are not changing the system and symmetry-breaking bifurcations drastically.

The case of intermediate delay shown in Fig. 3.28 b) is more strongly distorted. The delay has reduced the regions of stable in-phase and anti-phase oscillations, and large parts of the parameter space are covered in higher order dynamics (grey

regions). The bidirectional ring thus exhibits the same trend as the unidirectional ring with intermediate delays. This also includes regions of multistability for large λ , that cover the entire coupling phase ϕ -dimension.

The bidirectional ring with large delay $\tau = 100$ shown in Fig. 3.28 c) differs greatly. The delay-coupling has destroyed all regions of stable in-phase and anti-phase solutions. Whether this is due to an extremely small basin of attraction of these states or whether they are completely unstable is not easily decidable with numerical investigations alone. However, the numerical simulations do strongly imply that it will be difficult to find stable fixed-amplitude oscillations in delay-coupled amplitude oscillator networks with a bidirectional ring topology. This is in contrast to the unidirectional ring, which at least showed stable rotating waves close to threshold and for large λ . Why exactly the bidirectional ring topology is so detrimental when coupling is delayed does not seem obvious and is a surprising result.

3.5 Discussion

3.5.1 Outlook: Symmetry-breaking and small chimera states in laser networks

A final aspect of symmetry-breaking in amplitude oscillators shall now be discussed here. The results of this section were published in Ref. [ROE16]. Symmetry-breaking can also be linked with a special type of pattern called ‘chimera states’. Chimera states were first reported by Kuramoto and Battogtokh in Ref. [KUR02a] in 2002, however the name was not coined until 2004 [ABR04] and similar states can also be found in earlier works [KAN90]. A chimera state is defined for a system of identically coupled oscillators, where one part of the system is synchronized, while the other part performs some irregular motion. The name ‘chimera’ is inspired by the beast of Greek mythology, which consisted of several incoherent parts. Chimera states were first described in systems of phase oscillators, but they have since been reported in many different systems.

Symmetry-breaking is clearly connected to the properties of chimera states. As most systems used to study chimera states original consist of N identically coupled and parametrized oscillators, the final state clearly divides the system into two different parts. This is a form of symmetry-breaking, where only the initial conditions decide which oscillators will end up as the unsynchronized region. However, many chimera states are only transient phenomena and not a stable solution of finite-sized networks [WOL11, OME16, SEM17]. Thus, they cannot be investigated as results of symmetry-breaking bifurcations in general. Furthermore, chimera states are hard to observe for small networks, as the definition of an ‘incoherent region’ becomes hard to evaluate.

Nevertheless, there exists a class of chimera states in a system of globally coupled lasers [BOE15, ROE16] that can be seen as a stable ‘tiny chimera state’. They represent a particular example, but in return allow for a more detailed study of their bifurcations. The system that shall be mentioned here consists of $N = 4$ coupled Lang-Kobayashi lasers with delay, and the topology is a global or ‘all-to-all’ network with self-feedback. The complex electric field amplitude E_n of laser n and its excess carrier density $N_{e,n}$ can then be modelled by the following DDE:

$$\frac{dE_n}{dt} = (1 + i\alpha)E_n N_{e,n} + e^{-i2\phi} \kappa \sum_{m=1}^N E_m(t - \tau), \quad (3.69)$$

$$\frac{dN_{e,n}}{dt} = \frac{1}{T}(p - N_{e,n} - (1 + 2N_{e,n})|E_n|^2), \quad (3.70)$$

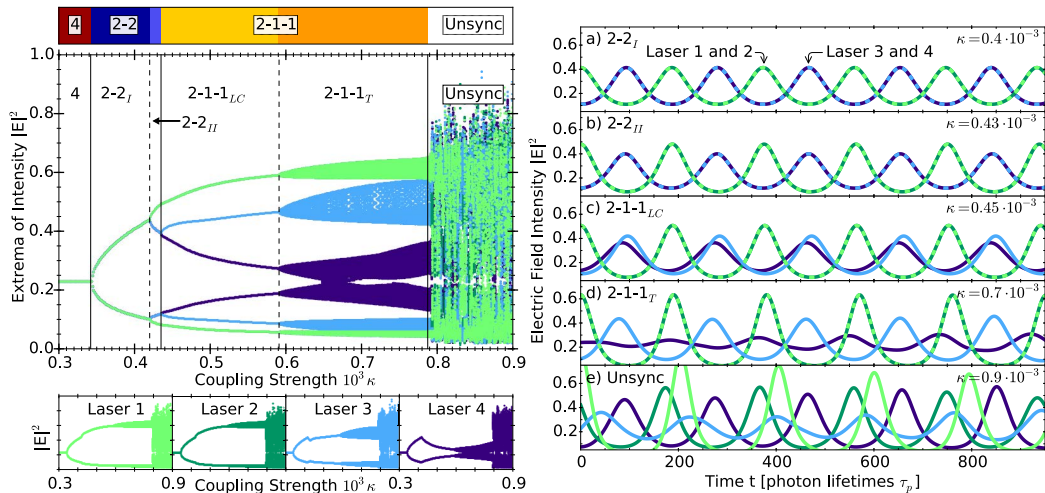


Figure 3.29: Left: Linescan over the coupling strength κ with the extrema of the electric field intensity $|E_n|^2$ shown in the different colours. The individual line scans for the different lasers are also separately shown in the bottom panels. The labels indicate the synchronization state of the system which is also indicated on the top in different colours. Right: Time series examples for the line scan, with the intensity $|E_n|^2$ shown as a function of time t for some of the non-trivial patterns. Parameters: $p = 0.23$, $T = 392$, $\alpha = 2.5$, $\phi = 2.15$, $\tau = 40$. Reprinted with permission from Ref. [ROE16].

where the parameters are as described in Sec. 2.4. Note, that due to geometric reasons outlined in Ref. [ROE16], the coupling phase ϕ appears with a prefactor of -2 and that the laser index goes from $n = 1$ to $n = 4$.

Figure 3.29 shows the chimera state for Eqs. (3.69) and (3.70), with a line scan of the electric field intensity $|E_n|^2$ on the left and sample time series for different non-trivial states on the right. The overall bifurcation landscape of this small network system is even more complex, but the line scan here shows how non-trivial system state evolves from a regular rotating wave state to a tiny chimera state. Note, that the time-series shows the intensity, i.e. $|E|^2$, where previous time series in this thesis showed the real part $\text{Re}(Z)$. Hence, any oscillation seen in Fig. 3.29 corresponds to an amplitude oscillation and would have been classified as a ‘higher order dynamic’ previously. The labels indicate the number of intensity clusters, i.e. ‘2-2’ consists of two clusters with 2 laser each, that share their intensity.

The line scan on the left of Fig. 3.29 begins with the in-phase synchronized state ‘4’ for small coupling strengths κ . No time series for this state is shown, but it corresponds to the rotating wave patterns of index $j = 0$ as previously discussed, i.e. $E_1 = E_2 = E_3 = E_4$. For $\kappa \approx 0.34$ the system undergoes a symmetry-breaking torus bifurcation, leading to the $2 - 2_I$ state. The time series is shown in Fig. 3.29 a). This state is characterized by two intensity clusters of lasers of size 2

each. Because the topology is an all-to-all network, which laser synchronized with which other solely depends on the initial conditions. The bifurcation that gives rise to this state is in particular interesting, because so far the focus has been on symmetry-broken amplitude and phase-coupling states. Torus bifurcations always lead to amplitude oscillations, so their symmetry-breaking properties have not been investigated in this chapter. The amplitude oscillations are initially sinusoidal, but their amplitude grows for larger κ . For $\kappa \approx 0.42$ the two-cluster solution undergoes an additional symmetry-breaking pitchfork of limit cycles bifurcation. The time-series for the newly created state $2-2_{II}$ is shown in Figure 3.29 b). The important difference to the $2-2_I$ state here, is that the intensity clusters can now be distinguished, i.e. they no longer are time-shifted versions of each other. This also means, that the $2-2_I$ state is lag-synchronized, while the $2-2_{II}$ is not. This bifurcation cascade reveals a previously not mentioned aspect of nonlinear oscillators: lasers and amplitude oscillators that already exhibit amplitude oscillations can still exhibit symmetry-breaking bifurcations and symmetry considerations are still applicable for them. However, due to the presence of limit cycle dynamics analytic solutions are harder to find for such systems than for the previously discussed SBL states.

A second symmetry-breaking pitchfork of limit cycles bifurcation occurs for $\kappa \approx 0.43$, leading to the appearance of the small chimera state $2-1-1_{LC}$. The subscript LC indicates, that it still behaves like a limit cycle. This state is characterized by two synchronized lasers $E_1 = E_2$, and two lasers that exhibit a different amplitude. The time series is shown in Fig. 3.29 c). The variant $2-2_T$ differs in that the clusters in this state perform quasi-periodic amplitude oscillations (see Fig. 3.29 d)). For larger coupling strength κ the system is in the unsynchronized regime, and a time series example is shown in Fig. 3.29 e).

These tiny chimera states of Fig. 3.29 c) and d) thus clearly originate from symmetry-breaking bifurcations. First, the system breaks into intensity clusters, representing a first symmetry-breaking. Then, some of the sub-clusters lose their internal stability in subsequent bifurcations. The system reaches a state where a large cluster still remains, forming the synchronized region of the chimera state, while the rest of the network exhibits unsynchronized behaviour. This is also a possible creation mechanism for chimera states in larger networks. However, it is not clear how this bifurcation scenario would scale for larger laser networks, as to create an incoherent region of solitary oscillators, a large cascade of symmetry-breaking pitchfork of limit cycle bifurcations may be necessary. A systematic study of such bifurcations is still an open question. One interesting avenue to be investigated could potentially be trying to find similarities to so called ‘solitary states’ [MAI14a], which have been reported for chaotic maps and seem superficially similar. A detailed investigation will however have to be left for future studies.

3.5.2 The role of symmetries for regular oscillator networks

Networks of Stuart-Landau oscillators can exhibit a large variety of dynamics and patterns. Because the system is mathematically relatively simple, many of the solutions can be calculated analytically. The system of two instantaneously coupled Stuart-Landau oscillators was thoroughly investigated in Sec. 3.1 using both analytical and numerical tools. Even this simple system exhibits an intriguing interplay of different symmetries, allowing for the emergence of symmetry-breaking bifurcations. In particular, a symmetry-broken amplitude- and phase-locking (SBL) was reported and can be described by a simple analytical ansatz. Due to the particular nature of these states that combine regular harmonic oscillations with a broken exchange symmetry, the Stuart-Landau must arguably be the smallest and simplest nonlinear oscillator model to exhibit such symmetry-broken solutions. The SBL solutions emerge in a symmetry-breaking pitchfork bifurcation, where they inherit the stability of the preceding solution. Additionally, they can emerge from a saddle-node of limit cycles bifurcation. Two branches of SBL states exist, one for both of the fundamental oscillatory solutions of the system (the in-phase and the anti-phase solution). Due to the consequences of the *equivariant branching lemma* the SBL states are naturally multistable.

The coupled Stuart-Landau oscillators can also be seen as an approximation of a laser close to threshold. To investigate the differences and similarities, Sec. 3.2 showed a corresponding system of two instantaneously coupled Lang-Kobayashi-type systems. There, extensive bifurcation analysis was already published, so that a comparison with the Stuart-Landau system was a natural question to be investigated. The Lang-Kobayashi system includes an additional carrier equation, that allows for more complex dynamical properties. Nevertheless, the laser system was found to be similar to the Stuart-Landau case. This is caused by the fact that both the system of two Stuart-Landau oscillators and the system of two Lang-Kobayashi-type lasers exhibit the same symmetry properties. Symmetries play such an important role in coupled nonlinear oscillators, that many of the primary properties are determined purely by the symmetries. This in particular holds for the fundamental oscillatory solutions (in-phase and anti-phase synchronization in the case of two instantaneously oscillators), and as such general amplitude oscillator dynamics can be explored with a variety of models, yielding similar results.

The realization that symmetries are often more important than the details of the local nonlinear oscillator model naturally leads to the question of the properties for larger and highly symmetric systems. The properties of rings of instantaneously coupled Stuart-Landau oscillator models were therefore studied, with unidirectional rings in Sec. 3.3 and bidirectional rings in Sec. 3.4. Both types of rings contain a larger amount of phase-synchronized solutions. These are the so called ‘ponies

on a merry-go-round' or rotating wave states, and there exists N different labelled with index j for a ring network of size N . However, while all of these solutions can be reduced to the in-phase synchronized solution for the unidirectional ring, see Eq. (3.46), the bidirectional ring exhibits no such general relation. In a bidirectional ring, only the in-phase synchronized solution $j = 0$ and for even numbers of oscillators N the anti-phase synchronized solution $j = N/2$ are preferred. The map of stable solutions for the bidirectional ring looks very similar independent of the number of oscillators N , in particular it always resembles the case of two coupled oscillators $N = 2$ as discussed in Sec. 3.1. In contrast, ever more stable rotating wave solutions appear for larger unidirectional rings with increasing size. This contrast can be related to the fact, that the bidirectional ring has a higher symmetry than the unidirectional ring. The stricter symmetry requirements lead to a smaller number of stable states, reducing the complexity of the bifurcation diagrams.

Both the unidirectional and the bidirectional ring networks can exhibit symmetry-broken amplitude- and phase-locking states. In both cases, these states can be seen as an extension of the symmetry-breaking bifurcations for the system of two Stuart-Landau oscillators. In particular, for the case of $N = 4$ oscillators in a ring network, both the unidirectional and the bidirectional ring can exhibit cluster states with two clusters of two oscillators each, which directly correspond to the SBL states of the two oscillator system. However, for the ring networks additional symmetry-broken solutions can appear, which also include a symmetry-breaking mostly in the phase-direction, leading to novel SBL states that have no corresponding $N = 2$ solutions.

Larger unidirectional and bidirectional rings were also investigated (sizes $N = 6, 8, 9, 12$). A general scaling trend for both kinds of ring topologies was visible, but differed in shape. While the unidirectional ring becomes increasingly multi-stable between a vast number of phase-synchronized solutions, the bidirectional ring network only shows 2 basic patterns regardless of size N . An exception was found for the case of bidirectional rings of uneven size, where 3 different rotating wave patterns can be found to be stable. Symmetry-breaking occurs for both large unidirectional and large bidirectional rings. However, the bidirectional ring shows a much larger variety of stable SBL states. Finding a systematic way of classifying and counting all possible SBL states for a given ring topology is still an open problem. The numerical results of this thesis can only serve as an indication, that bidirectional rings have a larger number of stable SBL states than the unidirectional ring, and strictly speaking only for the parameters investigated.

The influence of delay on the solutions of regular ring networks of Stuart-Landau oscillators was also studied briefly. A few general trends were apparent: For small delays, the system structure has only slightly been distorted, when compared to

the case without delay. For increasing delay times τ , the coupling phase ϕ loses importance, and the regions of stable phase-locked behaviour begin to depend less on ϕ . Additionally, for high λ large multistabilities exist, while for small λ regions of higher order dynamics become prevalent. For very long delay times, the unidirectional ring still exhibited a recognizable structure, with regions where all rotating wave patterns were simultaneously stable. The bidirectional ring, however, lost its well-defined bifurcation structure and was characterized by a complete loss of fixed amplitude solutions.

Overall, this chapter illustrates how much the symmetry of the system dictates the basic solutions. The Stuart-Landau oscillator is especially suited for the study of these effects, as its mathematical simplicity allow for analytical results and easy numerical integration. Symmetry-breaking is a ubiquitous phenomenon, so that paradigmatic models are needed to study it and the results of this section will be valid for a plethora of different systems.

3 SYMMETRY-BREAKING IN NETWORKS

4

RESERVOIR COMPUTING IN NETWORKS

This chapter covers the application of networks of lasers and oscillators as the core elements in the neuro-inspired machine-learning paradigm called 'reservoir computing'. The aim here is explicitly not to set new records in the performance of such systems. Rather, the general setting of regular oscillator and laser networks will be used to explore fundamental principles of reservoir computing. This also connects with ideas from the more general field of analogue computing and the question of the *general computational capabilities* of dynamical systems. This is a complex scientific problem for which definitive answers are rare. This current thesis will therefore offer a start by working with basic questions and concepts. Open questions and fruitful future avenues of research will be pointed out.

The chapter is structured by the type of system investigated, going from simple to more complex. Section 4.1 investigates a virtual network approach consisting of a single Stuart-Landau oscillator with delayed feedback. Here, some general properties of time-multiplexing, parameter dependence and the influence of reservoir computing hyper parameters are investigated. Section 4.2 then extends the investigations to larger reservoirs called 'time-multiplexed networks', which incorporate both time-multiplexing and delay-coupling. Thus, these networks have both 'virtual nodes' created by time-multiplexing and several 'real' physical nodes. The influence of the balance between these two groups is systematically studied.

4.1 Single-node with delay

This section introduces a system consisting of a single Stuart-Landau oscillator with a long delayed feedback and uses it as the dynamical core of a reservoir computing scheme. This simple example is used to illustrate basic properties of the reservoir computing and time-multiplexing algorithm, such as the dependence on the delay time τ , system parameters such as λ and hyper-parameters such as the training length K_{training} . Many of the fundamental aspects of how systems react as reservoir computing components are discussed in a general framework that can be applied to different systems.

4.1.1 Stuart-Landau oscillator with delayed feedback

To connect with the previous topics of this thesis and to allow for a simple and efficient description, the first system that is used for reservoir computing is a single Stuart-Landau oscillator as introduced in Sec. 2.3. However, in addition to the local dynamics as introduced in Eq. (2.24), a delayed feedback loop is added to the system. This delayed feedback will play the role of extending the phase space dimension of the system, as outlined in Sec. 2.5.5: By the inclusion of delay, the system state is no longer described by a mere vector of real numbers $\mathbf{X} \in \mathbb{R}^N$, but needs to be described over the whole delay interval $\mathbf{X}(t)$ for $t \in [0, \tau]$. This also means that the equation of motion ceases to be an ODE and becomes a DDE (see Sec. 2.1.5 of the theory for an introduction to DDEs). The complete equation for the single Stuart-Landau oscillator with delayed feedback used for reservoir computing is then given by:

$$\frac{dZ}{dt} = \left(\lambda + GJ(t) + i\omega + \gamma|Z|^2 \right) Z + \kappa e^{i\phi} Z(t - \tau), \quad (4.1)$$

where λ is the bifurcation parameter of the Stuart-Landau system, ω is the solitary frequency and γ is the nonlinearity. The feedback term $Z(t - \tau)$ is delayed by the delay time τ and is similar in nature to the usual feedback term in lasers, such as in the Lang-Kobayashi system [LAN80b, ALS96]. The feedback strength is κ and the feedback phase is ϕ . Eq. (4.1) is a delay-differential equation (DDE), for which special methods of numerical integration have to be used (cf. Sec. 2.1.5).

The information is injected via the time-dependent input term $J(t)$. The masked signal $J(t)$ enters the Stuart-Landau oscillator in Eq. (4.1) in a way that it can be seen as a modification of the Stuart-Landau bifurcation parameter λ . Due to the analogy between the Stuart-Landau model and laser models such as the Lang-Kobayashi system, this kind of information injection is similar to the case of an electrically pumped laser, where data is fed via a time-varying pump current.

Recall, that the reservoir computing paradigm is based on the injection of data into a high-dimensional dynamical system and the subsequent read-out of the input-induced transients. When the system is not highly parallel, i.e. when most of the complexity of the phase space transients occurs *in time*, the standard approach of data injection and readout needs to be modified to include 'time-multiplexing'. The mathematical details of the time-multiplexing procedure and how it is applied to delay-based reservoir computing are shown in Sec. 2.5 of the theory. Only the most important aspects shall be repeated here and the special implementation used for Eq. (4.1) shall be explained: The dynamical system that constitutes the 'reservoir' of information and transients is driven by an input sequence u_k . The state of the reservoir is recorded at certain times to produce a high-dimensional state vector \mathbf{X}_k , which encodes the response of the system. For the single Stuart-Landau oscillator with delayed feedback of Eq. (4.1) the masked input signal is given by the term $J(t)$ and scaled with the input gain parameter G . A high G corresponds to a stronger drive, while a small G is a weak input forcing. The masked input $J(t)$ has to be calculated from the raw input sequence u_k and this is done via the masking formula:

$$J(t) = u_k M(t \bmod T), \quad \text{where} \quad (k-1)T < t \leq kT. \quad (4.2)$$

where T is the input clock cycle, and M is the mask-function, which is defined in the interval $[0, T]$. The mask in this thesis is not further investigated with respect to its influence, but previous publications indicate that it can be chosen freely from a large array of different functions, such as binary masks, low-frequency noise or chaotic timeseries [NAK16]. Here, the method of Appeltant *et al.* is used [APP11], and the mask is always taken as a binary bit-pattern of length N_V , where N_V is the 'virtualisation factor'. The mask function $M(t)$ of length T is divided into N_V equidistant 'virtual nodes', with every node lasting θ in time:

$$\theta = \frac{T}{N_V} \quad (4.3)$$

Thus, N_V can also be seen as the total number of virtual nodes in the system of Eq. (4.1), as only a single Stuart-Landau oscillator is used. This will not be the case in general, when larger networks are discussed later in this chapter. The mask function M for Eq. (4.1) then is a sequence of N_V values M_j with $M_j = 0$ or 1 such that:

$$M(t) = M_j, \quad \text{where} \quad (j-1)\theta < t \leq j\theta, \quad (4.4)$$

for t in $[0, T]$ with clock cycle T .

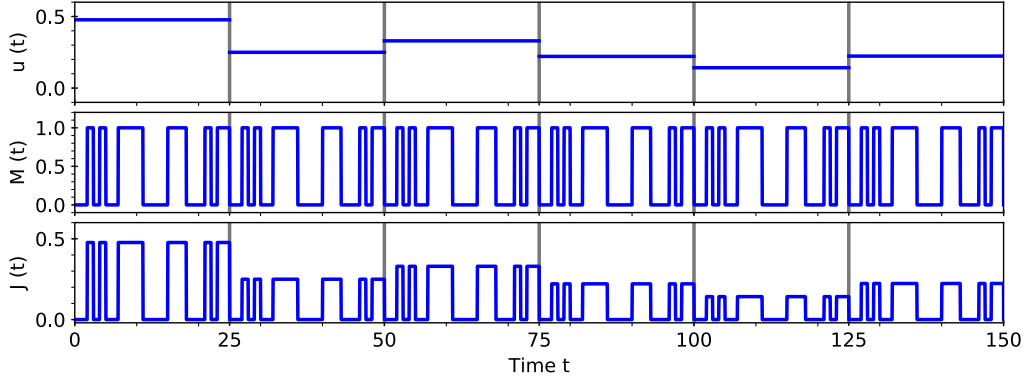


Figure 4.1: Examples of the piece-wise constant input signal $u(t)$ (top), the T -periodic mask $M(t \bmod T)$ (centre) and the masked signal $J(t)$ (bottom). $T = 25$, $N_V = 25$, $\theta = 1$. The vertical grey lines denote full clock cycles T .

To illustrate the relationship and to visualize the masking process, Fig. 4.1 shows an example. The top panel of Fig. 4.1 shows the raw input sequence $u(t)$, which is a simple piece-wise constant function with piece-length T and heights according to the input sequence u_k . The mask $M(t)$ (centre panel of Fig. 4.1) is a random binary pattern and is here repeated for every T . The masked signal $J(t)$ (bottom panel of Fig. 4.1) is then obtained by simple multiplication. In Fig. 4.1 the clock cycle is $T = 25$ with a virtualisation factor of $N_V = 25$, i.e. there are 25 virtual nodes each in a window of length $\theta = 1$. Note, that the mask is chosen randomly from the binary distribution $[0, 1]$, so that not every θ the mask value changes. The divisions between the different clock cycles T are indicated by the grey vertical lines in Fig. 4.1. The input sequence (top panel of Fig. 4.1) is based on the input sequence u_k for the NARMA10-task, i.e. random numbers drawn from the uniform distribution in the interval $[0, 0.5]$. Thus, the final masked signal also has a maximum strength of $0.5 = 0.5 * 1$.

Implementation details

To construct the reservoir computing scheme, a high dimensional system state \mathbf{X}_k has to be recorded to encode the response of the system to the input u_k . This also implicitly means, that the information read-out and the input u_k have to be always operating at the same speed, i.e. share the same clock cycle T . They are never allowed to drift with respect to each other, as otherwise this would nullify the learning of the system. The readout of the system state necessary for reservoir computing can be done in multiple ways. In principle, the numerical integration of the Stuart-Landau oscillator with delay of Eq. (4.1) can be done at arbitrarily small time-resolutions, at least to the level of the *C++-double* precision. Naturally, in

such a numerical simulation, all data points are available to be recorded. However, this is neither desirable nor is it realistic for a comparison with experiments. The readout of the single-Stuart-Landau oscillator is therefore done in the same way as introduced by Appeltant *et al.* [APP11]: The system is read-out *once per virtual node*, i.e. every θ . In the implementation used in this thesis, the readout always happens exactly at the end of the time window of length θ that corresponds to a certain virtual node. The read-out is done irrespective of the phase-information of the system, only the absolute squared $|Z|^2$ is recorded. Thus, during every clock cycle T , N_V different recordings of the system state $|Z|^2$ are made. Hence, the system response is recorded as an N_V -dimensional vector to every input value u_k for the solitary Stuart-Landau oscillator with delayed feedback of Eq. (4.1).

4.1.2 System parameter scan for NARMA10 task

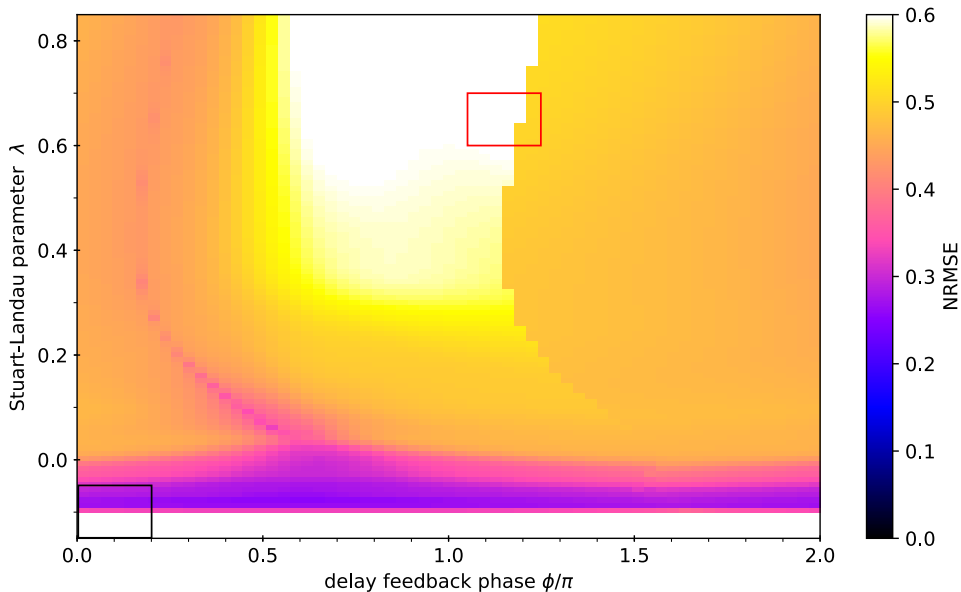


Figure 4.2: Parameter scan for the single Stuart-Landau oscillator with delayed feedback as given by Eq. (4.1) for different feedback phases ϕ and Stuart-Landau parameters λ . The colour code indicates the NRMSE of the NARMA10 task in the testing, i.e. for the independent evaluation after the training. The parameter scan was done with fixed mask and fixed NARMA10 series. Parameters: $\gamma = -0.1$, $\omega = 1$, $G = 0.01$, $\kappa = 0.1$, $\tau = 2176$, $N_V = 128$, $T = 1536$, $\theta = 12$, $K_{\text{training}} = 5000$, $K_{\text{testing}} = 5000$, $K_{\text{buffer}} = 1000$.

The ability of reservoir computers to perform tasks is dependent on the system parameters. For example, Appeltant *et al.* [APP11] investigated the importance of balancing between nonlinear and linear parts of the parameter space. As the

system response is critically dependent not only on the input, but also on the underlying phase-space topology, a complex dependence on the system parameters is typical for reservoir computers. Some of the fundamental parameters of the system can drastically influence the resulting reservoir computing capabilities. This will be illustrated using the single Stuart-Landau oscillator of Eq. (4.1) with delayed feedback in this section.

Figure 4.2 shows the two-dimensional parameter scan for the performance of the single Stuart-Landau oscillator with delayed feedback as given by Eq. (4.1). The normalized root mean squared error (NRMSE) as defined in Eq. (2.54) was used to evaluate the NARMA10-task and the NRMSE is shown in colour code versus the feedback phase ϕ and Stuart-Landau parameter λ in Fig. 4.2. The system was trained with a training length of $K_{\text{training}} = 5000$ data points and evaluated for another $K_{\text{testing}} = 5000$ data points with an additional buffer of $K_{\text{buffer}} = 1000$ being fed in before starting to record the system states. To not introduce any other sources of uncertainty of the evaluation, both the binary mask and the NARMA10 series was random but identical for all combinations of feedback phase ϕ and Stuart-Landau parameter λ in Eq. (4.1). Additionally, the system was always initialized with the same initial conditions. Thus, all variations in NRMSE seen in the colour code of Fig. 4.2 are purely due to changes in the system response caused by differing parameters ϕ and λ .

Causes of NRMSE variation

The structure of the NRMSE shown by the colour code in Fig. 4.2 is non-trivial, with several abrupt transitions for some parameter combinations, and smooth variations for others. Understanding the causes for good and performance in a reservoir computing system is a hard problem in general. The example of the single Stuart-Landau oscillator will be used to determine several influencing factors and to explain some of the main causes in the following paragraphs. They concern four different classes of features of Fig. 4.2: Regions of no response (white, NRMSE = 1), bifurcations, attractor basins and the trade-off between linear memory and nonlinearity.

First, there exists a critical border at $\lambda = -0.1$ below which the error is constant at NRMSE= 1 (bottom white part in Fig. 4.2). This is the region where the Stuart-Landau oscillator with delayed feedback of Eq. (4.1) is permanently locked into its trivial off-state $Z = 0$, like a Lang-Kobayashi system below the laser threshold. Usually, the threshold for the onset of oscillations in a solitary Stuart-Landau oscillator is at $\lambda = 0$. However, the threshold is located at $\lambda = -0.1$ in Fig. 4.2 due to the choice of the feedback strength $\kappa = 0.1$. Constructive interference with the delay term reduces the effective damping and causes a threshold reduction, similar

to the external cavity mode (ECM) solutions of a Lang-Kobayashi laser system. Below this threshold, the only stable solution of Eq. (4.1) is the trivial off-state $Z = 0$.

The off-state is very harmful to the reservoir computing abilities of the system: The single Stuart-Landau oscillator with delayed feedback of Eq. (4.1) is modulated by the input $J(t)$. Due to the choice of how to include the input, $J(t)$ can be seen as modifying the Stuart-Landau bifurcation parameter λ in Eq. (4.1). Thus, the system response has to be excited by a change in $\lambda + GJ(t)$. However, the stable off-state is independent of λ , i.e. its amplitude and frequency do not depend on λ . Therefore, if the system is fed with input data $J(t)$, the time series of the trivial off-state is not changed and the system does not react at all. The amplitude simply remains zero $Z = 0$ for all times, regardless of the input $J(t)$. In such a setting, no information processing can be obtained, as the system simply does not react at all to the incoming information. The maximum error that the NRMSE can produce is 1. Because regions for $\lambda < -0.1$ perform as bad as possible, the trivial off-state in Fig. 4.2 shows an NRMSE of 1 (white colour).

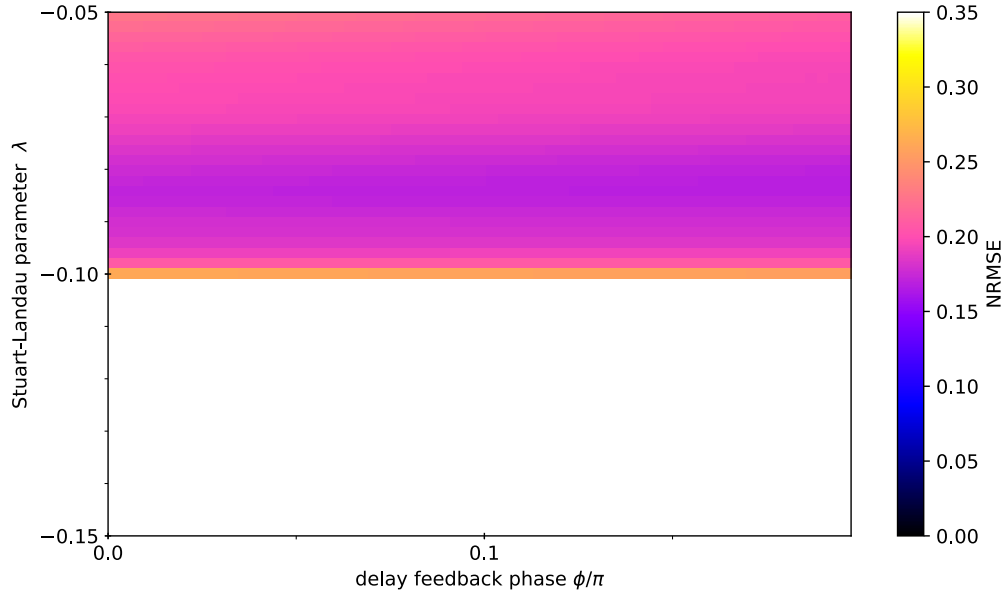


Figure 4.3: Zoom of the parameter scan for the single Stuart-Landau oscillator with delayed feedback marked by the bottom square in Fig. 4.2. The colour code indicates the NRMSE of the NARMA10 task in the testing, i.e. for the independent evaluation after the training. The parameter scan was done with fixed mask and fixed NARMA10 series. Parameters: $\gamma = -0.1$, $\omega = 1$, $G = 0.01$, $\kappa = 0.1$, $\tau = 2176$, $N_V = 128$, $T = 1536$, $\theta = 12$, $K_{\text{training}} = 5000$, $K_{\text{testing}} = 5000$, $K_{\text{buffer}} = 1000$.

For large enough Stuart-Landau parameter λ , the NRMSE is less than 1 and changes both with λ and feedback phase ϕ in Fig. 4.2. This is due to changes of the underlying phase space topology and the change in the stability of the embedded solutions. One such bifurcation is the aforementioned threshold of oscillations for $\lambda = -0.1$. This bifurcations can be seen as an *abrupt* changes in the NRMSE: There is a clear boundary between the off-solution (bottom white region in Fig. 4.2, see the zoom of the bottom square also in Fig. 4.3) and the regions where the system is oscillating and dynamically active (blue and purple regions for $\lambda > -0.1$ in Fig. 4.2 and 4.3)). This is a general aspect of the NRMSE landscapes and applies to all reservoir computing systems: The NRMSE is abruptly modified at bifurcation lines.

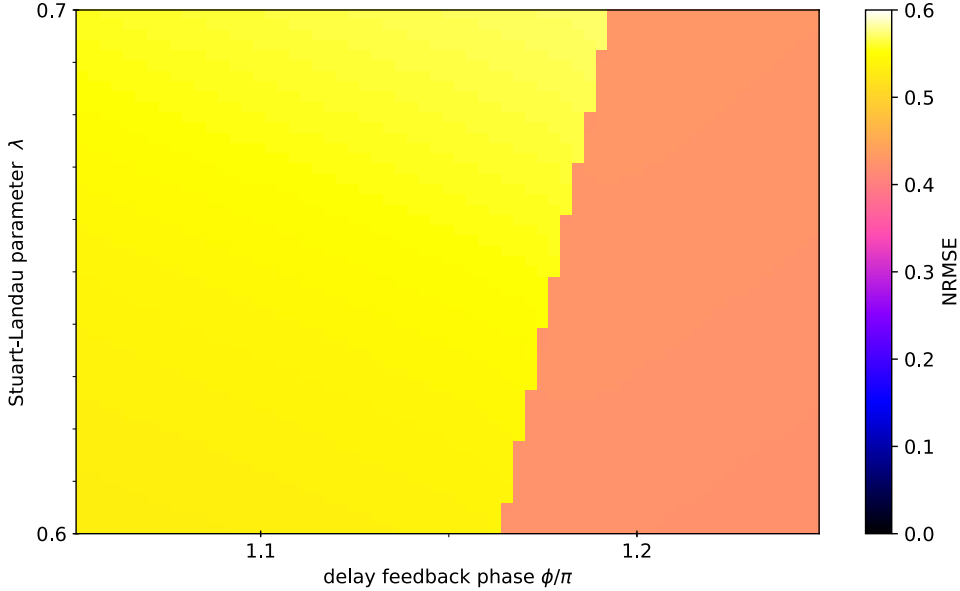


Figure 4.4: Zoom of the parameter scan for the single Stuart-Landau oscillator with delayed feedback marked by the top square in Fig. 4.2. The colour code indicates the NRMSE of the NARMA10 task in the testing, i.e. for the independent evaluation after the training. The parameter scan was done with fixed mask and fixed NARMA10 series. Parameters: $\gamma = -0.1$, $\omega = 1$, $G = 0.01$, $\kappa = 0.1$, $\tau = 2176$, $N_V = 128$, $T = 1536$, $\theta = 12$, $K_{\text{training}} = 5000$, $K_{\text{testing}} = 5000$, $K_{\text{buffer}} = 1000$.

An additional abrupt change in the NRMSE can be seen for feedback phases $\phi \approx 1.2\pi$ in Fig. 4.2 (inside the top square), where the error abruptly jumps between two intermediate NRMSE. A zoom of this parameter region is shown in Fig. 4.4. This is not too different from what one can expect to see at the boundary of a bifurcation. However, there is an alternative explanation tied to the details of the numerical simulations underlying Fig. 4.2: The system as given by Eq. (4.1)

was always initialized with the same initial conditions. The natural solutions of the Stuart-Landau oscillator with delayed feedback are ECM-like solutions that for a delay as long as $\tau = 2176$, as used for Fig. 4.2, are stable over the entire range of feedback phases ϕ . However, there are multiple stable ECM-like solutions, as the number of ECMs in general increases with delay [ROT07]. The abrupt change in the NRMSE seen at feedback phases $\phi \approx 1.2\pi$ in Fig. 4.2 is not caused by a bifurcation, but rather by the fixed initial condition converging to a different ECM-like solution. This is an effect that can only be observed, when the initial condition is fixed and very finely controlled, and as such would therefore be rather hard to see in an experimental setting. The stability and phase-space neighbourhood of different ECMs is slightly different, as for example they have different amplitudes $|Z|^2$. This will ultimately lead to a different transient response to the input, and thus a visibly different NRMSE in Fig. 4.2. This is an important fact to be aware of: When a system has multiple stable solutions, the performance will differ between them.

The difference between an abrupt change in the NRMSE caused by a bifurcation and that caused by simply converging to a different stable solution can also possibly be detected by the qualitative change of the NRMSE near those transitions: A supercritical bifurcation has the solution on both sides of the bifurcation line change its stability, while in a subcritical bifurcation at least on one side a solution its stability. This means, that at least on one side the leading Lyapunov exponent will converge to zero. Such a drastic change in the leading Lyapunov-exponent should also consistently result in a drastic change of the NRMSE, regardless of the task observed. On the other hand, if the system merely converges to a different attractor during initialization, the border between the different parameter ranges will not be marked by a vanishing leading Lyapunov-exponent on either side, as neither solution changes stability. Thus the following hypothesis can be raised: If an abrupt change in the NRMSE as a function of a parameter is accompanied at least on one side of the transition by a strongly, but smoothly changing NRMSE with the distance from the critical point, it is likely to be caused by a bifurcation. Conversely, if an abrupt change is not accompanied by a scaling behaviour of the NRMSE near the transition, i.e. of the NRMSE is constant on both sides of the critical parameter, the system is likely simply switching between multi-stable solutions.

For the two-dimensional parameter scan shown in Fig. 4.2 this means that the system undergoes a supercritical Hopf-bifurcation for $\lambda = -0.1$ because it does change the reservoir computing capabilities as a function of λ (see the NRMSE for $\lambda > -0.1$ in the zoom of Fig. 4.3). On the other hand, the abrupt change for high λ and feedback phases $\phi \approx 1.2\pi$ shown in Fig. 4.4 is merely a switching of the

attractor basin of the initial condition, and thus both the regions to the left and to the right of it do not exhibit a strongly changing NRMSE as a function of λ .

The last general aspect of the parameter dependence of reservoir computing systems that will be discussed on the example of the Stuart-Landau oscillator with delayed feedback is the linearity-nonlinearity trade off. As discussed by Ref. [DAM12], a reservoir computer has to allocate its response between nonlinear and linear contributions. Each specific task has different requirements and differing amounts of linear recall and memory that are needed. When the reservoir computer cannot offer the required memory or nonlinear transformation, the resulting NRMSE will be high. The results for the NARMA10 NRMSE shown in Fig. 4.2 do not only show abrupt changes in the NRMSE (colour code), but also smooth evolutions over large parameter values. As the NARMA10 task requires quite a significant amount of linear memory, these evolutions can be best understood by looking at the linear memory capacity, as will be done in the next section. In general, predicting *a priori* at which parameter combinations favourable conditions for a specific task can be found is still an open problem.

4.1.3 Parameter scan of the memory capacity

A measure of the linear memory of a system, i.e. its ability to internally store information that it has received in the past, was introduced in Sec. 2.5.7 of the theory. The linear memory capacity C_L^m can be deduced by training the system to perform a linear recall of length m . The target for this training is to output $o(k) = u(k - m)$, i.e. a time shifted version of the input u_k . The linear memory capacity C_L^m is normalized to be 1 for a system with perfect linear memory m -steps into the past, whereas $C_L^m = 0$ for a system without linear memory m -steps in the past (it may still have non-linear memory [DAM12]). When the memory capacity is plotted as a function of m , the linear memory curve of a system is obtained.

Figure 4.5 shows one example of a linear memory curve for the Stuart-Landau oscillator with delayed feedback as given by Eq. (4.1), with parameters as indicated in the figure caption. The linear memory capacity C_L^m after training is shown for a training and testing length of $K_{\text{training}} = K_{\text{testing}} = 5000$. The linear memory capacity C_L^m is almost 1 for $m \leq 15$. This shows that the system can perfectly linearly recall the last 15 inputs that it has been fed. On the other hand, the linear memory capacity drops off sharply for $m > 18$ in Fig. 4.5. The system has almost no linear memory for inputs that are more than 18 steps in the past. The shape seen in Fig. 4.5 is typical for a linear memory curve, with an initially high plateau $C_L^m \approx 1$ for small m and then a sharp decline for some critical m_c . Note, however, that there remains a residual memory capacity $C_L^m > 0$ even for very high m . This

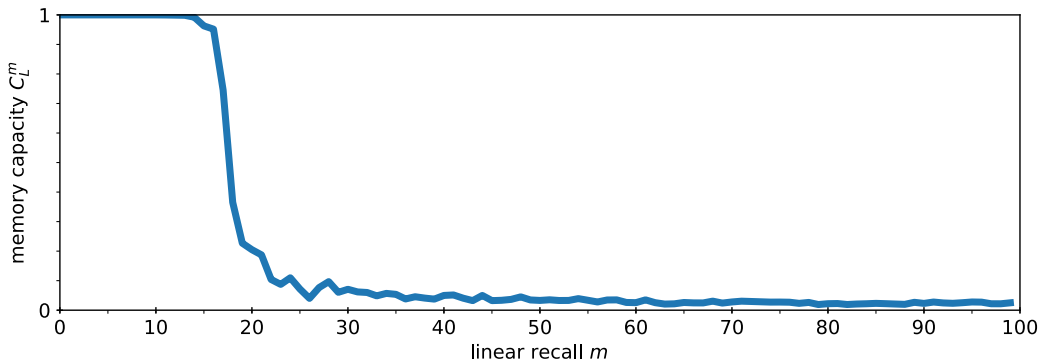


Figure 4.5: Examples of a memory curve, i.e. the linear memory capacity C_L^m in testing as defined in Eq. (2.58) for the m -step linear recall as a function of the step m , where higher m lie further back in the past. Parameters: $\text{Im}(\gamma) = -0.1$, $\omega = 1$, $\lambda = -0.02$, $\phi = 0$, $G = 0.01$, $\kappa = 0.1$, $\tau = 2176$, $N_V = 128$, $T = 1536$, $\theta = 12$, $K_{\text{training}} = 5000$, $K_{\text{testing}} = 5000$, $K_{\text{buffer}} = 1000$.

is due to numerical precision and the strictly positive definition of C_L^m and does not represent a real memory of the system.

The memory curve of Fig. 4.5 is only an example for one specific combination of λ and feedback phase ϕ , and therefore to explain the variations of the NRMSE in the two-dimensional scan shown in Fig. 4.2 such a memory curve has to be calculated for every parameter combination. One of the great advantages of the reservoir computing paradigm is the ability to train different output weights for different tasks simultaneously, as the training does not affect the internal dynamics of the reservoir. This means, that the linear memory capacity can be calculated for all step lengths m simultaneously from the same random number base and this is also how it is done in this thesis, as this saves a lot of computational effort. However, to present the results of the linear memory capacity in a two-dimensional form comparable to Fig. 4.2, the information needs to be compressed better. Different methods are possible, of which three shall be discussed in the following.

A simple way to summarize the complex information contained in the memory curve of Fig. 4.5 is to calculate the total linear memory capacity $C_{L,tot} = \sum_{m=0}^{\infty} C_L^m$. Because the linear memory capacity typically drops rather quickly towards high m , this means that the total memory capacity is a measure of the length of the systems memory. However, as mentioned in Sec. 2.5.7 of the theory and as can be seen in the example memory curve of Fig. 4.5, the numerically obtained linear memory capacity C_L^m never drops perfectly to 0 due to the finite numerical precision. Because the individual memory capacities C_L^m of length m are always positive, this means that $C_{L,tot}$ would just grow unbounded if larger and larger m are included,

even when the underlying system has already completely lost all memory. To prevent this behaviour from overshadowing the real system characteristics, the total memory capacity is therefore calculated by summing the truncated linear memory capacities C_L^m , where every $C_L^m < 0.05$ has been set to 0. This is enough to ensure numerical stability for the parameters used here. The exact value of this threshold does not drastically shift the outcome.

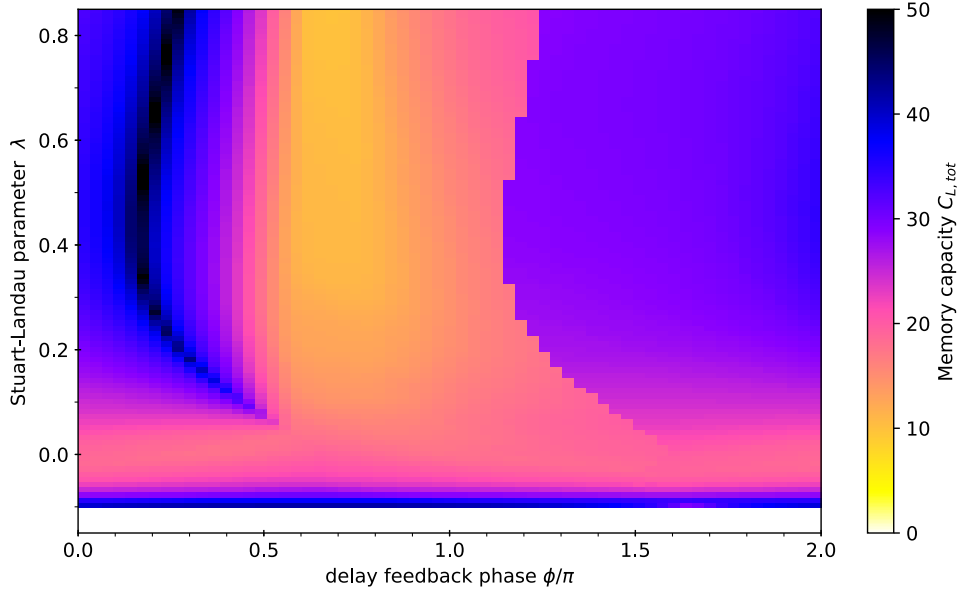


Figure 4.6: Parameter scan for the single Stuart-Landau oscillator with delayed feedback as given by Eq. (4.1) for different feedback phase ϕ and Stuart-Landau parameter λ . The colour code indicates the total linear memory capacity $C_{L,tot}$ as defined in Eq. (2.59). Every $C_L^m < 0.05$ was not counted and set to zero to correct for numerical precision. The memory capacity was evaluated with the same random numbers as produced for NARMA10 and all parameters and hyper-parameters are identical to Fig. 4.2. Parameters: $\gamma = -0.1$, $\omega = 1$, $G = 0.01$, $\kappa = 0.1$, $\tau = 2176$, $N_V = 128$, $T = 1536$, $\theta = 12$, $K_{\text{training}} = 5000$, $K_{\text{testing}} = 5000$, $K_{\text{buffer}} = 1000$.

Fig. 4.6 shows the results for the two-dimensional parameter scan of the single Stuart-Landau oscillator with delayed feedback as given by Eq. (4.1) for different feedback phase ϕ and Stuart-Landau parameter λ , where the colour code now indicates the total linear memory capacity $C_{L,tot}$ as defined in Eq. (2.59). All parameters, masks, and even the random numbers used as training and testing data are identical to the NARMA10 plot shown in Fig. 4.2. There is a clear variation of the total memory capacity $C_{L,tot}$ across the parameter scan shown in Fig. 4.6, with values ranging from 0 (no memory) to more than 50 (very long linear

memory). When studying the landscape more in detail, one can also see that the regions of higher linear memory capacity generally coincide with those of good NARMA10 performance, i.e. low NRMSE in Fig. 4.2. This is not too surprising, as the NARMA10 task is known for having a rather long memory requirement. Naturally, the regions where the system does not react at all to input show a total memory capacity of $C_{L,tot} = 0$ and are visible as the white regions in Fig. 4.6 for $\lambda < 0$. The abrupt change in the memory capacity for large λ and feedback phases $\phi \approx 1.2\pi$ also coincide with the abrupt change of the NRMSE in Fig. 4.2 for the NARMA10 task. This shows that both a qualitative change in the system state by switching attractor basins and bifurcations can leave a visible mark in the total linear memory capacity.

However, studying the total linear memory capacity $C_{L,tot}$, i.e. the sum of all memory capacities, is not the only way to evaluate the memory curve presented in Fig. 4.5. Especially for a case such as the NARMA task, which is always defined with respect to a certain length (here always NARMA10), it only seems natural that inputs far in the past should not play any role. Hence, $C_{L,tot}$ could be artificially inflated and become irrelevant. Only the memory capacity C_L^m for a specific m may be important for the task at hand. Thus, in the next step the memory function shall be evaluated at a specific point m .

Figure 4.7 shows the two-dimensional parameter scan of the single Stuart-Landau oscillator with delayed feedback as given by Eq. (4.1) for different feedback phase ϕ and Stuart-Landau parameter λ . This time, the colour code now indicates the linear memory capacity C_L^{15} as defined in Eq. (2.58). This is chosen, as the NARMA10 task is not only dependent on the last 10 inputs, but also an iterative formula of length 10 itself, so that a longer memory should still benefit the system. The parameters, random numbers and memory curves are exactly the same as evaluated for Fig. 4.6, which showed the total linear memory capacity. Hence, the agreement between these two evaluation methods is very good.

Large regions of the parameter space are coloured in black in Fig. 4.7, indicating that the linear memory C_L^{15} for 15-steps into the past is almost perfect. These are also the regions, where the total linear memory capacity $C_{L,tot}$ is larger than 15 in Fig. 4.6. Conversely, where C_L^{15} is small in Fig. 4.7 (white regions), the total linear memory capacity is also markedly lower in Fig. 4.6 (white and yellow regions). However, the overall variation when just looking at one particular value of the memory curve is less drastic, as large parts of the parameter space in Fig. 4.7 show a saturated, maximal linear memory capacity close to 1. On the other hand, these regions (black in Fig. 4.7) still show variations in the total linear memory capacity (Fig. 4.6) and the NARMA10 task (Fig. 4.2). Focusing just on one specific linear memory capacity C_L^m therefore in general is of limited use. The sole advantage of

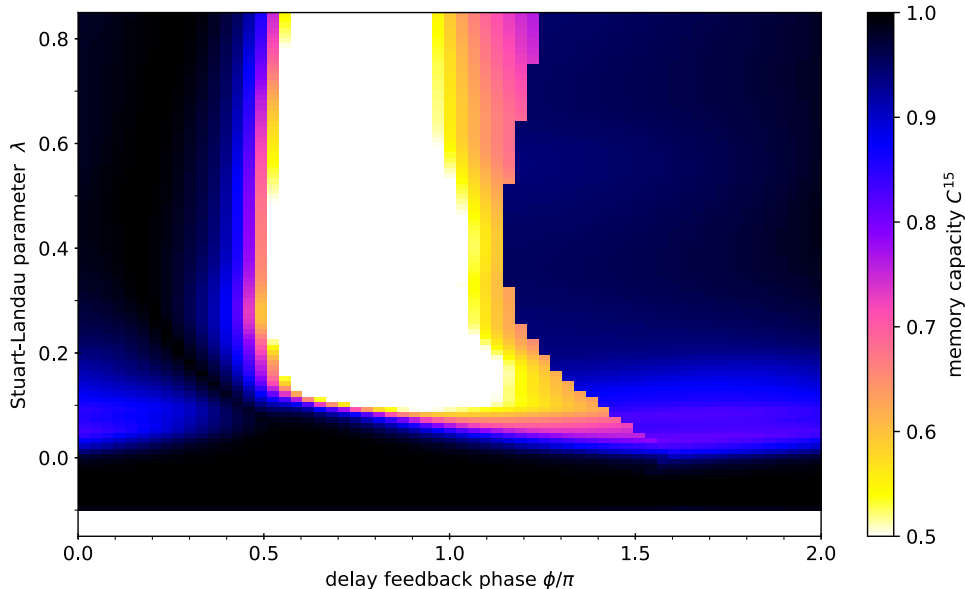


Figure 4.7: Parameter scan for the single Stuart-Landau oscillator with delayed feedback as given by Eq. (4.1) for different feedback phase ϕ and Stuart-Landau parameter λ . The color code indicates the linear memory capacity C_L^m as defined in Eq. (2.58) for $m = 15$ steps in the past. The memory capacity was evaluated with the same random numbers as produced for NARMA10 and all parameters and hyperparameters are identical to Fig. 4.2 and Fig. 4.6. Parameters: $\gamma = -0.1$, $\omega = 1$, $G = 0.01$, $\kappa = 0.1$, $\tau = 2176$, $N_V = 128$, $T = 1536$, $\theta = 12$, $K_{\text{training}} = 5000$, $K_{\text{testing}} = 5000$, $K_{\text{buffer}} = 1000$.

this approach is the easy implementation, as only a single linear recall has to be evaluated.

Figure 4.8 shows a third and final version for an evaluation of the memory for the two-dimensional parameter scan of the Stuart-Landau oscillator with delayed feedback, which will be explained now. The parameters, masks, initial conditions and random numbers are identical to the previous figures and given in the caption. The total linear memory capacity shown in Fig. 4.6 can start adding up contributions for steps very far back in the past, i.e. large m , and hence yield unrealistically large variations. On the other hand, when only a specific memory capacity is studied, such as C_L^{15} in Fig. 4.7, many variations disappear as this particular linear memory capacity will be either close to 0 or close to 1. The final evaluation method shown in Fig. 4.8 therefore makes use of the usually clearly distinct regions in the memory curve, such as in the example shown in Fig. 4.5: There is a critical m_c after which the memory capacities C_L^m rapidly drops off. In the example memory curve of Fig. 4.5 this critical memory length was roughly $m_c \approx 15$. For the eval-

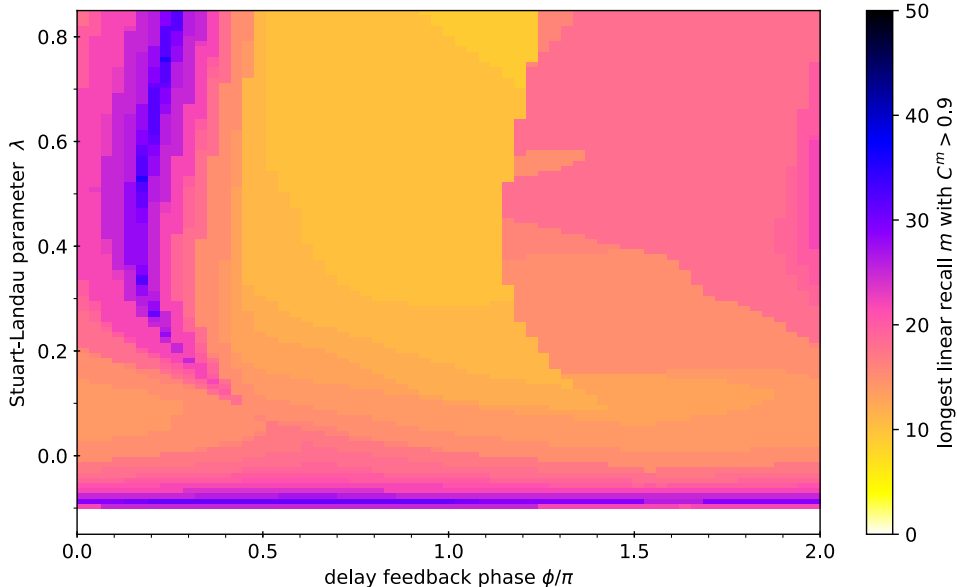


Figure 4.8: Parameter scan for the single Stuart-Landau oscillator with delayed feedback as given by Eq. (4.1) for different feedback phase ϕ and Stuart-Landau parameter λ . The color code indicates the length of the memory, i.e. the critical m_c for which $C_L^m > 0.9 \forall m < m_c$. The memory capacity was evaluated with the same random numbers as produced for NARMA10 and all parameters and hyperparameters are identical to Fig. 4.2, 4.7 and 4.6. Parameters: $\gamma = -0.1$, $\omega = 1$, $G = 0.01$, $\kappa = 0.1$, $\tau = 2176$, $N_V = 128$, $T = 1536$, $\theta = 12$, $K_{\text{training}} = 5000$, $K_{\text{testing}} = 5000$, $K_{\text{buffer}} = 1000$.

uation used in Fig. 4.8, this threshold is defined to be the largest m_c for which $C_L^m > 0.9 \forall m \leq m_c$. Blue and black colours in Fig. 4.8 therefore indicate a long memory of high quality, while yellow and white colours indicate that already inputs not very far in the past are being at least partially forgotten. This definition will be called ‘critical memory length m_c ’ from here on.

The critical memory length m_c is especially suited for the NARMA10 task. When the system exhibits an $m_c < 10$ this indicates that even for the last 10 inputs the linear memory quality is low. Because the NARMA task is defined with respect to a length, the critical memory length m_c can naturally be compared with this and in fact it is easy to see that regions with a critical memory length m_c shorter than 10 in Fig. 4.8 have a high NARMA10 NRMSE in Fig. 4.2.

The three methods of evaluating the memory curves studied here and shown in Fig. 4.6, 4.7 and 4.8 overall yield a similar picture when their extreme values are observed. They do however differ in the details. Moreover, the dynamical system used here is relatively simple. There is no mathematical reason demanding the memory

curve has to monotonically decay. If it indeed would start to exhibit 'resurgence peaks', this would drastically change the behaviour of some of the measures, especially between the total linear memory capacity $C_{L,tot}$ and the critical memory length m_c used for Fig. 4.8. Which way of summarizing the complex memory curve is the best will ultimately depend on the task that is being studied. Because the task of interest here is the NARMA10 task, the main method will be the critical memory length m_c .

4.1.4 Influence of the system timescales

The single Stuart-Landau oscillator system as shown in Eq. (4.1) contains three distinct time-scales, which will have to be optimally scaled with respect to each to obtain favourable reservoir computing performance: First, the Stuart-Landau oscillator without feedback has some intrinsic system time scale, especially with respect to its amplitude damping. This can be linked to the Lyapunov-exponents of the stable and unstable solutions, and is especially dependent on the parameter λ and typically of order 10 due to the choice of the nonlinearity $\text{Re}(\gamma) = -0.1$ in this thesis. A second timescale is obviously introduced by the delayed self-feedback in shape of the delay time τ . To facilitate an effective increase in the internal dimension of the system as would be required for optimal reservoir computing, this delay time τ should be *significantly larger* than the typical time scales of the oscillator without delay. If the time-scales were comparable, they could be absorbed into one 'effective' model with respect to this short time-scale, and the effect of the delay in increasing the phase-space dimension of the system would be rapidly diminished. However, finding a quantitative way to analyse the effectiveness of a particular delay length τ is still an open problem, as it is not entirely clear what constitutes a 'large' delay. Lastly, the reservoir computing system also contains the additional time scale of the clock cycle T of the input and read-out used in reservoir computing. This clock cycle T does not need to coincide with the delay-time τ of the system, despite this always being the studied case for the earlier publications using reservoir computing. How the timescales affect reservoir computing will be studied in this section.

To study the interplay of these time-scales, two of them will now be varied: The delay-time τ and the clock cycle T . The third one can be kept constant, as only its relative value to the other two is important. The delay time τ can be accessed by changing the length of the delayed feedback loop in an optical setting, while the clock cycle T should often be changeable with the help of the electronic controls of the reservoir computer. The intrinsic time scale of the system may also be the hardest to change in experiments, and thus changing only τ and T is a realistic procedure.

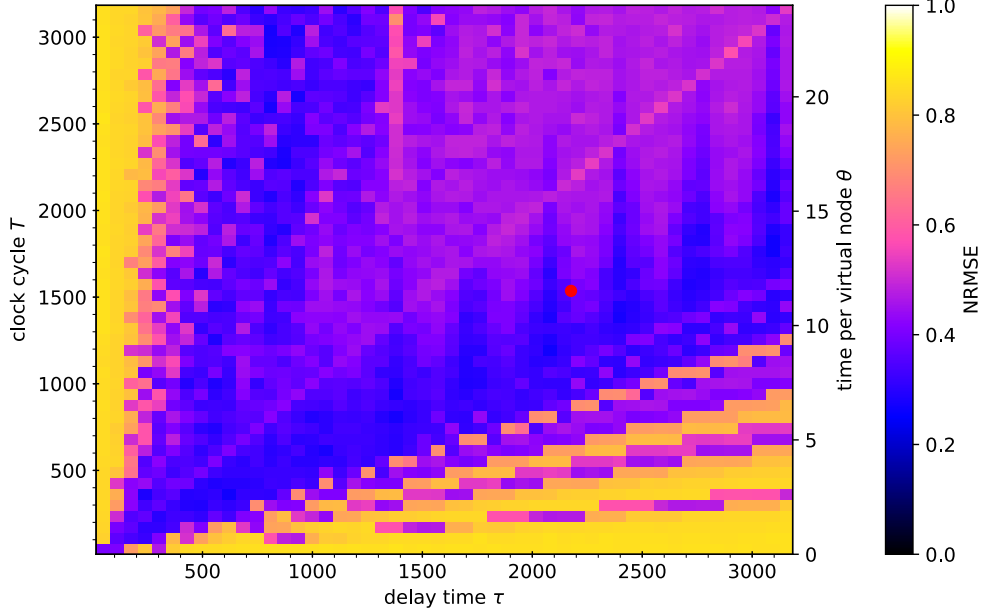


Figure 4.9: Influence of the time scales on the reservoir computing performance of the single Stuart-Landau oscillator with delayed feedback as given by Eq. (4.1). The color code indicates the NARMA10 NRMSE after the training and is plotted versus delay time τ and clock cycle T . Because the virtualization factor is fixed, the y-axis can also be converted into the time per virtual node θ (right y-axis labels). The parameters are identical to Fig. 4.2 with $\lambda = -0.02$ and $\phi = 0$. The red dot indicates the choice of τ and T used in the other simulations of Eq. (4.1). Parameters: $\gamma = -0.1$, $\omega = 1$, $G = 0.01$, $\lambda = -0.02$, $\phi = 0$, $\kappa = 0.1$, τ as indicated on the bottom axis, $N_V = 128$, T as on the y-axis, θ as on the second y-axis, $K_{\text{training}} = 5000$, $K_{\text{testing}} = 5000$, $K_{\text{buffer}} = 1000$.

Figure 4.9 shows a two-dimensional scan of the single Stuart-Landau oscillator with delayed feedback of Eq. (4.1), where the colour code indicates the NARMA10 NRMSE. Here, the x-axis is the delay time τ , while the y-axis is the clock cycle T . Because the virtualisation factor $N_V = 128$ is kept constant, the clock cycle T can also be converted into the time per virtual node θ , which is done with the second y-axis in Fig. 4.9. The parameters for the simulations of Fig. 4.9 are identical to those of the early NARMA10 scan of Fig. 4.2 with now fixed $\lambda = -0.02$ and $\phi = 0$. Conversely, the parameter choice of τ and T for all other simulations in this section is indicated by the red dot in Fig. 4.9. The NARMA10 NRMSE has a clear dependence on T and τ , as can be seen by the colour code of Fig. 4.9. For too small τ or T , the performance drastically drops down (yellow border regions in Fig. 4.9). On the other hand, there is a large portion of τ - T combinations that allow for a reasonably low NRMSE (blue regions in Fig. 4.9). These are centred around $\tau \approx T$ but allow for large deviations. There is a clear structure within these regions of

good NRMSE. For example, exactly on the diagonal of Fig. 4.9 for $\tau = T$, the NRMSE is visibly higher than in its direct neighbourhood. This is independent of the actual size of T , and seems to be only influenced by the resonance. There are further similar resonance lines that can be seen, for example $T = 2\tau$ or $T = \tau/3$. In fact, one can reasonably hypothesize that these resonances should be roughly located at:

$$p\tau = qT \quad \text{with} \quad p, q \in \mathbf{N}, \quad (4.5)$$

where resonances with higher p and q are less visible in Fig. 4.9. Naturally, the finite resolution of Fig. 4.9 only allows for so many resonances to be visible. The resonance structure of the NRMSE visible in Fig. 4.9 is not unique to the Stuart-Landau case, but can be observed in many different systems. These resonances were found for every system tried during the numerical preparations of this thesis and have also been known from the literature, where Ref. [PAQ12] appears to contain the earliest mention.

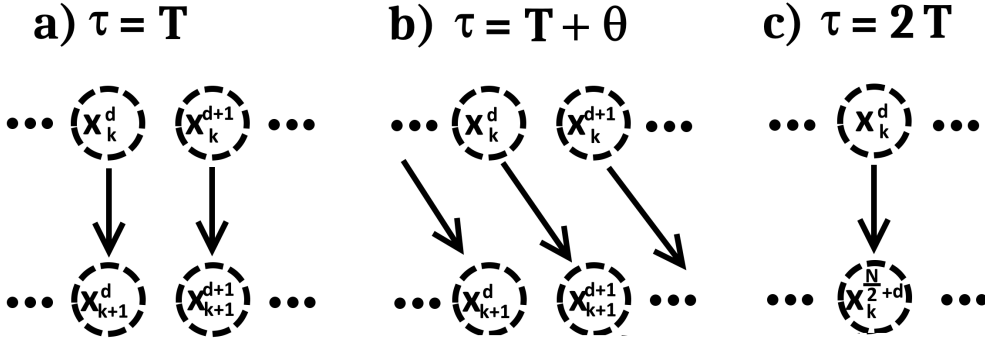


Figure 4.10: Sketch of the connections (arrows) between virtual nodes (dashed circles) representing the reservoir state x_k^d for a time-multiplexed reservoir for different τ and T . a) resonant case of $\tau = T$: every virtual node x^d connects to itself between timestep k and $k + 1$. b) $\tau = T + \theta$ every virtual node x_k^d from input time step k connects to its neighbour x_{k+1}^{d+1} in the next timestep $k + 1$. c) $\tau = 2T$ (resonance): Every node connects to the virtual node $N_V/2$ along the ring apart.

There exists an intuitive explanation for this effect, that is caused by the interplay of time-multiplexing and delay, which is sketched in Fig. 4.10: The time-multiplexing creates N_V 'virtual nodes' x^d , that are effectively time-slices along the delay-line of the system. However, they can also be approximated as a network [APP11], where nodes that influence each other are connected by an edge. Because the time-series has to be chopped into pieces of length T , these nodes live in discrete time of the input u_k , so that for each input step k a virtual network state

of N_V nodes exist as described by x_k^d with $d \in [0, \dots, N_V]$. The virtual nodes are shown as dotted circles in Fig. 4.10, with nodes from the same time-step k horizontally aligned and their connections indicated by the arrows pointing towards the next time step $k + 1$ below them. The resonant case of $\tau = T$ is detrimental to reservoir computing as can be seen from Fig. 4.9. The structural details of the virtual network topology for this $\tau = T$ are sketched in Fig. 4.10 a). Because the information returns exactly after τ due to the delay, each node will effectively be projected onto itself. This means that information is not strongly transferred to other virtual nodes. If, on the other hand, there is no resonance, the situation changes. In Fig. 4.10 b) the clock cycle T is one time per virtual node θ shorter than τ . This means, that after one round trip, the delay will return the information to the next virtual node x_{k+1}^{d+1} , and not the original. This at first may seem like a trivial difference: after all, the information should remain in the reservoir either way and shifting it to a different virtual node should hardly matter. However, the nodes are not interchangeable, as they have different input weights w^{in} due to the mask $M(t)$. In particular, there may be some virtual nodes with very small input weights $w^{in} = 0$. In a resonant case $\tau = T$, these nodes will barely contain information. However, if they are receiving input from their neighbouring node, they can serve as an effective storage for information and extend the memory of the system. With the information then being transferred to their neighbours in the next time step $k + 2$, such a non-resonant case provides a long and complex system response.

A different way of viewing this process can also be illustrated by thinking of the input weight vector W^{in} , i.e. the discrete mask values M^d as projecting the input u_k into some dimension in the high-dimensional phase space \mathbf{R}^D of the virtual network. For the resonant case of $\tau = T$ the delay term will be parallel to the weight vector W^{in} , as the delay is merely an echo of the previous time-step. Thus, the new information and the delay-transmitted information will be projected on top of each other in phase space and overwrite themselves. This reduces the memory capacity of the system, and hence also the NARMA10 NRMSE. If however, the delay is non-resonant, the projection will be in a different direction, as the weights of the delayed term will have shifted. The visualisation of Fig. 4.10 can therefore explain the complex behaviour of the time-scale resonance $\tau = T$ in Fig. 4.9.

The cause for the smaller resonances of Eq. (4.5) visible in Fig. 4.9 is similar to those of the main resonance $T = \tau$. The case for $\tau = 2T$, which is also visible in the colour code of the NRMSE in Fig. 4.9 is sketched in Fig. 4.10 c). For $\tau = 2T$ the virtual network is projecting its own state x_k^d onto the virtual node that is $N_V/2$ further along the virtual network. Going from input time-step k to $k + 1$, this may be a good projection as it spreads the information along the virtual network. However, for every second input cycle $k + 2$ this means that the information will

return to the original node. The return of the information to the original node is delayed by a bit, but the whole dimension of the virtual network is still poorly used in this case. This is why the $\tau = 2T$ is still clearly visible in the NRMSE in Fig. 4.9 and not as pronounced as the main resonance $\tau = T$. The same reasoning can of course be extended to all other resonances $p\tau = qT$, where their impact should be larger for smaller $p, q \in \mathbb{N}$.

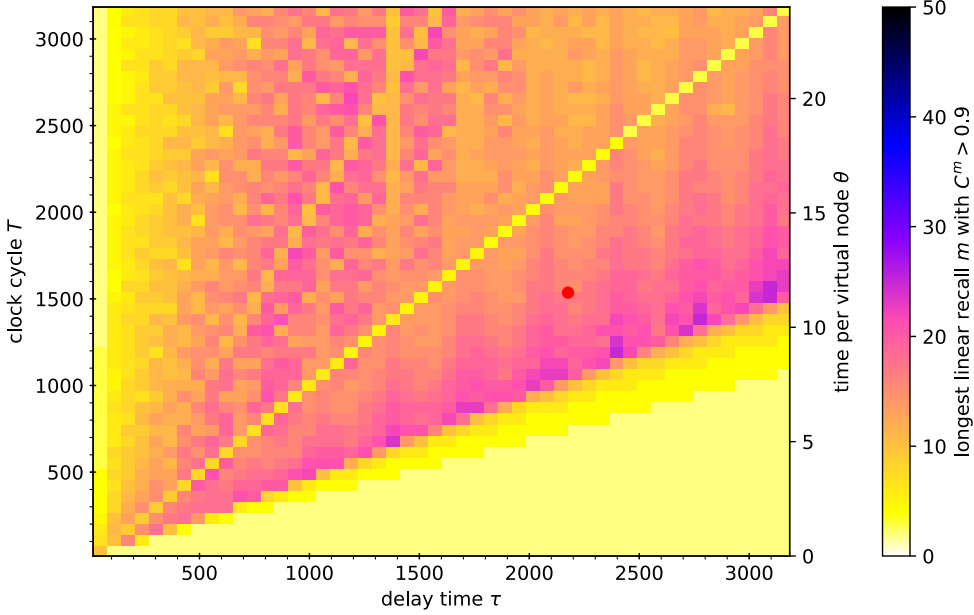


Figure 4.11: Influence of the time scales on the memory capacity of the single Stuart-Landau oscillator with delayed feedback as given by Eq. (4.1). The colour code indicates the lowest m_c , for which $C_L^m < 0.9$, i.e. where the linear memory starts to decline. The critical memory length m_c is plotted versus delay time τ and clock cycle T . The parameters are identical to Fig. 4.9. The red dot indicates the choice of τ and T used in the other simulations of Eq. (4.1). Parameters: $\gamma = -0.1$, $\omega = 1$, $G = 0.01$, $\lambda = -0.02$, $\phi = 0$, $\kappa = 0.1$, τ as indicated on the bottom axis, $N_V = 128$, T as on the y-axis, θ as on the second y-axis, $K_{\text{training}} = 5000$, $K_{\text{testing}} = 5000$, $K_{\text{buffer}} = 1000$.

The interplay of the different time-scales also influences the memory capacity. Figure 4.11 shows the memory of the Stuart-Landau system with delayed feedback versus variations of the delay time τ and clock cycle T . The colour code indicates the length of the linear memory as defined by the critical m_c as introduced in Sec. 4.1.3, i.e. Fig. 4.11 depicts which m_c the memory curve C_L^m drops below 0.9. Thus, higher values (dark and blue colours in Fig. 4.11) indicate a long memory, while low values (white and yellow in Fig. 4.11) are regions with short linear memory. The results of Fig. 4.11 clearly show the same resonance structure as the

NARMA10 NRMSE of Fig. 4.9. This proves, that the deterioration of the reservoir computing capabilities found previously for resonances of τ and T is at least partly caused by a loss of linear memory capacity. While the main resonance of $T = \tau$ is clearly visible in Fig. 4.11, the minor resonances are not as pronounced. This shows, that choosing the delay time τ and clock cycle T identical is almost the worst possible choice for the linear memory.

4.1.5 Influence of hyper-parameter K_{training}

In machine learning, the outcome of the training does not only depend on the system parameters, which define the local dynamics, e.g. the parameters λ , frequency ω , feedback strength κ and feedback phase ϕ in Eq. (4.1), but also on some parameters describing the training process itself. These parameters are usually called 'hyper-parameters', as they do represent parameters that are only used for the learning. They are important for fixing the weights of the reservoir computer. However, once the training is done they no longer play any role. The reservoir computing paradigm is relatively simple when compared to other machine learning schemes, and thus only the length of the training sequence K_{training} is a true hyper-parameter. The input scaling G and clock cycle T are not true hyper-parameters here, as they are still important even after the training. Some implementations of reservoir computing make use of a regularization of the training to prevent overfitting, in which case the regularization factor would also be a hyper-parameter. However, so far it has not seemed to be necessary for the system as used here. This section will shortly investigate the importance of the only hyper-parameter of the system: the training length K_{training}

The mathematical details of the training are presented in Sec. 2.5.4 of the theory chapter, but a short reminder of the importance of the training length K_{training} will be given here: The system has to learn to predict the desired outcome o_k , by being trained on an input u_k of length K_{training} . During the training step, the system is fed with the input and the system state is readout and recorded. This training time series is used to fix the output weights W^{out} in an optimal fashion. Afterwards, the system is fed a new input sequence u_k called the 'testing sequence', and its system response is once again recorded. The readout weights W^{out} are not changed in the testing run, the trained weights are merely applied. The performance of both the fitting procedure during the training as well as the testing afterwards are measured with NRMSE, memory capacities or other measures where applicable.

One can expect *a priori* that the system will become better with longer training sequences K_{training} , as the system will be exposed to more data and thus be able to generalize more. Even humans find it hard to predict from a small sample size to a large cohort, which is the cause of many cognitive biases. Similarly, a machine

learning system cannot learn to distinguish between important features of the task in general and statistical flukes that are only present in the training sequence u_k if the training is too short, i.e. K_{training} is small. When the system tries to learn some general features, shows very low errors for the training sequence, but then has much larger errors during the testing stage. This indicates a fundamental problem of the learning procedure. A system that is unable to solve more than the specific training sequence u_k suffers from so-called *over-fitting*. Over-fitting is conceptually related to the interpolation and regression of statistical analysis: Any sequence of K real numbers can in principle be perfectly fitted by a polynomial of order $K - 1$. However, when one is trying to find a trend in large amounts of (potentially noisy) data, the focus is on the average or mean trends, not on the particulars of the training. ‘Over-fitting’ in machine learning is similar, as the used learning scheme tries to ‘perfectly fit’ the training data instead of learning the underlying patterns. Like statistical models, machine learning systems such as reservoir computing can have large numbers of free parameters, allowing the system to easily ‘fit’ the presented training sequence u_k . Usually, over-fitting can be countered by regularization or longer training sequences.

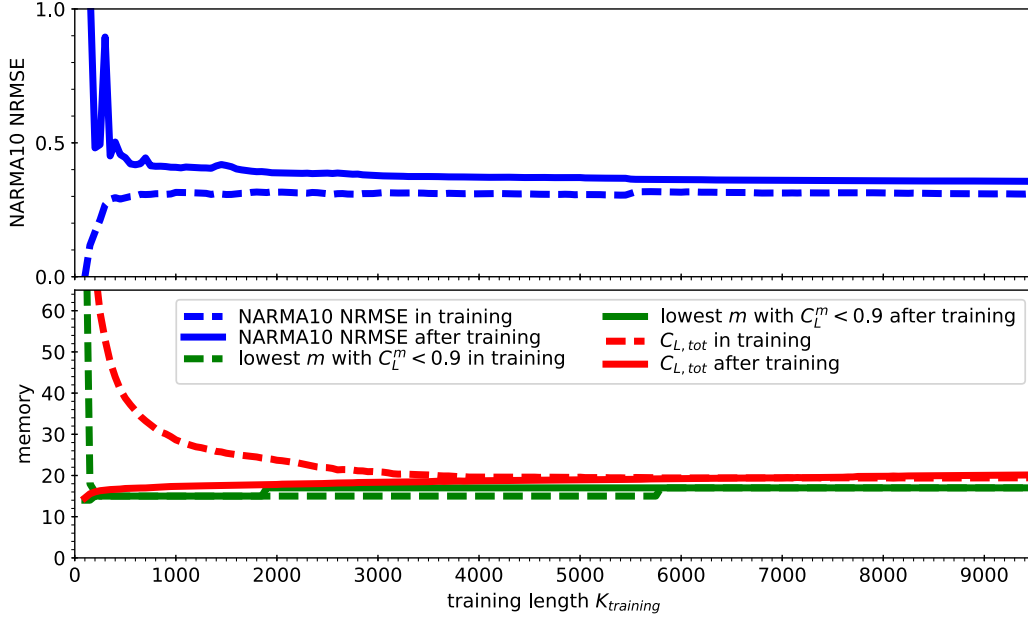


Figure 4.12: Influence of the training length K_{training} on the NARMA10 NRMSE (blue lines, top), total linear memory capacity (red lines, bottom) and memory cutoff m_{crit} (green, bottom). The values for the training (dashed lines) and for an independent testing run (solid lines) are shown. Parameters: $\text{Im}(\gamma) = -0.1$, $\omega = 1$, $\lambda = -0.02$, $\phi = 0$, $G = 0.01$, $\kappa = 0.1$, $\tau = 2176$, $N_V = 128$, $T = 1536$, $\theta = 12$, K_{training} as indicated along the x-axis, $K_{\text{testing}} = 5000$, $K_{\text{buffer}} = 1000$.

Figure 4.12 shows the result of a simulation for the influence of the training length K_{training} on the reservoir computing performance of the single Stuart-Landau oscillator with delayed feedback (Eq. (4.1)). The parameters are given in the caption and identical to the typical parameters used in this chapter so far. All variables were kept constant as far as possible during the simulations, i.e. the training was done on the same sequence of random numbers u_k , with only different cut-offs for the different K_{training} . Masks and testing sequences were also kept identical for all simulations used for Fig. 4.12.

The top panel of Figure 4.12 shows the results for the NARMA10 NRMSE (blue curves). The dashed line indicates the NRMSE during training. The error clearly increases with longer K_{training} . This may seem contradictory at first, but is the result of the previously mentioned problem of *over-fitting*. For small data samples, i.e. small K_{training} , the reservoir computing system contains more than enough degrees of freedom to fit almost any function. For the system used in Figure 4.12 the number of degrees of freedom was $N_V = 128$, so that the NRMSE of the NARMA10 task (blue dotted line) is virtually 0 for $K_{\text{training}} < 128$. On the other hand, if the system performance is then evaluated on an independent set after the training (blue solid line in Fig. 4.12), the resulting NARMA10 NRMSE is very large. This indicates a poorly trained reservoir. In general, when the system is not over-fitted, the NRMSE between training and testing should be very similar. Thus, the distance between the solid and dashed lines of the same colour in Fig. 4.12 can be used to estimate the over-fitting. For the NARMA10 task, there is a drastic improvement already for $K_{\text{training}} \approx 1000$. However, the testing NRMSE (blue solid line) continues to drop and approach the NRMSE during training (blue dashed line) for a much larger range of K_{training} .

The bottom panel of Fig. 4.12 shows the results of the influence of the training length on the memory capacity. Two different measures as introduced in Sec. 4.1.3 are shown: The total linear memory capacity $C_{L,tot}$ (red lines) and the critical memory length m_c (green lines), i.e. where the linear memory capacity C_L^m starts to fall below 0.9. The dashed and solid lines indicate training and testing results, respectively. The bottom panel of Fig. 4.12 reveals that the K_{training} -length required to prevent over-fitting of the total linear memory capacity $C_{L,tot}$ (red lines) is in the range of 5000, which is significantly longer than for the NARMA10 NRMSE (blue lines, top). The critical memory length (green lines in Fig. 4.12), on the other hand, converges very quickly. The jumps visible for $K_{\text{training}} \approx 1800$ and 5800 are due to the discrete nature of m_c and represent a change of 1 in m_c . In general it seems that the critical memory length m_c therefore is a more robust measure, i.e. less easily influenced by over-fitting. For the rest of the simulations in this thesis, the training will be set to $K_{\text{training}} = 5000$ to be on the safe side and avoid over-fitting, even if parameters and learning behaviour should slightly change.

The influence of the length of the evaluation step K_{testing} was also investigated. However, it has turned out that this step is not nearly as important for the resulting NRMSE and memory capacities. Even relatively small testing lengths $K_{\text{testing}} \geq 100$ yield an accurate prediction of the reservoir computing performance. Thus, the length of $K_{\text{testing}} = 5000$ used mostly in this thesis is more than enough. The importance of the training and evaluation lengths should be a general property of reservoir computing systems with the same number of trained parameters (i.e. read-out dimension). The preceding results and considerations are therefore applicable to other reservoir computing systems with a read-out dimension of 128, in particular also the systems of the next section.

4.1.6 Possible extensions

The single Stuart-Landau oscillator with delayed feedback can also be seen as an approximation of a laser with optical feedback, such as Ref. [BRU13a]. The experimental and theoretical literature contains a large variety of modified laser-based reservoir computing schemes, of which many could also be tested for the more general Stuart-Landau equations. For example, a popular alternative to direct optical feedback, as is indirectly modelled by Eq. (4.1) is the inclusion of 'opto-electronic feedback'. Optoelectronic means, that instead of the laser light being directly reflected back into the laser cavity, the intensity $|E|^2$ is externally measured. The injection current is then varied based on the measured intensity. This could be modelled by a modified version of the Stuart-Landau equation with feedback of Eq. (4.1) in the shape of:

$$\frac{dZ}{dt} = \left(\lambda + \kappa |Z(t - \tau)|^2 + GJ(t) + i\omega + \gamma |Z|^2 \right) Z, \quad (4.6)$$

where κ is now the opto-electronic delay-coupling strength. The delayed feedback term is given by $\kappa |Z(t - \tau)|^2$ and no longer contains any phase information. Due to the correspondence between the Stuart-Landau bifurcation parameter λ and the pump current p of the Lang-Kobayashi system, Eq. (4.6) approximates some features of opto-electronic feedback. However, it is important to note that the Lang-Kobayashi system contains both an additional equation in the form of the carrier density N_e , and also a richer dynamical phase space with the appearance of 'relaxation oscillations'. Thus, Eq. (4.6) will definitely yield a different behaviour than a true laser model.

Another choice that was made for the reservoir computing system as given by the single Stuart-Landau oscillator modelled by Eq. (4.1) was the read-out procedure. Inspired by how photodiodes are used to record the light intensity of a laser, only the absolute squared $|Z|^2$ of the complex amplitude was used for the reservoir

computing. This means, that the phase-information of the system has been entirely neglected. Recent results shown in Ref. [NGU15] show the possibility of the much faster phase dynamics that could potentially be used for the read-out instead. This is also possible to implement in the Stuart-Landau system. However the data-input $J(t)$ acts a like a modified pump-current in the scheme as shown so far, and does not directly excite phase dynamics. To make full use of the of the phase dynamics as well, the system likely requires 'optical injection' as well.

The Stuart-Landau oscillator with delayed feedback and pseudo-optical injection can be modelled by:

$$\frac{dZ}{dt} = \left(\lambda + i\omega_d + \gamma|Z|^2 \right) Z + \kappa e^{i\phi} Z(t - \tau) + \kappa_{inj}(Z_0 + GJ(t)), \quad (4.7)$$

$$(4.8)$$

where Z_0 is the base injection amplitude, ω_d now the difference frequency of the free-running oscillator and the injected complex amplitude and κ_{inj} the injection strength. To perform reservoir computing, a phase-sensitive readout then can be either based on the polar or Cartesian coordinates of Z : in the first case, each read-out step the absolute squared $|Z|^2$ and complex phase $\arg(Z)$ would be recorded, while in the second approach the system is measured in real $\text{Re}(Z)$ and imaginary part $\text{Im}(Z)$. It should be advantageous to record the system with respect to either the frequency of the injection or maybe even at its own average frequency (both cases become identical for injection-locking). Otherwise, the complex Stuart-Landau oscillator as modelled by Eq. (4.7) will have additional phase-oscillations due to the free-running frequency of the system, which could potentially completely scramble the phase-information if that frequency is very high.

The preceding paragraphs only outline a selection of possible extensions. The literature and experimental implementations for photonic reservoir computing have investigated many different aspects in recent years, and for many of these publications a similar Stuart-Landau system can be constructed. However, it is difficult to find general trends for the reservoir computing performance as a function of these changes, as these differences tend to merely change the interplay between non-linearity and linear memory. Thus, their influence on the performance strongly depends on the individual task that is considered. The focus here is on basic and quantifiable differences between systems. To connect with the first chapters of this thesis, no such complicated variations of Eq. (4.1) will be studied, but instead networks shall now be used as reservoir computers.

4.2 Time-multiplexed Networks

In this section ensembles of oscillators will be investigated as an extension of the individual Stuart-Landau oscillator with delayed feedback shown in the previous one. The general properties of networks of Stuart-Landau oscillators when used as a reservoir computer will be systematically studied.

Due to the change of the reservoir computing system from a single oscillator to an ensemble of oscillators, a few adaptations of the readout and information injection procedure have to be made. A network can already contain a large number of degrees of freedom by construction and thus may already intrinsically be a suitable system for reservoir computing. In fact, the original papers by Jäger [JAE01] and Maass *et al.* [MAA02] proposed the reservoir computing ideas purely in the context of networks. Only later was the reservoir computing paradigm extended to delay systems. Therefore, a variety of ‘echo state network’ and ‘liquid state machine’ papers from the early days of reservoir computing have already covered some of the properties of such reservoir computers. The networks covered in this thesis will differ from the literature in two fundamental ways: While previously, the system considered were mostly random networks, here the focus will be on regular networks, such as the ring networks introduced in Chap. 3. Furthermore, these regular networks will also include delay and make use of the time-multiplexing paradigm of the delay-based reservoir approach. Continuing from the results of the previous section of the single Stuart-Landau oscillator with delayed feedback, this section will investigate the behaviour of ‘time-multiplexed networks’, i.e. systems containing both long delays and multiple coupled units. The focus in this section will not be on symmetry-broken states or a detailed analysis of the bifurcation landscape, but on the implications of time-multiplexing in networks on the reservoir computing capabilities. The results of this section were published in Ref. [ROE18a].

4.2.1 Time-multiplexing in networks

Time-multiplexing is the process of using a mask and sequential read-out in delay-based reservoir computers. It makes use of the high dimensional phase-space transients that occur in such delay-systems. For large systems without time-multiplexing, observing the system state is trivial. For time-multiplexed systems, the sequential nature of the information processing in a delay-system necessitates the introduction of additional read-out timings θ and the virtualisation factor N_V (see Sec. 2.5.5). The situation becomes even more complex when a delay-coupled network is studied, where parallel and sequential elements of reservoir computing are mixed.

There are multiple ways in which time-multiplexing can be introduced into a system of coupled oscillators, i.e. a network. The first and most straightforward would be to merely treat the network as a single, complex local model. This local model then needs to be extended with an external delayed feedback loop, and from there on the same methods as in the previous section can be applied. However, this approach has two distinct disadvantages: First, it is not entirely clear how a delayed feedback loop should be applied to a complex model, as many different options exist: Connecting every node with itself, connecting only a subset of nodes, connecting nodes with different nodes via delay etc. This may be great from a customization perspective, but is beyond the scope of this work, where only the fundamental properties of a these system shall be investigated. As stated earlier, the goal is explicitly not to find new record-breaking reservoir computers, so unnecessary complexity will be avoided. The second problem of this type of time-multiplexing with delay is in the need for additional connections. In an experiment, these additional links would mean unnecessary complexity and require more physical components, increasing the cost, maintenance and points of failure of the system.

Therefore, a different approach for the time-multiplexing of networks will be taken here. Instead of introducing additional delayed feedback loops, the system will be constructed as a network with delayed connections from the beginning. This means, that the subject of study are essentially the delayed networks of Sec. 3.3.6 and 3.4.4. For simplicity, all delay-connections will be assumed to have the same delay length τ . However, it seems possible that a system with a set of different delays τ_i for different connections i would allow for a wider spectrum of applications. This will have to be left for future investigations. Furthermore, it will also be assumed that all connections have the same coupling strengths and coupling phases. Thus, the networks studied in this thesis merely represent a minimalistic example of time-multiplexed networks for reservoir computing and many possible extensions exist.

4.2.2 Real and virtual nodes

To adequately describe time-multiplexed networks, a few details and concepts will be explained in the following paragraphs. A network consists of multiple oscillators that are connected via edges. To discern them from the ‘virtual nodes’ created by time-multiplexing, let these nodes be called ‘physical nodes’, ‘real nodes’ or ‘oscillators’ and let the number of real nodes be N_R . Each individual oscillator is a Stuart-Landau oscillator described by the complex amplitude Z_n and the time evolution is given by the ODE of Eq. (2.24). The real nodes are connected with (delayed) links. Depending on the network topology, each node can have multiple

links, the links can be bidirectional or unidirectional, and the system may or may not have symmetries.

For effective reservoir computing in large systems, a few extensions of the information feed-in mechanism need to be made. First, if the system contains N_R nodes which can serve as input, in the best case all of these nodes should be stimulated by the input u_k . However, if the network is made up of identical nodes in a symmetric setting, there exists the danger of all nodes behaving identically. For example, if the system is in the in-phase synchronized state where all local states are identical, the transients for the different real nodes will not differ if the same input $u(t)$ is applied to all real nodes. This is detrimental, because if the oscillators all react identically, the effective phase-space dimension of the network will be that of a single oscillator. However, reservoir computing requires large phase spaces. So to avoid problems with the system being locked into perfect synchronization for all times, any synchronisation needs to be broken up. The easiest way to ensure this, is to not let the oscillators have the same inputs $u(t)$.

There are multiple ways to solve the problem of avoiding identical inputs for different real nodes. One way is to stagger the input on the node number, e.g. have node n receive an input sequence $u(k - n)$ that is delayed by n steps. This way, unless the input sequence is trivial, each oscillator will have a different input at each time step. This also has the advantage of potentially extending the linear memory of the system. However, most of the time a fast information processing is desired, and staggering the information in this way gives the current input time step u_k a very weak weighting, as only a single node receives an input that is up to date.

In this thesis a second approach is taken: To diversify the transients of the network system, the input of the oscillators is already preprocessed by the masking scheme $J(t) = M(t \bmod T)u(t)$. A simple yet effective extension of the masking scheme then is to give each oscillator a different mask $M_n(t)$. With a different mask, the resulting dynamics will also be different. As for the single Stuart-Landau oscillator, the mask M will be a piece-wise constant function drawn from a binary distribution (see also the sketch of the masking in Fig. 4.1). The piece-length is the time per virtual node $\theta = T/N_V$. The input to all oscillators has to be synchronized, i.e. they have to share the same clock cycle T . However, in principle there could be differing numbers of virtual nodes per real node, which would mean a θ that also differs for different real nodes. To stay in the simplest case possible, here all of the N_R real nodes will each have a virtualisation factor of N_V , thus having the equal numbers of virtual nodes. The total read-out dimension is the product of N_V and N_R . Each virtual node can be seen as the $T/N_V = \theta$ -long part of the trajectory of the oscillators time trace $Z_n(t)$. Such a reservoir computer with

both virtual and real nodes shall be called a 'time-multiplexed network' from here on.

4.2.3 Stuart-Landau time-multiplexed network equations

Once a reservoir computing system consists of several oscillators, the question of how to connect them arises. There are many different network topologies that can be used, and the results may critically depend on the structure. The earliest papers concerning reservoir computing often investigated 'echo state networks' created with a random topology. However, this makes a systematic evaluation complicated. To connect with the knowledge obtained from the investigation of symmetry-broken states of the network in Chap. 3, regular networks will be used in this thesis. The equation of motion is once again based on the Stuart-Landau oscillator model of Eq. (2.24):

$$\frac{dZ_n}{dt} = \left(\lambda + GJ_n(t) + i\omega + \gamma|Z_n|^2 \right) Z_n + \kappa e^{i\phi} \sum_{l=0}^{N_R-1} A_{nl} Z_l(t - \tau), \quad (4.9)$$

$$(4.10)$$

Here, Z_n is the complex amplitude of Stuart-Landau oscillator n , of which overall N_R are in the network (real number of oscillators). The local parameters of all oscillators are identical, with bifurcation parameter λ , solitary frequency ω and nonlinearity γ independent of n . The only difference is the inclusion of the driving term $GJ_n(t)$, where G is the input scaling and $J_n(t)$ the masked input signal. The shape of J_n is given by the mask $M_n(t)$, which will define the number of virtual nodes N_V . Similarly, the clock cycle T and the time per virtual node θ only affect how $J_n(t)$ is constructed and how often the network state Z_n is read-out for the reservoir computing, but are not direct factors in Eq. (4.9). The coupling is modified by the global coupling strength κ and coupling phase ϕ , as was used before. The coupling topology is given by the coupling matrix A and the coupling terms are delayed by τ . Note, that for certain coupling matrices $A_{ii} \neq 0$ the system of Eq. (4.9) also contains a delayed self-coupling. The network equation of Eq. (4.9) can be seen as a generalization of the single Stuart-Landau oscillator with delayed feedback, because Eq. (4.1) can be obtained for $N_R = 1$ and $A = [1]$.

4.2.4 Importance of the system size

The time-multiplexing procedure for the delay-based networks is a generalization of the procedure for a single oscillator. Comparisons between different reservoir computing systems in general are difficult as different models, tasks and parame-

ters can give rise to vastly different performances. One important aspect of time-multiplexed networks that needs to be investigated here is the effect of the number of real oscillators N_R and the virtualisation factor N_V .

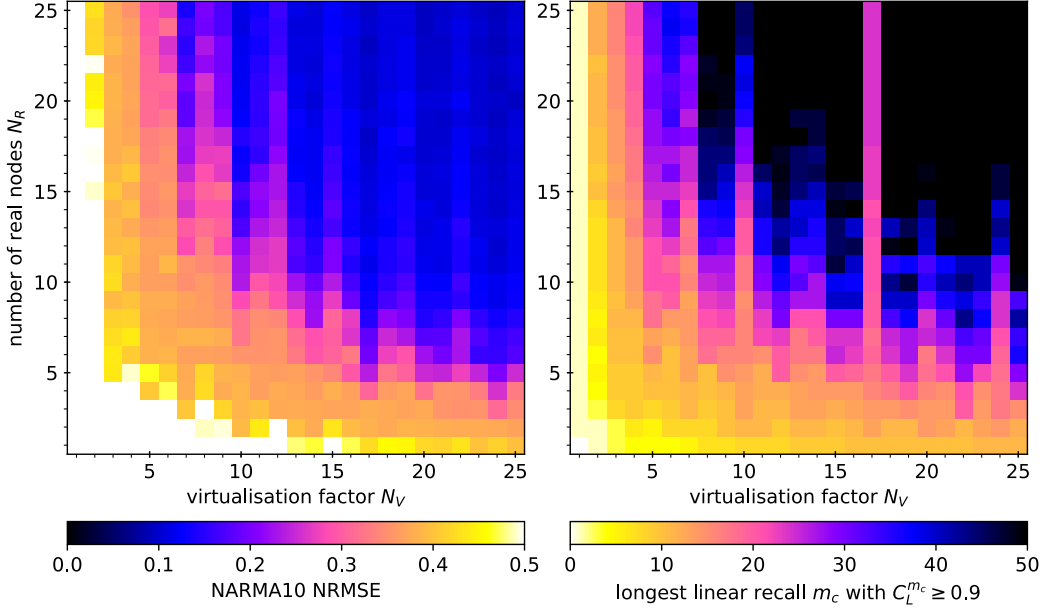


Figure 4.13: Influence of the system size on the reservoir computing capabilities of a Stuart-Landau oscillator network given by Eq. (4.9) using a unidirectional ring network topology. The number of real oscillators N_R (y-axis) and virtualisation factor N_V (x-axis) is changed from 1 to 25. The color code indicates the NARMA10 NRMSE after the training (left) and the critical memory length m_c (right). Parameters: $\gamma = -0.1$, $\omega = 1$, $G = 0.01$, $\lambda = -0.02$, $\phi = 0$, $\kappa = 0.1$, N_R on the y-axis, $\tau = 17N_V$, N_V on the x-axis, $T = 12N_V$, $\theta = 12$, $K_{\text{training}} = 5000$, $K_{\text{testing}} = 1000$, $K_{\text{buffer}} = 1000$.

Figure 4.13 shows a systematic scan to investigate the influence of the system size. The Stuart-Landau oscillator network was simulated as given by Eq. (4.9) and using a unidirectional ring network topology as introduced in Sec. 3.3. The number of real nodes N_R is varied on the y-axis and the virtualisation factor N_V on the x-axis. The colour code of the left panel in Fig. 4.13 shows the NARMA10 NRMSE after training, while the right panel shows the critical memory length m_c , i.e. the largest m for which the corresponding linear memory capacity C_L^m is greater than 0.9. The total read-out dimension of the system is the product $N_V N_R$, which ranges from 1 (bottom left corner in in Fig. 4.13) to 525 (top right corner in Fig. 4.13).

There is a clear and strong influence of the system size on the over all reservoir computing capabilities as can be seen in Fig. 4.13. In general, systems with larger

read-out size perform better, i.e. larger N_R and N_V (points further to the top and right in in Fig. 4.13 are darker). This is what would also be expected from a general machine learning perspective, as most artificial neural network schemes become more powerful with larger system sizes. Moreover, this is also in line with the theoretic considerations of Dambre *et al.* in Ref. [DAM12] and even the earliest reservoir computing works of Ref. [MAA02]: If the system contains more degrees of freedom to be read out, constructing an arbitrary output function $\hat{o}(t)$ out of this becomes easier. This increase of the reservoir computing power can be seen as the same effect that occurs in fitting of data points: Functions that have more degrees of freedom (free parameters) can be brought into closer agreement with the underlying data. In reservoir computing, the complexity of the *task* is independent of the system size. Meanwhile, larger systems have a larger set of phase space trajectories to reconstruct any desired target from, making them far more powerful in terms of reservoir computing capability.

As a side note, there is a clear loss of linear memory for $N_V = 17$ visible in the right plot of Fig. 4.13. This is due to the special parameter choice used in the simulations underlying Fig. 4.13: As discussed in Sec. 4.1.4 the system timescales greatly influence the performance. For the simulations of Fig. 4.13 the time per virtual node θ was kept fixed at 12, while the delay time τ was set to $17N_V$. Because both N_V and N_R have to be integers, this means that also the clock cycle T and delay time τ are integers. With the choice of time scales as is, for $N_V = 17$ there exists one of the resonances between T and τ . This causes the linear memory deteriorate, as discussed in Sec. 4.1.4.

4.2.5 Constructing networks of constant size

As the previous section showed, it is clear that larger system size has a large impact on the performance of reservoir computing systems. The reservoir computing scheme scales very well if the read-out dimension of the system is increased, which can be achieved by either increasing the number of real nodes N_R or the number of virtual nodes by increasing the virtualisation factor N_V . An increase in the computational power with larger systems is also known for other machine learning paradigms. For example, the popular 'deep learning' architectures gain much of their computational power by being 'deep', i.e. large, systems. Reservoir computing in particular profits from larger sizes, because the training procedure is so extremely simple in comparison. Fig. 4.13 clearly showed that over all system size greatly influences both the NARMA10 NRMSE and the linear memory capacity. One can generally expect the larger system to perform better. However, just determining the size of a reservoir computer still leaves a lot of room for variation.

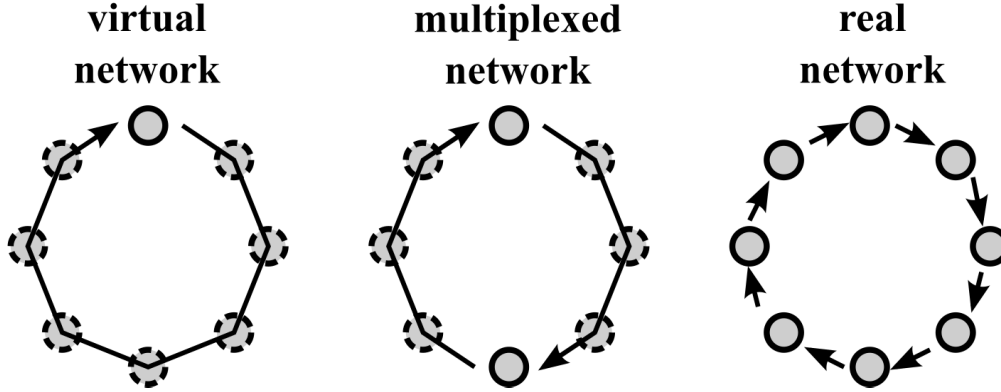


Figure 4.14: Sketch of different time-multiplexed networks. The real nodes are indicated by full circles, while the virtual nodes are sketched as dashed circles. The links are shown as arrows, where here a unidirectional ring topology was used. This sketch shows how networks of identical read-out dimension but different number of real oscillators N_R can be constructed. Left: A single node $N_R = 1$ with delayed feedback with $N_V = 8$ virtual nodes created by time-multiplexing (one virtual node coincides with the real node). Middle: $N_R = 2$ delay-coupled real nodes with $N_V = 4$ virtual nodes each. Right: A network of $N_R = 8$ real nodes.

But additionally, intermediate cases are also possible with $N_R > 1$ and $N_V > 1$ simultaneously, as sketched in Fig. 4.14 b).

Time-multiplexed networks can be constructed in a variety of ways, with different topologies, real node numbers N_R and virtualisation factors N_V . Fig. 4.14 shows a sketch of different time-multiplexed networks: At one of the extreme ends is the choice of $N_R = 1$, which results in a system of a single oscillator with delayed feedback as described Eq. (4.1) and sketched in Fig. 4.14 a). Similarly, at the other extreme end is the choice of $N_V = 1$ as sketched in Fig. 4.14 c). The resulting system is similar to the early echo state network papers (e.g Ref. [JAE02]): A large network of coupled oscillators, where every real node is read out simultaneously to construct the output $\hat{o}(t)$. These two extremes also correspond to the bottom row and left-most column of Fig. 4.13, where the influence of the system size was investigated.

The system size for two different time-multiplexed reservoirs is the same, if the product $N_V N_R$ is identical, which corresponds to hyperbolas $N_R = D/N_V$ in Fig. 4.13 for some fixed size D . However, it is important to realize that both the virtualisation factor N_V and the number of real nodes N_R need to be integers. There cannot be partial nodes. This means, that given a certain total system dimension, only the factors of the integer D can be used to construct time-multiplexed networks. For example, because $D = 23$ is prime, such reservoir computer would either have to contain only a single real node $N_R = 1$, $N_V = 23$ or no virtualisation

$N_R = 23$, $N_V = 1$. Obviously, numbers with more factors are more easily split up, e.g. $D = 6$ would allow for four different combinations between real nodes N_R and virtualisation factor N_V . This strict requirement for the dimension D could be relaxed, if the virtualisation factor N_V is not taken to be identical for all real nodes N_R , i.e if some real nodes are read out more often per clock cycle T than others. But this does contradict the assumption that all oscillators are identical in some way, and it also is unrealistic for an experimental realization, as any implementations would try to maximize its total dimension D , especially when it is only by a finer recording in time.

Thus D should be chosen in a fashion that it has many different factors. Similarly, for the context of this thesis the system size D should not be too large, as otherwise numerical integration times become too long for results to be obtained. Arguably the best choice for D then would be one of the ‘highly divisible numbers’, which are sometimes also called anti-primes. These are integers k , for which no $l < k$ has more divisors. For example, possible anti-primes for this thesis would be 120, 180 or 240. However, the step size in N_R and N_V can be quite irregular for these numbers. Moreover, the number of possible combinations should also not be too large, as this would necessitate too many numerical simulations to obtain results for all combinations of N_R and N_V . Thus, a somewhat simpler approach that still yields a sufficient number of divisors for the total dimension D is chosen: The system is build on powers of 2, with the total dimension $D = 128$. This number has 8 divisors: 1, 2, 4, 8, 16, 32, 64, 128. This results in the following combination of N_V and N_R :

N_R	1	2	4	8	16	32	64	128	(4.11)
N_V	128	64	32	16	8	4	2	1	
T	1536	768	384	192	96	48	24	12	
τ	2176	1088	544	272	136	68	34	17	

The steps between the different combinations shown in Tab. 4.11 are equidistant in a logarithmic sense. Each network has twice the number of real oscillators as the previous one when going from left to right. The case of $N_R = 1$ was already studied in the previous section as modelled by Eq. (4.1) and will therefore not be considered in the following. The clock cycle T is chosen so that the time per virtual node $\theta = 12$ is constant and thus also depends on N_V . Similarly, the delay time τ is modified accordingly, to keep the ratio of τ/T constant. To avoid strong resonances, this ratio is set to $\tau/T = 17/12$. The delay time τ and clock cycle T are shown in the last rows of Tab. 4.11.

Disadvantages of systems with large N_V

As the simulations of Sec. 4.1 for the single Stuart-Landau oscillator show, the system can perform very well as a reservoir computing system with only one real node $N_R = 1$ and large virtualisation $N_V = 128$. However, this has a big practical disadvantage that so far has not been mentioned: The time per virtual node θ should always be on the typical time scales of the system and is therefore kept constant in this thesis. This directly implies that the clock cycle T has to grow linearly with the virtualisation factor N_V . Thus, a system with a larger virtualisation factor N_V will be slower in its computational speed. This is only natural, as the whole idea of the time-multiplexing procedure is to encode ‘virtual nodes’ in time: The more virtual nodes the system contains, the more of the effective phase space is temporally encoded, and thus it takes longer to read it out.

The example of the single Stuart-Landau oscillator of Eq. (4.1) in this sense is the ‘slowest’ of the time-multiplexed network systems. Therefore, any other time-multiplexed network with more real nodes and thus a smaller virtualisation factor N_V would be faster. The single Stuart-Landau system already showed that it can work reasonably well as the core of a reservoir computer. The question, whether non-trivial time-multiplexed networks can, will be investigated in the following.

4.3 Reservoir computing results for time-multiplexed networks

This section shows the results of the reservoir computing performance of time-multiplexed networks based on the Stuart-Landau oscillator system. The main objective is to find the influence of different combinations of the number of real nodes N_R and the virtualisation factor N_V , while keeping the overall read out dimension $N_V N_R = \text{const.}$, as described in Sec. 4.2.5. The system topology is changed between different unidirectional and bidirectional ring networks as introduced in Chap. 3. Parts of this section were published in Ref. [ROE18a] and [ROE18x].

4.3.1 Unidirectional ring network

The unidirectional ring was investigated in Sec. 3.3 and consists of oscillators arranged in a ring, where each oscillator receives input from one of its two neighbours and influences the other. This in particular means, that there is an inherent direction in the unidirectional ring network.

The unidirectional ring equations, that were used to discuss the symmetry-breaking bifurcations and dynamic properties, were shown in Eq. (3.3). The corresponding equations for reservoir computing include additional features: The coupling terms are now delayed by the delay time τ and the system has an additional input $J(t)$. Thus, the evolution of the complex amplitude Z_n of the real oscillator n with $n \in [0, \dots, N_R - 1]$ is given by:

$$\dot{Z}_n = (\lambda + GJ_n(t) + i\omega + \gamma |Z_n|^2)Z_n + \kappa e^{i\phi} Z_{n-1}(t - \tau). \quad (4.12)$$

Most of the parameters will be kept fixed during the investigation of the reservoir computing capabilities: The input scaling $G = 0.01$, solitary frequency $\omega = 1$, nonlinearity $\gamma = -0.1$ (in particular this means that $\text{Im}(\gamma) = 0$) and the coupling strength $\kappa = 0.04$. The masked signal $J_n(t)$ is dependent on the real node number n and contains N_V virtual nodes, as per the time-multiplexing protocol for networks introduced in Sec. 4.2. Eq. (4.12) describes a set of equations, one for each of the N_R real oscillators. The total readout dimension is kept constant by keeping the product $N_R N_V = 128$ as per Tab. 4.11. The clock cycle T is always adapted to keep the time per virtual node $\theta = 12$, i.e. $\tau = 12N_V$ and the delay time is similarly scaled $\tau = 17N_V$ to keep the ratio of these time scales constant. This means, that larger networks will have shorter delays and clock cycles, i.e. be faster.

Figure 4.15 shows the influence of the total number of real nodes N_R on the reservoir computing capabilities of the unidirectional ring network as modelled by Eq. (4.12). Each panel shows the dependence on the Stuart-Landau bifurcation

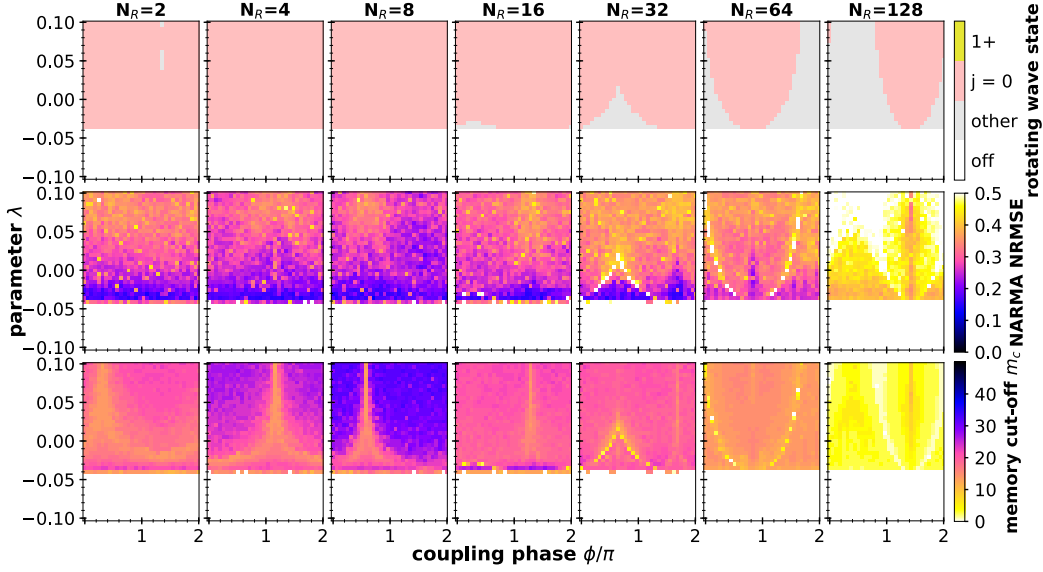


Figure 4.15: Results for the time-multiplexed unidirectional ring of Stuart-Landau oscillators as given by Eq. (4.12). Each individual panel shows the dependence on the Stuart-Landau bifurcation parameter λ and the delay coupling phase ϕ . The top row shows the observed rotating wave pattern for the system without input: White regions are the trivial off-state $Z_n = 0$, red regions the in-phase-synchronized states $Z_0 = Z_1 = \dots = Z_{N_R-1}$, yellow regions indicate all other phase-locked rotating wave states, and grey regions non-trivial behaviour. The middle row shows the result of the NARMA10 NRMSE in colour after training. The bottom row shows the critical memory length m_c , i.e. the longest recall m for which the linear memory capacity $C_L^m > 0.9$. The number of real oscillators N_R is changed throughout the columns. This also changes the delay time τ , clock cycle T and virtualisation factor N_V as per Tab. 4.11. Parameters: $\gamma = -0.1$, $\omega = 1$, $G = 0.01$, $\kappa = 0.04$, N_R atop the column, $N_V = 128/N_R$, $\tau = 17N_V$, $T = 12N_V$, $\theta = 12$, $K_{\text{training}} = 5000$, $K_{\text{testing}} = 5000$, $K_{\text{buffer}} = 1000$.

parameter λ (y-axis) and the delay-coupling phase ϕ (x-axis). The panels of the centre row of Fig. 4.15 show the NARMA10 NRMSE in colour code. This can be compared to the single Stuart-Landau oscillator case that was shown in Fig. 4.2. Similarly, the bottom row of Fig. 4.15 shows the critical memory length m_c as defined for Fig. 4.8. Furthermore, to help interpret these results, the top column of Fig. 4.15 shows the dynamical state of the system, where red is the in-phase synchronized state ($Z_0 = Z_1 = \dots = Z_{N_R-1}$) and yellow regions indicate all other phase-locked rotating wave states. The trivial off-state $Z_n = 0 \forall n$ occurs for parameter combinations that are marked in white in the top row of Fig. 4.15. Grey regions indicate non-trivial behaviour, e.g. limit cycles or quasi-periodic behaviour.

Each column of Fig. 4.15 corresponds to certain network size, i.e. a certain number of real nodes N_R . Thus, the three panels in each column can be seen

4.3 RESERVOIR COMPUTING RESULTS FOR TIME-MULTIPLEXED NETWORKS

as different aspects of the same system. The bottom and centre panel in each column are based on the same numerical simulation data, in particular they share the same mask and input sequence $J_n(t)$. The top panel differs in that it was recorded for a system without input, but the same initial conditions were used for the numerical integration of Eq. (4.12) across all three panels in each column. Thus, the top row of Fig. 4.15 gives an indication of the state the system was in once input started. Because the input is weak (input gain $G = 0.01$) it is unlikely that the system was driven out of its current stable state by the input. Thus, the system likely performed the reservoir computing around the state indicated by the colour code in the top row of Fig. 4.15. The system was initialised close the in-phase synchronized state. When the number of real nodes N_R is varied between the columns of Fig. 4.15, the clock cycle T , delay time τ and virtualisation factor N_V is also changed. The variations are shown in Tab. 4.11.

There are many common features for the time-multiplexed unidirectional rings of Stuart-Landau oscillators as shown in in Fig. 4.15 across different number of real oscillators N_R . One feature that stands out in particular, is a sudden border at $\lambda = -0.04$, where both the error of the reservoir computing as measured by the NARMA10 NRMSE becomes maximal and the critical memory length m_c goes to 0 (white areas in the centre and bottom row of in Fig. 4.15). This indicates the complete loss of all computational power and linear memory, i.e. the system becomes useless for computing applications. Looking at the underlying dynamics as shown in the top row of Fig. 4.15 it becomes clear, that this corresponds to the parameter combinations where the system is in the trivial off-state (white regions in the top row of Fig. 4.15). This effect was already observed and discussed for the results of the single Stuart-Landau oscillator with delayed feedback in Fig. 4.2 and 4.8. The off-state is so detrimental to the reservoir computing performance, because the system no longer reacts to input at all (at least for the input scheme used here in Eq. (4.12)). Thus, these ‘current-driven’ schemes need to ensure to operate above threshold, as otherwise reservoir computing will completely fail. Naturally, this is not a great restriction for experimental realization, as any measurement of the system state already requires the presence of some amplitude Z_n or no response would be recorded. However, this is a restriction that one needs to keep in mind, when larger or more complex reservoir computing setups are considered, as one must be careful not to introduce mechanics that suppress all oscillations.

A second prominent feature in the results for the time-multiplexed rings shown in Fig. 4.15 can be seen by studying the rotating wave state in the top row: Most parameter combinations that show oscillations lead to the in-phase synchronized solution ($j = 0$, red regions in Fig. 4.15). For the unidirectional ring, no other phase-locked states are observed. This is in part due to the choice of the initial condition, which was set to be very close to the in-phase synchronized state. How-

ever, the grey areas in the top row of Fig. 4.15 reveal some regions of more complex behaviour.

The border between the in-phase synchronized region (red in the top panels) and higher-order dynamics (grey in the top panels) are often visible as a drastic increase in the NARMA10 NRMSE (yellow-white lines in the centre panels) and a drop in the critical memory length m_c (compare the three panels within each column in Fig. 4.15, especially for $N_R = 32, 64, 128$). This is a generalization of the observations for the single Stuart-Landau oscillator with delayed feedback: The borders of the in-phase synchronized solutions correspond to bifurcations. Along these bifurcations, the system timescales and phase space trajectories can change drastically. Depending on the details, this can cause the system response to become too slow or too fast to be useful, and thus the error as seen by the centre panels in Fig. 4.15 becomes large.

The regions of in-phase synchronization marked in red in the top panels of Fig. 4.15 become less prevalent for higher number of real nodes N_R . This is mainly caused by the reduced influence of the delay, as the coupling delay time τ is scaled inversely with the number of real nodes, cf. Tab. 4.11. Large unidirectional rings without delay were investigated in Fig. 3.3.5 and show that the stability of the in-phase synchronized solution never covers more than π in the coupling phase dimension ϕ for the case without delay. The column for $N_R = 128$ in Fig. 4.15 for the unidirectional ring networks used for reservoir computing has the shortest delay of all the shown examples, and therefore is most similar to the delay-free case studied earlier. Only for sufficiently long delays does the unidirectional ring show stable in-phase oscillations for all coupling phases ϕ , e.g. for $N_R \leq 32$ (red regions in the top row of Fig. 4.15). Thus, choosing the delay too short may have a detrimental effect by causing a sensitivity to the coupling phase ϕ . This is usually not desired in an optical setup, as these coupling phases are hard to control and reliably manufacture. Here, networks with smaller numbers of real nodes N_R , larger virtualisation factors N_V and thus longer delay times τ have an advantage.

Overall, in the unidirectional ring as used in Fig. 4.15, intermediate size time-multiplexed networks greatly outperform the extreme cases of purely real or purely virtual networks. This is a surprising result, that will be discussed in more detail later. When looking at the reservoir computing performance and memory in general in the centre and bottom row of Fig. 4.15, the oscillation threshold once again plays an important role: As was the case for the singly Stuart-Landau oscillator, the lowest NARMA10 NRMSE and thus the best performance can be found close to the threshold $\lambda \geq -0.04$ (blue regions in the NRMSE in the centre row panels of Fig. 4.15). This is likely caused by an optimal interplay of nonlinear transformation capability and sufficient linear memory, as can be seen by the fact that $m_c > 15$ for most of the intermediate networks in the bottom row of Fig. 4.15. However,

4.3 RESERVOIR COMPUTING RESULTS FOR TIME-MULTIPLEXED NETWORKS

such regions of small NARMA10 error are not visible for time-multiplexed multiplexed networks with many real nodes. In particular, $N_R = 128$ shows a dramatic breakdown of performance (centre rightmost panel in Fig. 4.15). The loss of performance can also be seen by the critical memory length m_c in the bottom row of Fig. 4.15, where large networks show poor linear memory. It is the intermediate case of $N_R = 8$ that shows the longest linear memory for the unidirectional ring.

The dramatic loss of performance for large networks can be explained from different perspectives. First, it may be caused by the much smaller region of stability for the in-phase synchronized solution (red regions in the top row of Fig. 4.15), as discussed before. This is notable, because within the plane of parameters, those that correspond to the in-phase synchronized state (red regions in the top panel of the right-most column in Fig. 4.15) show the lowest error and longest critical memory length. Second, the number of possible rotating wave patterns is dependent on the number of real nodes. There are N_R different rotating waves for a unidirectional ring of size N_R . It is therefore easier for a large network to spontaneously switch from one attracting state to another, due to the higher multistability. Such an attractor-hopping would be highly detrimental to the reservoir computing capabilities, as it would destroy the reproducibility of the system response for similar inputs.

A final reason for the poor performance of large networks is related to the time-multiplexing procedure itself: The virtualisation factor N_V is smallest for the large N_R systems, cf. Tab. 4.11. In particular, for $N_R = 128$ the virtualisation factor is $N_V = 1$, corresponding to an absence of time-multiplexing. The original intent of the time-multiplexing procedure was to introduce a more complex transient behaviour into the system. Apparently, the system greatly suffers when the time-multiplexing is entirely removed. Now, one would expect the role of the lost virtual nodes to be taken over by the additional real nodes that are introduced for larger N_R . However, the trajectories of these nodes are potentially too similar, to be useful. In particular, the symmetry of the unidirectional ring may be hurting the performance. The unidirectional ring is also extremely sparsely connected, making it hard for information to circle around the ring many times. One way to alleviate some of these disadvantages is to augment the underlying topology of the system, which is done in the next section.

4.3.2 Unidirectional ring with jumps

The unidirectional ring discussed in the previous section showed good performance for small and intermediate number of real nodes N_R , but had a dramatic breakdown of performance for entirely ‘real’ networks. To test if this behaviour is tied to the particular topology, or if it is a general phenomenon, the topology will now

be changed. The unidirectional ring is very sparsely connected, and has a strict directional nature. To break both of these features without resorting to random links, specific shortcut links will be introduced to construct a ‘unidirectional ring with jumps’.

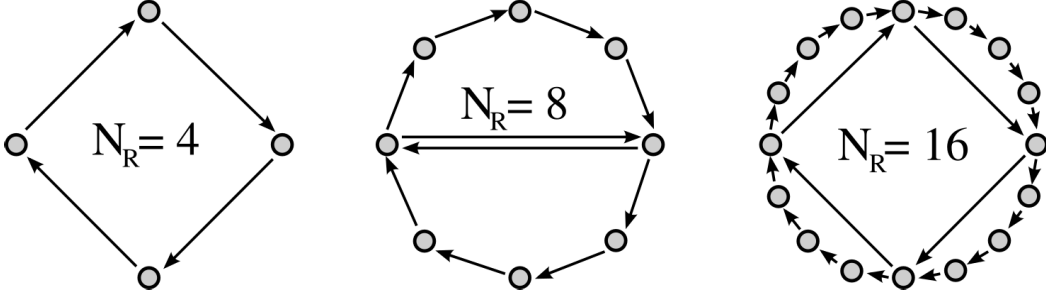


Figure 4.16: Sketch of three differently sized unidirectional rings with jumps. The basic structure is identical to the unidirectional ring, but additionally every fourth node is connected forwards jumping four nodes ahead. This means, that for $N_R = 4$ no extra links are included (left), for $N_R = 8$ (centre) two additional links are added and for $N_R = 16$ 4 additional links are made.

Figure 4.16 shows a sketch of unidirectional rings with the additional links included. Every fourth node has an additional forward connection that jumps four nodes ahead along the ring. This is only a well-defined network, when the total number of nodes N_R is divisible by four, but due to the factor 2-based construction used for time-multiplexing in this thesis, this is always fulfilled. When the total number of real nodes N_R is smaller than 4, no additional links are added and the system is identical to the standard unidirectional ring (see left example in Fig. 4.16). For $N_R > 4$ the number of additional links added is equal to $N_R/4$. Hence, $N_R = 8$ has two additional links (central sketch in Fig. 4.16) and for $N_R = 16$ there are four additional links (right example in Fig. 4.16). Especially for larger rings, the subset of nodes that is connected with these extra links provides some ‘fast-track’ connections for information to spread and mix around the ring. The effect of this on the reservoir computing performance will be analysed in this section.

For most of the real nodes n the typical unidirectional ring network equations still apply:

$$\begin{aligned} \dot{Z}_n &= (\lambda + GJ_n(t) + i\omega + \gamma |Z_n|^2)Z_n + \kappa e^{i\phi} Z_{n-1}(t - \tau), \\ &\text{if } n \bmod 4 \neq 0. \end{aligned} \quad (4.13)$$

The extra ‘jumps’ added for the unidirectional ring network only appear for every fourth node. Without loss of generality, these nodes are always chosen to be $n =$

4.3 RESERVOIR COMPUTING RESULTS FOR TIME-MULTIPLEXED NETWORKS

0, 4, 8, . . . as large as the ring permits. The coupling terms of these nodes contains the extra links:

$$\begin{aligned} \dot{Z}_n = & (\lambda + GJ_n(t) + i\omega + \gamma|Z_n|^2)Z_n + \kappa e^{i\phi} (Z_{n-1}(t - \tau) + Z_{n-4}(t - \tau)), \quad (4.14) \\ & \text{if } n \bmod 4 = 0 \end{aligned}$$

Note, that the extra links in Eq. (4.14) are included with the same coupling phase ϕ , coupling strength κ and delay-time τ . This is done for reasons of simplicity here, as no additional parameters need to be introduced. However, many possible generalizations exist. For example, one could argue that if the whole purpose of the 'shortcuts' is to facilitate a mixing of the information, then these extra links could also be instantaneous. On the other hand, this may not be too realistic when applied to experimental setups. Possible variations like that are left for future investigations.

Figure 4.17 shows the reservoir computing results for the unidirectional ring with jumps as given by Eq. (4.13) and (4.14). These results should be compared to those of the unidirectional ring without jumps of Fig. 4.15. Each panel is once again a two-dimensional parameter scan for the Stuart-Landau parameter λ and coupling phase ϕ . The number of real nodes N_R is changed in the different columns as per Tab. 4.11. As mentioned, due to construction the extra links in the unidirectional ring with jumps are not included for $N_R = 2$ and $N_R = 4$, and thus Fig. 4.17 is identical in these cases to Fig. 4.15.

The top row of Fig. 4.17 shows the dynamic state of the system, and for $N_R > 4$ the inclusion of the extra links has a direct and visible impact when compared to the pure unidirectional ring of Fig. 4.15: The inclusion of these extra links leads to a threshold reduction. The border between the off-state (white in the top row of Fig. 4.17) is decreased and now lies at $\lambda \approx 0.05$. Furthermore, no rotating wave patterns can be found for larger λ , all regions are marked in grey in the top row of Fig. 4.17. This is due to the breaking of the discrete circular symmetry that the unidirectional ring originally had. The inclusion of the extra jumps makes the real nodes non-identical and thus rotating waves are no longer the natural solutions of Eq. (4.13) and (4.14). The custom detection algorithms used in creating the dynamic state plots have not been adapted, and a detailed analysis of the bifurcation landscape of the unidirectional ring with jumps is out of the scope of this thesis.

When looking at the NARMA10 NRMSE in the centre row of Fig. 4.17, it is visible that the inclusion of the extra links over all has improved the performance of the system. The intermediate sizes of $N_R = 16$ and $N_R = 32$ have profited the most, underlining that the inclusion of the extra links has fulfilled its purpose. But also the largest ring networks for $N_R = 128$ (right most column in Fig. 4.17)

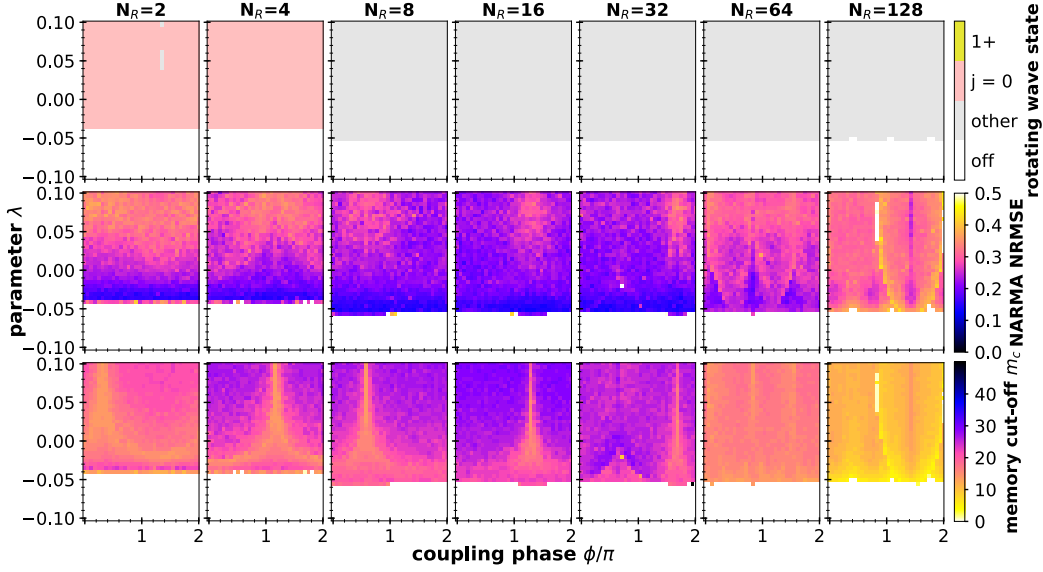


Figure 4.17: Results for the time-multiplexed unidirectional ring of Stuart-Landau oscillators with jumps as given by Eq. (4.13) and (4.14). Each individual panel shows the dependence on the Stuart-Landau bifurcation parameter λ and the delay coupling phase ϕ . The top row shows the observed rotating wave pattern for the system without input: White regions are the trivial off-state $Z_n = 0$, red regions the in-phase-synchronized states $Z_0 = Z_1 = \dots = Z_{N_R-1}$, yellow regions indicate all other phase-locked rotating wave states, and grey regions non-trivial behaviour. The middle row shows the result of the NARMA10 NRMSE in colour after training. The bottom row shows the critical memory length m_c , i.e. the longest recall m for which the linear memory capacity $C_L^m > 0.9$. The number of real oscillators N_R is changed throughout the columns. This also changes the delay time τ , clock cycle T and virtualisation factor N_V as per Tab. 4.11. For $N_R = 2$ and $N_R = 4$ the system is identical to the unidirectional ring without jumps shown in Fig. 4.15. Parameters: $\gamma = -0.1$, $\omega = 1$, $G = 0.01$, $\kappa = 0.04$, N_R atop the column, $N_V = 128/N_R$, $\tau = 17N_V$, $T = 12N_V$, $\theta = 12$, $K_{\text{training}} = 5000$, $K_{\text{testing}} = 5000$, $K_{\text{buffer}} = 1000$.

have lower errors when compared to the original ring without jumps of Fig. 4.15. The performance is still visibly worse than for smaller networks, but at least some parameter combinations allow for a decent computational power. It seems therefore likely, that larger networks may need an even more well-connected network than the unidirectional ring with jumps used here.

When studying the influence of the additional links of Fig. 4.17 on the critical memory length m_c shown in the bottom row, one curious feature becomes apparent when compared to the pure unidirectional ring in Fig. 4.15: $N_R = 8$ has in parts even lost some memory length, while $N_R = 16$ and $N_R = 32$ have improved. This shows, that the trade-off between mixing of information and linear memory

length is complex. The inclusion of the additional links has improved the system performance for the NARMA10 task, but that does not guarantee a larger linear memory. However, for the large network $N_R = 128$ the system with jumps of Fig. 4.17 shows a clear improvement in the memory length that is likely also the cause of the better NARMA10 performance. This indicates once again, that the pure unidirectional ring is too sparsely connected for effective computing, and that the additional links have improved the system performance.

4.3.3 Bidirectional ring

A second way of augmenting the unidirectional ring of Sec. 4.3.1 is to remove the directed nature of the graph. This way, a more complex spread of information within the system is enabled. If the links of the unidirectional ring are turned undirected one arrives at bidirectional ring networks. These were also studied with respect to their bifurcations, dynamics and symmetry-broken states in Sec. 3.4. A bidirectional ring is a simple nearest-neighbour coupling and can also be seen as an approximation of the one-dimensional diffusive Ginzburg-Landau equation with periodic boundary conditions [HAK92].

Here, the coupling is once again taken with delay, to make use of the extended phase-space dimension in DDE systems. The number of real nodes N_R and the virtualisation factor N_V are scaled as per Tab. 4.11. The equations of motion for the bidirectional ring of Stuart-Landau oscillators for reservoir computing are then given by:

$$\dot{Z}_n = (\lambda + GJ_n(t) + i\omega + \gamma|Z_n|^2)Z_n + \frac{\kappa}{2}e^{i\phi}(Z_{n-1}(t-\tau) + Z_{n+1}(t-\tau)), \quad (4.15)$$

where the complex amplitude of each oscillator is Z_n for index $n \in [0, \dots, N_R]$. Each index n should be understood to be taken modulo N_R . The bidirectional ring network described by Eq. (4.15) differs from the unidirectional ring of Eq. (4.12) only in the coupling term: In addition to the forward coupling from Z_{n-1} , the oscillator n also receives input in the backwards direction from Z_{n+1} . The coupling terms are delayed with the same delay time τ . The coupling strength appears scaled as $\kappa/2$ as was used in the bidirectional ring Eq. (4.15) to account for the additional connections of the network compared to the unidirectional ring. This way, both network types share similar bifurcation lines.

The reservoir computing results are shown in Fig. 4.18, which is to be compared to the results for the unidirectional ring of Fig. 4.15. The structure of the figure itself is the same, with rows showing the dynamics, NARMA10 NRMSE and critical memory length m_c , while the different columns show networks of different size, i.e. different number of real oscillators N_R , which also implicitly scales the clock cycle

T , delay time τ and virtualisation factor as per Tab. 4.11. Each panel is a parameter scan of λ and coupling phase ϕ .

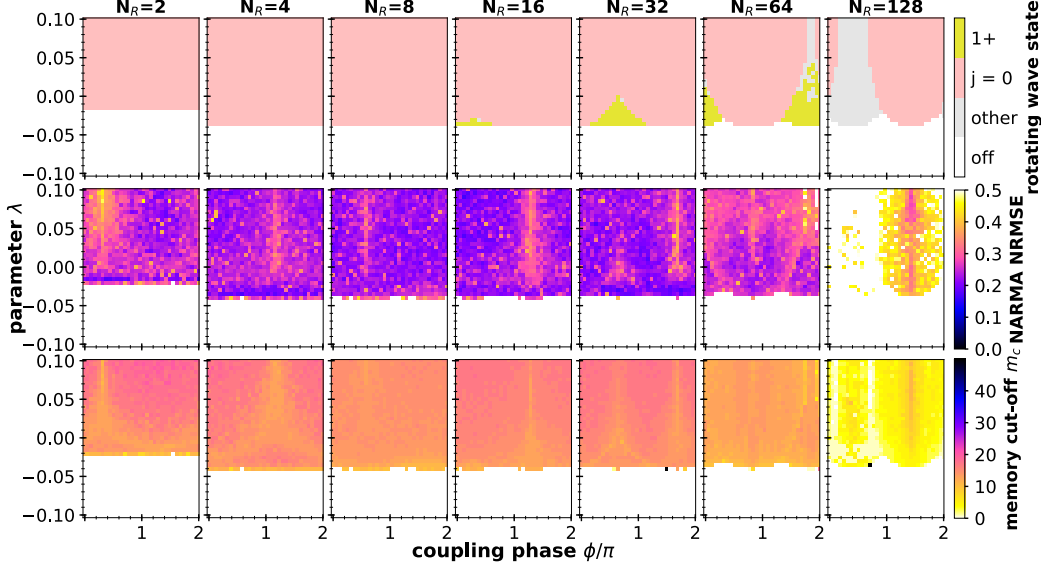


Figure 4.18: Results for the time-multiplexed bidirectional ring of Stuart-Landau oscillators as given by Eq. (4.15). Each individual panel shows the dependence on the Stuart-Landau bifurcation parameter λ and the delay coupling phase ϕ . The top row shows the observed rotating wave pattern for the system without input: White regions are the trivial off-state $Z_n = 0$, red regions the in-phase-synchronized states $Z_0 = Z_1 = \dots = Z_{N_R-1}$, yellow regions indicate all other phase-locked rotating wave states, and grey regions non-trivial behaviour. The centre row shows the result of the NARMA10 NRMSE in colour after training. The bottom row shows the critical memory length m_c , i.e. the longest recall m for which the linear memory capacity $C_L^m > 0.9$. The number of real oscillators N_R is changed throughout the columns. This also changes the delay time τ , clock cycle T and virtualisation factor N_V as per Tab. 4.11. Except for the topology, all parameters are identical to the unidirectional ring shown in Fig. 4.15. Parameters: $\gamma = -0.1$, $\omega = 1$, $G = 0.01$, $\kappa = 0.04$, N_R atop the column, $N_V = 128/N_R$, $\tau = 17N_V$, $T = 12N_V$, $\theta = 12$, $K_{\text{training}} = 5000$, $K_{\text{testing}} = 5000$, $K_{\text{buffer}} = 1000$.

The results of the bidirectional ring in Fig. 4.18 show some clear and interesting difference to the unidirectional ring case of Fig. 4.15, but also many similarities. In the bidirectional ring, the border between the off-state (white regions in the top row of Fig. 4.18) and the oscillating solutions (coloured regions in the top row of Fig. 4.18) is located at $\lambda = -0.04$, as the coupling term was correctly scaled in Eq. (4.15). The only exception being $N_R = 2$, where there is no real difference between unidirectional and bidirectional ring, so that the scaling of $\kappa/2$ reduced the threshold. As in the other studied cases so far, the regions of the off-state possess no computational power and will therefore be ignored from here on. The

4.3 RESERVOIR COMPUTING RESULTS FOR TIME-MULTIPLEXED NETWORKS

bidirectional ring in Fig. 4.18 shows stable in-phase synchronization (red regions) for most of the observed networks. For large networks, the effect of short delay once again reduced the regions of stability of the in-phase synchronized solutions, and allows for other rotating waves to be stable (yellow regions in the top row of Fig. 4.18) and partly shows more complex dynamics (grey regions).

The qualitative dependence of the NARMA10 NRMSE shown in the centre row of Fig. 4.18 on the number of real nodes N_R is similar to the unidirectional ring: Intermediate network sizes show the best performance, while the pure network case without time-multiplexing of $N_R = 128$ (right most column in Fig. 4.18) shows a dramatic breakdown of performance. Interestingly, despite this loss of computational power, the parameter regions that still perform best for $N_R = 128$ are those where the underlying system is in the in-phase synchronized regime: The red regions in the top row of the $N_R = 128$ column of Fig. 4.18 correspond to the regions of the lowest NRMSE in the panel below. This shows, that the more ‘well-behaved’ states of rotating wave solutions are better suited to reservoir computing than more complex dynamical behaviour. This is not too surprising, as complex amplitude oscillations can completely drown out the transients induced by the input, and thus make effective reservoir computing impossible. Especially with parameters as chosen here, where the input gain was relatively small $G = 0.01$, the system is prone to be dominated by its internal dynamics, if it has any.

The critical memory length m_c shown in the bottom row of Fig. 4.18 is overall low. The bidirectional ring seems to have a shorter linear memory than its unidirectional counterpart. This can be related to the nature of the bidirectional links. While the unidirectional ring network has a clear direction, information fed into different real nodes N_R interacts much earlier in the bidirectional ring. This causes a reduced linear memory. However, it may in turn also give rise to a larger nonlinear transformation capacity, and thus a bidirectional ring may be more suited for certain applications. It is clear, that the NARMA10 NRMSE does not suffer from the reduced linear memory of the bidirectional ring, because the critical memory length is still sufficiently long at $m_c \approx 15$ for most parameters. This is however not the case for the pure network for $N_R = 128$ (bottom right panel in Fig. 4.18): The memory length is clearly degraded drastically, strongly limiting the usefulness of the system for computational purposes.

4.3.4 Bidirectional ring with self-feedback

A final regular ring topology shall now be covered in this section. One important aspect of delay-coupled oscillator networks is that any self-feedback can no longer be absorbed into the local dynamics: In particular, for the Stuart-Landau oscillator without delay, self-coupling can be absorbed into the local bifurcation parameter

λ and solitary frequency ω . However, once delay is included, this is no longer possible. Thus, there is a fundamental difference between a network with delayed self-feedback and one without. Here, the bidirectional ring network of the previous section will be taken and the influence of additional self-feedback links will be investigated.

The bidirectional ring of Stuart-Landau oscillators with self-feedback can be implemented in different ways. One obvious choice would be to treat the self-feedback just as an additional link of the same strength and sign as all the others. However, here the approach will be based on considerations of a difference equation: In nature there are often coupling terms between two systems \mathbf{X}_1 and \mathbf{X}_2 that only depend on the difference of the two system states $\mathbf{X}_1 - \mathbf{X}_2$. In this case, the self-feedback has the opposite sign of all the other coupling terms. For a bidirectional ring network, there are two neighbours per node, and thus the difference will have to be taken twice:

$$\kappa e^{i\phi} (Z_{n-1} - Z_n) + \kappa e^{i\phi} (Z_{n+1} - Z_n) = \kappa e^{i\phi} (Z_{n-1} + Z_{n+1} - 2Z_n). \quad (4.16)$$

When the coupling terms are delayed with the delay time τ and the coupling strength is once again scaled by a factor of 2, the equation of motion for the bidirectional ring of Stuart-Landau oscillators is derived:

$$\begin{aligned} \dot{Z}_n = & (\lambda + GJ_n(t) + i\omega + \gamma |Z_n|^2) Z_n \\ & + \frac{\kappa}{2} e^{i\phi} (Z_{n-1}(t - \tau) + Z_{n+1}(t - \tau) - 2Z_n(t - \tau)), \end{aligned} \quad (4.17)$$

where all parameters otherwise are as before. Differently sized networks will be constructed as per Tab. 4.11.

Figure 4.19 presents the reservoir computing performance results for the bidirectional ring of Stuart-Landau oscillators with self-feedback as modelled by Eq. (4.17). Except for the underlying topology, all other aspects are identical to Fig. 4.15 for the unidirectional ring, the unidirectional ring with jumps of Fig. 4.17 and the bidirectional ring without self-feedback in Fig. 4.18.

Two important novel features appear in Fig. 4.19 that are caused by the inclusion of the additional self-feedback links: First, there is a threshold reduction when compared to the pure bidirectional ring network. This is to be expected, as any additional link usually allows at least for some solutions to appear earlier. This similar to the effect that the additional shortcut links had in the unidirectional ring with jumps of Fig. 4.17. However, a much more important feature is that the system no longer prefers to converge to the in-phase synchronized state (red regions in the top row of Fig. 4.17). Rather, the system approaches a different rotating wave pattern. Time series analysis reveals that these states are anti-phase

4.3 RESERVOIR COMPUTING RESULTS FOR TIME-MULTIPLEXED NETWORKS

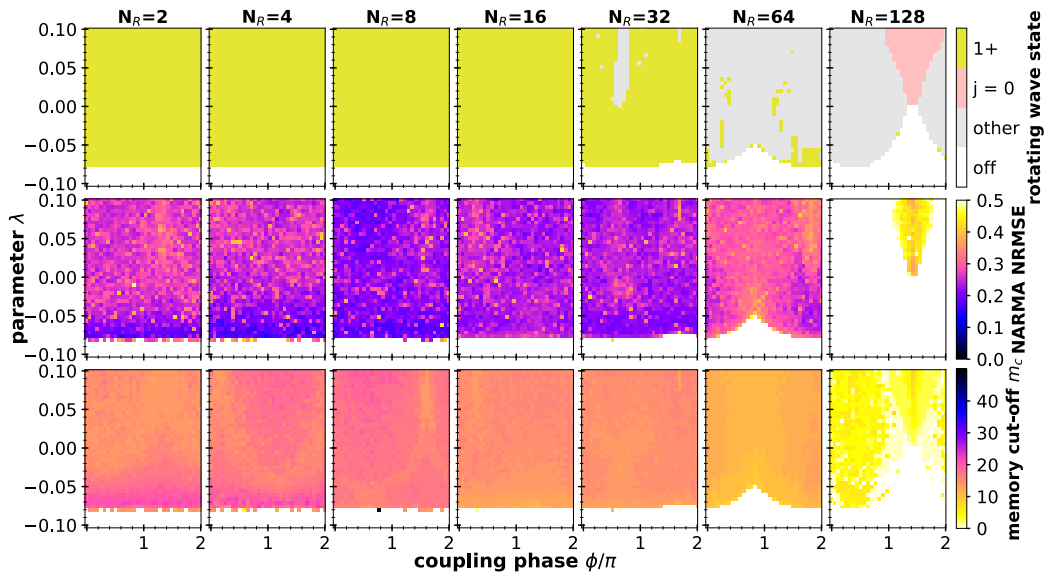


Figure 4.19: Results for the time-multiplexed bidirectional ring of Stuart-Landau oscillators with self-feedback as given by Eq. (4.17). Each individual panel shows the dependence on the Stuart-Landau bifurcation parameter λ and the delay coupling phase ϕ . The top row shows the observed rotating wave pattern for the system without input: White regions are the trivial off-state $Z_n = 0$, red regions the in-phase-synchronized states $Z_0 = Z_1 = \dots = Z_{N_R-1}$, yellow regions indicate all other phase-locked rotating wave states, and grey regions non-trivial behaviour. The centre row shows the result of the NARMA10 NRMSE in colour after training. The bottom row shows the critical memory length m_c , i.e. the longest recall m for which the linear memory capacity $C_L^m > 0.9$. The number of real oscillators N_R is changed throughout the columns. This also changes the delay time τ , clock cycle T and virtualisation factor N_V as per Tab. 4.11. Except for the topology, all parameters are identical to the unidirectional ring shown in Fig. 4.15. Parameters: $\gamma = -0.1$, $\omega = 1$, $G = 0.01$, $\kappa = 0.04$, N_R atop the column, $N_V = 128/N_R$, $\tau = 17N_V$, $T = 12N_V$, $\theta = 12$, $K_{\text{training}} = 5000$, $K_{\text{testing}} = 5000$, $K_{\text{buffer}} = 1000$.

rotating waves. This is likely caused by the exact shape that was used for the self-feedback in Eq. (4.17), where the self-feedback has a different sign than the inter-node coupling.

The influence of the self-feedback on the reservoir computing capabilities (centre row of Fig. 4.19) is not very strong. Apart from the threshold reduction, no major qualitative differences are apparent. The NARMA10 NRMSE for the bidirectional ring with self-feedback of Fig. 4.19 does not differ from the pure bidirectional ring shown in Fig. 4.15 in a significant way. The self-feedback can also not prevent the dramatic breakdown of performance for large networks ($N_R = 128$). Moreover, as the bottom row of Fig. 4.15 shows, the feedback does also not increase the critical

memory length m_c . This is a surprising observation. The system seems to not be influenced much by the self-feedback. Thus, it seems that to influence the computational capabilities of time-multiplexed networks it is much more useful to study the effect of additional intra-node links, like the shortcuts for the unidirectional ring of Sec. 4.3.2.

4.3.5 General influence of the number of real nodes N_R

In this section, the results of the previous four sections will be compacted. Each of the previous sections analysed the behaviour of a different kind of topology with respect to the influence of the system size as per Tab. 4.11. In particular, Fig. 4.15 show the results for the unidirectional ring, Fig. 4.17 the unidirectional ring with jumps, Fig. 4.18 the bidirectional ring and Fig. 4.19 the bidirectional ring with self-feedback. Additionally, the case of $N_R = 1$, i.e. the single Stuart-Landau oscillator with delayed feedback was covered in Sec. 4.1. Each figure in detail studied the influence of the Stuart-Landau bifurcation parameter λ and the coupling or feedback phase ϕ . However, this also makes it hard to get more than a qualitative impression of the influence of the number of real nodes N_R .

Compression of the information

The data from each individual λ - ϕ -plot will now be compressed into two single numbers. In an experimental setting using these systems, it may be too tedious to try out every combination of parameters. Thus, the operators will have to choose some combination of λ and ϕ to try out and record. If the area of the individual 2D-parameter scan of the figures of the previous sections was to represent the possible range of experimentally accessible values for λ and ϕ , then an experiment would be a randomly chosen point from that region. To quantitatively predict the expected figures of merit for the reservoir computing, such as the NRMSE or critical memory length m_c , under such circumstances is relatively simple: Because the 2D-parameter scans were done on an equally spaced grid, the average of all points can simply be taken. This average is then simply the ‘expected value’ of the reservoir. However, one small modification to the underlying data will be allowed: It can be expected that any experimentalist will quickly be able to determine whether their system is actually showing any dynamics or not. Therefore, for the sake of quantitative evaluation, the regions of the ‘off-state’ $Z_n = 0 \forall n$ will not be considered. These regions also showed no reservoir computing capability, i.e. had very high errors, so that their inclusion would greatly dominate the resulting average.

During the calculation of the average, it is also simple enough to calculate the standard deviation. Furthermore, to visually represent systems that had favourable

4.3 RESERVOIR COMPUTING RESULTS FOR TIME-MULTIPLEXED NETWORKS

parameter regions, the best value of each time-multiplexed network will also be recorded: The best value corresponds to the lowest NRMSE for the NARMA10 task or the longest critical memory length m_c .

Dependence of the NARMA10 NRMSE on N_R

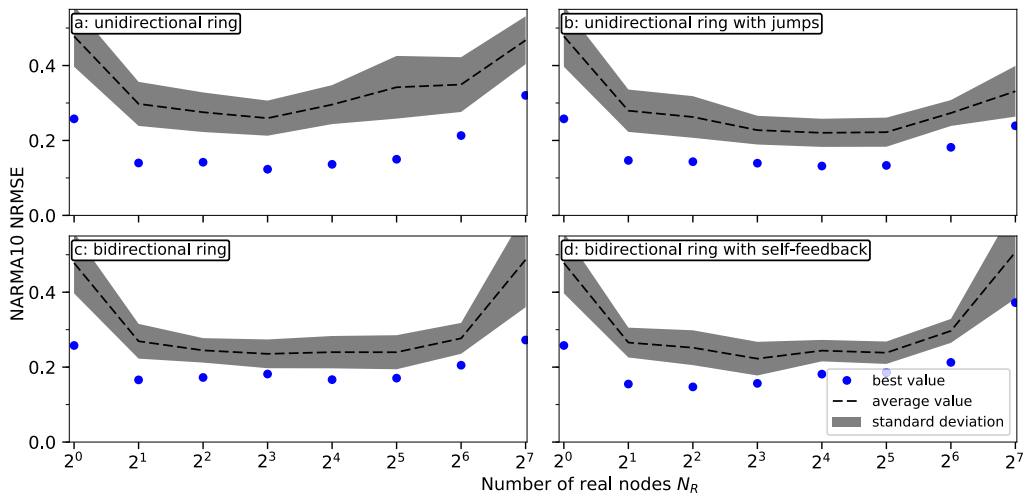


Figure 4.20: Influence of the number of real nodes N_R on the reservoir computing performance as measured by the NARMA10 NRMSE. Each figure shows the results for one of the four topologies investigated in Sec. 4.3, where the blue dots are the best observed performance, the black dashed line is the average performance and the grey area is one standard deviation. The left most data point is the same in all panels and is the observed performance of the single Stuart-Landau oscillator with delayed feedback of Sec. 4.1. a): Unidirectional ring based on Fig. 4.15, b): unidirectional ring with jumps based on Fig. 4.17, c): bidirectional ring based on Fig. 4.18, d): bidirectional ring with self-feedback based on Fig. 4.19. For parameters, see those figures.

Figure 4.20 shows the results for the NARMA10 NRMSE as quantitatively evaluated for the time-multiplexed networks that were investigated in this thesis. Each panel shows the results for a different topology as a function of the number of real nodes N_R . Note, that only the sizes N_R indicated on the x-axis were used, as per Tab. 4.11. The blue dot represents the best value that was found for that topology and size, while the black dashed lines shows the average with one standard deviation shown by the grey area. Each panel is based on one of the Figures in Sec. 4.3: The unidirectional ring is based on Fig. 4.15, the unidirectional ring with jumps on Fig. 4.17, the bidirectional ring on Fig. 4.18 and the bidirectional ring with self-feedback on Fig. 4.19. The left most data point shows the performance that was found for the single Stuart-Landau oscillator discussed in Sec. 4.1 and thus is the same in all panels.

The results in Fig. 4.20 confirm the general qualitative impression of the 2D-parameter scans: For all parameter scans both the best values (blue dots in Fig. 4.20) and the average values (black dashed link in Fig. 4.20)) are relatively flat for intermediate sized networks, allowing for good performance for many different numbers of oscillators. Both extreme cases, i.e. the largest networks with $N_R = 128$ and the solitary oscillator with $N_R = 1$, show a decrease in computational performance, marked by the sudden increase in the NRMSE in Fig. 4.20.

The different topologies show slightly different NRMSE. The unidirectional ring of Fig. 4.20 a) has the largest average NRMSE of all the topologies investigated. The comparison with Fig. 4.20 b) also shows, that the inclusion of the jumps has improved the average performance of the system (black dashed lines in Fig. 4.20), but mostly not the lowest NRMSE that was obtained (blue dots). The bidirectional ring networks shown in Fig. 4.20 c) and d) generally show a somewhat lower average error (black dashed lines) than the unidirectional ring of Fig. 4.20 a). However, the optimal value shown with blue dots in Fig. 4.20 is *worse* than for the unidirectional ring. This shows that the unidirectional ring has a much stronger parameter dependence, i.e. the values of the NRMSE are more spread out. This can also be seen by the larger standard deviation in Fig. 4.20 a) than in Fig. 4.20 c) and d) as shown by the grey area. One can hypothesize that this may be in part caused by the sparser connectivity of the unidirectional ring: When the network has fewer links, the properties of the individual oscillators are much more important and therefore a 2D-parameter scan will produce a larger spread of NRMSE. On the other hand, if there is a strongly connected network, then the global dynamics are much more dominated by collective effects and the change of local variables only influences the system slightly. Fig. 4.20 also shows that the inclusion of self-feedback barely changed anything for the NARMA10 NRMSE, as Fig. 4.20 c) and d) are highly similar.

The left most data point in all panels of Fig. 4.20 shows the NARMA10 NRMSE that was obtained for a single Stuart-Landau oscillator with delay, and as such is the same in all four panels as topology does not matter for a single oscillator. The performance is clearly worse by all measures for the solitary oscillator. This is an interesting observation, as it highlights the possible performance gain one can expect from going to time-multiplexed networks. The fact, that it is the extreme ends of $N_R = 1$ and $N_R = 128$ that show the worst results also leads to the following hypothesis: Reservoir computing systems are build on the intrinsic computational power of dynamical system. The more diverse and varied the transients in a system are, the better they can be exploited for reservoir computing. Thus, a system might profit substantially, if a *fundamentally new* dynamical aspect is added to it: For example, when going from a purely virtual network of $N_R = 1$ to the case of two coupled oscillators $N_R = 2$, the whole dynamical range of coupled cavity and

4.3 RESERVOIR COMPUTING RESULTS FOR TIME-MULTIPLEXED NETWORKS

oscillator dynamics is introduced into the system. This represents a fundamentally new dynamical aspect and can greatly enrich the transients of the reservoir. On the other hand, going from $N_R = 32$ to $N_R = 64$ only trades some virtual nodes for more real nodes, without introducing any fundamentally new aspects to the system and therefore also the performance in Fig. 4.20 barely differs between the two. A similar argument can be made for purely real networks of $N_R = 128$ in Fig. 4.20, where the total absence of time-multiplexing deprives the system of one of the fundamentally different dynamical aspects that intermediate size networks have.

Dependence of the critical memory length m_c on N_R

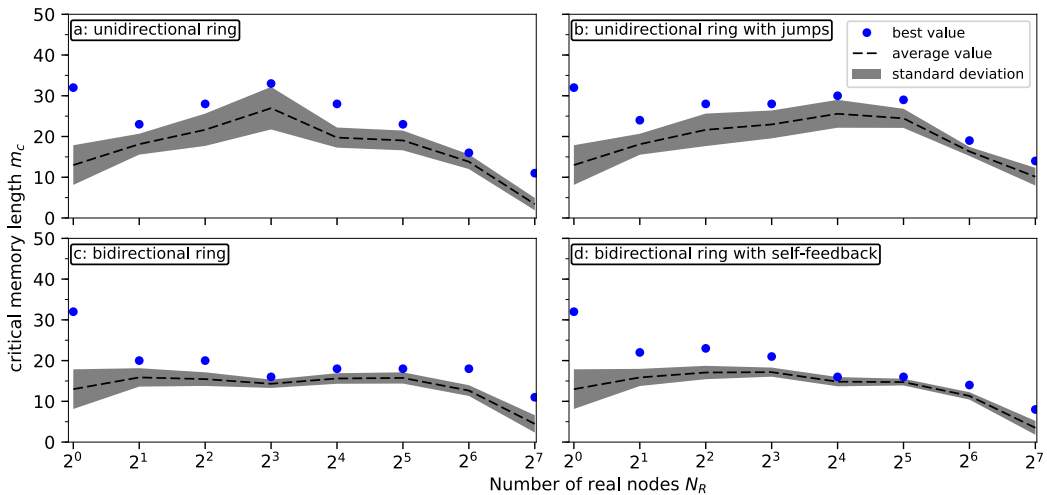


Figure 4.21: Influence of the number of real nodes N_R on the reservoir computing performance as measured by the critical memory length m_c , i.e the largest m_c for which $C_L^m > 0.9$ for all $m \leq m_c$. Each figure shows the results for one of the four topologies investigated in Sec. 4.3, where the blue dots are the best observed performance (highest m_c), the black dashed line is the average performance and the grey area are one standard deviation from that. The left most data point is the same in all panels and is the observed performance of the single Stuart-Landau oscillator with delayed feedback of Sec. 4.1. a): Unidirectional ring based on Fig. 4.15, b): unidirectional ring with jumps based on Fig. 4.17, c): bidirectional ring based on Fig. 4.18, d): bidirectional ring with self-feedback based on Fig. 4.19. For parameters, see those Figures.

Figure 4.21 shows the behaviour of the critical memory length m_c as a function of the number of real nodes N_R for the different topologies. This figure is based on the corresponding two-dimensional parameter scans of m_c shown in the bottom rows of Fig. 4.15 to 4.19. The blue dots show the highest m_c found and the black dashed line is the average m_c for all combinations of λ and ϕ . Once again, data

points where the system was in the off-state and thus had no computational power were not included in the calculation for Fig. 4.21.

The general trends of the critical memory length shown in Fig. 4.21 mirror the results of the NARMA10 NRMSE shown in Fig. 4.20: The worst performance (lowest m_c) can be found for the largest networks of $N_R = 128$, which do not have any time-multiplexing. This shows the poor linear memory of such large networks, e.g the right most best performance (blue dots in Fig. 4.20) barely exceeds 10, with the averages even lower.

The unidirectional rings show longer critical memory lengths m_c than their bidirectional counterparts, compare Fig. 4.20 a) and b) with c) and d). This may be due to the ordered nature of information flow within the unidirectional ring, which may favour a simple linear recall and prevent effective mixing of information. The bidirectional ring shows lower memory lengths, but the standard deviation is also smaller (grey areas in Fig. 4.20), i.e. a more reliable memory length is obtained.

The results for the single Stuart-Landau oscillator with delayed feedback correspond to the left most data point in Fig. 4.20, which is identical for all panels. One remarkable feature here is that the average is lower than for many time-multiplexed networks, but the best observed value (blue points in Fig. 4.20) is highest of all tested systems. This however may be an artefact of the numerical simulations: The 2D scan of the Stuart-Landau bifurcation parameter λ and feedback phase ϕ was done in a higher resolution for the single Stuart-Landau oscillator with delayed feedback in Sec. 4.1 than the numerical simulations for the time-multiplexed networks. So many time-multiplexed networks had to be simulated, that such a high resolution was not usable. In particular, looking at Fig. 4.8 reveals that the system contains only a very small region with $m_c > 30$. On coarser grid, these regions may have well been less pronounced. Thus, it may purely be the higher resolution used in the parameter scan for the single Stuart-Landau with self-feedback that may be the reason for the somewhat high best value of the critical memory length m_c . The average, naturally, does not depend that much on the resolution and therefore does show a somewhat shorter critical memory length m_c for the single Stuart-Landau oscillator than for the intermediate networks.

4.4 Discussion

4.4.1 Results

This chapter showed the reservoir computing performance of regular oscillator networks. Different aspects were investigated, such as the computational power of a single Stuart-Landau oscillator with delayed feedback as an example of the delay-architecture, that is popular in photonic reservoir computing [SAN17a]. The numerical simulations of this thesis clearly showed a few basic aspects of such reservoir computing systems: The influence of the off-state was clearly detrimental to the system performance, leading to a total loss of computational power and memory. This was easily explained by the lack of dynamic response to the input at such levels. Furthermore, bifurcations can directly shape the behaviour of the reservoir computer, leading to drastic changes of the associated measures such as NRMSE close to the critical parameters. Lastly, the single Stuart-Landau oscillator was also used to investigate the general properties of the memory capacities C_L^m and different ways of evaluating the memory curve. Here, a new way of compressing the information was introduced by the way of the critical memory length m_c , which was chosen in particular for the explanation of the NARMA10 task.

In the second part, hybrid systems consisting of both delay-lines and networks were studied. These ‘time-multiplexed’ networks contain both virtual nodes created by time-multiplexing as well as several real nodes. A way of constructing well-defined time-multiplexed networks of identical effective size but different virtual and real node numbers was introduced. The reservoir computing capabilities of these systems were investigated with respect to different real node numbers N_R and different underlying topologies. The results showed that hybrid systems outperformed both delay-line reservoir computers as well as pure networks. The interplay of delay and network dynamics leads to a richer dynamical landscape, allowing for a more effective approximation of the NARMA10 task. This is in particular interesting for experiments, as any reduction in the virtualisation factor N_V directly reduces the clock cycle T of the system, and thus increases the computational speed. Hybrid networks are therefore also faster than their fully virtual counterparts. Naturally, one has to pay a price in the form of the larger number of elements involved.

Different topologies were tested, with a focus on the regular networks introduced in Chap. 3. Here it was found, that the unidirectional ring showed a very poor performance for large node numbers N_R . This was partly related to the lack of connectedness, so that a modified version of a unidirectional ring with jumps was also investigated. The unidirectional ring with jumps did somewhat alleviate the problems, however the breakdown of performance for fully real networks could still

not be entirely prevented. Next, the bidirectional topology was studied, showing overall a worse but more consistent performance than the unidirectional rings in both NARMA10 NRMSE and critical memory length m_c . The influence of delayed self-feedback was studied with the inclusion of self-feedback in the bidirectional ring topology. However, the influence was so minute, that it can largely be ignored.

Overall, the results of this chapter are good news for experimentalists and designers of new reservoir computing platforms. They show that a wide variety of systems can be used, and that hybrid delay-network architectures are robust with respect to the underlying topology. In particular, while the unidirectional ring showed relatively large variations of the critical memory length m_c and NARMA10 NRMSE, it is also a topology that requires few connections. This could make it especially interesting for on-chip integration of lasers via optical waveguides, as not too many connections have to be made.

4.4.2 Towards a quantitative theory

Reservoir computing is still a relatively young field and, compared to other machine learning schemes, has a relatively small research community attached to it. Reservoir computing is also arguably conceptually more difficult to grasp than Deep Neural networks. The latter can be seen as a simple high-dimensional interpolation of the training data. Reservoir computing on the other hand uses the degrees of the system that are already present, i.e. it does not modify the reservoir itself. This leads to the problem of identifying and classifying suitable systems. Determining *a priori* which reservoir is suited for which application is a very difficult question. A quantitative theory of the computational power of dynamical systems could answer such questions, but such a theory would be almost identical to a general analogue computing theory. This seems like a very hard problem, that needs to be approached in steps. In this thesis, the influence of different parameters and topologies was investigated in the framework of regular oscillator networks. However, to obtain the performance for a single task, such as NARMA10, and a single mask and parameter combination, the full reservoir computing routine had to be executed, including long numerical integrations of DDEs. No clear way of predicting the reservoir computing capabilities were found, except for the fact that a completely inert system, i.e. a network in the off-state, does not work.

An attempt at better understanding the memory and transformative properties of reservoir computing systems was outlined in Ref. [DAM12] with the introduction of both linear and nonlinear memory. It may be possible to develop a quantitative theory of reservoir computing (or analogue computing in general) by further

developing their concepts. In particular, they propose to think of arbitrary transformations between input sequences u_k and output sequences o_k of the shape:

$$o_k = \mathbf{F}(u_k), \quad (4.18)$$

where \mathbf{F} is a function that can have an almost arbitrary shape and dependence on the entries of u_k . The space of all possible transformations \mathbf{F} will then be some vector space of functions V_{func} . Within their mathematical framework, the authors of Ref. [DAM12] can show that the computational power of any given reservoir computing system is necessarily limited. For example, the total linear memory capacity C_L^m can not exceed the total read-out dimension D of a system, i.e. the ‘effective phase space dimension’. This is due to the fact, that linear recalls of different lengths m are orthogonal in V_{func} . Every individual degree of freedom of the reservoir must lie along some direction in V_{func} . In the best case scenario, every out-put degree corresponds to one linear recall, allowing for the total linear memory capacity to approach its limit $C_L^m = D$. However, this would also mean that all other linear recalls that are not covered by any of the natural reservoir transformations are orthogonal to those in V_{func} , and thus that their associated linear memory capacity C_L^m is 0. The learning process for the reservoir computer is a pure linear combination, and thus only the parts of the function space V_{func} that are spanned by the transformations provided by the reservoir can be reached. A similar argument can be made for different nonlinear transformations \mathbf{F} as well, which can also be divided into orthogonal subspaces. When an appropriate base for V_{func} is chosen, it can be shown that the sum of both linear and nonlinear capacity of a any dynamical system must be smaller than D [DAM12].

It is important to realize that V_{func} is infinite dimensional. The reservoir computing system now has to allocate its (finite) computational power to a number of base vectors of this infinite dimensional vector space. Every degree of freedom of the reservoir performs some transient motion as excited by the input. Each of these transients can be seen as one particular transformation of the input u_k , and thus every degree of freedom is a single element in V_{func} . This directly means, that no finite-sized reservoir computing system will ever be able to solve every task. There will always be subspaces in V_{func} that are orthogonal to the current set of base vectors provided the reservoir.

In contrast, other machine learning systems, such as gradient descent rules for recurrent neural networks, have an advantage in this respect: The main difference compared to the reservoir computing paradigm is that they also change the weights of the network itself. Thus, the transformations provided by the system are changed, i.e. the part of the vector space of functions V_{func} that is accessible changes during training and can be optimized. In contrast, a reservoir computing

system is ‘frozen’, and the accessible parts of V_{func} are merely optimally used, but inaccessible transformations in V_{func} can never be reached.

If an easy, well-behaved and fast to compute set of base vectors of the space of all nonlinear transformations V_{func} could be found, this could be a first step for the creation of a quantitative theory of reservoir computing. Instead of testing a newly invented reservoir for different tasks, which tend to be somewhat randomly chosen by the operators sometimes, the reservoir could instead be characterized by its access to different parts of V_{func} . Now, as V_{func} is infinite dimensional, this all would hinge on finding a reasonably small subset of V_{func} that covers most of the relevant transformations. With such a general set of base vectors in play, one could then attempt to classify different reservoirs according to their transformative powers. One could also investigate the role of bifurcations, linear stability and system parameters on the directions in V_{func} .

On the flip side of this process, every applied reservoir computing task could also be located within V_{func} as described by this universal base vector set. Then, every reservoir whose accessible subspace of V_{func} contains the target task should be able to flawlessly execute it. Different tasks could then also quantitatively be classified according to their memory requirements and nonlinearity.

However, it is not entirely clear what the best base vectors of this space of functions V_{func} should be, and how feasible it is to find a reasonably small yet physically relevant subspace. For example, many interesting and important functions become infinite series when they are expressed as a Fourier series. A similar problem is likely to occur in V_{func} , because the number of different tasks for machine learning systems is so large and diverse. Furthermore, when the target transformation \mathbf{F} is not in the accessible part of V_{func} , it is not quite clear what the resulting NRMSE would be. A general formula for the quantitative mismatch between the reservoir and the target task would need to be found.

This thesis can only serve as a starting point in trying to understand fundamental aspects of reservoir computing. However, the results obtained here can still serve as a first test for every proposed quantitative theory. In particular, any proposed hypothesis for how exactly certain dynamical systems are suited better than others and which parameters are well-suited and which not would need to be able to explain some of the found properties:

- Why bifurcations have such a drastic influence on the performance
- How performance scales as distance from the bifurcations
- Why different multistable solutions show different performances
- Why the linear memory tends to decay monotonously with m

- Why resonances between T and τ exist and which are the strongest

As the field of reservoir computing is still growing, there is hope that at least some of these questions will be answered in the coming years. Moreover, the increasing interconnectedness of science itself enables a faster knowledge transfer between previously isolated scientific communities. In particular, reservoir computing could greatly benefit from the inclusion of more mathematically proven concepts and ideas from traditional computer science. Should a quantitative theory of the computational power be discovered, this would also greatly enhance the use of the reservoir computing scheme: With such a theory at hand, custom hardware could be constructed to perform desired computations.

4 RESERVOIR COMPUTING IN NETWORKS

5

CONCLUSIONS AND OUTLOOK

In this thesis, the properties of regular oscillator networks were investigated. New symmetry-broken solutions have been found and a new type of reservoir computing architecture consisting of hybrid delay-network systems was introduced.

First, the paradigmatic model of two instantaneously coupled Stuart-Landau oscillators was introduced. This is the simplest coupling scenario imaginable, and has been studied in the literature as well. The fundamental solutions found there were the in-phase and anti-phase synchronized states. These two states are not totally independent however, as due to the shape of the coupling there exists a π -translational symmetry in the coupling phase ϕ that links both states. Despite its importance for general coupled oscillatory systems, a full descriptions all the bifurcations of this system did not previously exist. Here, in particular the importance of the amplitude-phase coupling $\text{Im}(\gamma)$ was investigated, showing that it greatly increases the dynamical richness of the system. This also leads to the appearance of novel symmetry-broken amplitude- and phase-locking states, which break the exchange symmetry of the system without introducing amplitude oscillations. These states are therefore an excellent and easy accessible example of spontaneous symmetry-breaking in oscillatory systems and are also naturally multistable, making them excellent candidates for bistable switches. Their bifurcations and properties could be fully expressed analytically and it was found that they show great similarities to known symmetry-broken solutions from the laser literature.

To further study the role of symmetries, larger networks of Stuart-Landau oscillators were studied. First, the unidirectional ring was investigated and the fundamental symmetry properties of this system were introduced. The basic symmetry-abiding solutions called ‘ponies on a merry-go-round’ or rotating wave patterns were introduced and their bifurcation landscape investigated exemplarily for the network of 4 Stuart-Landau oscillators. They can be seen as an extension of the in-phase and anti-phase synchronization of two coupled Stuart-Landau-oscillators. For a ring of size N , N different patterns exist and they can all be linked via a ξ_j -translational symmetry. In the unidirectional ring there also exist symmetry-broken amplitude- and phase-locked solutions. In particular, two different types were identified for $N = 4$, with one being a cluster state analogous to the $N = 2$

5 CONCLUSIONS AND OUTLOOK

SBL states. SBL states were also found in larger unidirectional rings. Lastly, the influence of delay in the coupling terms was studied, showing a reduced phase-dependence and higher multistability with larger τ .

A second type of topology was then investigated in the form of the bidirectional ring. This system has a higher symmetry than the unidirectional ring, allowing for a larger variety of symmetry-breaking. The fundamental solutions are the rotating wave patterns and identical to the unidirectional ring. However, their bifurcation landscape is different, which leads to the total absence of stable regions for most rotating waves. This is in contrast to the unidirectional ring, where all patterns had identical properties due to the ξ_j -translational property. In the bidirectional ring this was not the case. For even numbers of oscillators, only a generalized in-phase and anti-phase oscillation was found to be stable, independent of network size. Like the unidirectional ring, the bidirectional ring can show symmetry-broken amplitude- and phase-locking states. Due to the higher symmetry, more symmetry-broken patterns were found. Especially larger bidirectional rings showed a plethora of different symmetry-breaking states. The influence of delay on the bidirectional ring revealed similar general trends as in the unidirectional ring. However, for very large delays it was found that the bidirectional ring completely loses all amplitude-oscillation free stability and always performs higher order dynamics. Both unidirectional and bidirectional rings were strongly influenced by the presence of amplitude-phase coupling $\text{Im}(\gamma)$.

Lastly, a connection with the famous ‘chimera state’ of phase oscillators and lasers was attempted. The symmetry-breaking bifurcations described in this thesis can be seen as a possible avenue towards a chimera state from the fully-synchronized state. In particular, they would consist of a cascade of ever smaller cluster states in which roughly half of the system maintains its synchronization, while the other half completely loses it.

In the second main portion of this thesis, the reservoir computing capabilities of regular oscillator networks were investigated. First, some general properties of Stuart-Landau oscillators, when used the core in a reservoir computer, were explored in the ‘delay-line’ setup. There, it was shown that this system can perform computations reasonably well, as tested by the NARMA10 task. Furthermore, the influence of bifurcations and initial conditions was explored. The linear memory as introduced by Jaeger [JAE02] was also studied, with a novel way of compacting the information introduced in the form of the critical memory length m_c . The interplay of the different dynamical time-scales in the system was explored, and it was found that delay times τ resonant to the clock cycle T yield a much lower performance. Furthermore, the influence of the only hyper-parameter K_{training} was shown and possible extensions of the system were discussed, including connections to photonic experiments.

Next, the details of hybrid delay-network systems were explained. In particular, the difference between real and virtual nodes and a particular time-multiplexing procedure was introduced. Time-multiplexed networks were tested and first the importance of the effective system size was studied. Here, it was found that systems with more read-out degrees usually out-perform smaller networks. Thus, to facilitate a fair comparison between networks of different numbers of virtual and real nodes, a way of constructing time-multiplexed networks of constant over all size was introduced and based on factors of 2.

The time-multiplexed networks of constant size but different numbers of real nodes N_R were then tested with the NARMA10 tasks and critical memory length m_c . The unidirectional ring was found to perform adequately for intermediate sized networks, but suffered from a dramatic breakdown of performance for fully real networks. This was in part caused by the sparse connectivity of the network, so that the inclusion of additional shortcut connections could somewhat remove this flaw. The bidirectional ring also showed a better performance for large networks. However, over all it showed a somewhat worse performance for intermediate networks than the unidirectional ring, in particular it had a shorter linear memory. The influence of the inclusion of self-feedback in the bidirectional ring was found to be negligible.

Over all, time-multiplexed networks of intermediate size, i.e. with both significant numbers of virtual and real nodes, showed the best performance. The extreme cases of a purely real network or a single oscillator with delay had a higher NARMA10 NRMSE and short critical memory length m_c . Here, the unidirectional ring showed a larger spread of performance as a function of the coupling phase ϕ and Stuart-Landau parameter λ . Nonetheless, all tested topologies were suitable as reservoir computers.

Open questions

For the future, a natural extension of the works of this thesis is the inclusion of noise. This includes both parameter mismatches between nodes in the networks (breaking the exchange symmetry) and noise during the simulations, i.e. the simulation of stochastic delay-differential equations. Some preliminary simulations have already been tried during the preparation of this thesis, showing that both the reservoir computing performance and the symmetry-broken amplitude- and phase-locking states are robust against small amounts of noise and parameter mismatch. In particular, different frequencies for the oscillators were tested.

A second extension obviously concerns the inclusion of more diverse sets of topologies for time-multiplexed networks. This thesis was focused on the study of the influence of the ratio of N_R to N_V and as such needed to find topologies

5 CONCLUSIONS AND OUTLOOK

that could be scaled for different numbers of real oscillators N_R . However, in general such a restriction for a single implementation is not necessary, so that a more diverse set of topologies could be tested. For example, random networks or custom-tailored topologies could be investigated.

Finally, there still exists a need for the development of a general quantitative theory of reservoir computing and the computational power of complex dynamical systems. This is an important open question, whose solution could greatly increase the applicability of the reservoir computing scheme.

A.1 Symmetry-broken amplitude and phase-coupling

This section covers the detailed calculations of Sec. 3.1, which can also be found in the appendix of Ref. [ROE18], where the standard calculations for the analytic bifurcation lines are also shown.

A.1.1 Analytical symmetry-broken solution

The analytical formulas for describing the symmetry-broken phase and amplitude locking states are derived in detail in the following pages. The two coupled ODEs describing two coupled Stuart-Landau oscillators are given by (also shown in Eq. 3.1 and 3.2 with $\sigma = \kappa \exp i\phi$):

$$\dot{Z}_1 = (\lambda + i\omega + \gamma |Z_1|^2) Z_1 + \sigma Z_2, \quad (\text{A.1})$$

$$\dot{Z}_2 = (\lambda + i\omega + \gamma |Z_2|^2) Z_2 + \sigma Z_1. \quad (\text{A.2})$$

Symmetry-broken states are in general given by $Z_2 = sZ_1 := sZ$ with constant $s \in \mathbb{C}$. With the rotating wave ansatz $\dot{Z} = i\tilde{\Omega}Z$ and assuming $Z \neq 0$, dividing by Z leads to

$$0 = (\lambda + i\Omega + \gamma |Z|^2) + s\sigma \quad (\text{A.3})$$

$$0 = (\lambda + i\Omega + \gamma |s|^2 |Z|^2) s + \sigma, \quad (\text{A.4})$$

where $\Omega = \tilde{\omega} - \tilde{\Omega}$. Four real-valued unknowns remain: $|Z|^2$, Ω , $\mathbf{Re}(s)$ and $\mathbf{Im}(s)$, for which the complex Eqs. (A.3) and (A.4) suffice. $s = \pm 1$ is always a solution of the system, corresponding to the in-phase and anti-phase orbits of coupled Stuart-

A APPENDIX

Landau oscillators. The real and imaginary part for Eq. (A.3) are used to determine $|Z|^2$ and Ω :

$$|Z|^2 = \frac{-\lambda - \mathbf{Re}(\sigma s)}{\mathbf{Re}(\gamma)} \quad (\text{A.5})$$

$$\Omega = c(-\lambda - \mathbf{Re}(\sigma s)) + \mathbf{Im}(\sigma s), \quad (\text{A.6})$$

with $c = \mathbf{Im}(\gamma)/\mathbf{Re}(\gamma)$ introduced for clarity. Using $s = \mathbf{Re}(s) + i\mathbf{Im}(s)$, $\sigma = \alpha + i\beta$ and the real and imaginary part of Eq. (A.4), closed polynomial equations for $\mathbf{Re}(s)$ and $\mathbf{Im}(s)$ can be deduced. With additional definitions $x = \mathbf{Re}(s)$, $y = \mathbf{Im}(s)$, $g = \alpha/\beta$ and $L = \lambda/\beta$ for visual clarity, these two equations for s result in the following equations for x and y :

$$0 = (gc - 1)(x^3 + xy^2 - x) - (g + c)(y^3 + x^2y + y) \quad (\text{A.7})$$

$$0 = (-L - gx + y)(y + cx)(1 - x^2 - y^2) + 2gxy + x^2 - y^2 - 1. \quad (\text{A.8})$$

Combining Eqs. (A.7) and (A.8) leads to a final quartic equation that is difficult to solve by hand. Using the *Solve*-function of *Wolfram Mathematica* to solve Eqs. (A.7) and (A.8), the following solutions are obtained: Apart from $s = \pm 1$, solutions are of the form:

$$\mathbf{Re}(s)_{1,2} = -T_1 - \frac{1}{2}\sqrt{T_2} \pm \frac{1}{2}\sqrt{T_3} \quad (\text{A.9})$$

$$\mathbf{Re}(s)_{3,4} = -T_1 + \frac{1}{2}\sqrt{T_2} \pm \frac{1}{2}\sqrt{T_4}, \quad (\text{A.10})$$

with the following definitions:

$$T_1 = \frac{L(c + g)(c^2 + 4cg - 3)}{4(g^2 + 1)(c^2 + 2cg - 1)} \quad (\text{A.11})$$

$$T_2 = \frac{(c + g)^2 \left((c^2 + 1)^2 L^2 - 8(cg - 1)(c^2 + 2cg - 1) \right)}{4(g^2 + 1)^2 (c^2 + 2cg - 1)^2} \quad (\text{A.12})$$

$$\begin{aligned} T_{3,4} = & \frac{(c + g)}{2(g^2 + 1)^2 (c^2 + 2cg - 1)^2} \\ & \times \left[-2(g^2 + 1)(c + g) \left(c^2(L^2 + 2) + 4cg + L^2 - 2 \right) \right. \\ & \pm (g^2 + 1)L(c^2 + 2cg - 1) \left[(c + 2g)^2 + 1 \right] \sqrt{4F_2} \\ & + L^2(c^2 + 4cg - 3)^2 (c + g) - 4g(c^2 + 2cg - 1)(c + g)^2 \\ & \left. - 2L^2(2c^3g + c^2(5g^2 - 1) - 6cg + g^2 + 3)(c + g) \right] \quad (\text{A.13}) \end{aligned}$$

A.1 SYMMETRY-BROKEN AMPLITUDE AND PHASE-COUPLING

The results returned by *Wolfram Mathematica* for imaginary part $y = \mathbf{Im}(s)$ are extremely long. This could be due to inefficient formatting, but no way of obtaining a clear description was found. Nevertheless, two ways of obtaining the imaginary part $y = \mathbf{Im}(s)$ from $\mathbf{Re}(s)$ are possible: First, the a -to- ψ formula obtained of Eq. 3.22 can be rewritten to obtain $\mathbf{Im}(s)$ as a function of $\mathbf{Re}(s)$. Alternatively, the fact that for each s the corresponding value $1/s$ is also a solution to the system of equations is used. Hence $s_1 = 1/s_2$ and $s_3 = 1/s_4$. Consequently, $\mathbf{Re}(s)$ and $\mathbf{Re}(1/s)$ are known and through some simple algebra $\mathbf{Im}(s)$ is obtainable. All of these approaches introduce some spurious solutions one needs to be careful not to include, for which numerical simulations were used in this thesis.

After splitting s into real and imaginary part both $\mathbf{Re}(s)$ and $\mathbf{Im}(s)$ need to be real-valued. Hence, the arguments of the square roots inside Eqs. (A.9) and (A.10) need to be positive and necessary conditions for the existence of symmetry-broken amplitude and phase locking states can be obtained. By solving $T_2 \geq 0$ the bifurcation line of the saddle-node of limit cycles (Eq. (3.23)) as described in Sec. 3.1.3 and plotted as the red line in Fig. 3.4 is obtained.

A.2 Unidirectional ring networks

This section covers the derivation of the characteristic equation and simple bifurcations of the unidirectional ring as used in Sec. 3.3.2. The system of N Stuart-Landau oscillators is given by Eq. (3.41):

$$\dot{Z}_n = (\lambda + i\omega + \gamma |Z_n|^2)Z_n + \kappa e^{i\phi} Z_{n-1}, \quad (\text{A.14})$$

where the oscillator index n is taken modulus N .

As outlined in Sec. 3.3.2, there exist N rotating waves or ‘ponies on a merry-go-round’ as defined in Eq. 3.42.

To derive the characteristic equation, the complex amplitude is split into real and imaginary part $Z_n = x_n + iy_n$, leading to two sets of equations:

$$\begin{aligned} \dot{x}_n = & \lambda x_n - \omega y_n + \text{Re}(\gamma) (x_n^2 + y_n^2) x_n - \text{Im}(\gamma) (x_n^2 + y_n^2) y_n \\ & + \kappa \cos \phi x_{n-1} - \kappa \sin \phi y_{n-1} \end{aligned} \quad (\text{A.15})$$

$$\begin{aligned} \dot{y}_n = & \lambda y_n + \omega x_n + \text{Re}(\gamma) (x_n^2 + y_n^2) y_n + \text{Im}(\gamma) (x_n^2 + y_n^2) x_n \\ & + \kappa \cos \phi y_{n-1} + \kappa \sin \phi x_{n-1} \end{aligned} \quad (\text{A.16})$$

The Jacobian J_N of the unidirectional ring of size N then is of size $2N$ in the new coordinates and given by:

$$J_N = \begin{pmatrix} L_0 & 0 & \dots & 0 & C_0 \\ C_1 & L_1 & 0 & \dots & 0 \\ 0 & C_2 & \ddots & \ddots & \vdots \\ \vdots & \ddots & \ddots & L_{N-2} & 0 \\ 0 & \dots & 0 & C_{N-1} & L_{N-1} \end{pmatrix} \quad (\text{A.17})$$

Where the L and C are 2×2 -dimensional matrices describing the local and coupling terms, respectively. The local dynamics L enter along the main-diagonal of J_N , while the coupling terms C appear for the sub diagonal. They are given by:

$$L_n = \begin{pmatrix} f_{xx} & f_{xy} \\ f_{yx} & f_{yy} \end{pmatrix} \quad (\text{A.18})$$

$$C_n = \begin{pmatrix} C_{xx} & C_{xy} \\ C_{yx} & C_{yy} \end{pmatrix} \quad (\text{A.19})$$

Where the following variables have been used:

$$f_n^{xx} = \lambda + \operatorname{Re}(\gamma) (3x_n^2 + y_n^2) - 2\operatorname{Im}(\gamma)x_n y_n \quad (\text{A.20})$$

$$f_n^{xy} = -\omega + 2\operatorname{Re}(\gamma)x_n y_n - \operatorname{Im}(\gamma) (x_n^2 + 3y_n^2) \quad (\text{A.21})$$

$$f_n^{yx} = \omega + 2\operatorname{Re}(\gamma)x_n y_n + \operatorname{Im}(\gamma) (3x_n^2 + y_n^2) \quad (\text{A.22})$$

$$f_n^{yy} = \lambda + \operatorname{Re}(\gamma) (x_n^2 + 3y_n^2) + 2\operatorname{Im}(\gamma)x_n y_n \quad (\text{A.23})$$

Because of the regular nature of J_N it may even be possible to solve, or at least factor, the characteristic equation $\det(J_N - \Lambda I) = 0$ analytically for all N . This thesis will present the case of $N = 4$ here, which was used to calculate the bifurcation lines of Sec. 3.3.2. As outlined in Sec. 3.3.2, only one of the rotating waves needs to be investigated, as all other follow from symmetry arguments. Hence, without loss of generality the in-phase synchronized state $j = 0$ is chosen:

$$Z_n = Z = r(t) \exp(i\theta(t)) \quad \forall n \quad (\text{A.24})$$

For the in-phase synchronized state, all Eqs. (A.14) decouple, and the radius r and frequency $\dot{\theta}$ of oscillations can be deduced like for the solitary oscillator in Sec. 2.3.3:

$$r = \sqrt{-\frac{\lambda + \kappa \cos \phi}{\operatorname{Re}(\gamma)}} \quad \dot{\theta} = \omega + \kappa \sin \phi - \lambda \frac{\operatorname{Im}(\gamma)}{\operatorname{Re}(\gamma)} \quad (\text{A.25})$$

Thus, the radius r is not time-dependent, and if ω is chosen correctly by applying an appropriate rotating frame, the phase velocity can be removed $\dot{\theta} = 0$. Hence, all secondary bifurcations of the periodic in-phase orbit become bifurcations of a fixed point with a single neutral eigenvalue in the correct rotating frame. Because of that neutral eigenmode (corresponding to the Goldstone mode of the original system), the global phase of Z_n can be chosen freely. To simplify the calculations, it is useful to choose $x_n = r$ and $y_n = 0$.

A APPENDIX

The Jacobian of the unidirectional ring of size $N = 4$ Stuart-Landau oscillators thus is:

$$J_4 = \begin{pmatrix} a & b & 0 & 0 & 0 & 0 & e & -f \\ c & d & 0 & 0 & 0 & 0 & f & e \\ e & -f & a & b & 0 & 0 & 0 & 0 \\ f & e & c & d & 0 & 0 & 0 & 0 \\ 0 & 0 & e & -f & a & b & 0 & 0 \\ 0 & 0 & f & e & c & d & 0 & 0 \\ 0 & 0 & 0 & 0 & e & -f & a & b \\ 0 & 0 & 0 & 0 & f & e & c & d \end{pmatrix} \quad (\text{A.26})$$

with

$$a = -2\lambda - 3\kappa \cos \phi \qquad b = \kappa \sin \phi \quad (\text{A.27})$$

$$c = -2(\lambda + \kappa \cos \phi) \frac{\text{Im}(\gamma)}{\text{Re}(\gamma)} - \kappa \sin \phi \qquad d = -\kappa \cos \phi \quad (\text{A.28})$$

$$e = \kappa \cos \phi \qquad f = \kappa \sin \phi \quad (\text{A.29})$$

The characteristic polynomial $\det(J_4 - \Lambda I) = 0$, where I is the identity matrix of size 8, can now be solved. This was done using the *CharacteristicPolynomial*-function of *Wolfram Mathematica* (v10.1). The lengthy expression was then reduced using the *Factor*-function, and an expression of 4 factors was obtained:

$$0 = \Lambda (\Lambda + 2\lambda + 2\kappa \cos \phi) R_3 R_4 \quad (\text{A.30})$$

where $R_{3,4}$ are still lengthy expressions. Equation (A.30) reveals several bifurcations: First, the neutral eigenmode is revealed, in that there is always an eigenvalue $\Lambda = 0$ from the first factor. The second factor of Eq. (A.30) becomes zero for:

$$\lambda = -\kappa \cos \phi, \quad (\text{A.31})$$

which correspond to the in-phase Andronov-Hopf bifurcation H_0 of Eq. (3.45), where the oscillations are created. The next factor R_3 can be solved using the *Solve*-function of *Mathematica*, yielding an eigenvalue of:

$$\begin{aligned} \Lambda = & -3\kappa \cos(\phi) - \lambda \\ & \pm \frac{1}{\sqrt{2}} \sqrt{-4\tilde{\alpha}\kappa^2 \sin(2\phi) - 8\tilde{\alpha}\kappa\lambda \sin \phi + 5\kappa^2 \cos(2\phi) - 3\kappa^2 + 4\kappa\lambda \cos(\phi) + 2\lambda^2}, \end{aligned} \quad (\text{A.32})$$

with $\tilde{\alpha} = \text{Im}(\gamma)/\text{Re}(\gamma)$. This becomes 0, i.e. a pitchfork bifurcation, for:

$$\lambda_P = -\frac{3\kappa + \kappa \cos(2\phi) + \tilde{\alpha}\kappa \sin(2\phi)}{2 \cos \phi + 2\tilde{\alpha} \sin \phi}, \quad (\text{A.33})$$

which is shown as P_0 in Fig. 3.11. The corresponding bifurcations for rotating waves of index j are then found via the symmetry-transformation: $P_j(\phi) = P_0(\phi + \xi_j)$, with the phase difference ξ_j as given by Eq. (3.43). The final factor R_4 yields 4 related eigenvalues:

$$\Lambda = -\lambda - (2 \pm i)\kappa \cos(\phi) \pm \frac{1}{\sqrt{2}}\sqrt{S} \quad (\text{A.34})$$

$$S = (4 - 4i)\tilde{\alpha}\kappa^2 \sin(2\phi) + (8 - 8i)\tilde{\alpha}\kappa\lambda \sin(\phi) \\ + (1 - 2i)\kappa^2 \cos(2\phi) + (1 + 2i)\kappa^2 + 4\kappa\lambda \cos(\phi) + 2\lambda^2, \quad (\text{A.35})$$

where the two \pm -signs are taken to be independent in Eq. (A.34). The eigenvalues given by Eq. (A.34) will occur in complex conjugate pairs when going through $\text{Re}(\Lambda) = 0$. Finding the roots of this last set of eigenvalues is difficult, so that their analytic form of Eq. (A.34) was simply numerically solved for $\Lambda = 0$.

A APPENDIX

LIST OF FIGURES

2.1	Stable points of balancing an egg	16
2.2	The human brain as an example of a network	22
2.3	An example graph and adjacency matrix	23
2.4	17th century sketch by Christiaan Huygens	28
2.5	Supercritical case of the Stuart-Landau oscillator	33
2.6	Time series example of the Stuart-Landau oscillator	35
2.7	Transients of the Stuart-Landau oscillator	35
2.8	Sketch of artificial neural networks	45
2.9	The reservoir computing principle	51
2.10	The masking procedure	56
2.11	Influence of the masking on the system response	57
2.12	The Santa Fe task	60
2.13	A NARMA10 series example	61
3.1	Solutions of two coupled Stuart-Landau oscillators	72
3.2	Parameter scan for two Stuart-Landau oscillators	74
3.3	Parameter scan for two coupled Stuart-Landau oscillators with non-zero shear	77
3.4	Regions of existence for symmetry-broken states in two coupled Stuart-Landau oscillators	84
3.5	Linescan of symmetry-breaking in two coupled Stuart-Landau oscillators	85
3.6	Parameter scan for two coupled Lang-Kobayashi-type systems	89
3.7	Parameter scan for two coupled Lang-Kobayashi-type systems with non-zero α	91
3.8	Examples of symmetry-broken amplitude- and phase-locking states in two coupled Lang-Kobayashi-type systems	93
3.9	Sketch of a unidirectional and a bidirectional ring	96

LIST OF FIGURES

3.10	Rotating wave patterns for the unidirectional ring with $N = 4$	99
3.11	Parameter scan of rotating waves for a unidirectional ring of $N = 4$.	102
3.12	Parameter scan for a unidirectional ring of size $N = 4$ with shear . .	105
3.13	Example of a symmetry-broken state in the unidirectional ring . . .	107
3.14	Example of the second type of symmetry-broken state in a unidirectional ring	109
3.15	Parameter scan for large unidirectional rings of Stuart-Landau oscillators	111
3.16	Example for a symmetry-broken state in a large unidirectional ring .	112
3.17	Phase representation of a symmetry-broken state in a large unidirectional ring	113
3.18	Parameter scan of the unidirectional ring with delay	114
3.19	Parameter scan of the bidirectional ring without shear	121
3.20	Parameter scan of the bidirectional ring with shear	124
3.21	Example timeseries for the symmetry-broken states of the bidirectional ring of $N = 4$ Stuart-Landau oscillators	126
3.22	Parameter scan for large bidirectional rings	131
3.23	Example timeseries for a symmetry-broken state in a large bidirectional ring	132
3.24	Second example timeseries for a symmetry-broken state in a large bidirectional ring	133
3.25	Third example timeseries for a symmetry-broken state in a large bidirectional ring	134
3.26	Fourth example timeseries for a symmetry-broken state in a large bidirectional ring	135
3.27	Fifth example timeseries for a symmetry-broken state in a large bidirectional ring	136
3.28	Parameter scans for the bidirectional ring with delay	138
3.29	Linescans and example timeseries for a symmetry-breaking bifurcation scenario leading to a small chimera state in 4 delay-coupled Lang-Kobayashi systems	141
4.1	Details of the masking procedure	150
4.2	Parameter scan of the NARMA10 NRMSE for the single Stuart-Landau oscillator	151
4.3	Zoom of the parameter scan of the NARMA10 NRMSE for the single Stuart-Landau oscillator	153

LIST OF FIGURES

4.4	Zoom of the parameter scan of the NARMA10 NRMSE for the single Stuart-Landau oscillator	154
4.5	Example of a memory curve for the single Stuart-Landau oscillator with delay	157
4.6	Parameter scan of the total linear memory capacity $C_{L,tot}$ for the single Stuart-Landau oscillator	158
4.7	Parameter scan of the linear memory capacity C_L^{15} for the single Stuart-Landau oscillator	160
4.8	Parameter scan of the critical memory length m_c for the single Stuart-Landau oscillator	161
4.9	Influence of the system time scales on the NARMA10 NRMSE for the single Stuart-Landau oscillator	163
4.10	Causes for the resonances in system time-scales for reservoir computing	164
4.11	Influence of the system time-scales on the critical memory length m_c for the single Stuart-Landau oscillator	166
4.12	Influence of the training length for the single Stuart-Landau oscillator	168
4.13	Influence on the system size in time-multiplexed networks	176
4.14	Sketch of different time-multiplexed networks	178
4.15	Reservoir computing results for the time-multiplexed unidirectional ring of Stuart-Landau oscillators	182
4.16	Sketch of unidirectional rings with shortcuts	186
4.17	Reservoir computing results for the time-multiplexed unidirectional ring with jumps of Stuart-Landau oscillators	188
4.18	Reservoir computing results for the time-multiplexed bidirectional ring of Stuart-Landau oscillators	190
4.19	Reservoir computing results for the time-multiplexed bidirectional ring with self-feedback of Stuart-Landau oscillators	193
4.20	Dependence of the NARMA10 NRMSE on N_R	195
4.21	Dependence of the critical memory length on N_R	197

LIST OF FIGURES

List of symbols

Symbol	Meaning
t	time
τ	delay time
a_{ij}	element of the adjacency or coupling matrix
Z	complex amplitude of the Stuart-Landau oscillator
ω	solitary frequency of the Stuart-Landau oscillator
λ	bifurcation parameter of the Stuart-Landau oscillator
γ	non-linearity prefactor of the Stuart-Landau oscillator
κ	the coupling strength
ϕ	the coupling phase
a	the real-valued amplitude ratio in a SBL state
ψ	the phase-difference in a SBL state
j	index of the rotating wave solution
E	complex electric field amplitude of the Lang-Kobayashi system
α	amplitude-phase coupling in the Lang-Kobayashi system
N_e	excess carrier density of the Lang-Kobayashi system
p	pump current of the Lang-Kobayashi system
T	ratio of carrier and photon lifetimes in the Lang-Kobayashi system or clock cycle for reservoir computing with delay
θ	an angle or the time per virtual node in reservoir computing
W_{in}	in-coupling matrix for reservoir computing
W_{out}	trained out-put weights for reservoir computing
$u(t)$	the input to the reservoir computer
$o(t)$	the target output of the reservoir computer
$\hat{o}(t)$	the approximated output of the reservoir computer
D	number of read-out degrees of the reservoir computer
$J(t)$	the masked input signal for reservoir computing
$M(t)$	the mask for reservoir computing
G	the input gain for reservoir computing
K_{training}	the number of training samples
K_{testing}	the number of testing samples
K_{buffer}	the number of buffer samples
C_L^m	the linear memory capacity for length m
$C_{L,tot}$	the total linear memory capacity
m_c	the critical memory length
N	the number of oscillators in a network
N_R	the number of real oscillators in a time-multiplexed network
N_V	the virtualisation factor for a time-multiplexed network

LIST OF ACRONYMS

List of acronyms

Acronym	Meaning
SBL	symmetry-broken amplitude- and phase-locking
NARMA	nonlinear auto-regressive moving average
MSE	mean-squared error
NRMSE	normalized root mean-squared error
ODE	ordinary differential equation
DDE	delay-differential equation

BIBLIOGRAPHY

- [ABE06] M. Abel, S. Bergweiler, and R. Gerhard-Multhaupt: *Synchronization of organ pipes: experimental observations and modeling*, J. Acoust. Soc. Am. **119**, 2467–2475 (2006).
- [ABR04] D. M. Abrams and S. H. Strogatz: *Chimera states for coupled oscillators*, Phys. Rev. Lett. **93**, 174102 (2004).
- [ACE05] J. A. Acebrón, L. L. Bonilla, C. J. Pérez Vicente, F. Ritort, and R. Spigler: *The Kuramoto model: A simple paradigm for synchronization phenomena*, Rev. Mod. Phys. **77**, 137–185 (2005).
- [AIZ76] Y. Aizawa: *Synergetic approach to the phenomena of mode-locking in nonlinear systems*, Prog. Theor. Phys. **56**, 703–716 (1976).
- [ALB02a] R. Albert and A. L. Barabási: *Statistical mechanics of complex networks*, Rev. Mod. Phys. **74**, 47–97 (2002).
- [ALS96] P. M. Alsing, V. Kovanis, A. Gavrielides, and T. Erneux: *Lang and Kobayashi phase equation*, Phys. Rev. A **53**, 4429–4434 (1996).
- [AND49] A. A. Andronov, S. E. Chaikin, and S. Lefschetz: *Theory of oscillations*. (Princeton Univ. Press, 1949).
- [ANT08a] E. A. Antonelo, B. Schrauwen, and D. Stroobandt: *Event detection and localization for small mobile robots using reservoir computing*, Neural Netw. **21**, 862–871 (2008), Computational and Biological Inspired Neural Networks, selected papers from ICANN 2007.
- [ANT16] P. Antonik, F. Duport, M. Hermans, A. Smerieri, M. Haelterman, and S. Massar: *Online training of an opto-electronic reservoir computer applied to real-time channel equalization*, IEEE Trans. Neural Netw. Learn. Syst. **28** (2016).
- [APP11] L. Appeltant, M. C. Soriano, G. Van der Sande, J. Danckaert, S. Massar, J. Dambre, B. Schrauwen, C. R. Mirasso, and I. Fischer: *Information processing using a single dynamical node as complex system*, Nat. Commun. **2**, 468 (2011).
- [APP12] L. Appeltant: *Reservoir Computing based on Delay-dynamical Systems*, Ph.D. thesis, Vrije Universiteit Brussel, Universitat de les Illes Balears (2012).

- [APP14] L. Appeltant, G. Van der Sande, J. Danckaert, and I. Fischer: *Constructing optimized binary masks for reservoir computing with delay systems*, Sci. Rep. **4**, 3629 (2014).
- [ARG16] A. Argyris, M. Bourmpos, and D. Syvridis: *Experimental synchrony of semiconductor lasers in coupled networks*, Opt. Express **24**, 5600–5614 (2016).
- [ARO90] D. G. Aronson, G. B. Ermentrout, and N. Kopell: *Amplitude response of coupled oscillators*, Physica D **41**, 403 (1990).
- [ATA03] F. M. Atay: *Distributed delays facilitate amplitude death of coupled oscillators*, Phys. Rev. Lett. **91**, 094101 (2003).
- [ATI00] A. F. Atiya and A. G. Parlos: *New results on recurrent network training: unifying the algorithms and accelerating convergence*, IEEE Trans. Neural Netw. **11**, 697–709 (2000).
- [BUE10b] L. Büsing, B. Schrauwen, and R. Legenstein: *Connectivity, dynamics, and memory in reservoir computing with binary and analog neurons*, Neural Comput. **22**, 1272–1311 (2010), PMID: 20028227.
- [BAN15] T. Banerjee: *Mean-field-diffusion-induced chimera death state*, Europhys. Lett. **110**, 60003 (2015).
- [BAR02a] A. L. Barabási, H. Jeong, Z. Néda, E. Ravasz, A. Schubert, and T. Vicsek: *Evolution of the social network of scientific collaborations*, Physica A **311**, 590–614 (2002).
- [BAR85] K. Bar-Eli: *On the stability of coupled chemical oscillators*, Physica D **14**, 242 (1985).
- [BEL54] R. Bellmann and J. Danskin: *A survey of the mathematical theory of time-lag, retarded control, and hereditary processes*, Tech. rep., RAND Corporation, Santa Monica, CA (1954), <https://www.rand.org/pubs/reports/R256.html>.
- [BEL59] B. P. Belousov: *Oscillations and traveling waves in chemical systems*, in *Collection of short papers on radiation medicine for 1958*, edited by (Med. Publ., Moscow, 1959).
- [BER04] T. W. Berg, J. Mørk, and J. M. Hvam: *Gain dynamics and saturation in semiconductor quantum dot amplifiers*, New J. Phys. **6**, 178 (2004).
- [BOG73] A. Bogatov, P. Eliseev, L. Ivanov, A. Logginov, M. Manko, and K. Senatorov: *Study of the single-mode injection laser*, IEEE J. Quantum Electron. **9**, 392–394 (1973).
- [BOE15] F. Böhm, A. Zakharova, E. Schöll, and K. Lüdge: *Amplitude-phase coupling drives chimera states in globally coupled laser networks*, Phys. Rev. E **91**, 040901 (R) (2015).

- [BOT86] D. Botez and D. E. Ackley: *Phase-locked arrays of semiconductor diode lasers*, IEEE Circuits and Devices Magazine **2**, 8–17 (1986).
- [BRO69] R. F. Broom: *Self modulation at gigahertz frequencies of a diode laser coupled to an external cavity*, Electron. Lett. **5**, 571–572 (1969).
- [BRU13a] D. Brunner, M. C. Soriano, C. R. Mirasso, and I. Fischer: *Parallel photonic information processing at gigabyte per second data rates using transient states*, Nat. Commun. **4**, 1 (2013).
- [BRU15] D. Brunner and I. Fischer: *Reconfigurable semiconductor laser networks based on diffractive coupling*, Opt. Lett. **40**, 3854–3857 (2015).
- [BUE17] J. Bueno, D. Brunner, M. C. Soriano, and I. Fischer: *Conditions for reservoir computing performance using semiconductor lasers with delayed optical feedback*, Opt. Express **25**, 2401–2412 (2017).
- [BUL07] J. M. Buldú, M. C. Torrent, and J. García-Ojalvo: *Synchronization in semiconductor laser rings*, J. Light. Technol. **25**, 1549–1554 (2007).
- [BUT13b] J. B. Butcher, D. Verstraeten, B. Schrauwen, C. R. Day, and P. W. Haycock: *Reservoir computing and extreme learning machines for non-linear time-series data analysis*, Neural Netw. **38**, 76–89 (2013).
- [CAL36] A. Callender, D. R. Hartree, and M. A. Porter: *Time-lag in a control system*, Philos. Trans. Royal Soc. A **235**, 415–444 (1936).
- [CAS90] J. R. Cash and A. H. Karp: *A variable order Runge-Kutta method for initial value problems with rapidly varying right-hand sides*, ACM Trans. Math. Softw. **16**, 201–222 (1990).
- [CHA11a] S. P. Chatzis and Y. Demiris: *Echo state Gaussian process*, IEEE Trans. Neural Netw. **22**, 1435–1445 (2011).
- [CHA13e] K. C. Chatzidimitriou and P. A. Mitkas: *Adaptive reservoir computing through evolution and learning*, Neurocomputing **103**, 198–209 (2013).
- [CHO94] W. W. Chow, S. W. Koch, and M. Sargent: *Semiconductor laser physics* (Springer, Berlin, 1994).
- [CHO09] C. U. Choe, T. Dahms, P. Hövel, and E. Schöll: *Controlling synchrony by delay coupling in networks: from in-phase to splay and cluster states*, Phys. Rev. E **81**, 025205(R) (2010).
- [CLE14] E. Clerkin, S. O’Brien, and A. Amann: *Multi-stabilities and symmetry-broken one-colour and two-colour states in closely coupled single-mode lasers*, Phys. Rev. E **89**, 032919 (2014).
- [COU10] P. Coulibaly: *Reservoir computing approach to Great Lakes water level forecasting*, J. Hydrol. **381**, 76–88 (2010).

- [CRA91] J. D. Crawford: *Introduction to bifurcation theory*, Rev. Mod. Phys. **63**, 991 (1991).
- [CRU10a] J. P. Crutchfield, W. Ditto, and S. Sinha: *Introduction to focus issue: intrinsic and designed computation: information processing in dynamical systems-beyond the digital hegemony*, Chaos **20**, 037101 (2010).
- [DAM12] J. Dambre, D. Verstraeten, B. Schrauwen, and S. Massar: *Information processing capacity of dynamical systems*, Sci. Rep. **2**, 514 (2012).
- [DEJ14] A. Dejonckheere, F. Duport, A. Smerieri, L. Fang, J. L. Oudar, M. Haelterman, and S. Massar: *All-optical reservoir computer based on saturation of absorption*, Opt. Express **22**, 10868 (2014).
- [DHU08] O. D’Huys, R. Vicente, T. Erneux, J. Danckaert, and I. Fischer: *Synchronization properties of network motifs: Influence of coupling delay and symmetry*, Chaos **18**, 037116 (2008).
- [DOC09] K. Dockendorf, I. Park, P. He, J. C. Principe, and T. B. DeMarse: *Liquid state machines and cultured cortical networks: The separation property*, Biosystems **95** (2009).
- [DOE09a] C. R. Doering: *The 3d Navier-Stokes problem*, Ann. Rev. Fluid Mech. **41**, 109–128 (2009).
- [DUP12] F. Duport, B. Schneider, A. Smerieri, M. Haelterman, and S. Massar: *All-optical reservoir computing*, Opt. Express **20**, 22783–22795 (2012).
- [DUP16] F. Duport, A. Smerieri, A. Akrouf, M. Haelterman, and S. Massar: *Fully analogue photonic reservoir computer*, Sci. Rep. **6** (2016).
- [DUP16a] F. Duport, A. Smerieri, A. Akrouf, M. Haelterman, and S. Massar: *Virtualization of a photonic reservoir computer*, J. Light. Technol. **34**, 2085–2091 (2016).
- [EIN05a] A. Einstein: *Über einen die erzeugung und verwandlung des lichtes betreffenden heuristischen gesichtspunkt*, Ann. Phys. (Leipzig) **322**, 132–148 (1905).
- [EIN17] A. Einstein: *Zur Quantentheorie der Strahlung*, Phys. Z. **18**, 121–128 (1917).
- [ERN10b] T. Erneux and P. Glorieux: *Laser Dynamics* (Cambridge University Press, UK, 2010).
- [ERZ05a] H. Erzgräber, B. Krauskopf, and D. Lenstra: *Mode structure of delay-coupled semiconductor lasers: influence of the pump current*, J. Opt. B **7**, 361 (2005).
- [ERZ05] H. Erzgräber, D. Lenstra, B. Krauskopf, E. Wille, M. Peil, I. Fischer, and W. Elsässer: *Mutually delay-coupled semiconductor lasers: Mode bifurcation scenarios*, Opt. Commun. **255**, 286–296 (2005).
- [ERZ06a] H. Erzgräber, B. Krauskopf, and D. Lenstra: *Compound laser modes of mutually delay-coupled lasers*, SIAM J. Appl. Dyn. Syst. **5**, 30–65 (2006).

- [ERZ09] H. Erzgräber, E. Wille, B. Krauskopf, and I. Fischer: *Amplitude-phase dynamics near the locking region of two delay-coupled semiconductor lasers*, *Nonlinearity* **22**, 585–600 (2009).
- [FER03] C. Fernando and S. Sojakka: *Pattern Recognition in a Bucket*, in *Advances in Artificial Life*, edited by 2003), pp. 588–597.
- [FRA18] A. Frank, J. Carroll-Nellenback, M. Alberti, and A. Kleidon: *The anthropocene generalized: Evolution of exo-civilizations and their planetary feedback*, *Astrobiol.* **18**, 503–518 (2018), PMID: 29791236.
- [GAN08] S. Ganguli, D. Huh, and H. Sompolinsky: *Memory traces in dynamical systems*, *Proc. Natl. Acad. Sci.* **105**, 18970 (2008).
- [GEF14] P. M. Geffert, A. Zakharova, A. Vüllings, W. Just, and E. Schöll: *Modulating coherence resonance in non-excitable systems by time-delayed feedback*, *Eur. Phys. J. B* **87**, 291 (2014).
- [GIA96] G. Giacomelli and A. Politi: *Relationship between delayed and spatially extended dynamical systems*, *Phys. Rev. Lett.* **76**, 2686 (1996).
- [GAR08] V. García-Morales and K. Krischer: *Nonlocal complex Ginzburg-Landau equation for electrochemical systems*, *Phys. Rev. Lett.* **100**, 054101 (2008).
- [GAR12b] V. García-Morales and K. Krischer: *The complex Ginzburg-Landau equation: an introduction*, *Contemp. Phys.* **53**, 79–95 (2012).
- [GAR99a] J. García-Ojalvo, J. Casademunt, M. C. Torrent, C. R. Mirasso, and J. M. Sancho: *Coherence and synchronization in diode-laser arrays with delayed global coupling*, *Int. J. Bifurc. Chaos* **9**, 2225 (1999).
- [GOL88a] M. Golubitsky and I. Stewart: *Singularities and Groups in Bifurcation Theory. Volume 2*, vol. 69 (Springer-Verlag, New York, 1988).
- [GON07b] C. M. González, C. Masoller, M. C. Torrent, and J. García-Ojalvo: *Synchronization via clustering in a small delay-coupled laser network*, *Europhys. Lett.* **79**, 64003 (2007).
- [GRI14] L. Grigoryeva, J. Henriques, L. Larger, and J. P. Ortega: *Stochastic nonlinear time series forecasting using time-delay reservoir computers: Performance and universality*, *Neural Netw.* **55**, 59 (2014).
- [GRI15] L. Grigoryeva, J. Henriques, L. Larger, and J. P. Ortega: *Optimal nonlinear information processing capacity in delay-based reservoir computers*, *Sci. Rep.* **5**, 12858 (2015).
- [HAD87] P. Hadley and M. R. Beasley: *Dynamical states and stability of linear arrays of josephson junctions*, *Appl. Phys. Lett.* **50**, 621 (1987).

- [HAK92] V. Hakim and W. J. Rappel: *Dynamics of the globally coupled complex ginzburg-landau equation*, Phys. Rev. A **46**, R7347–R7350 (1992).
- [HAR37] D. R. Hartree, A. Potter, A. Callender, and A. B. Stevenson: *Time-lag in a control system-ii*, Proceedings of the Royal Society of London A: Mathematical, Physical and Engineering Sciences **161**, 460–476 (1937).
- [HAE03] S. Häusler, H. Markram, and W. Maass: *Perspectives of the high-dimensional dynamics of neural microcircuits from the point of view of low-dimensional readouts*, Complexity **8** (2003).
- [HAY15] N. Haynes, M. C. Soriano, D. P. Rosin, I. Fischer, and D. J. Gauthier: *Reservoir computing with a single time-delay autonomous boolean node*, Phys. Rev. E **91**, 020801 (2015).
- [HEI99b] T. Heil, I. Fischer, and W. Elsässer: *Influence of amplitude-phase coupling on the dynamics of semiconductor lasers subject to optical feedback*, Phys. Rev. A **60**, 634 (1999).
- [HEI00c] T. Heil, I. Fischer, and W. Elsässer: *Stabilization of feedback-induced instabilities in semiconductor lasers*, J. Opt. B **2**, 413–420 (2000).
- [HEI01b] T. Heil, I. Fischer, W. Elsässer, J. Mulet, and C. R. Mirasso: *Chaos synchronization and spontaneous symmetry-breaking in symmetrically delay-coupled semiconductor lasers*, Phys. Rev. Lett. **86**, 795 (2001).
- [HEI03a] T. Heil, I. Fischer, W. Elsässer, B. Krauskopf, K. Green, and A. Gavrielides: *Delay dynamics of semiconductor lasers with short external cavities: Bifurcation scenarios and mechanisms*, Phys. Rev. E **67**, 066214 (2003).
- [HEI10] M. Heinrich, T. Dahms, V. Flunkert, S. W. Teitworth, and E. Schöll: *Symmetry breaking transitions in networks of nonlinear circuit elements*, New J. Phys. **12**, 113030 (2010).
- [HEN86] C. H. Henry and R. F. Kazarinov: *Instability of semiconductor lasers due to optical feedback from distant reflectors*, IEEE J. Quantum Electron. **22**, 294–301 (1986).
- [HER10] M. Hermans and B. Schrauwen: *Memory in linear recurrent neural networks in continuous time*, Neural Networks **23**, 341–355 (2010).
- [HER12] M. Hermans: *Expanding the Theoretical Framework of Reservoir Computing*, Ph.D. thesis, Universiteit Gent (2012).
- [HER15] S. Herman, M. C. Soriano, J. Dambre, P. Bienstman, and I. Fischer: *Photonic delay systems as machine learning implementations*, J. Mach. Learn. Res. **16**, 2081 (2015).

- [HER15a] M. Hermans, M. Burm, T. Van Vaerenbergh, J. Dambre, and P. Bienstman: *Trainable hardware for dynamical computing using error backpropagation through physical media*, Nat. Commun. **6**, 6729 (2015).
- [HIC11] K. Hicke, O. D’Huys, V. Flunkert, E. Schöll, J. Danckaert, and I. Fischer: *Mismatch and synchronization: Influence of asymmetries in systems of two delay-coupled lasers*, Phys. Rev. E **83**, 056211 (2011).
- [HIC13] K. Hicke, M. Escalona, D. Brunner, M. C. Soriano, I. Fischer, and C. R. Mirasso: *Information processing using transient dynamics of semiconductor lasers subject to delayed feedback*, IEEE J. Sel. Top. Quantum Electron. **19** (2013).
- [HOH97] U. Hohenester and W. Pötz: *Density-matrix approach to nonequilibrium free-carrier screening in semiconductor*, Phys. Rev. B **56**, 13177 (1997).
- [HOH99b] A. Hohl, A. Gavrielides, T. Erneux, and V. Kovanis: *Quasiperiodic synchronization for two delay-coupled semiconductor lasers*, Phys. Rev. A **59**, 3941–3949 (1999).
- [HOP42] E. Hopf: *Abzweigung einer periodischen lösung von einer stationären lösung eines differentialsystems*, Ber.Math.-Phys. Klasse Sachs. Akad. Wiss. **94**, 1 (1942).
- [HOU18] Y. S. Hou, G. Q. Xia, W. Y. Yang, D. Wang, E. Jayaprasath, Z. Jiang, C. X. Hu, and Z. M. Wu: *Prediction performance of reservoir computing system based on a semiconductor laser subject to double optical feedback and optical injection*, Opt. Express **26**, 10211–10219 (2018).
- [HOY06] R. Hoyle: *Pattern Formation: An Introduction to Methods*, Cambridge Texts in Applied Mathematics (Cambridge University Press, 2006).
- [HUY99] G. Huyet, J. White, A. J. Kent, S. P. Hegarty, J. V. Moloney, and J. G. McInerney: *Dynamics of a semiconductor laser with optical feedback*, Phys. Rev. A **60**, 1534–1537 (1999).
- [WEI93] IEEE: *Results of the time series prediction competition at the Santa Fe Institute* (1993).
- [PRO05] IEEE: *Echo State Networks: Appeal and Challenges* (2005).
- [INU17] M. Inubushi and K. Yoshimura: *Reservoir computing beyond memory-nonlinearity trade-off*, Sci. Rep. **7**, 10199 (2017).
- [JAE01] H. Jaeger: *The ‘echo state’ approach to analysing and training recurrent neural networks*, GMD Report 148, GMD - German National Research Institute for Computer Science (2001).
- [JAE02] H. Jaeger: *Short term memory in echo state networks*, GMD Report 152, GMD - Forschungszentrum Informationstechnik GmbH (2002).

- [JAV03] J. Javaloyes, P. Mandel, and D. Pieroux: *Dynamical properties of lasers coupled face to face*, Phys. Rev. E **67**, 036201 (2003).
- [JIR13] P. Jiruska, M. de Curtis, J. G. R. Jefferys, C. A. Schevon, S. J. Schiff, and K. Schindler: *Synchronization and desynchronization in epilepsy: controversies and hypotheses*, J. Physiol. **591.4**, 787–797 (2013).
- [KAN90] K. Kaneko: *Clustering, coding, switching, hierarchical ordering, and control in a network of chaotic elements*, Physica D **41**, 137–172 (1990).
- [KAN08a] I. Kanter, E. Kopelowitz, and W. Kinzel: *Public channel cryptography: chaos synchronization and Hilbert’s tenth problem*, Phys. Rev. Lett. **101**, 84102 (2008).
- [KAN10a] I. Kanter, M. Butkovski, Y. Peleg, M. Zigzag, Y. Aviad, I. Reidler, M. Rosenbluh, and W. Kinzel: *Synchronization of random bit generators based on coupled chaotic lasers and application to cryptography*, Opt. Express **18**, 18292–18302 (2010).
- [KAP12] M. Kapitaniak, K. Czolczynski, P. Perlikowski, A. Stefanski, and T. Kapitaniak: *Synchronization of clocks*, Phys. Rep. **517**, 1 (2012).
- [KAR07] R. Karnatak, R. Ramaswamy, and A. Prasad: *Amplitude death in the absence of time delays in identical coupled oscillators*, Phys. Rev. E **76**, 035201(R) (2007).
- [KEU17] L. Keuninckx, J. Danckaert, and G. Van der Sande: *Real-time audio processing with a cascade of discrete-time delay line-based reservoir computers*, Cogn. Comput. **9** (2017).
- [KIM05] M. Kim, R. Roy, J. L. Aron, T. W. Carr, and I. B. Schwartz: *Scaling behavior of laser population dynamics with time-delayed coupling: Theory and experiment*, Phys. Rev. Lett. **94**, 088101 (2005).
- [KOM17] Y. Kominis, V. Kovanis, and T. Bountis: *Controllable asymmetric phase-locked states of the fundamental active photonic dimer*, Phys. Rev. A **96**, 043836 (2017).
- [KOS13] A. Koseska, E. Volkov, and J. Kurths: *Oscillation quenching mechanisms: Amplitude vs. oscillation death*, Phys. Rep. **531**, 173–199 (2013).
- [KOZ00] G. Kozyreff, A. G. Vladimirov, and P. Mandel: *Global coupling with time delay in an array of semiconductor lasers*, Phys. Rev. Lett. **85**, 3809 (2000).
- [KU15] W. L. Ku, M. Girvan, and E. Ott: *Dynamical transitions in large systems of mean field-coupled landau-stuart oscillators: Extensive chaos and cluster states*, Chaos **25** (2015).
- [KUR84] Y. Kuramoto: *Chemical Oscillations, Waves and Turbulence* (Springer-Verlag, Berlin, 1984).
- [KUR02a] Y. Kuramoto and D. Battogtokh: *Coexistence of Coherence and Incoherence in Nonlocally Coupled Phase Oscillators.*, Nonlin. Phen. in Complex Sys. **5**, 380–385 (2002).

- [KUZ95] Y. A. Kuznetsov: *Elements of Applied Bifurcation Theory* (Springer, New York, 1995).
- [LAN44] L. D. Landau: *On the problem of turbulence*, C. R. Acad. Sci. UESS **44**, 311 (1944).
- [LAN80b] R. Lang and K. Kobayashi: *External optical feedback effects on semiconductor injection laser properties*, IEEE J. Quantum Electron. **16**, 347–355 (1980).
- [LAR12] L. Larger, M. C. Soriano, D. Brunner, L. Appeltant, J. M. Gutierrez, L. Pesquera, C. R. Mirasso, and I. Fischer: *Photonic information processing beyond turing: an optoelectronic implementation of reservoir computing*, Opt. Express **20**, 3241–3249 (2012).
- [LAR17] L. Larger, A. Baylón-Fuentes, R. Martinenghi, V. S. Udaltsov, Y. K. Chembo, and M. Jacquot: *High-speed photonic reservoir computing using a time-delay-based architecture: Million words per second classification*, Phys. Rev. X **7**, 011015 (2017).
- [LAZ09a] A. Lazar, G. Pipa, and J. Triesch: *Sorn: a self-organizing recurrent neural network*, Front. Comput. Neurosci. **3**, 23 (2009).
- [LEE13] W. S. Lee, E. Ott, and T. M. Antonsen: *Phase and amplitude dynamics in large systems of coupled oscillators: Growth heterogeneity, nonlinear frequency shifts, and cluster states*, Chaos **23**, 033116 (2013).
- [LEH14] J. Lehnert, P. Hövel, A. A. Selivanov, A. L. Fradkov, and E. Schöll: *Controlling cluster synchronization by adapting the topology*, Phys. Rev. E **90**, 042914 (2014).
- [LEH15b] J. Lehnert: *Controlling synchronization patterns in complex networks*, Springer Theses (Springer, Heidelberg, 2016).
- [LEN85] D. Lenstra, B. Verbeek, and A. Den Boef: *Coherence collapse in single-mode semiconductor lasers due to optical feedback*, IEEE J. Quantum Electron. **21**, 674–679 (1985).
- [LIN12b] B. Lingnau, K. Lüdge, W. W. Chow, and E. Schöll: *Failure of the α -factor in describing dynamical instabilities and chaos in quantum-dot lasers*, Phys. Rev. E **86**, 065201(R) (2012).
- [LOR63] E. N. Lorenz: *Deterministic nonperiodic flow*, J. Atmos. Sci. **20**, 130 (1963).
- [LOT20] A. J. Lotka: *Analytical note on certain rhythmic relations in organic systems*, Proc. Natl. Acad. Sci. U.S.A. **6** (1920).
- [LUK09] M. Lukosevicius and H. Jaeger: *Reservoir computing approaches to recurrent neural network training*, Computer Science Review **3**, 127–149 (2009).
- [MAA02] W. Maass, T. Natschläger, and H. Markram: *Real-time computing without stable states: A new framework for neural computation based on perturbations*, Neural Comp. **14**, 2531 (2002).

- [MAI60] T. H. Maiman: *Stimulated optical radiation in ruby*, Nature **187**, 493 (1960).
- [MAI14a] Y. Maistrenko, B. Penkovsky, and M. Rosenblum: *Solitary state at the edge of synchrony in ensembles with attractive and repulsive interactions*, Phys. Rev. E **89**, 060901 (2014).
- [MAT90] P. C. Matthews and S. H. Strogatz: *Phase diagram for the collective behavior of limit-cycle oscillators*, Phys. Rev. Lett. **65**, 1701–1704 (1990).
- [MES15a] C. Mesaritakis, A. Bogris, A. Kapsalis, and D. Syvridis: *High-speed all-optical pattern recognition of dispersive fourier images through a photonic reservoir computing subsystem*, Opt. Lett. **40**, 3416–3419 (2015).
- [MIR96] C. R. Mirasso, P. Colet, and P. GarciaFernandez: *Synchronization of chaotic semiconductor lasers: Application to encoded communications*, IEEE Photon. Technol. Lett. **8**, 299–301 (1996).
- [MOR92] J. Mørk, B. Tromborg, and J. Mark: *Chaos in semiconductor lasers with optical feedback-Theory and experiment*, IEEE J. Quantum Electron. **28**, 93–108 (1992).
- [NAK93] K. Nakagawa and Y. Kuramoto: *Collective chaos in a population of globally coupled oscillators*, Prog. Theor. Phys. **89**, 313–323 (1993).
- [NAK94a] N. Nakagawa and Y. Kuramoto: *From collective oscillations to collective chaos in a globally coupled oscillator system*, Physica D **75**, 74–80 (1994).
- [NAK16] J. Nakayama, K. Kanno, and A. Uchida: *Laser dynamical reservoir computing with consistency: an approach of a chaos mask signal*, Opt. Express **24**, 8679–8692 (2016).
- [NAR17] M. Naruse, Y. Terashima, A. Uchida, and S. J. Kim: *Ultrafast photonic reinforcement learning based on laser chaos*, Sci. Rep. **7**, 8772 (2017).
- [NGU14] R. M. Nguimdo, G. Verschaffelt, J. Danckaert, and G. Van der Sande: *Fast photonic information processing using semiconductor lasers with delayed optical feedback: Role of phase dynamics*, Opt. Express **22**, 8672–8686 (2014).
- [NGU15] R. M. Nguimdo, G. Verschaffelt, J. Danckaert, and G. Van der Sande: *Simultaneous computation of two independent tasks using reservoir computing based on a single photonic nonlinear node with optical feedback*, IEEE Trans. Neural Netw. Learn. Syst. **26** (2015).
- [NGU16] R. M. Nguimdo, G. Verschaffelt, J. Danckaert, and G. Van der Sande: *Reducing the phase sensitivity of laser-based optical reservoir computing systems*, Opt. Express **24**, 1238–1252 (2016).
- [NGU17] R. M. Nguimdo, E. Lacot, O. Jacquin, O. Hugon, G. Van der Sande, and H. G. de Chatellus: *Prediction performance of reservoir computing systems based on a diode-pumped erbium-doped microchip laser subject to optical feedback*, Opt. Lett. **42** (2017).

- [NIX12] M. Nixon, M. Fridman, E. Ronen, A. A. Friesem, N. Davidson, and I. Kanter: *Controlling synchronization in large laser networks*, Phys. Rev. Lett. **108**, 214101 (2012).
- [OLI16] N. Oliver, L. Larger, and I. Fischer: *Consistency in experiments on multistable driven delay systems*, Chaos **26**, 103115 (2016).
- [OME16] I. Omelchenko, O. E. Omel'chenko, A. Zakharova, M. Wolfrum, and E. Schöll: *Tweezers for chimeras in small networks*, Phys. Rev. Lett. **116**, 114101 (2016).
- [OTT02] E. Ott: *Chaos in dynamical systems* (Cambridge University Press, Cambridge, 2002).
- [OZT07] M. Ozturk, D. Xu, and J. C. Principe: *Analysis and design of echo state networks for function approximation*, Neural Comput. **19** (2007).
- [PAQ12] Y. Paquot, F. Duport, A. Smerieri, J. Dambre, B. Schrauwen, M. Haelterman, and S. Massar: *Optoelectronic reservoir computing*, Sci. Rep. **2** (2012).
- [PAT17] J. Pathak, Z. Lu, B. Hunt, M. Girvan, and E. Ott: *Using machine learning to replicate chaotic attractors and calculate lyapunov exponents from data*, Chaos **27**, 121102 (2017).
- [PAT18] J. Pathak, B. Hunt, M. Girvan, Z. Lu, and E. Ott: *Model-free prediction of large spatiotemporally chaotic systems from data: A reservoir computing approach*, Phys. Rev. Lett. **120**, 024102 (2018).
- [PEA95] B. Pearlmutter: *Gradient calculations for dynamic recurrent neural networks: A survey*, IEEE T. Neural. Networ. **6**, 1212–1228 (1995).
- [POP05] O. Popovych, C. Hauptmann, and P. Tass: *Effective desynchronization by nonlinear delayed feedback*, Phys. Rev. Lett. **94**, 164102 (2005).
- [PRE92] W. H. Press, B. P. Flannery, S. A. Teukolsky, and W. T. Vetterling: *Numerical Recipes in C (2nd ed.)* (Cambridge University Press, Cambridge, 1992).
- [PRE07] W. H. Press, B. P. Flannery, S. A. Teukolsky, and W. T. Vetterling: *Numerical Recipes (3rd ed.)* (Cambridge University Press, Cambridge, 2007).
- [PYR92] K. Pyragas: *Continuous control of chaos by self-controlling feedback*, Phys. Lett. A **170**, 421 (1992).
- [RAM98a] D. V. Ramana Reddy, A. Sen, and G. L. Johnston: *Time delay induced death in coupled limit cycle oscillators*, Phys. Rev. Lett. **80**, 5109–5112 (1998).
- [RAM99] D. V. Ramana Reddy, A. Sen, and G. L. Johnston: *Time delay effects on coupled limit cycle oscillators at hopf bifurcation*, Physica D **129**, 15–34 (1999).
- [RAM00] D. V. Ramana Reddy, A. Sen, and G. L. Johnston: *Experimental evidence of time-delay-induced death in coupled limit-cycle oscillators*, Phys. Rev. Lett. **85**, 3381–3384 (2000).

- [ROG06] E. A. Rogers-Dakin, J. García-Ojalvo, D. J. DeShazer, and R. Roy: *Synchronization and symmetry breaking in mutually coupled fiber lasers*, Phys. Rev. E **73**, 045201 (2006).
- [ROD11] A. Rodan and P. Tiño: *Minimum complexity echo state network*, IEEE Trans. Neural Netw. **22** (2011).
- [ROD12] A. Rodan and P. Tiño: *Simple Deterministically Constructed Cycle Reservoirs with Regular Jumps*, Neural Computation **24**, 1822–1852 (2012).
- [ROE10a] B. Roeschies and C. Igel: *Structure optimization of reservoir networks*, Logic Journal of the IGPL **18**, 635–669 (2010).
- [ROE16] A. Röhm, F. Böhm, and K. Lüdge: *Small chimera states without multistability in a globally delay-coupled network of four lasers*, Phys. Rev. E **94**, 042204 (2016).
- [ROE18a] A. Röhm and K. Lüdge: *Multiplexed networks: reservoir computing with virtual and real nodes*, J. Phys. Commun. **2**, 085007 (2018).
- [ROE18x] A. Röhm and K. Lüdge: *Reservoir computing with delay in structured networks*, Proc. SPIE **10689** (2018).
- [ROE18] A. Röhm, K. Lüdge, and I. Schneider: *Bistability in two simple symmetrically coupled oscillators with symmetry-broken amplitude- and phase-locking*, Chaos **28**, 063114 (2018).
- [ROT07] V. Rottschäfer and B. Krauskopf: *The ECM-backbone of the Lang-Kobayashi equations: A geometric picture*, Int. J. Bifurcation Chaos **17**, 1575–1588 (2007).
- [SCH04g] U. Schiller and J. Steil: *Analyzing the weight dynamics of recurrent learning algorithms*, Neurocomputing **63**, 5–23 (2004).
- [SCH08k] B. Schrauwen, M. D’Haene, D. Verstraeten, and J. V. Campenhout: *Compact hardware liquid state machines on fpga for real-time speech recognition*, Neural Networks **21**, 511–523 (2008).
- [SCH08n] B. Schrauwen, M. Wardermann, D. Verstraeten, J. Steil, and D. Stroobandt: *Improving reservoirs using intrinsic plasticity*, Neurocomputing **71**, 1159–1171 (2008), Progress in Modeling, Theory, and Application of Computational Intelligence.
- [SCH13l] J. Schumacher, H. Toutounji, and G. Pipa: *An analytical approach to single node delay-coupled reservoir computing*. Conference: 23rd International Conference on Artificial Neural Networks (2013).
- [SCH14h] G. Schaller, C. Nietner, and T. Brandes: *Relaxation dynamics of meso-reservoirs*, New J. Phys. **16**, 125011 (2014).
- [SCH14a] L. Schmidt, K. Schönleber, K. Krischer, and V. García-Morales: *Coexistence of synchrony and incoherence in oscillatory media under nonlinear global coupling*, Chaos **24**, 013102 (2014).

- [SCH15e] L. Schmidt and K. Krischer: *Chimeras in globally coupled oscillatory systems: From ensembles of oscillators to spatially continuous media*, Chaos **25**, 064401 (2015).
- [SCH14g] L. Schmidt and K. Krischer: *Clustering as a prerequisite for chimera states in globally coupled systems*, Phys. Rev. Lett. **114**, 034101 (2015).
- [SCH15a] L. Schmidt and K. Krischer: *Clustering as a prerequisite for chimera states in globally coupled systems*, Phys. Rev. Lett. **114**, 034101 (2015).
- [SEI17] M. Seifikar, A. Amann, and F. H. Peters: *Emergence of stable two-colour states in mutually delay-coupled lasers*, EPJ Web of Conferences **139** (2017).
- [SEM17] N. Semenova, G. Strelkova, V. S. Anishchenko, and A. Zakharova: *Temporal intermittency and the lifetime of chimera states in ensembles of nonlocally coupled chaotic oscillators*, Chaos **27**, 061102 (2017).
- [SHI89] M. Shiino and M. Frankowicz: *Synchronization of infinitely many coupled limit-cycle type oscillators*, Physics Letters A **136**, 103–108 (1989).
- [SHI07a] S. B. Shim, M. Imboden, and P. Mohanty: *Synchronized oscillation in coupled nanomechanical oscillators*, Science **316**, 95–99 (2007).
- [SIL13d] H. O. Sillin, R. Aguilera, H. H. Shieh, A. V. Avizienis, M. Aono, A. Z. Stieg, and J. K. Gimzewski: *A theoretical and experimental study of neuromorphic atomic switch networks for reservoir computing*, Nanotechnology **24**, 384004 (2013).
- [SIL16] D. Silver, A. Huang, C. J. Maddison, A. Guez, L. Sifre, G. van den Driessche, J. Schrittwieser, I. Antonoglou, V. Panneershelvam, and M. Lancto: *Mastering the game of Go with deep neural networks and tree search*, Nature **91**, 484 (2016).
- [SIL17] D. Silver, J. Schrittwieser, K. Simonyan, I. Antonoglou, A. Huang, A. Guez, T. Hubert, L. Baker, M. Lai, A. Bolton, Y. Chen, T. Lillicrap, F. Hui, L. Sifre, G. van den Driessche, T. Graepel, and D. Hassabis: *Mastering the game of Go without human knowledge*, Nature **550**, 354 (2017).
- [SNY13] D. Snyder, A. Goudarzi, and C. Teuscher: *Computational capabilities of random automata networks for reservoir computing*, Phys. Rev. E **87**, 042808 (2013).
- [SOR13] M. C. Soriano, J. García-Ojalvo, C. R. Mirasso, and I. Fischer: *Complex photonics: Dynamics and applications of delay-coupled semiconductor lasers*, Rev. Mod. Phys. **85**, 421–470 (2013).
- [SOR13a] M. C. Soriano, S. Ortin, D. Brunner, L. Larger, C. R. Mirasso, I. Fischer, and L. Pesquera: *Optoelectronic reservoir computing: tackling noise-induced performance degradation*, Opt. Express **21**, 12–20 (2013).
- [SOR15] M. C. Soriano, S. Ortin, L. Keuninckx, L. Appeltant, J. Danckaert, L. Pesquera, and G. Van der Sande: *Delay-based reservoir computing: Noise effects in a combined analog and digital implementation*, IEEE Trans. Neural. Netw. Learn. Syst. **26**, 388–393 (2015).

- [SPO05] O. Sporns, G. Tononi, and R. Kötter: *The human connectome: a structural description of the human brain*, PLoS Comput. Biol. **1**, e42 (2005).
- [STE07c] J. Steil: *Online reservoir adaptation by intrinsic plasticity for backpropagation-decorrelation and echo state learning*, Neural Netw. **20**, 353 (2007).
- [STR94a] S. H. Strogatz: *Nonlinear Dynamics and Chaos* (Westview Press, Cambridge, MA, 1994).
- [STR98a] S. H. Strogatz: *Nonlinear dynamics: Death by delay*, Nature **394**, 316 (1998).
- [STU60] J. T. Stuart: *On the non-linear mechanics of wave disturbances in stable and unstable parallel flows part 1. the basic behaviour in plane poiseuille flow*, J. Fluid Mech. **9**, 353 (1960).
- [THO90a] S. Thompson: *Stepsize control for delay differential equations using continuously imbedded runge-kutta methods of sarafyan*, J. Comput. Appl. Math. **31**, 267–275 (1990).
- [TIN13] P. Tino and A. Rodan: *Short term memory in input-driven linear dynamical systems*, Neurocomputing **112**, 58–63 (2013), Advances in artificial neural networks, machine learning, and computational intelligence.
- [TOT15] J. Tetz, R. Snari, D. Yengi, M. Tinsley, H. Engel, and K. Showalter: *Phase-lag synchronization in networks of coupled chemical oscillators*, Phys. Rev. E **92**, 022819 (2015).
- [TUR36] A. M. Turing: *On computable numbers, with an application to the Entscheidungsproblem*, Proc. London Math. Soc. **s2-42**, 230–265 (1936).
- [UCH08] A. Uchida, K. Amano, M. Inoue, K. Hirano, S. Naito, H. Someya, I. Oowada, T. Kurashige, M. Shiki, S. Yoshimori, K. Yoshimura, and P. Davis: *Fast physical random bit generation with chaotic semiconductor lasers*, Nat. Photonics **2**, 728 (2008).
- [USH05] O. V. Ushakov, H. J. Wünsche, F. Henneberger, I. A. Khovanov, L. Schimansky-Geier, and M. A. Zaks: *Coherence resonance near a Hopf bifurcation*, Phys. Rev. Lett. **95**, 123903 (2005).
- [VAN08a] K. Vandoorne, W. Dierckx, B. Schrauwen, D. Verstraeten, R. Baets, P. Bienstman, and J. V. Campenhout: *Toward optical signal processing using photonic reservoir computing*, Opt. Express **16**, 11182 (2008).
- [VAN11c] K. Vandoorne, J. Dambre, D. Verstraeten, B. Schrauwen, and P. Bienstman: *Parallel reservoir computing using optical amplifiers*, IEEE Trans. Neural Netw. **22**, 1469–1481 (2011).
- [VAN14] K. Vandoorne, P. Mechet, T. Van Vaerenbergh, M. Fiers, G. Morthier, D. Verstraeten, B. Schrauwen, J. Dambre, and P. Bienstman: *Experimental demonstration of reservoir computing on a silicon photonics chip*, Nat. Commun. **5** (2014).

- [SAN17a] G. Van der Sande, D. Brunner, and M. C. Soriano: *Advances in photonic reservoir computing*, *Nanophotonics* **6**, 561 (2017).
- [VER07] D. Verstraeten, B. Schrauwen, M. D’Haene, and D. Stroobandt: *An experimental unification of reservoir computing methods*, *Neural Netw.* **20**, 391–403 (2007).
- [VER17] G. Verschaffelt, M. Khoder, and G. Van der Sande: *Random number generator based on an integrated laser with on-chip optical feedback*, *Chaos* **27**, 114310 (2017).
- [VIN15] Q. Vinckier, F. Duport, A. Smerieri, K. Vandoorne, P. Bienstman, M. Haelterman, and S. Massar: *High-performance photonic reservoir computer based on a coherently driven passive cavity*, *Optica* **2** (2015).
- [VOL26a] V. Volterra: *Fluctuations in the abundance of a species considered mathematically*, *Nature* **118**, 558–560 (1926).
- [VAN95] G. H. M. van Tartwijk, A. M. Levine, and D. Lenstra: *Sisyphus effect in semiconductor lasers with optical feedback*, *IEEE J. Sel. Top. Quantum Electron.* **1**, 466–472 (1995).
- [WAN88] S. S. Wang and H. G. Winful: *Dynamics of phase-locked semiconductor laser arrays*, *Appl. Phys. Lett.* **52**, 1774–1776 (1988).
- [WEI92] J. Weiner, R. Holz, F. W. Schneider, and K. Bar-Eli: *Mutually coupled oscillators with time delay*, *J. Phys. Chem.* **96**, 8915–8919 (1992).
- [WIN88] H. G. Winful and S. S. Wang: *Stability of phase locking in coupled semiconductor laser arrays*, *Appl. Phys. Lett.* **53** (1988).
- [WIT12] D. Witthaut and M. Timme: *Braess’s paradox in oscillator networks, desynchronization and power outage*, *New J. Phys.* **14**, 083036 (2012).
- [WOL02] M. Wolfrum and D. V. Turaev: *Instabilities of lasers with moderately delayed optical feedback*, *Opt. Commun.* **212**, 127–138 (2002).
- [WOL11] M. Wolfrum and O. E. Omel’chenko: *Chimera states are chaotic transients*, *Phys. Rev. E* **84**, 015201 (2011).
- [YAM84a] Y. Yamaguchi and H. Shimizu: *Theory of self-synchronization in the presence of native frequency distribution and external noises*, *Physica D* **11**, 212–226 (1984).
- [YAM13] T. Yamazaki and J. Igarashi: *Realtime cerebellum: A large-scale spiking network model of the cerebellum that runs in realtime using a graphics processing unit*, *Neural Netw.* **47**, 103–111 (2013), *Computation in the Cerebellum*.
- [YAN04c] S. Yanchuk, K. R. Schneider, and L. Recke: *Dynamics of two mutually coupled semiconductor lasers: Instantaneous coupling limit*, *Phys. Rev. E* **69**, 056221 (2004).

- [YAN09] S. Yanchuk and P. Perlikowski: *Delay and periodicity*, Phys. Rev. E **79**, 046221 (2009).
- [ZAK13] A. Zakharova, A. Feoktistov, T. Vadivasova, and E. Schöll: *Coherence resonance and stochastic synchronization in a nonlinear circuit near a subcritical Hopf bifurcation*, Eur. Phys. J. ST **222**, 2481–2495 (2013).
- [ZAK14] A. Zakharova, M. Kapeller, and E. Schöll: *Chimera death: Symmetry breaking in dynamical networks*, Phys. Rev. Lett. **112**, 154101 (2014).
- [ZAK15b] A. Zakharova, M. Kapeller, and E. Schöll: *Amplitude chimeras and chimera death in dynamical networks*, J. Phys. Conf. Ser. **727**, 012018 (2016).
- [ZHA64] A. M. Zhabotinskii: *Periodic processes of the oxidation of malonic acid in solution*, Biofizika **9**, 306 (1964).

Acknowledgements

I would like to thank Prof. Kathy Lüdge for her supervision and support during the creation of this thesis. I would also like to thank Prof. Eckehard Schöll, Yulia Jagodzinski and Roland Aust for providing a fruitful scientific environment in the shape of the ‘Collaborative Research Center 910: Control of self-organizing nonlinear systems: Theoretical methods and concepts of application’, especially the monthly ‘Symposia’, and the Deutsche Forschungsgemeinschaft for their financial support. I have also greatly profited from the lessons and workshops of the ‘School of Nanophotonics’ of the CRC787 led by Prof. Kneissl.

I am grateful to all the members of my workgroup: To Dr. Lina Jaurigue for many discussions, to Dr. Benjamin Lingnau for his readiness in always assisting, to Christoph Redlich for being an excellent office partner. I would also like to thank Benjamin Miller, David Schicke, Cheng Wang, Larissa Bauer, Dr. Anna Zakharova, Dr. Iryna Omelchenko, Paul Geffert, Andrej Krimlowski, Vivien Londe, Oliver Esser, Stefan Meinecke, Jan Hausen and Miriam Wegert for being supportive and providing a friendly work environment. I would like to thank Jonas Albrecht in particular for finding a nasty bug in my code. I would like to thank my collaborators on past and future scientific publishing: Dr. Isabelle Schneider, Florian Stelzer and Serhiy Yanchuk. I would like to thank my sister and my family for being supportive throughout these last years.

Eigenständigkeitserklärung

Ich versichere, dass ich die vorgelegte Dissertation eigenständig und ohne fremde Hilfe verfasst, keine andere als die angegebenen Quellen verwendet und die benutzten Quellen entnommenen Passagen als solche kenntlich gemacht habe. Diese Arbeit wurde in dieser oder ähnlicher Form bei keinem anderen Lehrstuhl als Dissertation vorgelegt.

Ort, Datum

Unterschrift